Dissertation

submitted to

the Combined Faculties of the Natural Sciences and Mathematics

of the Ruperto-Carola-University of Heidelberg, Germany

for the degree of

Doctor of Natural Sciences

Put forward by

Natascha Margarita Rosa Elisabeth Rupp

born in Herbolzheim im Breisgau

Oral examination on 13th January, 2021

Radon Induced Background in the XENON1T Dark Matter Search Experiment and Studies on Xenon Purity in the HeXe System

Referees:

Priv.-Doz. Dr. Teresa Marrodán Undagoitia

JProf. Dr. Loredana Gastaldo

Illuminating the dark:
my parents, sisters and faithful companions.
Thank you for the support in the last years.

Abstract

The XENON1T experiment is aiming for the direct detection of dark matter in the form of weakly interacting massive particles (WIMPs) scattering off xenon nuclei. Detecting these rarely-interacting particles requires an unprecedented low background level. In XENON1T, the noble gas ^{222}Rn induces the dominant background, either as electronic recoil (ER) background admixed in the liquid xenon (LXe) volume or as surface background on the Time-Projection-Chamber's (TPC) wall. In the first part of this thesis, we constrain the amount of ^{222}Rn induced ER background during the complete run-time of the experiment. We furthermore survey the considerable ^{222}Rn reduction during the XENON1T operation, resulting in a final activity concentration of $(4.5 \pm 0.1)\,\mu\mathrm{Bq/kg}$, the lowest one ever achieved in a LXe dark matter experiment. Conclusions drawn are relevant not only for the interpretation of the background level in XENON1T, but also for the next-generation experiment XENONnT. The ^{222}Rn induced surface background can be removed from the PTFE (Polytetrafluoroethylene) wall of the TPC by dedicated surface cleaning methods based on $32\,\%$ HNO_3. In the second part of this work, we constructed a small-scale LXe TPC, the HeXe set-up, to test for the first time if a PTFE surface cleaning based on $32\,\%$ HNO_3 degrades the xenon purity and the performance of a TPC. No degradation of the xenon purity is observed within the system's sensitivity, indicating that $32\,\%$ HNO_3 is a promising candidate for PTFE surface cleaning in LXe TPCs. Our result lays the groundwork for future research towards confirming that the treatment is applicable in large-scale LXe detectors.

Zusammenfassung

Das XENON1T Experiment hat den direkten Nachweis von dunkler Materie zum Ziel, in Form von schwach wechselwirkenden massiven Teilchen (engl. WIMPs), die mit Xenon Atomkernen stoßen. Um diese sehr selten wechselwirkenden Teilchen zu detektieren, muss der Untergrund auf ein zuvor unerreichtes Level minimiert werden. Das Edelgas ^{222}Rn verursacht den dominierenden Untergrund in XENON1T. Zum einen hervorgerufen durch Stöße mit den Xenon Hüllenelektronen (engl. ER) im Flüssig-Xenon (engl. LXe) Volumen und zum anderen als Oberflächenuntergrund an den Wänden der Spurendriftkammer (engl. TPC). Im ersten Teil der Arbeit schränken wir den Anteil des ^{222}Rn verursachten ER Untergrundes ein, und zwar über die gesamte Messdauer des Experiments. Zudem quantifizieren wir die betächtliche Reduzierung des ^{222}Rn Levels während des Experiments, die zu einer finalen Aktivitätskonzentration von $(4.5 \pm 0.1)\,\mu\mathrm{Bq/kg}$ führt, dem niedrigsten jemals erreichten Wert in einem LXe dunkle Materie Experiment. Die daraus gezogenen Schlussfolgerungen sind nicht nur für die Interpretation des Untergrunds in XENON1T wichtig, sondern auch für das zukünftige XENONnT Experiment. Der ^{222}Rn verursachte Oberflächenuntergrund auf den PTFE (Polytetrafluorethylen) Wänden der TPC kann durch eine auf $32\,\%$ HNO_3 basierenden Oberflächenbehandlung entfernt werden. Im zweiten Teil dieser Arbeit bauen wir eine kleine LXe TPC, HeXe-Aufbau genannt, um zum ersten Mal den Einfluss einer auf $32\,\%$ HNO_3 basierenden Oberflächenbehandlung auf die Xenon Reinheit und die TPC Leistungsfähigkeit zu testen. Innerhalb der Sensitivitätsgrenze der TPC haben wir keine Xenon Verunreinigung beobachtet, was $32\,\%$ HNO_3 zu einer vielversprechenden Oberflächenreinigungsmöglichkeit in LXe TPCs macht. Unser Ergebnis legt den Grundstein für weitere Messungen zur Bestätigung, dass die Oberflächenbehandlung auch für großen LXe Detektoren geeignet ist.

List of Publications and Author's Contribution

The following publications, referred to in the text by their Roman numerals, are included in this thesis. Co-authored XENON1T consortium publications are not listed.

Publication I:

- E. Aprile et al. (XENON Collaboration), "^{222}Rn emanation measurements for the XENON1T experiment", *arXiv:2009.13981v2* (under review in the European Physical Journal C), 2020.
- I analysed the XENON1T data belonging to the presented ^{222}Rn and ^{218}Po evolutions as part of this thesis. In addition, I performed ^{222}Rn emanation measurements of the XENON1T detector as part of my Master thesis that are included in this publication. I wrote major parts of the manuscript and I am one of the two corresponding authors.

Publication II:

- S. Bruenner et al., "Radon daughter removal from PTFE surfaces and its application in liquid xenon detectors", *arXiv:2009.08828v1* (under review in the European Physical Journal C), 2020.
- I majorly contributed to the design, construction and commissioning of the HeXe TPC at MPIK. With this TPC, I performed measurements of the xenon purity and I supplied the data analysis of the presented results. I wrote major parts of the manuscript and I am one of the two corresponding authors.

Publication III:

- N. Rupp, "Radon background in liquid xenon detectors", *JINST 13 (2018) no.02, C02001*, 2018.
- This proceedings paper summarizes the talk I gave at the conference "LIDINE 2017: LIght Detection In Noble Elements" at SLAC National Accelerator Laboratory. It summarizes and explains methods to determine the radon level before detector assembling and radon removal techniques during detector operation.

Contents

Chapter 1

The Quest for Dark Matter

Not being described by the Standard Model of Particle Physics, the nature of dark matter is one of the biggest questions in modern Particle Physics. This thesis is carried out in the framework of the search for dark matter. In the following sections, we want to give a brief introduction on dark matter and the experiments that search for it by direct detection methods as XENON1T. Thereby, we do not aim for a complete description and we refer to [1, 2] for a general overview and to detailed reviews on direct dark matter detection [3, 4] for more information.

1.1 Evidence for dark matter

Historically, the first indications for dark matter arose from astronomical observations. In 1933, the astronomer Zwicky investigated the velocity dispersion of the galaxies in the Coma cluster [5]. It was so high that, to keep the system stable, the average mass density in the system would have to be much higher than the deduced one from the observed visible matter. Further indications were found by studying the rotation curves of galaxies. They are diagrams that represent the orbital velocity of gas and stars in galaxies as function of their distance r to the galactic center. From Newtonian motion, one would expect that the rotation velocity v of objects in a gravitational potential is described as $v \propto 1/\sqrt{r}$. Instead, the rotational velocity was found to stay constant as the radius increases [6]. Both observations, the high velocity in clusters and the rotational curves of galaxies, can be explained by an uniformly-distributed halo of dark matter. An alternative approach to explain these observations is to assume a modified theory of Newtonian gravity (MOND) [7]. However, on larger scales such as the CMB structure (described below), MOND cannot be confirmed [8].

Another observational evidence for dark matter comes from gravitational lensing [9, 10]. It describes the deflection of light by massive objects which results in different typologies, such as object deformations, multiple images or Einstein rings [11]. By

measuring the degree of this deflection, the amount of mass that causes the deflection can be calculated. This value is then compared to the mass that is determined from the sum of all luminous objects inside the lens radius. The obtained discrepancy between the two mass values can be explained by some type of invisible matter component. Gravitational lensing is also used to identify the mass center in relics of galaxy-cluster collisions. By comparing the mass center to the measured center of luminous matter, one identifies a clear separation among them, most famously in the "Bullet-Cluster" [12, 13]. It is interpreted such that the ordinary matter interacted during the collision, whereby the dark matter centers could pervade unaffected due to their small or non-existent self-interaction cross-section. It also shows that dark matter interacts certainly not electromagnetically, since this would lead to the emission of detectable photons, which are not observed.

One of the strongest indications for the existence of dark matter are the temperature anisotropies observed in the cosmic microwave background (CMB). The CMB is constituted by the photons that started to stream freely, once the Universe became transparent for optical wavelengths and cooled down to an average temperature of $\sim 2.7\,\mathrm{K}$ nowadays, due to the expansion of the Universe. The exact CMB spectrum was measured initially by the COBE satellite [14] and then, with a higher accuracy by the WMAP [15] and the PLANCK satellite [16]. The CMB exhibits small temperature fluctuations at $\mathcal{O}(10^{-5}\mathrm{K})$, created by oscillations of the baryon-photon fluid and dark matter. To study their cause, one calculates the average temperature difference between two points on the CMB sphere as a function of their angular distance. This result, expanded in spherical harmonics is shown in Fig. 1.1 as a function of multipole l. This power spectrum can be evaluated by the ΛCDM model (Λ cold dark matter), a six parameter model that describes, among others, the amount of dark matter, dark energy and baryonic matter in the Universe. Thereby, Λ stands for the cosmological constant that is associated to the dark energy. The model predicts that the dark matter component is $\sim 26\,\%$ of the Universe's energy content. Around $69\,\%$ are due to dark energy, responsible for the accelerated expansion of the Universe. Hence, only $5\,\%$ is made of baryonic matter. Furthermore, the temperature fluctuations in the CMB represent small overdensities in the early Universe that tend to grow due to gravitational attraction. The resulting structure formation of the Universe, modeled with N-body simulations, can be explained with the presence of cold dark matter. These simulations of the cosmic web match the observation of galaxy surveys [17, 18].

1.2 Particle candidates

From the cosmological observations, constraints on the nature of dark matter particles are set. They are expected to interact gravitationally, feature weak or no self-

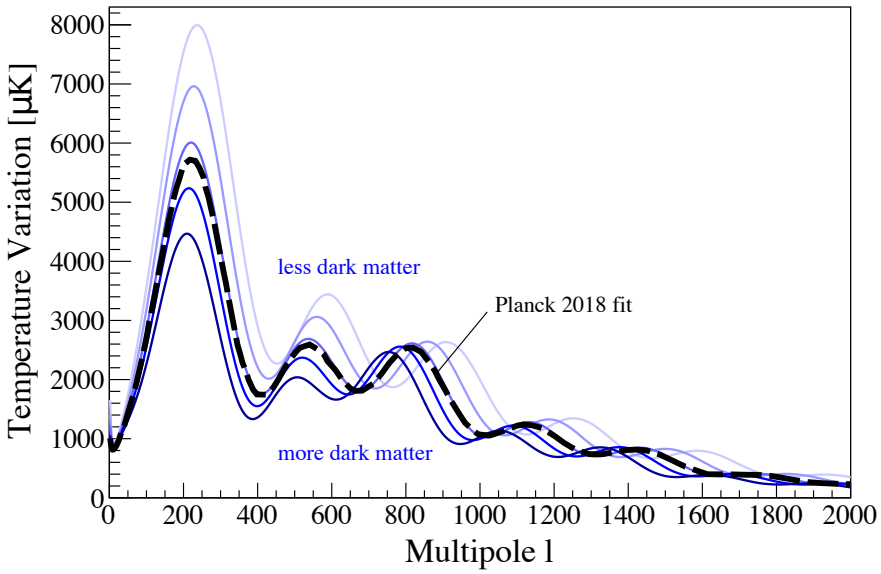

Figure 1.1: Temperature power spectrum of the cosmic microwave background (CMB) for a cold dark matter density contribution Ω_{CDM} varying between 0.11 and and 0.43 (blue lines). All all other input parameters of the model are kept constant. The dashed black line shows the best fit to the Planck data from the 2018 release [16]. Small (large) multipole l correspond to large (small) angular scales: the main acoustic peak at $l \sim 200$ is at $\sim 1°$; $l = 1800$ corresponds to $\sim 0.1°$. Figure taken from [3].

interaction and they are neutral. Since the effect of dark matter is observed over the entire age of the Universe, the dark matter particles must be stable on these time scales. Furthermore, their free streaming length must be small, and they have to account of the observed gravitational potentials. The majority of the dark matter has to be non-baryonic, since the derived baryon density from the CMB agrees well with the value obtained from existing models of nucleosynthesis. Within the Standard Model of Particle Physics, these constraints would be fulfilled by neutrinos, in case their mass was larger and their free streaming path smaller, so that they could account for the structure formation on the galactic and intergalactic scales [19, 20]. Several extensions of the Standard Model of Particle Physics are suggested that could also provide a dark matter particle candidate. Among them are sterile neutrinos, introduced to explain the small masses of the three observed neutrinos [21] and axions or axion like particles (ALPs), that are proposed to solve the strong CP-problem [22]. Another candidate is the so-called weakly interacting massive particle (WIMP). It is assumed that WIMPs are in thermal equilibrium in the early Universe, since they have small but appreciable interaction with Standard Model particles. As they move with non-relativistic velocities, they are a prime candidate for cold dark matter. If the WIMP mass is around the weak scale and if WIMP particles couple with Standard Model particles with a strength similar to that of the Standard Model electroweak interactions, these assump-

tions would lead to the observed dark matter relic density [23]. This scenario is called the "WIMP miracle". Independent of this cosmological predictions, the WIMP also arises naturally in many theories beyond the Standard Model. Two candidates are e.g. the lightest supersymmetric particle (LSP) in supersymmetry theories or the lightest Kaluza-Klein particle (LKP) in theories with extra spacetime dimensions [24, 25]. The WIMP constitutes a rather model-indepedent class of dark matter particles with interaction expected cross-section in the range of 10^{-41} to $10^{-51}\,\mathrm{cm}^2$ and masses from ~ 1 to $\sim 10^5\,\mathrm{GeV/c}^2$ [26]. It is a widely studied dark matter candidate and the main target of the XENON1T dark matter searches. Therefore, we will focus on it in the following.

1.3 Detection methods

The search for dark matter is a multidisciplinary effort that involves different experimental detection techniques. In Fig. 1.2 the potential interactions of a dark matter particle χ and a Standard Model particle P are shown. One approach are collider searches that aim to detect the dark matter particles produced in the particle collisions. Indirect detection experiments seek detection of dark matter via decay or annihilation into Standard Model particles. Lastly, direct detection experiments are designed to observe the scattering of dark matter particles with ordinary matter.

Dark matter particles will not create a visible signal in collider experiments such as ATLAS [27] or CMS [28] at the LHC, due to their weak interaction with Standard Model particles. However, the presence of dark matter can be inferred from transverse momentum conservation. The net momentum in the perpendicular plane of the two colliding beams must be conserved. An imbalance, termed missing transverse momentum or energy, is the main hint for direct dark matter production. Collider searches are only able to ascertain the dark matter stability on the timescale required for these particles to exit the detector. The big advantage of collider experiments is that they are not affected by astrophysical backgrounds and associated uncertainties. A review on these searches at the LHC can be found in [29].

The self-annihilation of dark matter particles or their decay is predicted to create γ-rays, neutrinos, positrons, antiprotons or even antinuclei. Typically, these potential dark matter signatures are investigated in experiments that perform sky surveys in γ-rays or that measure the cosmic-ray intensities and composition. There are celestial regions where dark matter searches are more promising. The gravitational based accumulation of dark matter particles in e.g. the galaxies center or stars enhances the probability of self-annihilation or decay into Standard Model particles, creating a measurable particle flux. Indirect dark matter searches require a profound understanding of the astrophysical background, the dark matter distribution and the uncertainty on

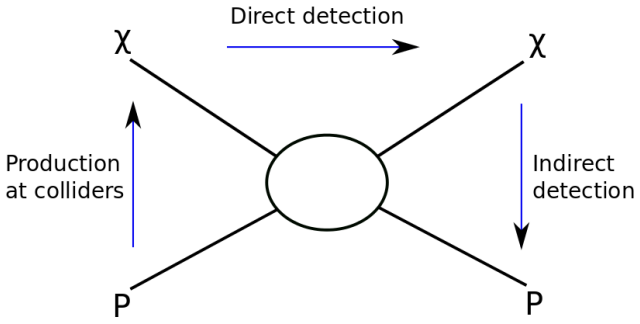

Figure 1.2: Schematic showing the possible detection channel for dark matter particles χ and Standard Model particles p, as detailed in the text. Figure taken from [4].

the imposed dark matter model. More information on this detection technique are e.g. found in [30].

The scattering of a dark matter particle off a Standard Model particle, probed in direct detection experiments, would investigate the direct coupling to the constituents of the ordinary matter. We will discuss this detection technique in more detail in the subsequent sections, as it is in the focus of the present work. The discussion follows at large part the detailed reviews on direct detection experiments, found in [3,4].

1.4 Recoil rate in direct search experiments

In most models, it is assumed that the WIMP will elastically scatter off the atomic nucleus in the target material used in the specific direct detection experiment. The momentum transfer creates a nuclear recoil, which might be measurable.

In the Standard Halo Model (SHM), the Earth is moving through a halo of dark matter particles with mass m_χ and a local dark matter density ρ. It is assumed that the dark matter halo is an isothermal sphere with an isotropic velocity distribution $f(\mathbf{v})$, parameterized at first approximation by a Maxwellian function and centered in the rest frame of the galaxy. The expected differential event rate in direct detection experiments is then expressed as

$$\frac{dR}{dE}(E,t) = \frac{\rho}{m_\chi \cdot m_N} \cdot \int_{v_{min}}^{v_{esc}} v \cdot f(\mathbf{v}) \cdot \frac{d\sigma}{dE}(E,v)\, d^3v \tag{1.4.1}$$

where $\frac{d\sigma}{dE}(E,v)$ is the differential dark matter cross-section and m_N is the mass of the target nucleus [31]. The lower integration bound is the minimal velocity

$$v_{min}(E_{th}) = \sqrt{\frac{m_N \cdot E_{th}}{2\mu^2}} \tag{1.4.2}$$

a dark matter particle must have to cause a detectable recoil. E_{th} is the energy threshold of the detector and μ is the reduced mass of the WIMP-nucleus system. The upper integral bound is the escape velocity v_{esc} at which the dark matter particles overcome the gravitational bound from the Milky Way. For direct detection experiments the parameters of interest are σ and m_χ. The other parameters are inferred from astrophysical measurements. Even though more recent measurements are available [31], one commonly uses $v_{esc} = 544\,\mathrm{km/s}$ and $\rho = 0.3\,\mathrm{GeV/c^2cm^3}$ for a simplified result comparison of different experiments. The most common approach in direct detection experiments is the attempt to measure the energy spectrum of dark matter interactions. The typical recoil energy is expected to be $\mathcal{O}(10\mathrm{keV})$ only, whereby the largest contribution to the rate in detectors is at low recoil energies, due to the exponentially decreasing energy spectrum towards high energies.

Another attempt for dark matter detection is the investigation of the signal rate modulation during one year, which is expected to follow a cosine function. It is caused by the relative motion of the solar system through the dark matter halo and the Earth rotation around the Sun [32]. A further approach is to measure the characteristic directionality of nuclear recoils tracks within the detector. In the local coordinate system of an earthbound detector, the dark matter particles are expected to come from a preferred direction, approximately the Cygnus constellation. This results supposedly in an asymmetry in the number of events scattering in the backward and forward direction [33].

Beside the assumptions on the astrophysical content, the specific models on particle and nuclear physics affect the expected signal signature in direct detection experiments. The WIMP is expected to couple to the quarks, the constituents of protons and neutrons that are contained in the target nucleus. Thereby, one differentiates between spin-independent (SI) or spin-dependent (SD) interactions and the differential cross-section in Eq. 1.4 takes the following form

$$\frac{d\sigma}{dE} = \frac{m_N}{2\mu^2 v^2} \cdot \left(\sigma_0^{SI} \cdot F_{SI}^2(E) + \sigma_0^{SD} \cdot F_{SD}^2(E)\right) \ . \tag{1.4.3}$$

In SD-interactions only unpaired nucleons contribute, whereas in SI-interactions the contribution from both neutrons and protons is considered. The parameter σ_0 de-

scribes the WIMP-nucleus cross-section at zero momentum transfer q. At small q, all partial waves of the nucleus add up and the WIMP scatters coherently with the entire nucleus. At higher q, the de Boglie wavelengths of the WIMP is smaller and only a part of the nucleon contributes to the interaction. This loss of coherence is accounted for by the form factors F(E). For SI-interactions we have

$$\sigma_0^{SI} \propto (Z \cdot f^p + (Z + A) \cdot f^n)^2, \tag{1.4.4}$$

where A is the atomic and Z the mass number of the target nucleus. The parameter f^p and f^n refer to the SI WIMP-proton and WIMP-neutron coupling, respectively. Typically, one assumes $f^p = f^n$. The resulting proportionality of σ_0^{SI} to the mass number A^2 is the reason why many direct detection experiments employ a target material with a high atomic mass, such as germanium ($A = 72$) or xenon ($A = 129$). In case of the SD-interactions, the cross-section at zero momentum transfer becomes

$$\sigma_0^{SD} \propto \frac{(J+1)}{J} \cdot \left(a_p \cdot \langle S^p \rangle + a_n \cdot \langle S^n \rangle\right)^2 \ . \tag{1.4.5}$$

The parameter J corresponds to the nuclear spin, a_p (a_n) is the effect proton (neutron) coupling and $\langle S^p \rangle$ ($\langle S^n \rangle$) refers to the expectation value of the nuclear spin content of the protons (neutrons) in the nucleus. In probing SD-scattering, only the nucleus' spin structure is relevant and not its atomic number, as in the case of SI-interactions. By employing e.g. natural xenon as target material one can prope the SD-cross-section since it contains xenon isotopes with non-zero nuclear spin.

1.5 Current status of direct detection experiments

Since an extremely low signal rate is expected from dark matter interactions, an extraordinarily low background environment is required for the detection. To suppress background arising from cosmic-rays, direct detection experiments are typically located in deep underground laboratories. Environmental neutron and γ-background is reduced by passive shielding or an active veto. More dangerous than the external background are intrinsic contamination that are distributed within the target material. Another source of background arises from the coherent neutrino-nulceus scattering from solar and atmospheric neutrinos. This irreducible background will eventually limit the sensitivity of direct detection experiments [34].

In most direct dark matter experiments, the particles' energy deposition is converted into either thermal motion (phonons), ionization (charge) or excitation (scintillation photons) of the target material. The relative size of these signals depends on the deposited energy and the interaction type. To date, direct detection experiments can read

up to two of these detection channels simultaneously. This leads to a more powerful discrimination between different interaction types and the suppression of background events. The timing shape of the involved energy depositions is a further possibility to reject background events.

Detectors employing noble liquids are spearheading for WIMP searches in the mass range above $\sim 6\,\mathrm{GeV/c^2}$. Argon and xenon are the two types of noble elements that are widely used in direct detection experiment. In dual-phase time projection chambers (TPCs), that are filled with the liquid noble element and a gaseous phase on top, the excitation (S1) and ionization (S2) signal can be read out (called S1-S2 NR search). In single-phase detectors only the scintillation photons are detected. In Fig. 1.3, the leading direct detection limits on spin-independent WIMP-nuleon cross-sections versus the WIMP mass are shown. Currently, the most stringent limits at WIMP masses above $\sim 6\,\mathrm{GeV/c^2}$ are placed by the dual-phase liquid xenon TPCs of XENON1T, LUX and PandaX-II [35–37] .

Crystalline detectors allow for the measurement of heat signal from phonons, by detecting the temperature increase caused by a particle interaction. The detection sensitivity is enhanced when operating the crystal at cryogenic temperatures. In addition, modern cryogenic experiments also measure a second signal channel, which can be either ionization or scintillation. The main advantage of this detection technique is the precise energy measurement and the low detection threshold, allowing for the search of WIMPs with light masses. Ge-crystals are employed by the EDELWEISS and (Super)CDMS experiments to read out the charge and phonon signals [38, 39]. The CRESST-III experiment uses $CaWO_4$-crystals, detecting phonons and scintillation light. In Fig. 1.3, the experiment's limit on spin-independent WIMP - nucleon cross sections is shown, based on the S1-S2 NR search [40].

There is another approach in noble element TPCs to extend the dark matter search beyond light WIMP masses $\lesssim 6\,\mathrm{GeV/c^2}$. These light dark matter particles cannot transfer enough energy to the argon or xenon nuclei to yield a measurable scintillation light at a sufficient rate. In contrast, the induced nuclear recoils still produce enough ionization signals in the medium to be detected (called S2-only NR search). This allows to lower the detection threshold of noble element detectors to a comparable level as in cryogenic experiments. The most stringent limits, based on this ionization-signal only, are placed by DarkSide-50 and XENON1T Collaboration in a mass range from $1.8\,\mathrm{GeV/c^2}$ to $6\,\mathrm{GeV/c^2}$ [41, 42], as illustrated in Fig. 1.3.

The dark matter search can be extended to even lower particle masses, by measuring the secondary radiation (Bremstrahlung [43] and the Migdal effect [44]) that ac-

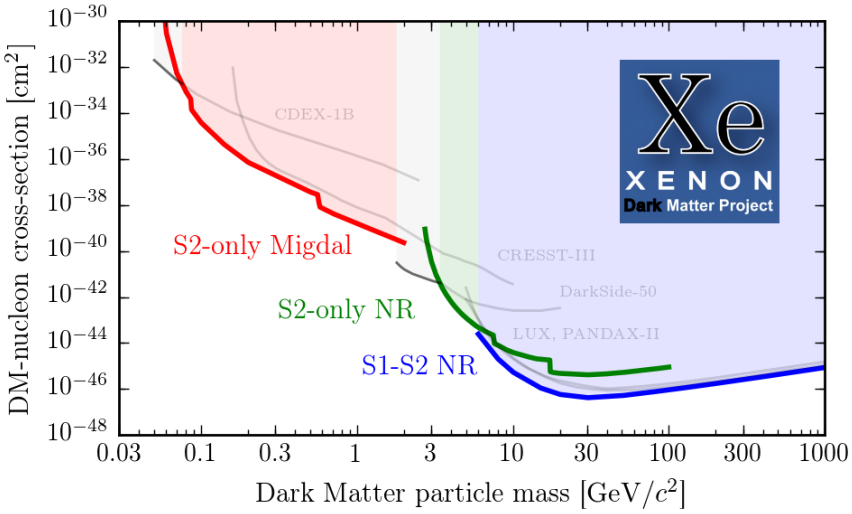

Figure 1.3: The current status of the experimental parameter space of WIMP - nucleon cross sections. Not all published results are shown. The red [45], green [42] and blue [35] curves illustrate the limits set by the XENON1T experiment applying different analysis methods, as explained in the text. Other shown limits are set by CDEX-1B [46], CRESST-III [40], DarkSide-50 [41], LUX [36] and PandaX-II [37]. Figure courtesy of Jelle Aalbers.

companies the elastic nuclear scattering of a dark matter particles. In liquid noble element experiment, this radiation interacts with the atomic electrons, generating *electronic recoils*. The most stringent limit on the spin-independent WIMP-nucleon interaction cross-section for masses between $0.085\,\mathrm{GeV}/c^2$ and $1.8\,\mathrm{GeV}/c^2$ is placed by the XENON1T Collaboration, by measuring the ionization signal only of the generated electronic recoils [45]. The result is shown as the red curve in Fig. 1.3. Below masses of $0.085\,\mathrm{GeV/c^2}$, the CDEX-1B experiment places the most stringent limits by incoperating the Migdal effect in the analysis [46]. This experiment uses point-contact germanium detectors operating at liquid nitrogin temperature, reading out the charge signals induced by a particle interaction.

A large part of this thesis was carried out in the framework of the XENON1T experiment. In the next Chapter, we continue with a more detailed introduction to its detection technique and reported results on the search of spin-independent WIMP-nucleon interactions based on the standard S1-S2 NR search.

Chapter 2

The XENON1T Experiment

One technique for direct dark matter detection are dual-phase Time-Projection-Chambes (TPCs), employing xenon as target material. This method is used by the XENON collaboration, that operated the XENON10 and, subsequently, the XENON100 detector [47, 48]. A large part of this thesis is carried out in the framework of the successor detector, XENON1T, that finished operation at the end of 2019. The detector was upgraded to the XENONnT experiment, which is under commissioning at the time of writing.

This Chapter starts with a general overview on the TPC detection principle in section 2.1 and the creation of measurable signals from energy depositions in the xenon target in section 2.2. For the data analysis in XENON1T, these signals have to be corrected for losses (section 2.3), and their location within the TPC has to be reconstructed (section 2.4). In section 2.5, the set-up of the XENON1T detector and connected subsystems is described. The background components in XENON1T are outlined in section 2.6. Lastly, the scientific results of spin-independent WIMP-nucleon scattering are summarized in section 2.7, based on the results published in [35, 49].

2.1 The dual-phase TPC detection principle

The working principle of a dual-phase Time-Projection-Chamber (TPC) is illustrated in Fig. 2.1 in the left panel. The detector is filled with liquid xenon (LXe) with a thin layer of gaseous xenon on top. A particle entering the xenon reservoir can scatter off the xenon nuclei (in case of WIMPs and neutrons) or interact with the electrons in the atomic shells of the xenon atoms (in case of γ-, β- and α-radiation). The resulting recoil ionizes and excites the xenon atoms. Some energy is also transferred into atomic motion. However, this channel is not measurable in XENON1T. The prompt deexitation of the excited xenon atoms leads to scintillation light, called S1 signal, which is detected by photomultiplier tubes (PMTs) arranged at the top and bottom of the TPC. An

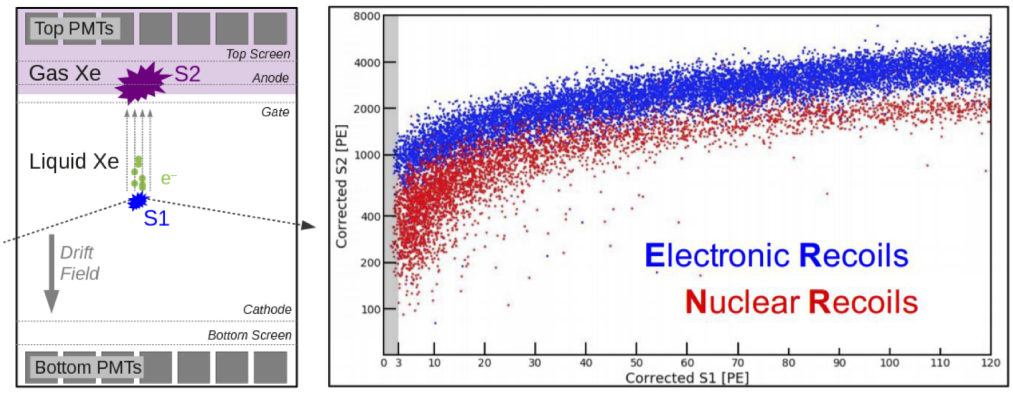

Figure 2.1: (Left) Working principle of a dual-phase Time-Projection-Chamber (TPC). A particle interaction in the liquid xenon (LXe, white) generates promt S1 scintillation light (blue) and ionization electrons (green). The ionozation electrons are drifted to the liquid-has interface by an drift field applied between the cathode and gate electrodes. They are extracted by a stronger field, between the gate and anode electrode, into the gas phase (GXe, light purple) and induced a delayed S2 scintillation signal (purple). Both, the S1 and S2 signal are detected photomultiplier tubes (PMTs) installed at the top and bottom of the TPC. Figure taken from [51]. (Right) The so-called discrimination space showing the corrected S1 vs. the corrected S2 signal size of particles interacting in the XENON1T detector. The red population is generated by neutron calibration that corresponds to potential WIMP interactions or background from neutrons. The blue population is produced by a calibration source that generates electronic recoils, such as background from γ-and β radiation. Figure taken from [52].

electric field is established between the negatively biased cathode mesh, at the bottom of the TPC, and the grounded gate mesh, located a few mm below the liquid surface. This so-called drift field guides the liberated ionization electrons from the interaction site upwards. The strong extraction field (typically $\sim 10\,\mathrm{kV/cm}$ [50]), between the gate mesh and the positively-biased anode mesh, causes their extraction and acceleration. Thereby, the electrons get enough energy to ionize and excite the xenon atoms in the gas gap and generate a secondary scintillation signal, called S2 signal, proportional to the number of extracted electrons. The creation of these two signals, S1 and S2, offer several methods to reject unwanted background events. As indicated in Fig. 2.1 (right), the ratio of the S1 and S2 signal sizes depends on the particle type and its energy [53]. Thus, the ratio is used to discriminate between nuclear recoils (NRs) from potential signal events (in this case neutron calibration data in red) and background induced electronic recoils (ERs from calibration data in blue). More details are found in section 2.2. Another advantage of TPCs is the possibility of spacial event reconstruction, whereby the pattern of the S2 signal in the top PMT array determines the (x,y) - position, while the time between S1 and S2 signals is a measure of the event's interaction depth (section 2.4). The position reconstruction on the event-by-event basis can be used for the suppression of external background events, as they more likely deposit

energy in outer TPC regions. The selection of an inner fiducial volume (FV), used for data analysis, is termed fiducialization. More details on noble element TPCs in general can be found in [54, 55].

2.2 Energy deposition in the detection medium xenon

The noble element xenon offers several advantages for the detection of rare events. First of all, liquid xenon has a large density of $\sim 3\,\mathrm{g/cm^3}$ and a high atomic number of $Z = 54$ that results in a large stopping power for particles. On one hand, this enhances the chance to detect WIMPs, as they are expected to have a small cross-section with matter. On the other hand, external radiation is stopped efficiently and the background level in the inner xenon volume is reduced (xenon self-shielding). Another important characteristic of xenon is that energy depositions of particles generate scintillation photons and charge carriers, that can be read out in a TPC. The combination of both detection channels offers a precise determination of the particles' properties [56]. This also allows for an efficient background mitigation. Another advantage is that intrinsic contamination from radioactive xenon isotopes are sub-dominant.

In general, a particle interactions in xenon lead to motion, ionization and excitation of the atoms and, depending on the particle type, these three channels are differently pronounced [54]. The products of ionization (electrons) and excitation (scintillation photons) are measurable in XENON1T. After ionization, the Xe^+ ion can collide with another neutral xenon atom from the surrounding medium and form Xe_2^+. The Xe_2^+ can recombine with a free electron and form a Xe^{**} and a neutral xenon atom. The Xe^{**} subsequently decays to an excited xenon atom Xe^*. An excited xenon atom Xe^* is as well formed in case of an initial excitation of the xenon atom by a particle interaction. Hence, from this point on the description of scintillation light creation is the same for the ionization and excitation channel. In both channels, the excited xenon atom Xe^* combines with a surrounding xenon atom to form an eximer Xe_2^*. The eximer relaxes to one of two electronic excited states, a spin singlet or a spin triplet state, from which it decays back into two ground-state xenon atoms. In this transition, VUV photons are emitted with a wavelength centered around $175\,\mathrm{nm}$ to which the xenon is transparent [57]. The spin singlet has a lifetime of $(3.1 \pm .7)\,\mathrm{ns}$ and the spin triplet has a lifetime of $(24 \pm 1)\,\mathrm{ns}$ [58]. The relative amount of the fast and slow excimers produced is different for different sources, which means the S1 pulse shape could be used to discriminate electronic and nuclear recoils. This method is effectively used in liquid argon, because the two components feature a large time separation [59]. In liquid xenon, the two decay components are more challanging to separate due to their small time separation.

The described energy depositions can be written as

$$\mathrm{E} = (\mathrm{n}_i + \mathrm{n}_{ex}) \cdot \mathrm{W} \cdot \mathrm{L} \tag{2.2.1}$$

where E is the energy, and n_{ex} and n_i are the numbers of initially created excitons and electron-ion pairs, respectively. The parameter W is the average energy needed to create a single excited or ionized atom and its value is W = $(13.7 \pm 0.2)\,\mathrm{eV}$ [60]. NRs lose a large part of their energy in elastic scatters on surrounding xenon atoms. Additionally, also biexcitonic quenching can occur in the NR tracks of high ionization density. This energy quenching is expressed by the Lindhard factor L, which has typically a value of L = $0.1 - 0.2$ in liquid xenon [61]. In contrast to that, energy loss into heat is negligible for ERs as the mass of the recoiling electron is much smaller than the xenon nucleus, hence L = 1.

The recoil type determines the ratio of immediately produced excited states n_{ex} to electron-ion pairs n_i. For ERs the number of ions typically exceeds the number of excited states by far. In the XENON1T data analysis, the ratio $\mathrm{n}_{ex}/\mathrm{n}_i$ is constrained between 0.06 and 0.2 [62]. For NR, this ratio is modeled as a function of deposited energy and field strength. At an electric field of $81\,\mathrm{kV/cm}$, the ratio is $0.7 - 1.0$ for NR energies from 5 - $40\,\mathrm{keV}$ [62]. The number of created exitons n_{ex} and electron-ion pairs n_i can be translated into a number of detectable photons N_γ and electrons N_e as

$$\mathrm{N}_\gamma = \mathrm{n}_i \cdot \mathrm{r} + \mathrm{n}_{ex} \quad \text{and} \quad \mathrm{N}_e = \mathrm{n}_i \cdot (1 - \mathrm{r}) \tag{2.2.2}$$

where the parameter $\mathrm{r} \in [0, 1]$ is referred to as the recombination fraction. It depends on the applied drift field, the energy transfer and the ionization track structure of the incoming particle [60]. Because of its rather large scattering length, an electron will deposit energy along its trajectory with a comparably low ionization density. A hypothetical WIMP, which is much heavier than an electron, will mainly lose its energy in recoils with xenon nuclei of comparable mass. Hence, the resulting ionization density caused by the nuclear recoil is larger than the one by electronic recoils. Consequently, the recombination probability of the ionized xenon atoms with their electrons differs along the track of the ionizing particles. The lower recombination probability of electronic recoils leads to a larger ionization (S2) and a more strongly quenched scintillation (S1) signal. The described effects are the basis for the capability of LXe to discriminate nuclear from electronic recoils, as shown in Fig. 2.1 on the right panel. In there, the corrected quantities, cS1 and cS2, are shown that can be inferred from the number of N_γ and N_e, respectively, as explained in the next section 2.3.

2.3 Signal corrections

The number of prompt scintillation photons N_γ are directly measured by the PMT arrays of the TPC. When photons strike a PMT's photocathode, they can get converted into so-called photoelectrons (PE) via the photoelectric effect. These photoelectrons are amplified within the PMTs and readout. The total number of photoelectrons determines the size of the S1 signal, which is proportional to the initial number of generated scintillation photons N_γ. As described before, the created ionization electrons are extracted and strongly accelerated into the gas phase, where they also create scintillation photons by means of electroluminescence [63]. The photons of this delayed S2 signal are converted into photoelectrons in the same way as for the S1 signal. The total amount of detected photoelectrons determines the size of the S2 signal, which is proportional to the initial number of extracted electrons N_e.

The sizes of the S1 and S2 signals can be reduced due to signal losses. Following the notation in [62] the correction factor $g_1'(x,y,z)$ is introduced to correct the amount of S1 light, while the factor $g_2'(x,y)$ is applied in the S2 correction. In the S1 case, the correction factor describes the probability of one emitted scintillation photon to be detected as one photoelectron. The S2 correction factor accounts for the amplification of the charge signal. The correction factors are defined as

$$g_1'(x,y,z) = (1 + p_{dpe}) \cdot \epsilon_L(x,y,z) \cdot \epsilon_{QE} \cdot \epsilon_{CE} \quad \text{and} \quad g_2'(x,y) = \epsilon_{ext} \cdot G(x,y). \tag{2.3.1}$$

The single parameters will be explained in the following.

2.3.1 Prompt scintillation signal (S1)

Light collection efficiency $\epsilon_L(x,y,z)$: the light collection efficiency (LCE) is defined as the fraction of emitted photons that reach a PMT photocathode. Most of the created scinitllation light is reflected at the liquid-gas interface and the photons have to undergo more reflections at the PTFE walls, the further away they are created from the bottom PMT array. In this process, signal loss can occure because of the limited reflectivity for VUV light on PTFE and the light attenuation in xenon, due to traces of impurities (e.g.water vapor) [56]. For these reasons, the LCE is higher in the center of the (x,y) plane than at outer TPC regions and increases along the z-axis towards larger depths. The LCE is maximal close to the bottom PMT array. Due to local and time varying field inhomogeneities, the amount of created photons has an additional dependency [64]. To correct the mentioned efficiencies a three-dimensional correction map is derived, based on the homogeneously distributed and monoenergetic calibration with ^{83m}Kr.

Quantum efficiency ϵ_{QE}: a VUV photon hitting the photocathode of a PMT has a cer-

tain probability to be converted into a photoelectron, which is called quantum efficiency (QE). The PMTs with the highest QE are installed in the bottom array because the LCE is highest in this region.

Collection efficiency $\epsilon_{\mathbf{CE}}$: the created photoelectrons are amplified by an electric field within the PMT to a measurable current at its anode. The collection efficiency (CE) quantifies this electron multiplication mechanism and it is around $90\,\%$ for the XENON1T PMTs [65].

Double PE probability $\mathbf{p_{dpe}}$: the PMT photocathode has a certain probability p_{dpe} to emit two, instead of one photoelectron when absorbing one scintillation photon. For the XENON1T PMTs this probability is $18 - 24\,\%$ [66].

2.3.2 Secondary scintillation signal (S2)

Gas gain $\mathbf{G(x,y)}$: this gain factor describes the number of detected photoelectrons per ionization electron, that is extracted into the gas phase. Its value depends on the physical properties of the gas gap, such as electric field strength, electron track length and vapor pressure. It can be measured directly by the quantized charge spectrum in PE that is generated by multiples of single extracted electrons [67]. Thus, the measured gas gain incorporates the PMT-related efficiencies ϵ_{QE}, ϵ_{CE} and p_{dpe}. In XENON1T, G varies from an average yield of $96\,\%$ in the center of the TPC to $70 - 80\,\%$ at outer regions [68]. To compensate for these effects, a 2D-correction map is required, based on uniformly distributed charge signals from an internal ^{83m}Kr source.

Extraction efficiency $\epsilon_{\mathbf{ext}}$: the drifting ionization electrons have to overcome an energy barrier when being extracted from the liquid into the gas phase. The extraction efficiency depends on the extraction field. A minimum extraction field of $\sim 1.5\,\mathrm{kV/cm}$ is required for extraction [50]. At the employed extraction field in XENON1T of $\sim 8.1\,\mathrm{kV/cm}$ [68], the extraction efficiency was measured to be $\sim 96\,\%$ [51].

Electron lifetime τ: a further correction, not yet mentioned, is necessary due to the possible attachment of drifting electrons to electronegative impurities (e.g. O_2) that are present in small traces within the xenon [56]. This leads to an exponential reduction of the initial electron amount depending on the drift time (a measure for interaction depth inside the TPC) between interaction point and liquid-gas interface. The reduction is described by the so-called *electron lifetime* τ, a decay parameter that depends on the concentration of impurities and the field-dependent electron attachment rate [69]. By characterizing the signal loss across the TPC from mono-energetic charge signals, the electron lifetime can be measured and

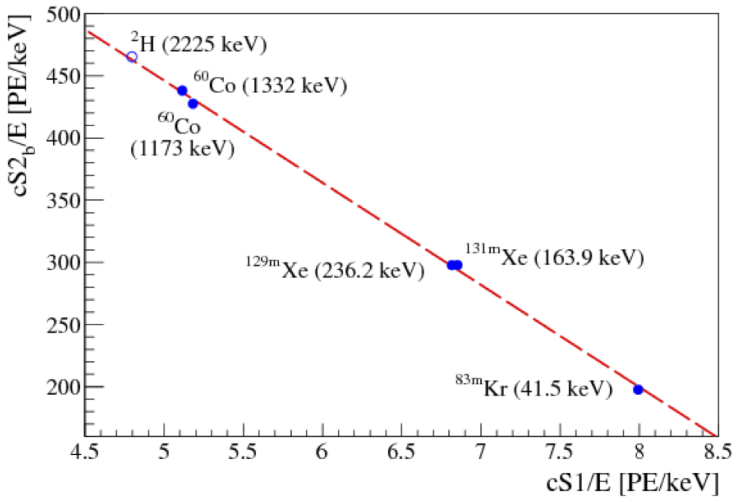

Figure 2.2: The corrected scintillation (cS1) and ionization signals ($cS2_b$, which is based on the S2 size detected by the bottom PMT only) for various mono-energetic ER sources, corrected for position dependent effects and normalized to the line energy. The fit to the data allows the extraction of the primary g_1 (in PE/γ) and secondary scintillation gain g_2 (in PE/e^-). The signal at $2.2\,\mathrm{MeV}$ is due to de-excitation γ-rays from neutron capture on hydrogen. It is not used for the fit, but demonstrates that the detector response is well-known over a large energy range. Figure taken from [51].

the observed S2 is corrected for this effect. The measurement is performed every few weeks while the xenon is constantly purified by gas purifiers, leading to an improvement of the electron lifetime over time [68].

2.3.3 Corrected signals and ER energy scale

In the previous sections 2.3.1 and 2.3.2 we discussed the correction factors for the S1 and S2 signals. The corrected quantities are denoted as cS1 and cS2 and are defined as

$$\mathrm{cS1} = \mathrm{S1} \cdot \frac{g_1}{g_1'(x,y,z)} \quad \text{and} \quad \mathrm{cS2} = \mathrm{S2} \cdot \frac{g_2}{g_2'(x,y)} \cdot e^{z/(v_d \cdot \tau)} \tag{2.3.2}$$

where v_d is the drift velocity of the electrons. The parameter z is the covered track length of the electrons along the field lines, described in more detail in section 2.4. The g_1 and g_2 factors in Eq. 2.3.2 are the averages of $g_1'(x,y,z)$ and $g_2'(x,y)$ over the entire active xenon volume. They are commonly known as primary and secondary scintillation gain and are detector-specific parameters, independent of the drift field and the same for all deposited energies. They can also be defined as $g_1 = \mathrm{cS1}/n_{ex}$ and $g_2 = \mathrm{cS2}/n_i$, whereby n_{ex} and n_i are the numbers of produced scintillation photons and electron-ion pairs. Hence, we can write 2.2.1 as

$$E = (n_{ex} + n_i) \cdot W = \left(\frac{\mathrm{cS1}}{g_1} + \frac{\mathrm{cS2}}{g_2} \right) \cdot W. \tag{2.3.3}$$

On one hand, the g_1 and g_2 factors are used to correct the S1 and S2 signal generated by NRs or ERs. On the other hand, as shown in Eq. 2.3.3, they are used to define a combined energy scale for ERs. To determine the values of g_1 and g_2, one commonly calculates first the light yield (LY) and charge yield (CY) for the energy depositions of at least two or more mono-energetic ER sources, as shown in Fig. 2.2 [51]. The LY (CY) is defined as the amount of PEs from the cS1 (cS2) signal per total deposited energy E. By re-arranging Eq. 2.3.3 and applying a linear fit to the points in Fig. 2.2, one can infer g_1 and g_2 from the slope and interception with the y-axis, respectively [70]. In XENON1T, they are determined to be $g_1 = (0.144 \pm 0.007)$ PE/γ and $g_{2b} = (11.5 \pm 0.8)$ PE/e^- [51]. Due to a more homogeneous LCE, the XENON1T analyses typically use the $cS2_b$ signal size measured by the bottom PMT array only. Therefore, g_{2b} is defined based on $cS2_b$.

2.4 Position reconstrcution and spacial corrections

One of the main advantages of dual-phase TPCs is the ability to perform a three-dimensional event position reconstruction. This allows for a fiducialization of the LXe volume and the rejection of multiple-scatter events. Furthermore, position-dependent background models [62] and signal corrections (see section 2.3.1 and 2.3.2) can be developed.

Position reconstruction: the z position of an event is defined as its vertical position within the TPC, anti-parallel to the drift field. The origin is set to the gate mesh position and it reaches down to the position of the cathode mesh at $-97\,\mathrm{cm}$ [68]. The detection times t(S1) and t(S2) of the event's S1 and S2 signal and the electron drift time v_d for the given drift field are used to calculate the observed z coordinate as

$$z = (t(S1) - t(S2)) \cdot v_d \quad . \tag{2.4.1}$$

The event's position in the lateral plane (x,y position) is dictated by the PMT hit pattern induced by the S2 signal in the top PMT array. Two algorithms are used to reconstruct the position: the *Top Pattern Fit* (TPF) and a *Neural Net* (NN). The TPF uses the LCE map as input and compares the expected amount of PE in all top PMT channels, according to the LCE map for a given position in (x,y) with the measured one. The NN uses Monte Carlo (MC) data as input, which is generated by a GEANT4 toolkit [71].

Field distortion correction: a precise position reconstrcution necessitates a homogeneous drift field constituted by straight and parallel field lines along the z axis of the TPC. As the operational drift field in XENON1T is lower than the designed value, the electric field becomes inhomogeneous, especially in outer TPC regions [68]. The resulting radial inwards bias of the field lines with increasing depth causes a path distortion of the drifted electrons. In addition to that,

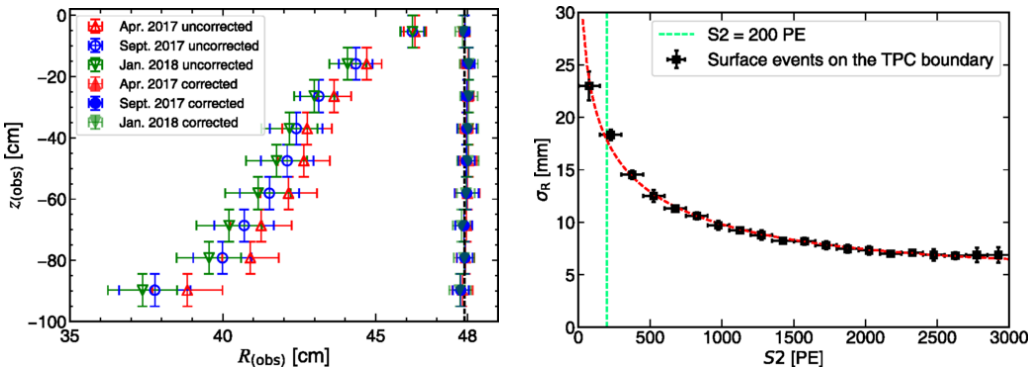

Figure 2.3: (a) Maximal TPC radius reconstructed from signals of surface events in three time intervals and in bins of z. Open (closed) markers show the radii before (after) position correction. Horizontal error bars indicate the radial width of the event distribution. Vertical error bars mark the z bin width. The black dashed vertical line indicates the geometrical TPC radius. (b) Radial position resolution σ_R in bins of S2 signal size for surface events. Vertical uncertainties are derived from a Gaussian fit of the S2 distribution while horizontal error bars mark the S2 bin width. The red dashed line indicates the best-fit of an empirical function. Both figures and description taken from [68].

a time-dependent inwards bias is observed, caused by an accumulation of negative charges on the PTFE wall over time [64]. This effect is most profoundly visible for events known to be located at the TPC wall, as illustrated in Fig. 2.3a (open markers). The reconstructed TPC radius of these so-called surface events is shifted inwards over time. A data-driven and time-dependent field distortion correction map was developed, whose impact can be seen in 2.3a (closed markers) [68]. After correction, the radial position of the surface events coincides with the TPC boundaries. Events on the PTFE surface can be used to study the position resolution at the maximum radius of the TPC over a large range of S2 sizes. The standard deviation σ_R of the radial distribution in bins of S2 signal size is shown in Fig. 2.3b [68]. For a S2 size of $200\,\mathrm{PE}$ (dark matter lower analysis threshold), the radial resolution is $1.9\,\mathrm{cm}$ at the maximum TPC radius. The resolution for surface events is decreasing towards lower S2 signal sizes. Towards the center of the TPC the resolution is expected to be improved [68]. The mentioned surface events are generated by ^{222}Rn progenies plated-out on the TPC walls. Their S2 signal size can be minimized due to charge loss at the wall, which might result in a S2/S1 ratio compatible with the one of NRs and signal events. Hence, these events cause an important background in XENON1T [35, 49]. In addition to the improvement of the radial position reconstruction, the reduction of these surface events is crucial to reduce the probability of their leakage into the sensitive volume.

2.5 The XENON1T detector system

In this section, we outline the XENON1T detector, which is located in the Abruzzi region in Italy, inside the INFN Laboratori Nazionale del Gran Sasso (LNGS). A more complete treatment of its design, components, and performance can be found in [51].

the TPC has a height and diameter of $\sim 1 \times 1\,\mathrm{m}$ and is housed in a stainless steel, double-walled cryostat containing $3.2\,\mathrm{t}$ of liquid xenon. Out of them, $2\,\mathrm{t}$ are inside the TPC active volume, enclosed by PTFE panels with a high reflection index for vacuum ultraviolet (VUV) light [72]. The residual xenon is used for shielding. A picture of the TPC can be seen in Fig. 2.4 (right). The electrode meshes are made from stainless steel (SS) and optimized for a high field homogeneity, as well as a high optical transparency. During the main periods of data taking the established drift field was either $120\,\mathrm{V/cm}$ or $81\,\mathrm{V/cm}$, whereas the extraction field was always $8\,\mathrm{kV/cm}$ [68]. The TPC is surrounded by field shaping rings made from low-radioactivity copper to ensure a homogeneous drift field. To keep and adjust a stable liquid surface, a diving bell design is applied at the top of the TPC. The liquid level is measured by custom-made level meters. The top PMT array contains 127 photosensors and the bottom array 121 (3-inch Hamamatsu R11410-21) [73]. The top and bottom PMT arrays are shown in Fig. 2.4 (left). All components in or near the TPC are made from extremely-low radioactivity materials and underwent extensive screening campaigns [73,74] [I]. Furthermore, a $\sim 10 \times 10\,\mathrm{m}$ high water tank surrounds the cryostat for a passive shielding against external background. It is also instrumented with 85 PMTs to detect muons via their Cherenkov light [75]. The detector is located underground at an average depth of $3600\,\mathrm{m}$ water-equivalent to reduce cosmic radiation and muons.

Xenon cooling and purification: in Fig. 2.5, the XENON1T cryogenic and purification systems are shown. The constantly evaporating xenon from the cryostat is directed into a pipe leading to the cryogenic system, where it gets liquefied by PTRs (pulse-tube refrigerators), collected in a funnel and streams back to the cryostat. In another pipe, liquid xenon from the cryostat is guided into a heat exchanger that evaporates it and cools, at the same time, the return gas from the connected purification system. This system contains two gas purifiers to remove nitride, carbide and oxide impurities that constantly outgas into the xenon and lead to a diminution of the charge and light signals. Additionally, the system is equipped with three recirculation pumps (QDrive pumps) for the gas transfer. These pumps were exchanged by a magnetically coupled piston pump during the run-time of the experiment, as detailed in Chapter 3. In a third pipe, PMT cables and cables from various other sensors are guided through a gas-tight cable feedthrough to the DAQ system.

Xenon storage and distillation: the so-called ReStoX system is a vacuum insulated SS

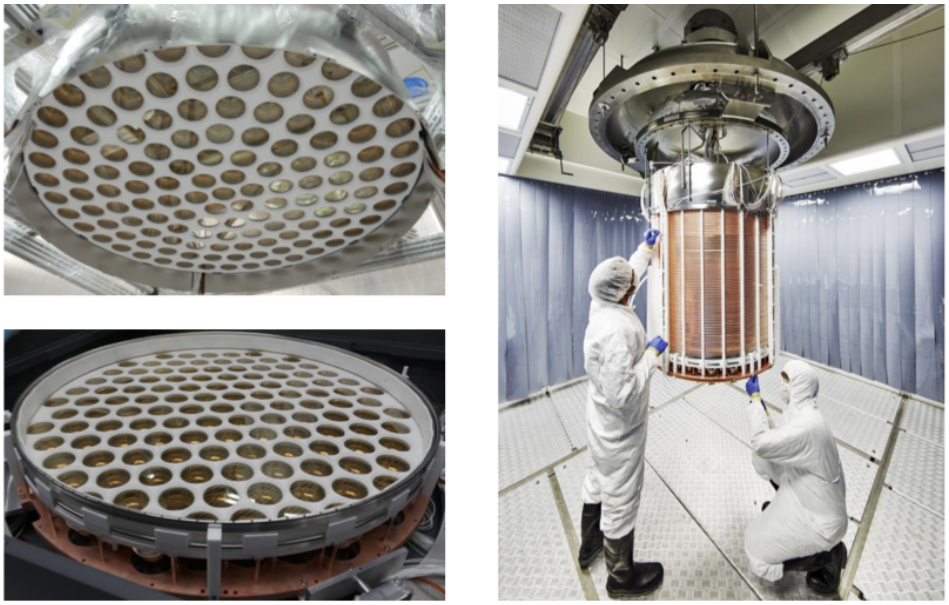

Figure 2.4: (Left) Top and bottom PMT arrays of XENON1T before TPC assembly. The white surface between the PMTs is made from PTFE, a material that has a high reflectivity for xenon scintillation light. (Right) Assembled XENON1T TPC inside the temporally clean room. The TPC is supsended from the cryogenic pipe that leads to various sub-systems of the XENON1T detector. Figures taken from [52].

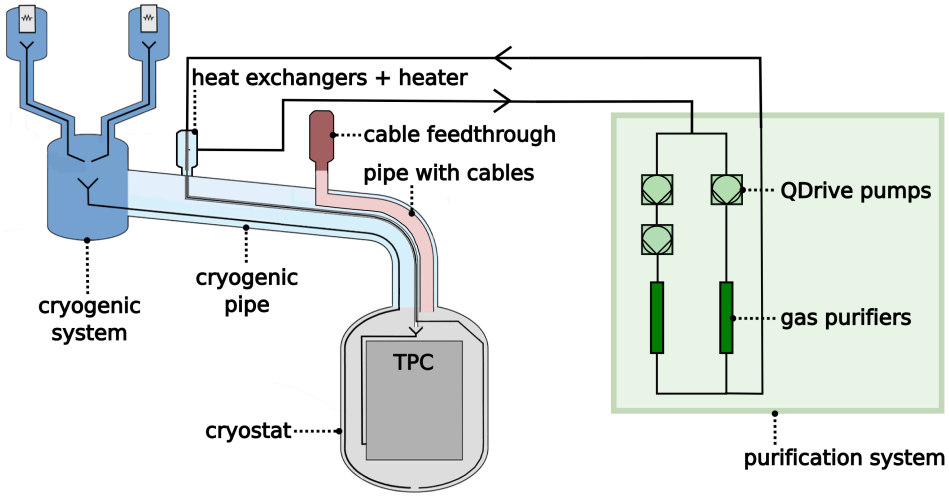

Figure 2.5: XENON1T detector system. The TPC is hosted in the cryostat which is connected via the cryogenic pipe to the cryogenic system used to liquefy the xenon. The sensor cables from the TPC are guided through a cable pipe to the air-side. The xenon is continuously purified by the gas purifiers installed in the purification system. More details are found in the text. The color code of the sketch is used in Chapter 3 when describing the ^{222}Rn emanation rate per detector part. Figure published in [I].

sphere with a diameter of $2.1\,\mathrm{m}$ that can be cooled with nitrogen even in a cooling failure of the remaining detector system. It is designed to savely store up to double the xenon mass used in XENON1T and it can be used in case of an emergency for a fast xenon recovery. The anthropogenic ^{85}Kr is always present in commercially available xenon and one of the main electronic recoil background sources in XENON1T. A distillation column is integrated into the XENON1T purification system to reduce the krypton background by means of cryogenic distillation. The xenon can be distilled both before being filled into the detector and during operation. Operated in reverse mode, the distillation column was also used in XENON1T to reduce the leading background component induced by the noble gas ^{222}Rn [76].

DAQ and event reconstruction: the XENON1T data acquisition (DAQ) records individual PMT pulses above a digitization threshold. Pulses closely spaced in time are grouped into signals by an online event builder. If a signal causes a trigger based on the signal's pulse size, a period of $\pm 1\,\mathrm{ms}$ is stored around this signal. The custom-made offline processor PAX [77] calculates the properties of the signals in one event and classifies them as S1 or S2 peak. Thereby, a S1 (S2) peak has a typical rise time of $\sim 100\,\mathrm{ns}$ ($\sim 1\mu$s) and the PMT coincidence level is set to > 2 (> 3) [68]. Finally, in each event the S1 and S2 peaks are paired into interactions, starting with the largest peaks of each type. More information on the XENON1T DAQ system can be found in [78].

2.6 Backgrounds

Since only a few dark matter interactions are expected to occur per year in the XENON1T TPC, the suppression of background events is one of the main challenges of the experiment. Particles interacting via a single-scatter NR present a crucial source of background, as they have the same signature as a WIMP. Due to the large discrimination power between NRs and ERs in xenon, only $\sim 0.3\,\%$ of the ERs are misidentified as a NR in the dark matter search region [68]. Nevertheless, ERs are an important background source in the rare-event search. Two more background categories are identified in XENON1T, the so-called accidental coincidences (AC) and background originating from the inner surface of the TPC walls. Normalized to the full $1.3\,\mathrm{t}$ LXe volume of XENON1T (called $1.3\,\mathrm{t}$ fiducial volume, FV), the surface background is most dominant in the WIMP energy region of interest. By selecting a smaller FV, the surface background is reduced and ERs become the leading background source. In this section, the origin of the mentioned background sources are explained. Thereby, we summarize the background components relevant for XENON1T's primarily search for WIMP dark matter [35, 49].

2.6.1 Background from nuclear recoils

Neutron and neutrino interactions with the LXe can generate NRs that are indistinguishable from the ones potentially created by a WIMP. Thereby, the largest contribution arises from radiogenic neutrons [79]. They are generated in the decay chains of primordial elements through spontaneous fission and via (α,n) reactions. The created neutrons can have energies in the MeV region, and hence penetrate several cm into the active volume, creating single scatter NR events. The background from radiogenic neutrons is simulated based on the measured radioactivity of the detector materials [74]. Moreover, cosmogenic muons can produce high-energetic neutrons along their path through the rock and the detector material surrounding the TPC. However, due to the water Cherenkov Muon Veto this source of neutron background is negligible in XENON1T [75]. Another source of NR background arises from coherent elastic neutrino nucleus scattering (CEνNS), mainly from ^{8}B solar neutrinos.

2.6.2 Background from electronic recoils

Material: the γ-rays generated by radioactive decays within the construction material can penetrate $\mathcal{O}(\mathrm{cm})$ into the active volume. Thus, low energetic Compton scatters can lead to background events in the signal's energy region. By making use of the xenon self-shielding property and selecting only an inner FV, this source of background can be reduced efficiently. Beforehand, only materials with a sufficiently low radioactivity were selected for constructing the detector based on measurements using low-background high-purity germanium spectrometers [80–82] and standard analytical mass spectroscopy methods (ICP-MS,GD-MS). The measurements are summarized in [73,74] and serve as input for Monte Carlo simulations [79] to estimate the background level from materials in XENON1T.

Radon: the materials of the XENON1T detector components contain small traces of the primordial ^{232}Th and ^{238}U isotopes whose decay chains include isotopes of radon. Due to its long half-life of $3.8\,\mathrm{days}$, the noble gas ^{222}Rn from the ^{238}U chain is most relevant in XENON1T. Once created, it can leave the detector materials and enter the xenon reservoir where it distributes. The β-decay of its daughter isotope ^{214}Pb inside the sensitive volume can lead to ER background. The background induced by ^{222}Rn makes up the largest fraction of ER background in XENON1T. In order to select detector materials with a low ^{222}Rn emanation rate an intensive screening campaign was performed before the experiment started as described in [I]. Cryogenic ^{222}Rn distillation [83] allowed for a reduction of the ^{222}Rn concentration while the experiment was taking data [76]. The radon induced background in XENON1T was thoroughly studied in the framework of

this work (see Chapter 3).

^{85}Kr: as being extracted from the atmosphere, the target material xenon contains natural krypton ^{nat}Kr at the ppm level [79], as well as the anthropogenic β-decaying isotope ^{85}Kr. It has a half-life of $10.8\,\text{years}$ and a concentration of $^{85}\text{Kr}/^{nat}\text{Kr} = 2 \cdot 10^{-11}$ in the atmosphere [84]. Similar to the background induced by radon, the ^{85}Kr energy spectrum extends into the energy region of interest for dark matter search. Another similarity to radon is that ^{85}Kr is homogeneously distributed in the TPC and cannot be reduced by fiducialization but with cryogenic distillation [85]. Thus, before and during the first few weeks of data taking in XENON1T, the ^{85}Kr concentration was lowered by around five orders of magnitude to a sub-dominant average background level [35, 76].

Solar neutrinos: neutrinos produced in the Sun can elastically scatter off shell electrons of the xenon atoms and create ER background. Thereby, the largest contribution arises from *pp* neutrinos ($92\,\%$) [79]. In the dark matter analysis solar neutrinos are considered to be a sub-dominant source of background.

^{136}Xe: the two-neutrino double-β emitter is contained in natural xenon at a level of $8.9\,\%$ [79]. It has a half-life of $2.17 \cdot 10^{21}\,\text{years}$ and is a sub-dominant in XENON1T.

In Chapter 4, we discuss the time evolution of the descriped ER background components during the two dark matter runs of XENON1T.

2.6.3 Background from accidental coincidences

There is a chance that, in non-active regions of the TPC, either the S1 or S2 signal, belonging to one interaction, can be lost, resulting in lone S1 or lone S2 signals. For example in energy depositions close to the gate mesh, the scintillation signal might get blocked whereas for example below the cathode, the ionization signal is not produced [35, 62]. The uncorrelated lone S1 and S2 signals can accidentally coincide and consequently mimic a real interaction.

2.6.4 Background from surface

During the assembly of the TPC, long-lived daughter nuclei of ^{222}Rn from ambient air can plate-out on the inner PTFE surfaces of the active volume. The disintegration of these daughter isotopes on the surface can lead to a reduction of the charge signal and, consequently, to a S2/S1 ratio compatible with the one of NRs and signal events [35, 49]. These surface events, in combination with a limited position reconstruction (section 2.4), lead to the so-called surface background. It is the dominating background contribution in outer TPC regions. Moreover, the α-decays of the radon daughters can cause (α,n) reactions in the PTFE, leading to neutron background (see Chapter 3). One

way to mitigate the out-plated radon daughters is their removal by means of surface treatment [II].

2.7 Scientific results

Two data taking periods were analyzed for the XENON1T main results on the standard NR WIMP search. The so-called science run 0 (SR0) spanned from November 22, 2016 until January 18, 2017 (with $32.1\,\mathrm{days}$ of high data quality), when an earthquake caused an interruption. The second science run (SR1) lasted from February 2, 2017 until February 8, 2018 (with $246.7\,\mathrm{days}$ of high data quality). The data from SR0 were published [49] and re-analyzed in combination with the data of SR1 [35]. In the following, we want to briefly outline the result of the combined science run analysis. We refer to [68] for more details on the signal reconstruction, calibration and event selection and to [62] for the details regarding the signal and background models as well as the statistical treatment. This data set and many of the analysis methods were also used in other XENON1T publications [45, 86–89], addressing different scientific questions.

Several selection criteria are applied to the data (so-called "cuts") to ensure that the events are well-reconstructed and known background is suppressed. The first class of data quality cuts rejects certain time periods independent of the events within those periods. They ensure that the DAQ is ready to take data, that events occurring simultaneously to a trigger of the Muon Veto are excluded, or that events caused by detector effects such as light-emitting PMTs are removed.The second class are cuts that remove poorly reconstructed events. Furthermore, the third class of cuts only allows S1-S2 pairs for which the reconstructed spacial position matches the one of the S1 and S2 signal measured individually. As a dark matter particle is expected to scatter at most once in the detector the fourth class of cuts requires single scatter interactions. The calculated acceptance to detect a dark matter particle after applying these cuts is $(91\pm4)\,\%$.

For the statistical interpretation of the dark matter data, precise knowledge on the conversion from energy depositions to measured cS1 and cS2 signal is demanded. This knowledge is based on a simulated detector response model of energy depositions from NRs and ERs [62]. It incoperates a description of the signal production process in LXe (section 2.2) as well as a characterization of detector reconstruction effects (section 2.3 and 2.4). The response model is extracted from fits to calibration data from ^{241}AmBe and a D-D generator for NRs, and ^{220}Rn for ERs. These fits constrain the so-called nuisance parameters, free parameters that describe the detector response model.

With this response model, the background and the WIMP signal models are constructed

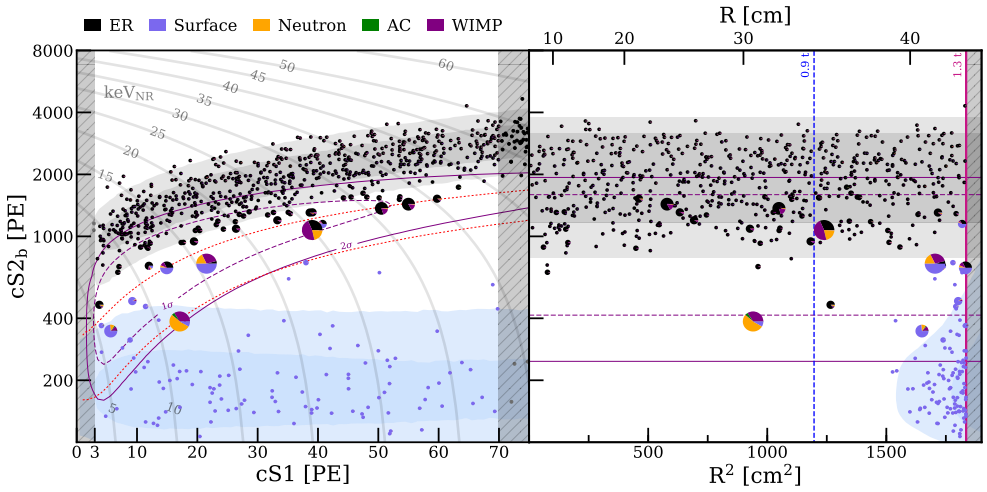

Figure 2.6: Dark matter search data in $1.3\,\mathrm{t}$ fiducial mass in (cs1,cS2$_b$) and (R,cS2$_b$) parameter spaces. Shaded regions show the projection in each space of surface (blue) and ER (gray) background components for SR1. The 1σ (purple dashed) and $2\,\sigma$ (purple solid) percentiles of a $200\,\mathrm{GeV/c^2}$ WIMP signal are overlaid for reference. Vertical shaded regions are outside the region of interest. The NR signal reference region (left, between the two red dotted lines) and the maximum radii (right) of the $0.9\,\mathrm{t}$ (blue dashed) and $1.3\,\mathrm{t}$ (magenta solid) masses are shown. Gray lines show the iso-energy contours in NR energy. The measured events are indicated as pie charts, illustrating the individual probabilities of being background or signal. Figure and description taken from [35].

[62]. They are realized by probability density functions (PDF) in the analysis space (cS1,cS2$_b$,R,Z). Thereby, the WIMP NR energy spectra, constrained by cosmological assumptions of e.g the local WIMP velocity and density, is transformed into the analysis space. This is done for WIMP masses between $6\,\mathrm{GeV/c^2}$ and $1000\,\mathrm{GeV/c^2}$. Furthermore, the ER and NR background models are simulated based on the detector response model. In contrast, the background models for AC and surface background are based on data-driven methods.

In Fig. 2.6, all events that pass the described selection cuts are shown in the parameter spaces (cs1,cS2$_b$) and (R,cS2$_b$). The energy region of interest is defined in a cS1 interval of $[3, 70]\,\mathrm{PE}$. This translates into an energy interval $[1.4, 10.6]$ keV$_{\mathrm{ER}}$ for ER and $[4.9, 40.9]$ keV$_{\mathrm{NR}}$ for NR.

In Fig. 2.6 (left) the NR energy in units of keV$_{\mathrm{NR}}$ is indicated as gray lines. As mentioned, the WIMP signal model depends on the dark matter mass. In Fig. 2.6 (left) the $1\,\sigma$ (purple dashed) and $2\,\sigma$ (purple solid) contour of a signal from a $200\,\mathrm{GeV/c^2}$ WIMP is illustrated. The NR reference region is shown between the two red dotted lines. The shaded regions indicate the surface (blue) and ER (gray) background components.

The maximal FV of $1.3\,\mathrm{t}$ is indicated by the red solid line in Fig. 2.6 (right). It is de-

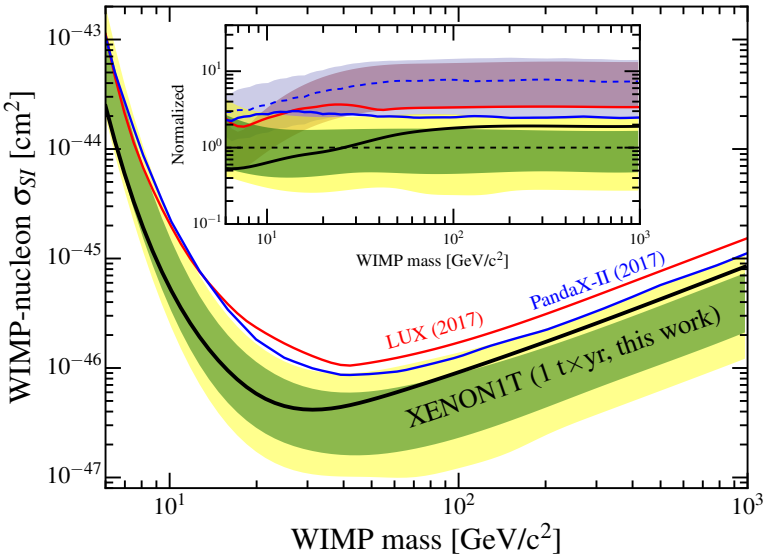

Figure 2.7: Illustrated as black line is the $90\,\%$ confidence level upper limit for σ_{SI} with the $1\,\sigma$ (green) and $2\,\sigma$ (yellow) sensitivity bands. Previous results from LUX [36] and PandaX-II [37] are shown for comparsion. The inlet shows these limits and the corresponding $\pm 1\sigma$ bands normalized to the median of shown sensitivity band. The normalized median of the PandaX-II sensitivity band is shown as dotted line. Figure and description taken from [35].

fined such that radio-impurities from detector materials are subdominant relative to the other background components. Additionally, the upper threshold on the number of expected surface events is < 100. An inner region with a mass of $0.9\,\mathrm{t}$ is restricted by a smaller radius in comparison to the total volume (blue line in (R,cS2$_b$) space). In this so-called reference region the surface background is negligible. By a further reduction to an inner so-called core volume of $0.65\,\mathrm{t}$ the background from neutrons is significantly lowered (not indicated in Fig. 2.6). During data analysis a part of the (cS1,cS2$_b$) space is blinded. This means that it is not accessible until the cut selection, background and signal models are finalized to prevent human bias.

An unbinned profile likelihood analysis is performed with the entire data of SR0 and SR1 in the $1.3\,\mathrm{t}$ FV. It determines the individual background rates, the shape of the ER band and, most importantly, the WIMP-nucleon spin-independent elastic scatter cross-section σ_{SI} as a function of the WIMP mass [90, 91]. Relative probabilities for being background or signal can be assigned to each event in the described parameter spaces. This is illustrated by pie charts in Fig. 2.6. They show these relative probabilities for each event, assuming a WIMP of mass of $200\,\mathrm{GeV/c^2}$ and the resulting best-fit for the spin-independent WIMP-nucleon cross-section of $\sigma_{SI} = 4.7 \cdot 10^{-47}\mathrm{cm}^2$. The larger the WIMP probability, the larger the pie chart is drawn.

The profile likelihood analysis indicates no significant excess of signal at any WIMP

mass. Based on this result, the upper limit on σ_{SI} can be calculated at $90\,\%$ confidence level as shown in Fig. 2.7 (black line). The green and yellow band are the 1σ and 2σ sensitivity bands. The sensitivity is defined as the median upper limit one would obtain in repeated experiments, with only background present and no signal. For this, the amount of background is statistically varied in Monte Carlo simulations based on the prediction from the background model. To date, XENON1T places the most stringent limits for WIMP masses $> 6\,\mathrm{GeV/c^2}$ with a minimum at a WIMP mass of $30\,\mathrm{GeV/c^2}$ and cross-section of $\sigma_{SI} = 4.1 \cdot 10^{-47}\mathrm{cm}^2$. The inlet in Fig. 2.7 compares the XENON1T limit and sensitivity to other LXe TPC experiments [36, 37].

Chapter 3

Radon induced Background in XENON1T

One of the main challenges in the rare-event searches of XENON1T is the efficient mitigation and correct characterization of background components. Thereby, radon induced background contributes to the overall background at large part. Being a noble gas, radon can spread within the whole liquid xenon target in contrast to external background radiation or surface contaminations, that can be suppressed by the large xenon self-shielding property. In the following Chapter, we aim for a characterization of the disintegration and dynamic signature of radon and its decay daughters in the XENON1T detector.

In section 3.1, we discuss the origin of radon induced background. Great effort is spent on its mitigation in XENON1T and the reduction strategies applied in the experiment are outlined in section 3.2. In section 3.3, we explain the analysis methods to constrain the amount of the radon induced background in XENON1T. Its spacial distribution within the TPC is characterized in section 3.4. The ^{222}Rn signal yields are used to continuously monitor the detector stability, as shown in section 3.5. In section 3.6, the time evolutions of radon and its decay daughters are described. In section 3.7, we discuss neutron background induced by surface contamination, originating from airborn radon. Finally, we summarize the impact of radon induced background on the WIMP dark matter search in section 3.8.

3.1 Origin of radon induced background

Depending on its origin and location inside the detector, we divide the radon induced background into two categories. In the first category, the background events arise from radon that originates from the detector material itself and which distributes within the whole liquid xenon target. This category is the dominant part of the electronic recoil

(ER) background in XENON1T and it is the main focus of this work. In the second category, the background events are caused by radon plate-out on the detector surfaces. This contamination arises from ambient radon and it is still present in the run-time of XENON1T. In the following, we will discuss these two categories in more detail.

3.1.1 Background within the xenon target

Basically all materials contain small traces of the primordial isotopes ^{238}U and ^{232}Th. The decay of these two nuclides lead eventually to the creation of ^{222}Rn and ^{220}Rn, respectively. Since these two radon isotopes have by far the longest half-lives among all other radon isotopes in nature, they are most relevant in the description of radon induced background in XENON1T. The half-life of ^{222}Rn and ^{220}Rn is $T_{1/2} = 3.8\,\text{days}$[1] and $T_{1/2} = 56\,\text{seconds}$, respectively. The radon atoms are continuously produced in the detector materials and they can leave their site of creation and enter the xenon reservoir in two ways. One option is driven by the recoil energy that the radon nucleus receives in the α-decay of its mother nuclide radium. For radon atoms directly on or below the surface, this recoil energy is sufficient to eject it from the material. The second option is the diffusion of the noble gas radon through the material and its subsequent emanation. Like this, also radon atoms from deeper material layers can escape, depending on the diffusion length of the specific material. In the following, we summarize both options under the term *radon emanation*. The emanating noble gas radon can mix with xenon target and distribute within the entire active volume of the TPC. Hence, in contrast to external background from e.g. materials' radioactivity, radon induced background cannot be reduced by profiting from the liquid xenon (LXe) self-shielding capacity.

Fig. 3.1 presents the decay series of ^{238}U and ^{232}Th, respectively. Starting from ^{222}Rn and ^{220}Rn, they feature a similar decay structure. Both isotopes disintegrate in each case via the emission of an α-particle to an isotope of polonium, followed by a further α-decay to an isotope of lead. The following β-decay of ^{214}Bi (^{212}Bi) appears in a close time-coincident with the subsequent α-decay of ^{214}Po (^{212}Po). The ^{220}Rn series ends with the stable ^{208}Pb. In contrast, the ^{222}Rn chain contains further decays subsequent to ^{210}Pb. The accumulation of ^{210}Pb on the detector surfaces can lead to background, as discussed in section 3.1.2. However, the contribution from potential plate-out caused by intrinsic ^{222}Rn emanation during the run-time of the experiment is strongly suppressed, due to the rather small ^{222}Rn concentration in the detector and the long half-life of ^{210}Pb.

The α-decays within the radon series deposit energies in the MeV range, more than

[1] All relevant information in this work on nuclear data, such as decay energies or half-lives, is taken from [92]

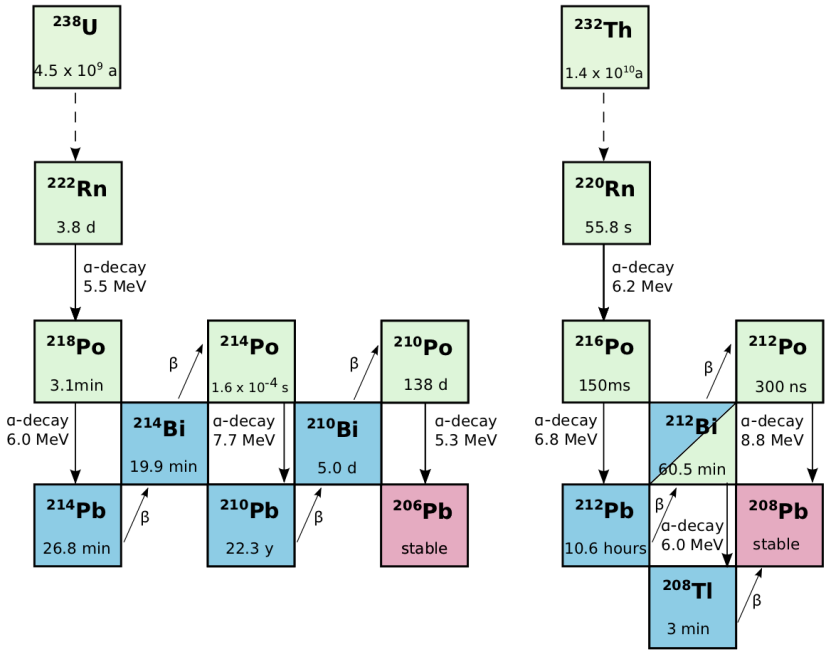

Figure 3.1: ^{238}U and ^{232}Th decay series that include ^{222}Rn and ^{220}Rn and their decay daughters.

two orders of magnitude above the energy region of interest in the dark matter search. Hence, they do not contribute to the background events. In [93] the energy spectra of the β-decays within the two radon chains are simulated. The spectra are shown in Fig. 3.2 in two different energy ranges. Thereby, the same initial ^{222}Rn and ^{220}Rn activity concentration of $10\,\mu\mathrm{Bq/kg}$ is assumed, homogeneously distributed within the liquid xenon of the detector. The continuous energy spectra are reaching down to zero kinetic energy and overlap with the region of interest in dark matter search, shown in the right panel of Fig. 3.2. Therefore, these β-decays are potential sources of background events. Multiple scatter events are generated by the coincident β-decay of ^{214}Bi (^{212}Bi) and the subsequent α-decay of ^{214}Po (^{212}Po) . Since only single-scatter events are accepted in the dark matter analysis, these decays are efficiently removed in XENON1T. Hence, most relevant in terms of potential background are the β-decays of ^{214}Pb and ^{212}Pb.

Comparing the decay spectra of ^{212}Pb and ^{214}Pb, the former induces a higher rate at low energies by a factor of $\sim$ 3, if the initial radon activity concentration is the same. The reason is the lower end-point energy of the ^{212}Pb decay spectrum with respect to ^{214}Pb. In this work, we show that the ^{212}Pb activity concentration is sub-dominant with respect to the ^{214}Pb activity concentration. The main reason is presumably the much shorter half-life of ^{220}Rn with respect to ^{222}Rn, which suppresses the amount of ^{220}Rn atoms reaching the active xenon volume before they decay.

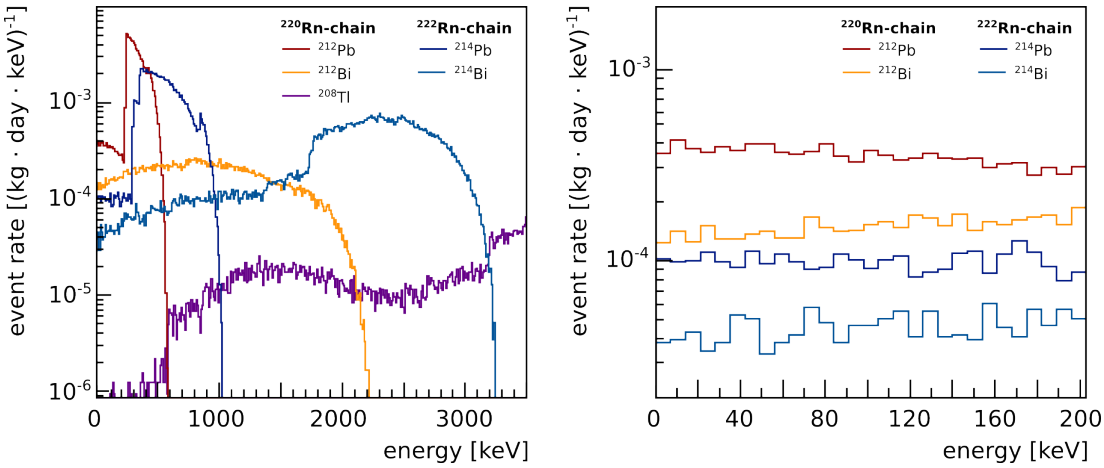

Figure 3.2: Simulated β-decay spectra within the ^{222}Rn and ^{220}Rn chains in the complete energy region (left) and at low energies which are most important for dark matter search (right). Thereby, the same initial activity concentration of $10\,\mu\mathrm{Bq/kg}$ is assumed, which is homogeneously distributed within the liquid xenon. As explained in the text, the β-decays of ^{214}Pb to the ground state is the most important ER background contributions in XENON1T. Figure taken from [93].

In XENON1T, the main contribution to the ER background arises from the ^{214}Pb β-decay to the ground state of ^{214}Bi. In this case no additional γ-radiation is emitted and the resulting single-scatter event can mimic a dark matter interaction. The branching ratio for this decay channel is 10.9% [79]. However, decays to other energy levels are also potentially dangerous since the accompanying γ can exit the detector undetected. This depends on the location of the event relative to the detector borders and the energy of the emitted γ-ray. However, in the rather large liquid xenon volume of the XENON1T TPC, this contribution is assumed to be minor.

3.1.2 Background from detector surfaces

^{222}Rn daughters contained in ambient air can plate-out on detector surfaces during the detector construction and lead to background events. The ^{222}Rn series includes the metal ^{210}Pb that can accumulate on surfaces. Due to the long half-life of ^{210}Pb ($T_{1/2} = 22.3\,\mathrm{years}$), this isotope and consequently its progenies are still present inside the detector during the run-time of the experiment. Since the radon activity in air is much larger than the activity of intrinsic ^{222}Rn emanation from the detector surfaces, the contribution from airborn radon to surface background is not suppressed by the long half-life of ^{210}Pb. Since the ^{220}Rn series does not include such long-lived isotopes, no surface contamination of the detector is caused by this radon isotope. This is also the reason why ^{220}Rn is employed as calibration source of the ER background, and particularly of its main component from ^{222}Rn, in XENON1T.

In XENON1T, the surface background is generated by the decay of ^{210}Pb and its daugh-

ters. Thereby, the β and γ-rays at low energies, that are emitted in the ^{210}Pb and ^{210}Bi decays on the inner surface of the TPC, might create an ER. The ER may exhibit charge-loss, due to S2-forming ionization electrons being trapped on the surface. This can lead to a S2/S1 ratio compatible with the one of a signal-like nuclear recoil (NR). In contrast to that, a NR can be generated by the α-decay of ^{210}Po. On one hand, the recoiling daughter nucleus ^{206}Pb has enough energy ($103\,\mathrm{keV}$) to create a NR. On the other hand, the α-particle from the ^{210}Po decay can trigger (α ,n) reactions with the fluorine, contained in the PTFE (C_2F_4) that covers the inner surface of the XENON1T TPC [94]. The emitted neutron can induce a signal-like NR as well.

With an optimal 3D position reconstruction, surface events close to the boundaries of the TPC can be excluded from the analysis by fiducialization. However, due to a limited position reconstruction in XENON1T, especially at large TPC radii, the probability of an surface background event to fall into the volume used for analysis is increased. Dedicated studies on the impact of the surface background in the dark matter search are described in [62]. In contrast, neutrons created by the described (α ,n) reactions cannot be rejected by fiducialization, as they can travel into the center of the TPC and create a NR. Their amount can be reduced by mitigating the surface contamination before the start of the experiment [II]. In section 3.7, we estimate the ^{210}Po activity on the PTFE walls and the resulting amount of neutron background in XENON1T.

3.2 Radon mitigation techniques in XENON1T

XENON1T pursues several strategies to mitigate the radon induces background. One method is a careful material selection of radio-pure materials used for detector construction. To select materials of low radioactivity, XENON1T performed a comprehensive bulk impurity screening campaign employing High Purity Germanium (HPGe) spectroscopy and Inductively Coupled Plasma Mass Spectrometry (ICP-MS) [74]. With these techniques, the bulk activity of ^{226}Ra, the mother nucleus of ^{222}Rn, can be inferred. However, this bulk activity can be different from the actual ^{222}Rn emanation rate, because the radium atoms might be inhomogeneously distributed in the material and the emanation rate depends on the radon diffusion length in the particular material. Therefore, ^{222}Rn emanation measurements of most materials and subsystems were performed in XENON1T before detector assembly, summarized in [I]. Based on the measurements, a ^{222}Rn activity concentration of $(10.0 \pm 0.7)\,\mu\mathrm{Bq/kg}$ was expected in XENON1T, normalized to the full liquid xenon mass of $3.2\,\mathrm{t}$ inside the detector. The relative contributions from the different detector components are depicted in Fig. 3.3. Out of them, the three pumps (called QDrive pumps), employed to recirculate the xenon, make up the largest fraction. These pumps were exchanged during the run time of the experiment with a pump of negligible radon emanation rate. This results in a

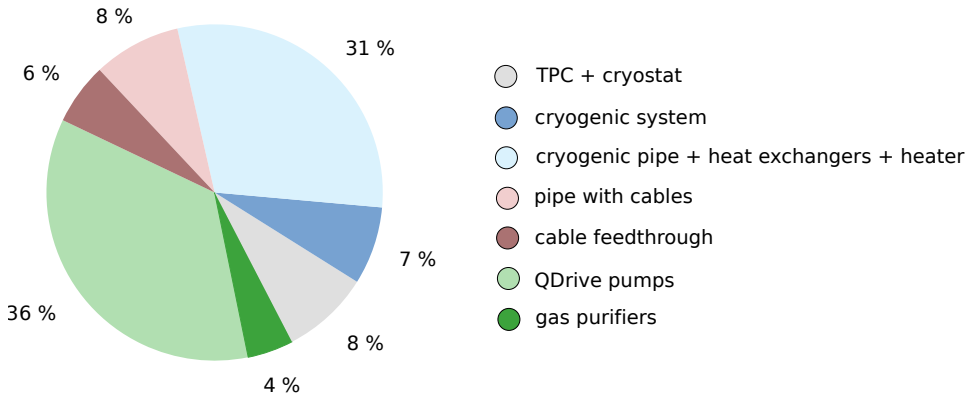

Figure 3.3: Relative contribution from different XENON1T subsystems to the total ^{222}Rn budget in the detector. The largest fraction is made up by the recirculation pumps (QDrive). By exchanging them with a pump that features a negligible radon level, the ^{222}Rn budget of the experiment was significantly reduced, as analyzed in section 3.6. The color code of the pie chart matches the one of the detector sketch in Chapter 2, to illustrate the locations of the ^{222}Rn souces. Figure published in [I].

significant reduction of the ^{222}Rn concentration, as analyzed in section 3.6.

A further possibility to reduce the radon induced background is the installation of an online radon removal system in the xenon purification loop. It separates the xenon and the radon atoms and retains the latter until their disintegration. One technique of such a radon removal system is based on physical adsorption, as discussed in [95–97]. However, in XENON1T the radon removal is realized by cryogenic distillation [76, 83, 98]. The principle of cryogenic distillation is based on the different vapor pressures of two components in an ideal binary mixture, like radon in xenon. In a single distillation stage of a liquid xenon reservoir featuring a gaseous phase on top, the more volatile component (xenon) is accumulating in the gas phase, whereas the less volatile contaminant (radon) is enriched in the liquid xenon phase. The accumulating radon atoms are retained in this reservoir and decay. The described xenon distillation allowed for a radon reduction during the run-time of XENON1T, as detailed in section 3.6. An overview on the radon mitigation techniques in liquid xenon detectors is also given in [III].

3.3 Identifying radon and its daughter decays in XENON1T

The methods used to select the different isotopes from the ^{222}Rn and ^{220}Rn series in the XENON1T data are described in the following section. Based on the selections, various aspects as the spacial event distribution or the rate evolution over time can be investigated. Most important, the background arising from ^{214}Pb and ^{212}Pb can be constrained. Due to the continuous energy spectrum of lead, it cannot be identified on the

event-by-event basis. However, the activity concentration of its mother isotopes radon and polonium and its daughter isotope bismuth sets limits on the lead background in XENON1T.

3.3.1 Data selection and first remarks

In this work, we analyse data from the three science runs (SRs) performed in XENON1T. Thereby, the primary dark matter results of XENON1T are based on SR0 and SR1 [35,49]. The subsequent data taking period, called SR2 was mainly used for R&D studies in XENON1T. For these reasons, it is discussed separately from SR0 and SR1 in this work. The SRs spanned over the following periods:

SR0 October 2016 - January 2017 with $31.1\,\mathrm{days}$ of corrected livetime and a drift field of $120\,\mathrm{V/cm}$

SR1 February 2017- February 2018 with $246.7\,\mathrm{days}$ of corrected livetime and a drift field of $81\,\mathrm{V/cm}$

SR2 February 2018 - December 2018 with $24.4\,\mathrm{days}$ of corrected livetime, whereby a larger data fraction could be used for the presented analysis. The drift field varied due to the R&D studies in a range of $[0-81]\,\mathrm{V/cm}$.

Most figures in the next sections show the full SR1 data. Cross-checks for SR0 and SR2 were performed in order to validate that the same analysis methods can be used for these data sets as well. We applied the so-called livetime cuts on all data, detailed in [68], since the rate evaluation is based on the corrected livetime. The livetime cuts remove certain time intervals, regardless of the properties of the events contained within, if, for example the Muon Veto is triggered or not all channels of the DAQ are ready to record data. Hence, no impact on the described analyses is expected.

We start with a first look at the α-decaying isotopes within the ^{222}Rn and ^{220}Rn decay chains in the XENON1T data. In Fig. 3.4 we show the corrected light signal cS1 at high energies as a function of the TPC depth z. Thereby, the cS1 signal size is based on the amount of light detected by both PMT arrays. The three pronounced lines belong, in ascending cS1 size to the α-decays of ^{210}Po, ^{222}Rn and ^{218}Po. The energy resolution is not sufficient to clearly resolve the ^{220}Rn population at a slightly higher energy than ^{218}Po. At around $60\,000\,\mathrm{PE}$, the faint population of ^{216}Po is noticeable, followed by a rather smeared-out population. The latter belongs to the α-decay of ^{214}Po. At highest energies, we observe a population that will be assigned to the decay of ^{212}Po.

S1 saturation effect: the light signal of the individual isotope lines stays constant with decreasing z in a range of $\sim [-8, -55]\,\mathrm{cm}$. Below and above this range, the S1

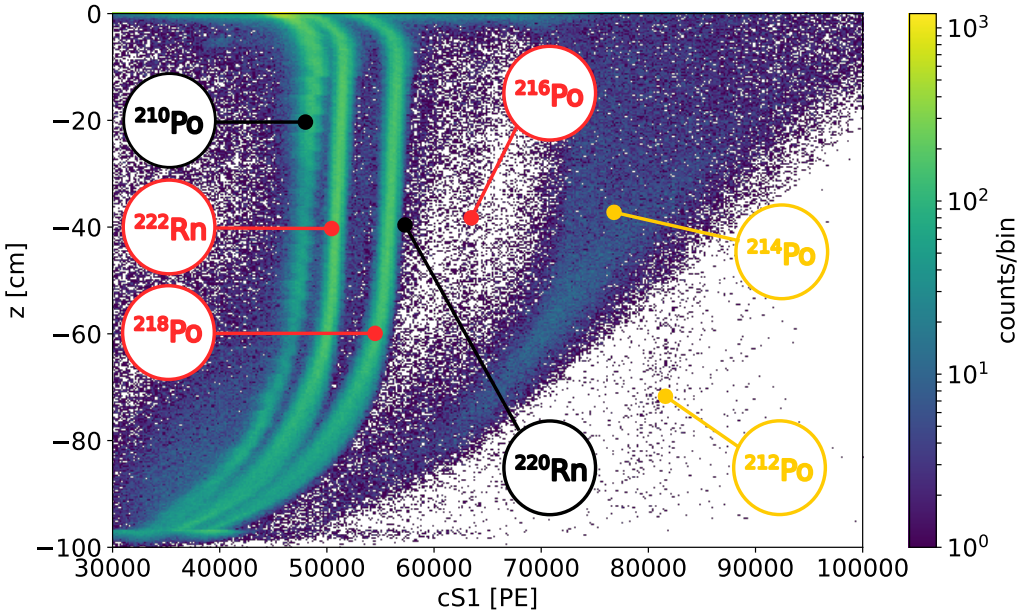

Figure 3.4: Light signal cS1 as function of interaction depth for the α-decaying isotopes within the ^{222}Rn and ^{220}Rn chains. Red circles illustrate the Pure α-Emitters, whereas the yellow circles indicate the BiPo events. Both event classes require different selection methods. In black, we show the ^{210}Po and ^{220}Rn line, that are not selected, as detailed in the text.

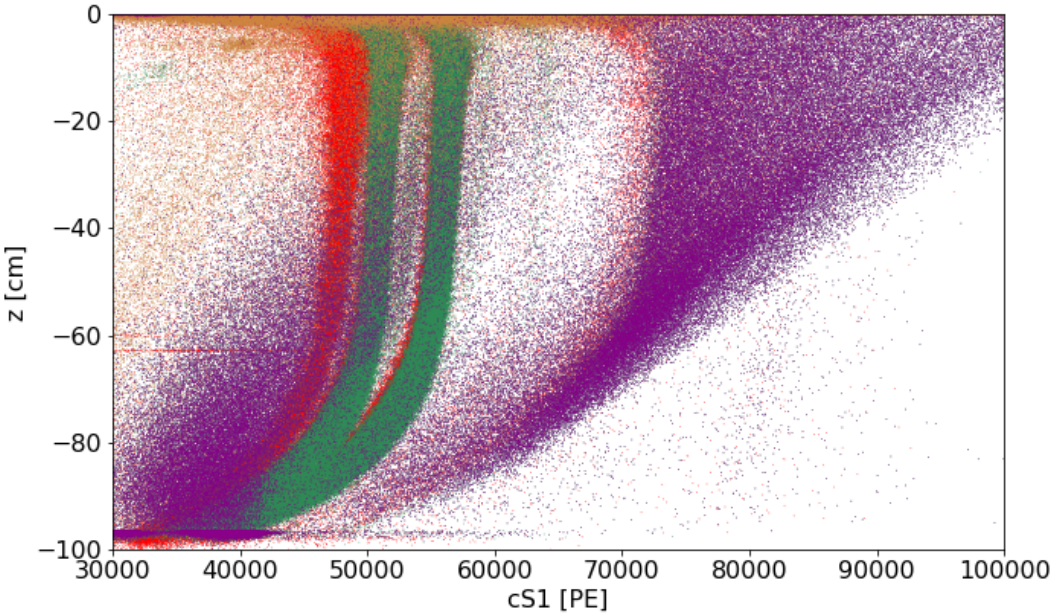

Figure 3.5: Cut overview plot: corrected S1 signal vs. z coordinate of α-decaying isotopes. In green, we show the selected Pure α-Emitters. The events in red are removed by the *Radial Cut*, the events in brown are removed by the *Lower cS2 Cut* and the ones in purple are excluded by the *Upper cS2 Cut*.

signal is minimized due to a saturation effect. The high amount of light created by an α-decay can lead to the saturation of the ADC (analog-to-digital converter) of the individual PMT channels if the maximum input voltage is reached. The closer the decay happens to one of the PMT arrays, the higher is the risk of information loss of the deposited energy and the S1 signal gets seemingly diminished. Due to the higher light collection efficiency at the bottom PMT array (see section 2.3.1), this saturation effect is larger in the lower TPC part than in its upper part.

Pure α-Emitters: for the following analysis, we divide the isotopes into two groups. In the first group, the α-decay is the only interaction within a recorded XENON1T event window (waveform). We call the isotopes of this group Pure α-Emitters and they are indicated by red circles in Fig. 3.4. In section 3.3.2, we will explain how the Pure α-Emitters can be selected in XENON1T data mainly based on their S1 spectrum (also termed α-spectroscopy).

BiPo events: furthermore, we define a second group as so-called BiPo events, including the ^{214}Po and ^{212}Po decays. Due to the relatively short half-life of polonium, its decay is always recorded within the same waveform as the preceding β-decay of bismuth. Due to this delayed-coincidence signature, the class of BiPo events requires a different selection method than the one of Pure α-Emitters. This selection is explained in in section 3.3.3. In case of the ^{214}BiPo events, the delayed-coincidence signature is also the reason for the smeared ^{214}Po distribution in Fig. 3.4, as we will explain below.

^{210}Po and ^{220}Rn: these two isotopes are indicated as black circles in Fig. 3.4. Technically, these two isotopes also belong to the Pure α-Emitters, but we will not include them in the following selection. ^{210}Po events are mainly located at the TPC walls. Due to their location, they suffer from light and charge loss and the exact determination of the ^{210}Po activity concentration in the XENON1T TPC is not trivial and different from the selection of Pure α-Emitters. However, in section 3.7, we will place an upper and lower limit on the ^{210}Po activity concentration. This estimate allows us to constrain the induced neutron background, triggered by the ^{210}Po α-decays. Since the ^{220}Rn population is not resolvable, we cannot select these decays, which will be shown in section 3.3.2.

3.3.2 Identifying Pure α-Emitters

The Pure α-Emitters can be identified by the selection cuts presented below. Furthermore, we will introduce a S1 z-correction to correct for the described S1 saturation effect. This is necessary to select the Pure α-Emitter in the full TPC volume based on their S1 signal size.

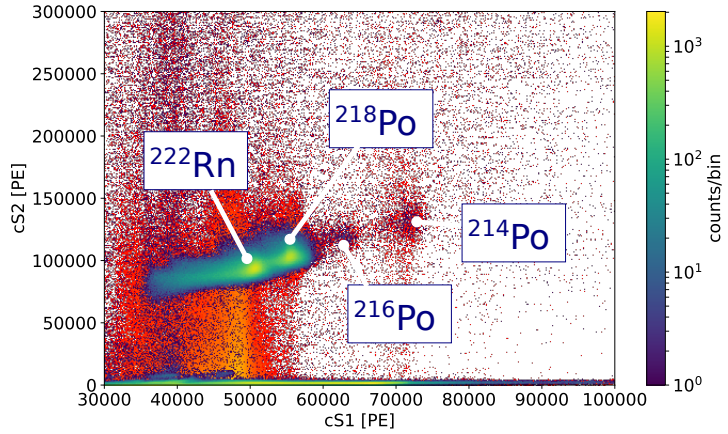

Figure 3.6: cS1 vs. cS2 for the PURE α-EMITTERS. In blue, four distinct populations are identifiable, belonging to the decay of ^{222}Rn, ^{218}Po, ^{216}Po and ^{214}Po, respectively. The events highlighted in red are removed by a *Radial Cut*.

Selection criteria

Describing the PURE α-EMITTERS within the sensitive volume used for the dark matter search is most relevant for the WIMP analysis. We introduce in this section selection criteria to describe the events in the dark matter fiducial volume (DM FV) that is defined in a z-range of $[-8, -94]\,\mathrm{cm}$ and a TPC radius smaller than $42.8\,\mathrm{cm}$. The FV used for the dark matter analysis in [35, 49] has a slightly different definition, but it is contained within the boundaries of the DM FV. By removing the criteria for the event selection within the DM FV, we can select the events in the full TPC and show their spacial distribution in section 3.4.

Fig. 3.5 presents the same parameter space as shown already in Fig. 3.4. Therein, we highlight the events according to the selection cuts that we define in the following. Illustrated in green are the PURE α-EMITTERS, namely ^{222}Rn, ^{218}Po and ^{216}Po, which we eventually want to select.

cS1 Cut: the high and mono-energetic decay energies $> 5\,\mathrm{MeV}$ of the PURE α-EMITTERS allow for their clear separation from β and γ-interactions, that deposit lower energies in the liquid xenon and consequently create smaller S1 signals than an α-decay. As a first cut, we select events with cS1 $> 30\,000\,\mathrm{PE}$. Therefore, the cS1 axis of all plots in this section only start at this cS1 value.

Radial Cut: Fig. 3.6 shows the PURE α-EMITTERS in their cS1-cS2 parameter space, after applying the *cS1 Cut*. In blue, we identify four event population that have a rather defined cS1 to cS2 ratio. The smearing of the cS1 signal towards lower values, the best visible for the ^{222}Rn and ^{218}Po events, is caused by the described S1 saturation effect. In red, we show the events that are removed by the *Radial Cut* of the DM FV. Since they mainly belong to the ^{210}Po contamination at the TPC wall, they suffer from signal loss and consequently their cS1 to cS2 ratio is less defined. The removed events are also shown in red in the cut overview plot

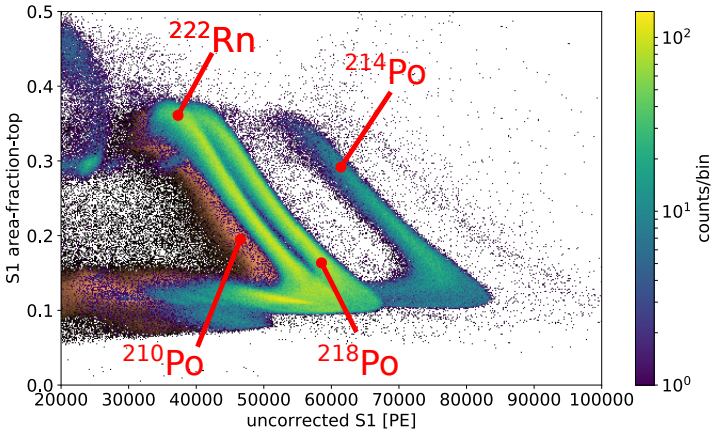

Figure 3.7: S1-area-fraction-top versus the uncorrected S1 signal for the PURE α-EMITTERS. In brown those events are highlighted that feature a cS2 $< 50\,000$ PE.

in Fig. 3.5, whereby their S1 signal size matches indeed the one of ^{210}Po.

Lower cS2 Cut: in Fig. 3.6 we furthermore observe a population of events in blue at rather small S2 sizes along the entire cS1 range, that are not removed by the *Radial Cut*. Eventually, we will remove them with a lower cut on cS2 $> 50\,000$ PE, as they do not belong to the PURE α-EMITTERS.

To study their origin, we apply the *cS1 Cut* and *Radial Cut* and show the uncorrected S1 signal of the remaining events as a function of their S1 area-fraction-top (aft) parameter in Fig. 3.7. The aft parameter indicates the fraction of S1 light detected by the top PMT array in comparison to the total light detected by both arrays. Typically, the interaction depth is calculated with the time difference between the S1 and S2 signals. In contrast, the aft parameter is a S2-independent measure of the interaction depth in the TPC, being maximal at the top of the TPC and decreasing towards the bottom part. In Fig. 3.7, we observe four main event populations, belonging to the PURE α-EMITTERS and ^{214}Po. In brown, we show the events under investigation, with cS2 $< 50\,000$ PE. Due to their S1 signal size, we can attribute them clearly to ^{210}Po decays that are still present after the *Radial Cut*. A requirement for the *Radial Cut* is that the event's S2 signal is not completely lost, since it is necessary for the position reconstruction in the (x,y)-plane. However, the presented ^{210}Po events lost their S2 completely and consequently the correct information on their location is irrecoverable. In these cases, a random S2 signal is matched to the ^{210}Po S1 signal, occurring inside the radius of the DM FV. For this reason, this class of ^{210}Po is not removed by the *Radial Cut*. As we will learn in section 3.4, a large fraction of BIPO is also prone to charge loss due to their location at the TPC edges. Hence, some of the events highlighted in brown also belong to BIPO events.

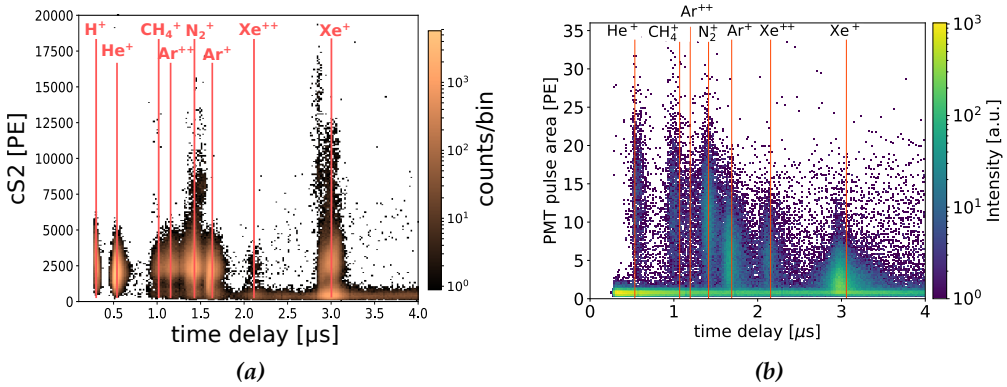

Figure 3.8: (a) cS2 size vs. drift time of Pure α-Emitters. The characteristic line spectrum is similar to the one generated by after-pulses in XENON1T. The PMT afterpulse spectrum measured in the XENON1T PMTs is shown in (b). Figure (b) courtesy of Luisa Hoetzsch.

In the cut overview plot (Fig. 3.5), we highlight the events with cS2 $< 50\,000$ PE in brown. Most of them are located at rather small z-values in the TPC. The event's z-value is based on the drift time of the S2-forming ionization electrons. In Fig. 3.8a the cS2 size as a function of drift times is shown for events with low cS2 sizes. The event distribution features distinct accumulation at specific drift time values. The reason becomes clear by comparing this pattern to the so-called after-pulse spectrum of the XENON1T PMTs, shown in Fig. 3.8b. Ideally, the volume of the PMT should be under vacuum, but residual contaminants are inevitably present. If scintillation photons strike the photocathode of a PMT, the liberated photo-electrons can ionize these residual molecules along their trajectory towards the anode. The created positive ions can return to the photocathode and eject further photo-electrons which cause the after-pulse. The time delay of such after-pulses depends on the mass and charge of the ions as shown in Fig. 3.8b. The S1 light of the ^{210}Po decay can trigger the after-pulse which can potentially serve as wrongly matched S2 signal. The probability of this process is enhanced for α-decays, due to the larger amount of created S1 scintillation light.

In an additional process, the S1 light can also ionize the metallic gate electrode close to the liquid xenon surface. The emitted photo-electrons can also form a S2 signal that might be wrongly matched to the S1 signal. As the emitted photo-electrons have to overcome only short drift distance before being extracted into the gas phase, these events are also reconstructed at rather small z-values. We conclude that events with cS2 $< 50\,000$ PE do not belong to the class of Pure α-Emitters and are therefore removed in our selection.

Upper cS2 Cut: in Fig. 3.6 we furthermore observe a population of events in blue at rather large S2 sizes along the entire cS1 range, that are not removed by the

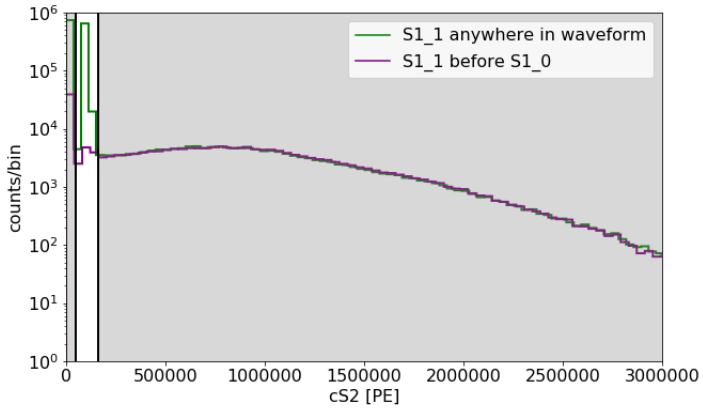

Figure 3.9: cS2 spectrum that either feature an arbitrary time ordering of the largest S1 (S1[0]) and second largest S1 (S1[1]) (green) or for which the S1[1] is followed by the S1[0] (purple). The gray shaded region indicates the events, that are removed by the S2 cuts. The green peak in the non-shaded region is mainly generated by the Pure α-Emitters.

Radial Cut. These events will be removed by an upper cut on the S2 size at cS2 $< 150\,000$ PE.

We want to study the origin of the events featuring rather large S2 signal sizes. As described, for the Pure α-Emitters we expect only one interaction and hence only one S1 signal in the waveform. However, there are a few mechanisms that can cause further S1s. We denote the largest S1 signal as S1[0] and the second largest S1 signal S1[1] in a waveform. In Fig. 3.9 we show the cS2 spectra for (a) events for which the S1[1] occurs *before* the S1[0] in purple and (b) events without specific S1 time-ordering in green. As shown, basically all events with a large cS2 signal belong to the category (a). In section 3.3.3 we will learn that this event class constitute of BiPo events, whose main characteristic is exactly this specific S1 time-ordering of the S1[0] and S1[1]. The BiPo event include a β-and α-decay in their waveform. The large cS2 values is caused by energy depositions of the emitted β-and γ-radiation at $\mathcal{O}(10^6\,\mathrm{PE})$. In contrast, the typical cS2 size of an α-particle is at $\mathcal{O}(10^5\,\mathrm{PE})$. Another indication, that the large-S2 events are caused by BiPo events is shown in the cut overview plot Fig. 3.5. The events with cS2 $> 150\,000$ PE are highlighted in purple. The comparison of their position in the cS1-z space with the one in Fig. 3.4 verifies that they belong to those events featuring an ^{214}Po decay in their waveform.

As described in category (b), there are also events featuring the second largest S1 in the same waveform after the main S1. In this case, the S1[1] can be falsely identified from noise signals or by a PMT baseline fluctuation, due to the high amount of photo-electrons from the S1[0], generated by the high-energetic α-particle. We conclude that events with cS2 $> 150\,000$ PE do not belong to the class of Pure α-Emitters and are therefore removed in our selection.

z Cuts: for the calculation of the activity concentration inside the DM FV we select a z-range of $[-8, -94]\,\mathrm{cm}$.

The described criteria allow us to select the Pure α-Emitters inside the full TPC or in the DM FV. Thereby, the cuts either remove a certain part of the TPC volume (*Radial Cut* and z *Cuts*) or reject events different from Pure α-Emitters (*cS1 Cut*, *Lower cS2 Cut* and *Upper cS2 Cut*). Hence, acceptance losses on the number of selected Pure α-Emitters, normalized to the xenon volume, are thought to be negligible. In the next section, we show the cS1 value of the selected Pure α-Emitters as function of z, after the applied selection cuts.

S1 z-correction

In Fig. 3.10 the cS1 parameter of the Pure α-Emitters is shown as function of z, after applying the described selection cuts (except of the z *Cuts*). The isotope lines are well distinguishable in a z-range of $[-8, -55]\,\mathrm{cm}$, indicated by the non-shaded region.This allows us to select them in the top TPC part of the DM FV. This is done in the next section based on the S1 signal size.

To calculate the activity concentration of the Pure α-Emitters in the full DM FV, we also have to select the events in a z-range $< -55\,\mathrm{cm}$. In this range, the S1 scintillation light of the α-decays saturates the PMTs' ADCs. This saturation effect causes the isotope lines to bend and overlap, making a clear event selection impossible. The probability of the saturation effect is smaller, the larger the distance between the S1 light generation and the bottom PMT array. We make use of this property, by displaying the light signal $\mathrm{S1_{top}}$, detected with the *top PMT array only* for events at $z < -55\,\mathrm{cm}$ in Fig. 3.11a. In this parameter space, the isotope lines become resolvable. To select the events in the bottom TPC part, we will first have to apply a z-correction on the $\mathrm{S1_{top}}$ signal, as described in the following.

We construct the $\mathrm{S1_{top}}$ z-correction in the z-range $< -55\,\mathrm{cm}$, similar as done in [99]. We explain the z-correction based on the ^{222}Rn distribution and the correction for the ^{218}Po events is analogue. In the first step, the histogram in Fig. 3.11a is binned into $400\,\mathrm{bins}$ along the z-axis. Subsequently, the 50th percentile of the ^{222}Rn distribution in each bin is determined, denoted as $\mathrm{S1_{top}^{mean}}$. A 2D fit is performed through the $\mathrm{S1_{top}^{mean}}$ values along the z-axis. The fit is shown in red for the ^{222}Rn events. Thereafter, each the $\mathrm{S1_{top}}$ of each event is corrected per bin and the corrected $\mathrm{cS1_{top}}$ value is defines as

$$\mathrm{cS1_{top}} = \mathrm{S1_{top}} + \mathrm{S1_{corr}} = \mathrm{S1_{top}} + |\mathrm{S1_{top}^{mean}}(\mathrm{z} = -55\mathrm{cm}) - \mathrm{S1_{top}^{mean}}| \tag{3.3.1}$$

where $\mathrm{S1_{corr}}$ is the reference $\mathrm{S1_{top}^{mean}}$ value at $z = -55\,\mathrm{cm}$ to which the $\mathrm{S1_{top}}$ values per z-slice get aligned by the correction. Similarly, the ^{218}Po distribution is corrected with

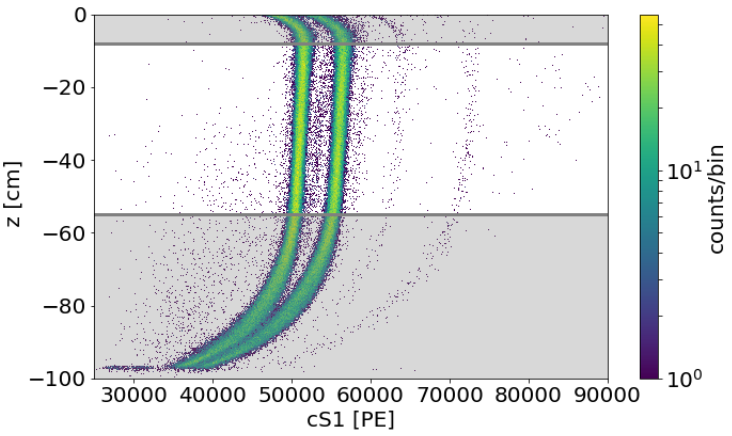

Figure 3.10: cS1 signal of the PURE α-EMITTERS along the z-axis of the TPC, after applying the introduced selection cuts. The gray shaded region in a z-range of $[0, -8]\,\mathrm{cm}$ illustrates the events removed by the DM FV z cut. The events below $-55\,\mathrm{cm}$ are affected by S1 saturation and therefore not selected in the shown cS1 parameter space.

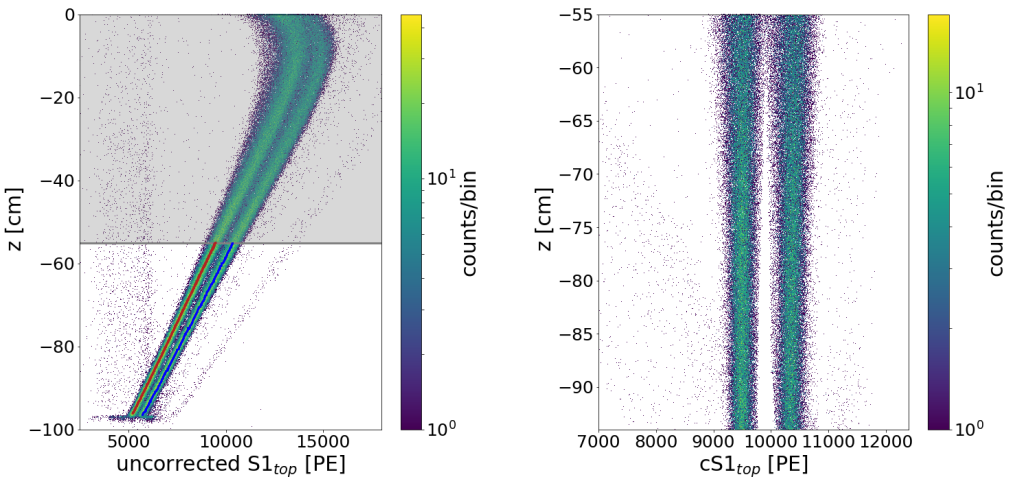

(a) ***(b)***

Figure 3.11: (a) the uncorrected S1 light signal detected by the top PMT array ($S1_{top}$) vs. the TPC depth. The isotope line in the non-shaded regions are resolvable. The red and blue lines presents the 2D fit to the line of ^{222}Rn and ^{218}Po distribution, respectively. The fits are used for the z-correction. (b) z-corrected $cS1_{top}$ vs. TPC depth.

the correction function shown in blue in Fig. 3.11a. Due to the small event number, the ^{216}Po line could not be fit independently and it was corrected with the ^{218}Po correction function. Fig. 3.11b illustrates the z-corrected isotope lines in the cS1$_{\text{top}}$ parameter space.

S1 spectra of Pure α-Emitters

We show the cS1 (cS1$_{\text{top}}$) spectrum of the events in a z-range of $[-8, -55]$ cm ($[-55, -94]$ cm) in Fig. 3.12 on the left (right) panel.

Fit of S1 spectra: the individual peaks in the cS1 (cS1$_{\text{top}}$) spectrum are fitted with a Gaussian function. This enables us to determine the respective mean μ and σ values. By assuming a linear S1 scale, the fitted mean value of the ^{222}Rn peak and its known decay energy allows for a prediction of the theoretical ^{218}Po and ^{216}Po S1 peak positions. The expected mean values are indicated by the vertical lines in Fig.3.12. The mean value of the ^{218}Po peak is in both spectra comparable with the expectation as well as the ^{216}Po peak position in the cS1 spectrum. For ^{216}Po in the cS1$_{\text{top}}$ spectrum, we identify a larger discrepancy between the S1 peak position and the expectation. In this case, the size of the S1 signal is only corrected in the z-dimension and not in three dimensions (in contrast to cS1). Furthermore, the S1 value of the ^{216}Po events is corrected with the z-correction function of the ^{218}Po distribution, which might introduce an additional bias. We also show the theoretical position of the ^{220}Rn distribution. As mentioned, this peak is not clearly resolvable.

Energy resolution: we furthermore compare the energy resolution σ(E)/μ(E) of the S1 peaks in the top and bottom detector part. We obtain for the ^{222}Rn, ^{218}Po and ^{216}Po peaks of the cS1 spectrum in the top TPC part a resolution of $1.1\,\%$, $1.1\,\%$ and $1.8\,\%$, respectively. In this case, the S1 light signal is detected with both PMT arrays and a 3D signal correction is applied. For the ^{222}Rn, ^{218}Po and ^{216}Po peaks in the cS1$_{\text{top}}$ energy spectrum in the bottom TPC region, the energy resolution is $1.4\,\%$, $1.5\,\%$ and $2.6\,\%$, respectively. The slightly worse energy resolution in the bottom TPC part can be explained as follows. The S1 scintillation light is in this case only detected by the top PMT array. Once created in the liquid xenon volume, it can be reflected by the liquid-gas interface before reaching the top PMT array. Therefore, its path length can be longer than for scintillation light detected by the bottom PMT array. This longer path length enhances the risk of signal loss due to adsorption by impurities diluted in the liquid xenon, causing a worse resolution of the light signal. Signal loss can also occur due to the limited reflectivity of scintillation light at the TPC walls. A further reason for the comparable worse resolution is that the cS1$_{\text{top}}$ is only corrected in the z-dimension and not in 3D as in the case of the cS1 parameter. The general observation

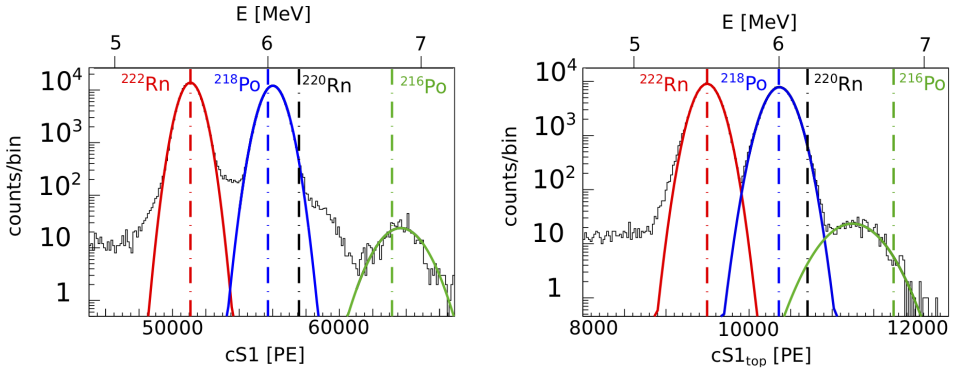

Figure 3.12: (left) cS1 spectrum in a z-range of $[-8, -55]\,\mathrm{cm}$. (right) cS1$_{\mathrm{top}}$ spectrum in a z-range of $[-55, -94]\,\mathrm{cm}$. The peaks are fitted by Gaussian functions, as described in the text. The vertical dashed lines indicate the decay energy of the individual α-decays.

of a very good energy resolution at the percent level, in both spectra, can be explained by the relative large amount of created scintillation photons by an α-decay in the liquid xenon.

Event selection: based on these spectra, we select the PURE α-EMITTERS in both TPC volumes. The number of events in each peak is calculated by integrating over a certain S1 range and scaling up this number to the complete peak width. We also show the theoretical ^{220}Rn peak position in Fig. 3.12. The peak itself cannot be resolved in both spectra and we estimate its contamination to the ^{218}Po and ^{216}Po distribution in the following.

Fit of cS1 spectrum in top TPC part:

^{222}Rn: we restrict the ^{222}Rn event selection to the $\pm 2\sigma$ cS1 region, centered around the fitted mean value $\mu_{^{222}\mathrm{Rn}}$, as in this region the ^{218}Po peak does not overlap. The number of selected events is $0.05\,\%$ larger when selecting the $\pm 3\sigma$ cS1 region, that includes the events between the ^{222}Rn and ^{218}Po peak (always after having scaled the event number to the full peak width). The ^{222}Rn peak is smeared towards smaller cS1 values, due to the slight bias of the cS1 standard correction (see Fig. 3.10). The number of events at cS1 $< (\mu_{^{222}\mathrm{Rn}} - 3\sigma)$ is $3\,\%$ in comparison to the scaled event number covered by the $\pm 2\sigma$ cS1 region. We quadratically add the $0.05\,\%$ and $3\,\%$ systematic uncertainty to estimate a combined uncertainty of $3\,\%$ on the number of selected ^{222}Rn events. In comparison, the statistical uncertainty is negligible.

^{218}Po: the ^{218}Po events are selected in the $\pm 2\sigma$ cS1 region around the fitted mean value $\mu_{^{218}\mathrm{Po}}$. Similar as in the ^{222}Rn case, we estimate the systematic uncertainty due to the events between the two peaks by comparing the scaled number of ^{218}Po events in the $\pm 2\sigma$ cS1 region and $\pm 3\sigma$ cS1 region and obtain a difference

of $0.04\,\%$. ^{220}Rn events are potentially contaminating the ^{218}Po distribution. The ^{220}Rn peak cannot be fitted and the black dashed line in Fig. 3.12 (left) indicates its theoretical mean value. To estimate the contribution of ^{220}Rn to ^{218}Po events, we compare the scaled number of events in the $[\mu_{^{218}\mathrm{Po}},-2\sigma_{^{218}\mathrm{Po}}]$ cS1 region, in which the ^{220}Rn contribution is presumably small with the scaled number of events in the $[\mu_{^{218}\mathrm{Po}},+2\sigma_{^{218}\mathrm{Po}}]$ cS1 region. The difference is $1\,\%$ which we assume to be the maximal ^{220}Rn contamination in the ^{218}Po distribution. Furthermore, we calculate the number of events between the ^{218}Po and ^{216}Po peak at higher cS1 values, by integrating over the cS1 interval of $[\mu_{^{218}\mathrm{Po}}+2\sigma_{^{218}\mathrm{Po}},\mu_{^{216}\mathrm{Po}}-2\sigma_{^{216}\mathrm{Po}}]$. The maximal contribution from these events to the ^{218}Po distribution is $3\,\%$. Since we cannot definitely determine whether they originate from ^{220}Rn, ^{216}Po or ^{218}Po, we include this contribution in the systematic uncertainty. From the described uncertainties, we estimate a combined uncertainty of $3\,\%$ on the number of ^{218}Po events. The statistical uncertainty is negligible in comparison.

^{216}Po: the ^{216}Po events are selected in a cS1 interval of $[\mu_{^{216}\mathrm{Po}},+2\sigma_{^{216}\mathrm{Po}}]$ to reduce the potential contamination of ^{220}Rn events. We estimate an uncertainty on this number by comparing it with the number of events in the interval of $[\mu_{^{216}\mathrm{Po}},+3\sigma_{^{216}\mathrm{Po}}]$. The obtained difference of $2\,\%$ is quadratically added to the statistical uncertainty of $4\,\%$. Thus, the combined uncertainty of the ^{216}Po events is $4\,\%$.

Fit of $\mathrm{cS1_{top}}$ spectrum in bottom TPC part:

^{222}Rn: the ^{222}Rn events are selected in the $\pm2\sigma$ $\mathrm{cS1_{top}}$ region centered around the fitted mean value to avoid a ^{218}Po contamination. The number of selected events is $0.7\,\%$ larger when selecting the $\pm3\sigma$ $\mathrm{cS1_{top}}$ region, that includes the events between the ^{222}Rn and ^{218}Po peak.The systematic uncertainty from events at low $\mathrm{cS1_{top}}$, that are not covered by the $\pm2\sigma$ range, is $3\,\%$. We quadratically add the $0.7\,\%$ and $3\,\%$ systematic uncertainty to estimate a combined uncertainty of $3\,\%$ on the number of selected ^{222}Rn events. In comparison, the statistical uncertainty is negligible.

^{218}Po: the ^{218}Po events are selected in the $\pm2\sigma$ $\mathrm{cS1_{top}}$ region around the fitted mean value $\mu_{^{218}\mathrm{Po}}$. The number of selected events is $0.8\,\%$ larger when selecting the $\pm3\sigma$ $\mathrm{cS1_{top}}$ region, that includes the events between the ^{222}Rn and ^{218}Po peak. Within its $\pm2\sigma$ $\mathrm{cS1_{top}}$ region, the ^{218}Po peak could be contaminated by ^{220}Rn and ^{216}Po events. By comparing the number of calculated ^{218}Po events in the $[\mu_{^{218}\mathrm{Po}},-2\sigma_{^{218}\mathrm{Po}}]$ and $[\mu_{^{218}\mathrm{Po}},+2\sigma_{^{218}\mathrm{Po}}]$ $\mathrm{cS1_{top}}$ regions, we estimate its contribution of ^{220}Rn and ^{216}Po events of $4\,\%$. We quadratically add the $0.8\,\%$ and $4\,\%$ systematic uncertainty to estimate a combined uncertainty of $4\,\%$ on the number of selected ^{218}Po events. In comparison, the statistical uncertainty is negligible.

isotope	con. top [µBq/kg]	con. bottom [µBq/kg]	ratio top/bottom	average con. [µBq/kg]
^{222}Rn	13.3±0.4	13.2±0.4	1.01 ± 0.04	13.3±0.6
^{218}Po	12.7±0.4	12.6±0.5	1.01 ± 0.05	12.7±0.6
^{216}Po	0.071±0.003	0.12±0.005	0.6± 0.04	0.09±0.01

Table 3.1: Integral isotope activity concentration of Pure α-Emitters in a volume of either $[-8, -55]$ cm (top) and $[-55, -94]$ cm (bottom), respectively, and r $<$ 42.8 cm. The third column shows the ratio between the isotope's top and bottom activity concentration. The fourth column presents the activity concentration averaged over both detector parts. In the calculation of these activity concentration, periods of radon removal are excluded.

^{216}Po: the number of events is calculated by integrating over the $[\mu_{^{216}\mathrm{Po}}, +2\sigma_{^{216}\mathrm{Po}}]$ $\mathrm{cS1}_{\mathrm{top}}$ range to reduce the potential ^{220}Rn contamination. The systematic uncertainty by integrating over the $[\mu_{^{216}\mathrm{Po}}, +3\sigma_{^{216}\mathrm{Po}}]$ $\mathrm{cS1}_{\mathrm{top}}$ range is 3 %. The statistical uncertainty of 2 % is added quadratically and we obtain a combined uncertainty of 4 % on the number of ^{216}Po events.

Pure α-Emitters activity concentration: in the following, we calculate of the activity concentration for each Pure α-Emitters in dark matter search data of SR0 and SR1. Thereby, we exclude periods of radon removal by cryogenic xenon distillation, since the distillation causes a temporally reduced activity concentration of radon and its daughter products, that is discussed in section 3.6. To determine the individual activity concentrations, we divide the extracted number of events per isotope and TPC volume by the corrected livetime and by the liquid xenon mass inside respective volume. The activity concentration are summarized in Table 3.1. We make the following observations:

- the ^{222}Rn (^{218}Po) activity concentration in the top and bottom detector part are compatible, which points to a homogeneous spacial distribution within the xenon volume. On contrary, the ^{216}Po activity concentration in the two detector regions differ from one another which indicates a inhomogeneous spacial distribution. The spacial distributions are discussed in more detail in section 3.4.

- we also state the activity concentrations averaged over both detector parts in Table 3.1. Due to the short-half life of ^{218}Po with respect to the one of ^{222}Rn, the decay rate of ^{218}Po is in equilibrium with the one of ^{222}Rn. Therefore, we expect the same activity concentration of ^{222}Rn and ^{218}Po inside the detector, which is not the case as seen in Table 3.1. This phenomenon becomes clear when discussing the spacial distributions in section 3.4.

- furthermore, the ^{216}Po activity concentration is $\lesssim$ 1 % of the ^{218}Po activity concentration in both detector parts. Whereas the ^{216}Po decay is part of the ^{220}Rn series, ^{218}Po is the daughter isotope of ^{222}Rn. The large difference between the

polonium activity concentration indicates that the ^{220}Rn induced background is much smaller than the one generated by the ^{222}Rn series.

- the measured ^{218}Po (^{216}Po) activity concentration can be transferred into an upper limit on the low energy ^{214}Pb (^{212}Pb) activity concentration as discussed in section 3.8.

3.3.3 Identifying BiPo events

In contrast to the Pure α-Emitters, the BiPo events feature a more complex event signature, as two decays occur in the same waveform. The polonium nuclei has a short half-life of $T_{1/2} = 300\,\mathrm{ns}$, in the case of ^{212}Po and $T_{1/2} = 164\,\mu\mathrm{s}$ for ^{214}Po. Hence, they decay promptly after the β-decay of their mother nuclei bismuth, such as:

$$^{212}\mathrm{Bi} \rightarrow {}^{212}\mathrm{Po} + \beta^- + \bar{\nu}_\mathrm{e} \xrightarrow{T_{1/2}= 300\mathrm{ns}} {}^{208}\mathrm{Pb} + \alpha \tag{3.3.2}$$

$$^{214}\mathrm{Bi} \rightarrow {}^{214}\mathrm{Po} + \beta^- + \bar{\nu}_\mathrm{e} \xrightarrow{T_{1/2}= 164\mu\mathrm{s}} {}^{210}\mathrm{Pb} + \alpha \tag{3.3.3}$$

The largest S1 in the waveform is always associated with the high energetic α-decay. They feature decay energies of $8.8\,\mathrm{MeV}$ and $7.7\,\mathrm{MeV}$ for the ^{212}Po and the ^{214}Po decay, respectively and we denote them as $S1_\alpha$. The second largest S1 in the waveform, occurring *before* the $S1_\alpha$ is named $S1_\beta$ and is related to the β-decay with a Q-value of $2.25\,\mathrm{MeV}$ ($3.27\,\mathrm{MeV}$) for the ^{212}Bi (^{214}Bi) decay.

Potentially wrong S2 matching: the two-fold S1 signals from the coincident decays offer a powerful selection criteria for the BiPo events. However, the correct matching of the *two* S1-S2 pairs in the same waveform is not guaranteed by the XENON1T data processor, as it is optimized for single-scatter events. The XENON1T processor searches for valid S1-S2 pairs in a waveform, by starting with the largest peaks of each kind [68]. This means that the $S1_\alpha$ is paired with the largest S2 peak after the $S1_\alpha$. However, in the case of BiPo events, it is not clear whether this S2 is generated by the α-decay or the β-decay. Even though the energy deposition of the α-particle is much larger than the one of the β-particle, the $S2_\alpha$ is not necessarily the largest S2 in the waveform. The reason is the dense track of the α-particle in the xenon, that causes many liberated ionization electrons to recombine. Hence, the number of ionization electrons that can be extracted from the interaction site by the applied drift field is reduced, causing the $S2_\alpha$ size to be quenched (we discuss the quenching effect in more detail in section 3.5). The $S2_\beta$ size depends on the continuous energy spectrum of the β-particle. Hence, its size ranks over a large range down to zero and it can be both smaller and larger as the $S2_\alpha$. As the correct S1-S2 pairing is not guaranteed, the spacial position reconstruction of BiPo events is not possible by default. In connection to this, the signal size corrections

are not attainable as they rely on the spacial position. These are the reasons why the ^{214}Po distribution in Fig. 3.4 is smeared out.

Scaling factor for ^{212}Bi activity concentration: whereas the described bismuth in the ^{222}Rn chain always decays to polonium via a β-decay, the bismuth in the ^{220}Rn chain has a probability of $64.06\,\%$ for this decay mode. In the remaining $35.94\,\%$, it decays via the emission of an α-particle to ^{208}Tl (see Fig. 3.1). As ^{208}Tl has a comparatively long half-life of $3\,\mathrm{min}$, the ^{212}Bi - ^{208}Tl decay can not be identified based on the delayed-coincidence signature. Therefore, we have to keep in mind that the determined ^{212}BiPo amount has to be scaled to calculate the ^{212}Bi activity concentration inside the TPC.

In the following section *S1-Only Analysis*, we determine the BiPo amount within the *full* TPC. Thereby, we only use the time information of the $S1_\beta$ - $S1_\alpha$ ordering, without including a S2 signal. The advantage is that we can determine the BiPo activity concentration free from charge loss effects, that can occur for BiPo events as described below. In section *S1-S2 Analysis*, we involve the S2 signal again to determine the exact event position and the BiPo activity concentration in the DM FV. For this purpose, an algorithm was developed for a correct S1-S2 pairing.

S1-Only Analysis

To select the BiPo events within the full TPC, based on their $S1_\alpha$ and $S1_\beta$ properties, we apply the following selection criteria:

S1 Cut: we require that $S1_\alpha$ of the high-energetic α-particle exceeds $30\,000\,\mathrm{PE}$.

S1 time-ordering Cut: the correct time-ordering of the $S1_\alpha$ and $S1_\beta$ is the most distinctive characteristic for the BiPo decay selection. We demand that the second largest S1 ($S1_\beta$) occurs *before* the largest S1 ($S1_\alpha$). With this cut, we explicitly require two S1 signals within the same waveform. The time difference T($S1_\alpha$) - T($S1_\beta$) will be denoted as ΔS1.

ΔS1 Cut: furthermore, we make use of the large difference among the half-lives of ^{212}Po and ^{214}Po and chose specific ΔS1 ranges for their respective selection. In the case of the ^{214}BiPo identification we demand $\Delta\mathrm{S1} > 2\,\mu\mathrm{s}$ because at this lower threshold the contribution from ^{212}BiPo decays is negligible. For the classification of the ^{212}BiPo events we require $0.22\,\mu\mathrm{s} < \Delta\mathrm{S1} < 2\,\mu\mathrm{s}$, whereby the lower threshold is chosen such as two S1 signals can be clearly separated from one another by the XENON1T data processor. The known ^{214}BiPo contamination within this ΔS1 range is considered for the ^{212}BiPo rate determination. In both BiPo classes, these constraints on ΔS1 lead to an acceptance loss which can be calculated by the radioactive-decay law and for which it will be corrected in the following studies.

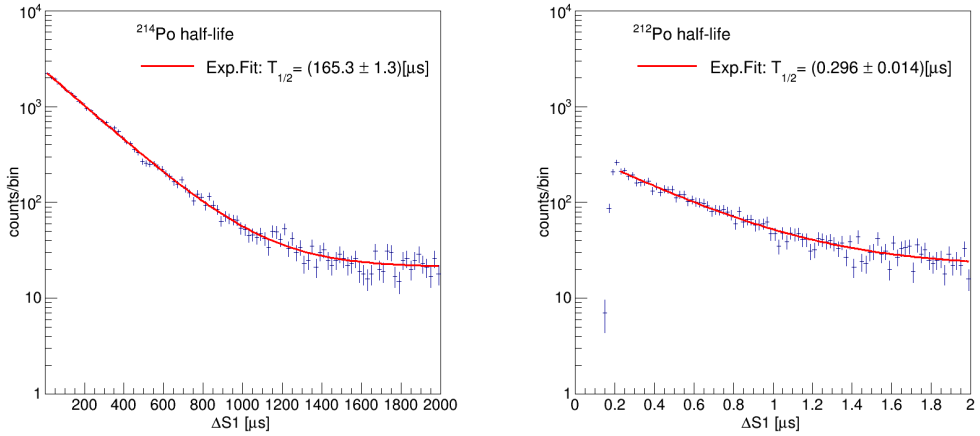

(a) *(b)*

Figure 3.13: Time-difference ΔS1 between the bismuth and polonium decay of the (a) ^{214}BiPo and (b) ^{212}BiPo events, based on the *S1-Only Analysis*. The red line indicates the fit of an exponential plus constant term. The determined half-lives of ^{214}Po and ^{212}Po agree with the literature values.

After applying these selection cuts, the distribution of the time-difference ΔS1 is shown in Fig. 3.13a and 3.13b for the ^{214}BiPo and ^{212}BiPo events, respectively. In each case, an exponential function plus a constant term is fitted. The constant term accounts for the pedestal arising from random coincidences in the TPC. From these fits, the measured half-life for ^{214}Po and ^{212}Po can be extracted, resulting in (165.3 ± 1.3) µs and (296 ± 14) ns, respectively. The measured values are in agreement with the literature values. This result demonstrates that the identification of BiPo events is possible by relying solely on their S1 light signals.

BiPo level from S1-Only Analysis: we calculate the BiPo rates inside the full TPC volume based on this analysis. For this purpose, the constant offset of the distributions in Fig. 3.13a and 3.13b is subtracted. Furthermore, we account for the acceptance loss due to the stated ΔS1 cuts. As a result, we measure an average ^{214}BiPo activity concentration of (9.2 ± 0.1) µBq/kg and (0.14 ± 0.01) µBq/kg in case of the ^{212}BiPo events inside the full TPC volume. This result will be discussed at the end of this section.

S1-S2 Analysis

The selection of BiPo events inside the DM FV necessitates a correct S1-S2 pairing. Therefore, an algorithm is developed similar to the one in [100]. It essentially matches those S1-S2 pairs that occur at the same S1-S2 drift time, which is a measure for the interaction depth. As we will see later, this algorithm is only relevant for ^{214}BiPo events on which we will concentrate in the following.

^{214}BiPo selection: as a first step in this analysis, the *S1 Area Cut* and the *S1 Time-Ordering Cut* are applied as described for the *S1-Only Analysis*. Subsequently, the time differences of both, the $S1_\beta$ and $S1_\alpha$ to all subsequent S2s in the same waveform are determined. They are denoted as $\Delta(S1_\beta S2_i)$ and $\Delta(S1_\alpha S2_j)$. In order to fulfill the condition that the underlying ^{214}Bi and ^{214}Po events occurred at the same depth, the time differences $\Delta(S1_\beta S2_i)$ and $\Delta(S1_\alpha S2_j)$ must be the same within a time window ΔT. We consider the time differences to match if $\Delta T_{ij} = |\Delta(S1_\beta S2_i) - \Delta(S1_\alpha S2_j)| < 10\,\mu s$, whereby $10\,\mu s$ is the order of time resolution to determine the mean S2 position.

In the described algorithm, several matching scenarios are possible as shown in Fig. 3.14. In the case (1), one match is found and the largest S2 signal is assigned to $S1_\alpha$, whereas it is the opposite for the match shown in case (2). The β-decay of ^{214}Bi can be accompanied by the emission of γ-rays at several energies. Among them, most dominant are the ones at $609\,\mathrm{keV}$ ($46\,\%$ probability), $1120\,\mathrm{keV}$ ($15\,\%$) and $1765\,\mathrm{keV}$ ($15\,\%$). These γ-rays undergo (multiple) Compton scatter with attenuation lengths of $\mathcal{O}(\,\mathrm{cm})$ in LXe (Fig. 2.2 in [101]). They can induce additional $S2_\gamma$s in the waveform as shown as case (3) in Fig. 3.14, at typical time differences at $\mathcal{O}(10\,\mu s)$ to the $S2_\beta$. The $S2_\gamma$ cannot be distinguished from the $S2_\alpha$ or $S2_\beta$ by its size, as it can as well deposit energy over a large range. Consequently, it can be misidentified, leading to more than one valid combination of S1-S2 pairs within the time window ΔT. In this case of numerous matches, no clear assignment of the correct spacial position is possible. Contrariwise, ^{214}BiPo

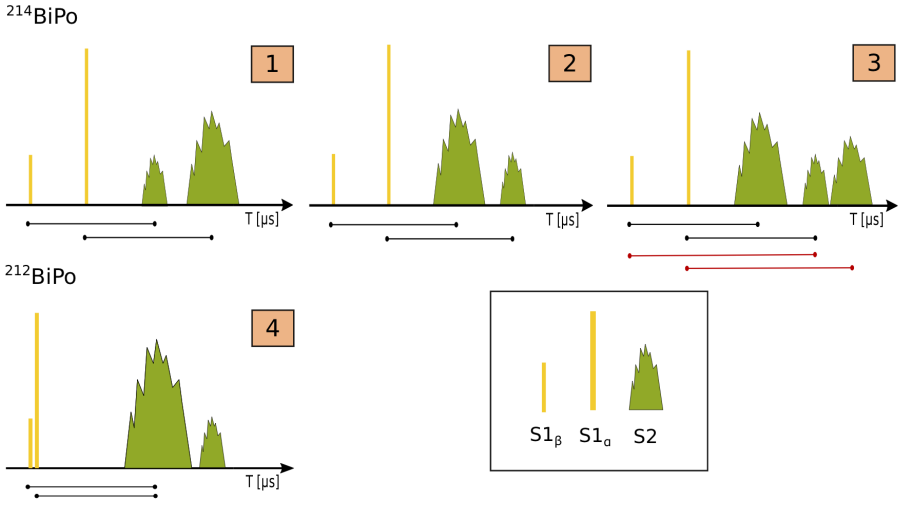

Figure 3.14: Decay scheme of BiPo events. The upper row indicates the S1-S2 matching possibilities for ^{214}BiPo events. In the case (1), one match is found for which the largest S2 signal is assigned to $S1_\beta$, whereas it is the opposite for the match shown in case (2). In case (3) multiple matches are possible due to the accompanied γ-ray emission in the bismuth decay. The lower row illustrates that in the case of ^{212}BiPo events, for which the $S2_\alpha$ and $S2_\beta$ cannot be resolved.

events with one match can be attributed to an unambiguous spacial position, since no additional $S2_\gamma$ is present. Therefore, we will only rely on these single-match events in our study and estimate the efficiency loss $\varepsilon_{\text{BiPo}}$ caused by multiple-match ^{214}BiPo events.

Efficiency $\varepsilon_{\text{BiPo}}$: to study the efficiency loss, we first select a pure, background-free ^{214}BiPo sample. For this purpose, we first apply the *S1 Area Cut*, the *S1 Time-Ordering Cut* and the Δ*S1 Cut*. Next, we select ^{214}BiPo events in a middle volume of the TPC, in which no charge nor light loss occurs. As we do not know their spacial position based on the correctly matched S1-S2 pairs, we select the events based on their S1-aft parameter. As mentioned, this parameter describes the S1 light-fraction detected in the top PMT array and it serves as measure of the interaction depth independent of the time information of the S2 signal. Since the S1-S2 matching of the the Pure α-Emitters is reliable, we use these events to infer the correlation between the S1-aft of an event and its actual reconstructed position in units of cm. We select the pure ^{214}BiPo sample in a S1-aft range that corresponds to a z-range of roughly $[-52, -20]\,\text{cm}$, based on their S1-aft parameter. The S1-aft selection range is limited by the described S1 light saturation effect that also affects the high-energetic ^{214}Po decays. We verify that we indeed only selected ^{214}BiPo events by obtaining the correct ^{214}Po half-life of the ΔS1 distribution. Thereby, the constant term is compatible with zero. Subsequently, we apply the S2-matching algorithm on this pure sample. An efficiency of $\varepsilon_{\text{BiPo}} = (61 \pm 3)\,\%$ is obtained of selecting single-match ^{214}BiPo events. This efficiency can be used to correct the amount of identified ^{214}BiPo events in TPC regions without signal loss. In the calculation of the uncertainty of the activity concentration, we quadratically add the uncertainty arising from $\varepsilon_{\text{BiPo}}$, the statistical uncertainty and the uncertainty of the liquid xenon mass inside the selected volume.

For the selection of the ^{214}BiPo in the full DM FV, we apply the *S1 Area Cut*, the *S1 Time-Ordering Cut* and the S2 matching algorithm. In Fig. 3.15 the ΔS1 distribution of the identified ^{214}BiPo events is shown (not yet $\varepsilon_{\text{BiPo}}$ corrected). The ^{214}Po half-life suits the expected one in the fit range of $[10, 2000]\,\mu\text{s}$ and no offset is present anymore, as it was the case of the *S1-Only Analysis*. At ΔS1 values below $10\,\mu\text{s}$ the distribution starts to drop due to the limited S2 resolution. In the calculation of the activity concentration, we also apply the Δ*S1 Cut*. The number of selected ^{214}BiPo events is corrected for efficiency losses due to the selected ΔS1 and $\varepsilon_{\text{BiPo}}$. We obtain a ^{214}BiPo activity concentration of $(5.1 \pm 0.2)\,\mu\text{Bq/kg}$ in the DM FV. This result will be discussed at the end of this section.

^{212}BiPo selection: in Fig. 3.14, we illustrate the decay scheme of a ^{212}BiPo event as case (4). Due to the short half-life of ^{212}Po with $T_{1/2} = 300\,\text{ns}$ and the compara-

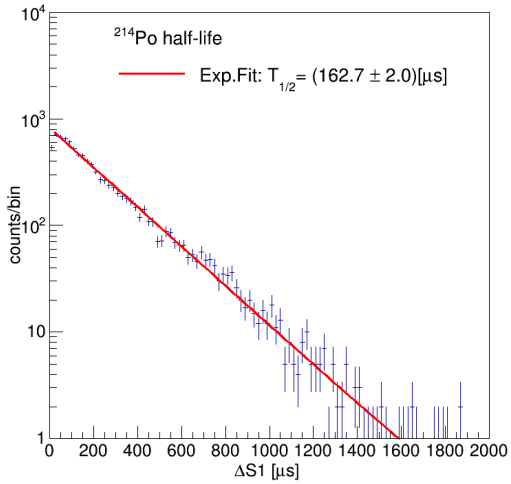

Figure 3.15: Time-difference ΔS1 between the bismuth and polonium decay of the ^{214}BiPo events, based on the *S1-S2 Analysis*. The red line indicates the fit of an exponential plus constant term, whereby the latter is compatible with zero. The determined half-life of ^{214}Po agrees with the literature value.

tively large S2 resolution, the involved S2$_\beta$ and S2$_\alpha$ cannot be distinguished and will be merged to the combined largest S2 in the waveform. As mentioned, the standard data processor identifies the main interaction within a waveform as the match of largest S1 and largest S2 signal. Therefore, we can make use of it for the ^{212}Po selection, which always induces the largest S1. As the reconstructed position and the rate of the ^{212}Po events is supposedly the same as for the ^{212}BiPo events, we can identify the latter simultaneously. Based on these reconstructed positions, events within the DM FV are selected, after applying the *S1 Area Cut* and *S1 Time-Ordering Cut*.

In Fig.3.16a the S1 signal vs. the z-coordinate is shown for events with an $0.22\,\mu\text{s} <$ ΔS1$< 2\,\mu$s. The isotope line at smaller cS1 sizes is generated by ^{214}Po decays, that are also present in the chosen ΔS1 range of the ^{212}BiPo events. The line at higher energies is from ^{212}Po events. We assign events with an cS1 value larger than $76\,000\,\text{PE}$ to the ^{212}Po population. For z-values $< -60\,\text{cm}$ the ^{212}Po and ^{214}Po start to overlap. The leakage of ^{214}Po events is considered in the systematic uncertainty, that we determine by varying the cS1 cut threshold. Thus, we obtain a ^{212}Po rate of $(0.05 \pm 0.01)\,\mu\text{Bq/kg}$ inside the DM FV, after correction for the efficiency loss due to the chosen ΔS1 range. As mentioned, we consider the ^{212}BiPo activity concentration to be identical. In Fig. 3.16b the ΔS1 distribution of the identified ^{212}BiPo events is shown. It is fitted with an exponential function plus constant term, whereby the latter is compatible with zero. The extracted ^{212}Po half-life agrees within the 2-σ range with the literature value.

Similar as for ^{214}Bi decays, additional γ-rays can be emitted in the β-decay of ^{212}Bi. In the latter, the probability is smaller with $\sim 13\,\%$, whereby the γ-ray of $609\,\text{keV}$ is most likely ($\sim 7\,\%$). As its generated S2 signal can be larger than the merged one of the S2$_\beta$ and S2$_\alpha$, the position of the ^{212}Po can get unavoidably misreconstructed. This can

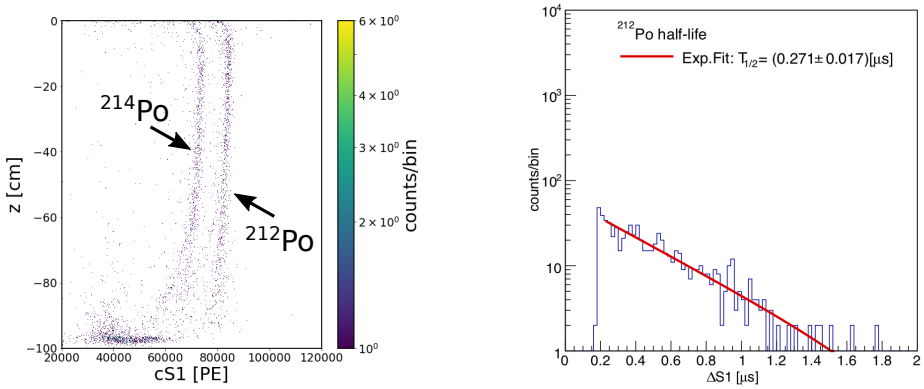

(a) *(b)*

Figure 3.16: In (a) the $S1_\alpha$ size of selected ^{212}Po events is shown along the z-axis of the TPC at around 80 000 PE. The distribution at around 70 000 PE is generated by ^{214}Po events. (b) Time-difference ΔS1 between the bismuth and polonium decay of the ^{212}BiPo events, based on the *S1-S2 Analysis*. The red line indicates the fit of an exponential plus constant term, whereby the latter is compatible with zero. The determined half-life of ^{212}Po agrees within the 2-σ range with the literature value.

cause an incorrect calculation of the ^{212}Po (and hence ^{212}BiPo) activity concentration inside the DM FV, if the events are not homogeneously distributed within the TPC and γ-rays from other BiPo events are leaking inside the DM FV. Fig.3.16a shows the ^{212}Po distribution as function of the TPC depth. We observe an event accumulation at the cathode region of the TPC. From this region γ-rays could leak in the DM FV with attenuation lengths at $\mathcal{O}(\,\mathrm{cm})$ and alter the ^{212}Po activity concentration. To estimate their influence, we determine the ^{212}Po activity concentration in an upper TPC part, several attenuation lengths of the γ-rays away from the cathode. We compare it with the ^{212}Po activity concentration close to the cathode and find agreeing values. Therefore, we neglect the potential change of selected ^{212}Po events due to γ-ray emission.

BiPo activity concentrations: in Table 3.2 the results of the BiPo selection are summarized. We either select the events in the full TPC based on the *S1-Only Analysis* or in the DM FV with the *S1-S2 Analysis*. Since only $\sim 2/3$ of the ^{212}Bi atoms decay via the ^{212}BiPo channel, the identified activity concentration of the latter is scaled up accordingly. From the results in Table 3.2, we make several observations.

- the amount of the respective BiPo events is smaller inside the DM FV in comparison to the full TPC volume. This points towards an inhomogeneous BiPo activity concentration inside the full TPC volume and some signal loss, as discussed in section 3.4.
- since the ^{222}Rn (^{220}Rn) series is in equilibrium, we expect the same amount of ^{214}BiPo (^{212}Bi) events inside the DM FV than the one of either ^{218}Po (^{216}Po).

isotope	concentration [µBq/kg]	volume	method
^{214}BiPo	9.2±0.1	full TPC	S1-only
^{214}BiPo	5.1±0.2	DM FV	S1-S2 based
^{212}BiPo	0.14 ± 0.01	full TPC	S1-only
^{212}BiPo	0.05 ± 0.01	DM FV	S1-S2 based
^{212}Bi	0.08 ± 0.02	DM FV	S1-S2 based

Table 3.2: BiPo activity concentrations for the two decay chains of radon. The activity concentrations are calculated either by the *S1-Only Analysis*, for the full FV, or by the *S1-S2 Analysis* in the DM FV. From the ^{212}BiPo activity concentration the actual ^{212}Bi activity concentration is calculated. The latter is higher, as the ^{212}BiPo selection is not sensitive to the additional α-decay branch of ^{212}Bi.

The ^{218}Po and ^{216}Po activity concentrations are $(12.7 \pm 0.4)\,\mu\mathrm{Bq/kg}$ and $(0.09 \pm 0.01)\,\mu\mathrm{Bq/kg}$, respectively (see Table 3.1). In the case of ^{212}Bi this expectation holds, whereas in case of the ^{214}BiPo events we obtain a reduced activity concentration with respect to the one of ^{218}Po. This phenomenon will be explained as well in section 3.4.

- in the discussion of the Pure α-Emitters, we compared the polonium activity concentration in the ^{222}Rn and ^{220}Rn series and observed a large difference. A similar difference is observed in the activity concentration of ^{214}BiPo and ^{212}BiPo events. The ^{212}BiPo activity concentration is $\lesssim 1\,\%$ of the ^{214}BiPo activity concentration for both analysis methods (*S1-Only Analysis* and *S1-S2 Analysis*).

- the ^{214}BiPo and ^{212}Bi activity concentrations inside the DM FV present the lower limit on the background from ^{214}Pb and ^{212}Pb decays as detailed in section 3.8.

S1 spectra

Bismuth spectra: a comparison of the bismuth S1 spectra is shown in Fig. 3.17. The bismuth spectra are based on the second largest S1 in the waveform of the selected events. The ^{212}Bi spectra uses the cS1 signal size and the ^{214}Bi is based on the uncorrected S1 signal size, due to the different selection methods. Both spectra feature a typical shape of a β-decay spectrum and are alike to the simulated ones in Fig. 3.2. The increase of events in the ^{214}Bi spectrum at high energies is caused by γ-rays released in the β-decays, that are not resolvable. We can compare the ratio of the endpoints of the two measured bismuth decays spectra with the theoretical ratio. For the ^{212}Bi-decay this endpoint is at $2.2\,\mathrm{MeV}$ and $3.3\,\mathrm{MeV}$ in case of the ^{214}Bi-decay, resulting in a theoretical ratio of $2.2\,\mathrm{MeV}/3.3\,\mathrm{MeV} = 0.67$. The measured ratio is $\sim 16000\,\mathrm{PE}/21600\,\mathrm{PE} = 0.74$, which is comparable with the theoretical ration and thus an additional proof of a correct BiPo selection.

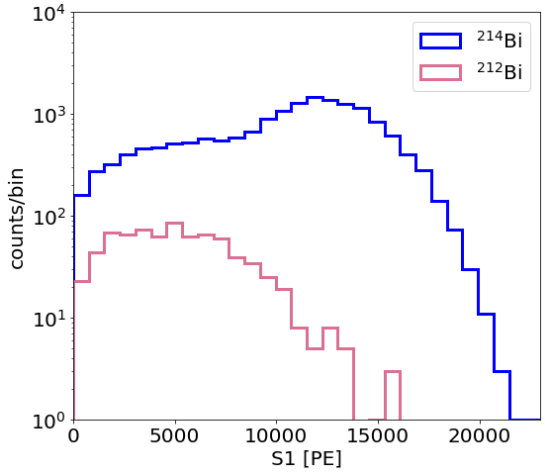

Figure 3.17: β-decay spectrum of ^{212}Bi (rose) and ^{214}Bi (blue). The increase of events towards higher energies in the ^{214}Bi spectrum is caused by γ-ray emission in the β-decays.

^{214}Po: we close this section by showing the $S1_\alpha$ of the identified ^{214}Po events as function of z in Fig.3.18a. In comparison to the ^{214}Po events in Fig. 3.4, without a proper S1-S2 matching, the ^{214}Po distribution in Fig.3.18a is more defined. Due to the missing 3D S1 signal corrections, the ^{214}Po line in Fig.3.18a is more inclined as the distribution from the Pure α-Emitters in Fig. 3.4. The broadening of the ^{214}Po distribution close to the bottom PMT array arises from the described S1 saturation effect.

At the cathode location, we observe an accumulation of ^{214}BiPo events. Their S1 size is further reduced due to its absorption by the mesh wires. Close to this accumulation, events are leaking into the LXe volume, shown by the red box. In Fig. 3.18b we compare the $S1_\beta$-spectra of these events and events in the middle of the TPC, indicated by the blue box. The events inside the red box feature an $S1_\beta$ mainly at rather high energies, revealing that the leakage events originate from γ-rays. For ^{214}BiPo events close to the cathode, the S2 signal from the β-particle can be absorbed by the cathode mesh. In this case, the requirement of a single-match can still be fulfilled by the presence of a γ-ray that induces an S2 signal. As the γ-ray can penetrate into the LXe volume, the position of the ^{214}BiPo events is misreconstructed inside the volume. In the calculation of the activity concentration, we removed these leakage events by cut on the S1 size.

3.4 Spacial distribution

In the last sections, we learned how the Pure α-Emitters and BiPo events can be identified and we determined their respective activity concentrations. The spacial distribution of the individual isotopes gives insight on the discrepancy we observed between the different components of the ^{222}Rn and ^{220}Rn series, respectively. Understanding the dynamics of radon and its decay daughters in the liquid xenon volume of the TPC is also important for the interpretation of the radon induced background in XENON1T.

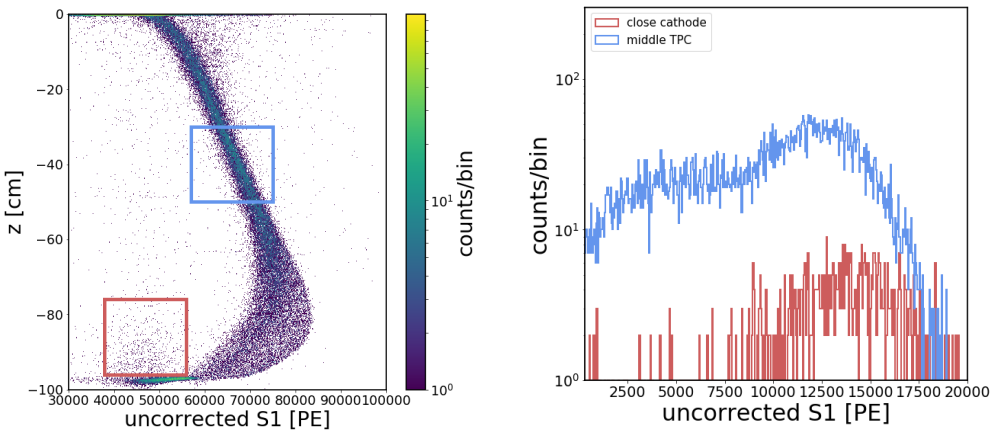

(a) *(b)*

Figure 3.18: In (a) the $S1_\alpha$ size of selected ^{214}Po events is shown along the z-axis of the TPC. The $S1_\beta$ spectra for events in the red or blue box are shown in (b). The events close to the cathode (red box) feature more likely high $S1_\beta$ values, indicating that they are generated by γ-rays that penetrate into the LXe volume.

We display the spacial position of the Pure α-Emitters and BiPo events in the entire volume of the XENON1T TPC. In case of the Pure α-Emitters, we introduced so far how the events can be selected for $z < -8\,\mathrm{cm}$. To extend the Pure α-Emitters selection towards larger z-values at the top of the TPC, we apply a rough cS1 cut on the well distinguishable isotope lines in Fig. 3.10. In case of the ^{214}BiPo we apply the S2-matching algorithm to determine the spacial coordinates. As described, this algorithm is only valid to determine the exact position inside the TPC regions without signal loss, as the DM FV. However, as we do aim for calculating the exact ^{214}BiPo activity concentration outside the DM FV, we can still apply the algorithm to locate those ^{214}BiPo events that do not suffer from signal loss.

The selected events of each isotope are shown in the (x, y) - and (z, r^2) parameter space in Fig. 3.19. Therein, the red lines indicates the boundaries of the DM FV. The z - distributions of the isotopes are depicted in Fig. 3.20, whereby the DM FV radial cut is applied to remove the ^{210}Po contamination at the TPC wall. The gray shaded region indicates the DM FV cut on z. In Fig. 3.21 the r^2 - distribution is shown for the events, after applying the DM FV z-cuts. The DM FV radial cut is shown in gray. In the following the spacial distribution of each isotope is explained in more detail:

^{222}Rn and ^{218}Po: the z -and r^2 - distributions in Fig. 3.20 and Fig. 3.21 indicate a homogeneous distribution of the ^{222}Rn and ^{218}Po events inside the DM FV. This is compatible with the agreeing measurements of the ^{222}Rn (^{218}Po) activity concentrations in the top and bottom TPC part, obtained in section 3.3.2 (Table 3.1).

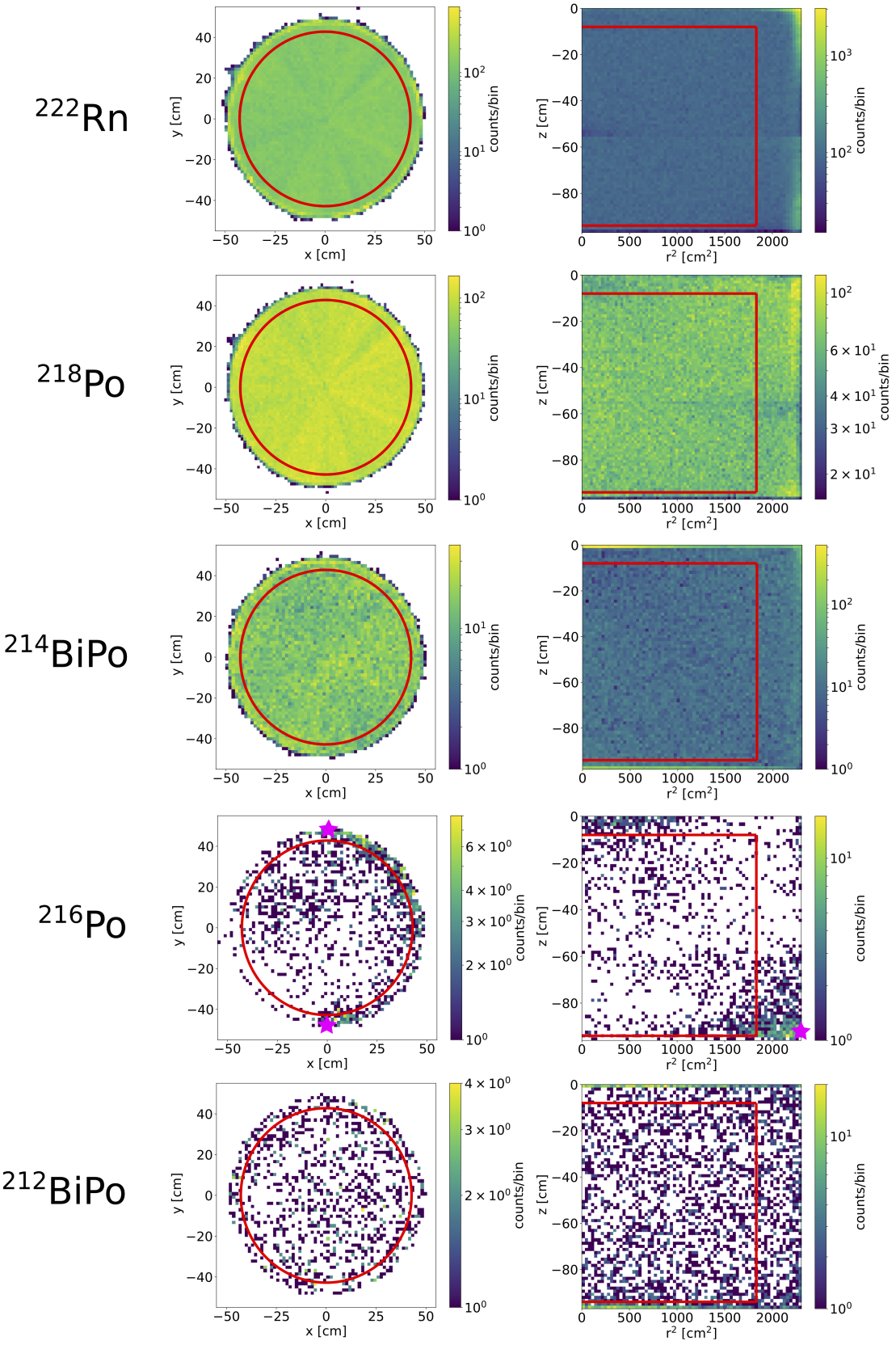

Figure 3.19: (x, y) - and (z, r^2) parameter spaces of the Pure α-Emitters and BiPo events. The red contours depict the boundaries of the DM FV. The pink stars in the ^{216}Po distributions illustrate the LXe tube inlets from the recirculation system, that contains the ^{220}Rn calibration source box.

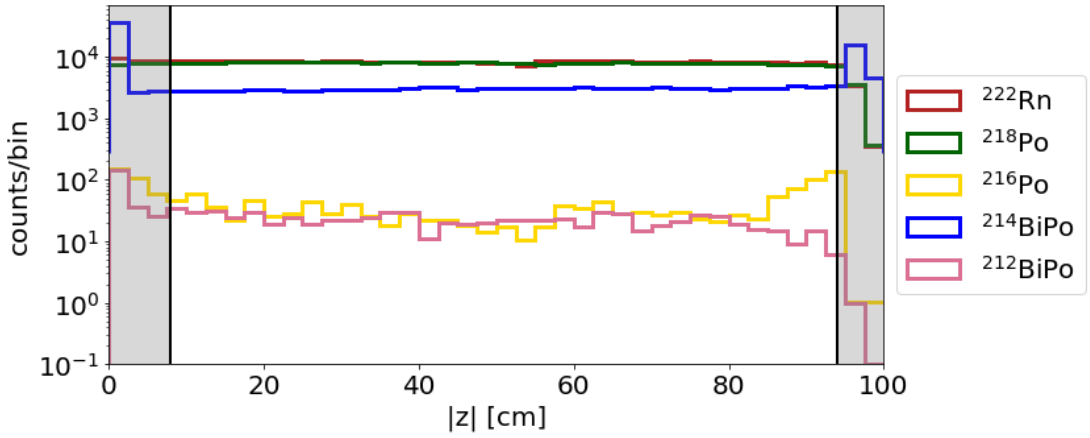

Figure 3.20: z - distribution of Pure α-Emitters and BiPo events for $r < 42.8\,\mathrm{cm}$. The gray shaded region indicates the events removed by the z cut of $-8\,\mathrm{cm} > z > -94\,\mathrm{cm}$.

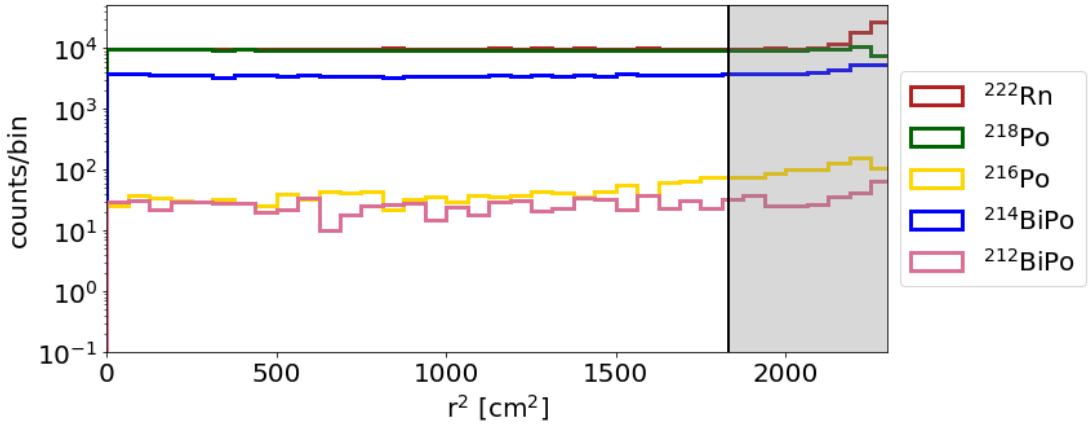

Figure 3.21: r^2 - distribution of Pure α-Emitters and BiPo events for $-8\,\mathrm{cm} > z > -94\,\mathrm{cm}$. The gray shaded region indicates the events removed by the radial cut of $r < 42.8\,\mathrm{cm}$.

This result is not affected by the slight underfluctation of events at $z = -55\,\mathrm{cm}$ in the (z, r^2) parameter space in Fig. 3.19. At this position the the events of the upper and lower TPC part are merged, after the z-correction of the S1 signal in the lower detector part. This z-correction is insufficient in low z-regions $z < -94\,\mathrm{cm}$, which explains the decrease of ^{222}Rn and ^{218}Po events in this region. In the (x,y) parameter space, we observe a structure which is compatible with the ring-like pattern of the PMTs in the top array. This structure arises from deficiencies of the standard S2 spacial correction algorithm in XENON1T. Apart from this artificial feature, the spacial density appears homogeneous. At the TPC walls, outside the DM FV, the ^{222}Rn and ^{218}Po distribution increases because of the limited S1 resolution, that does not allow for a clear separation from the ^{210}Po events, which are located at the wall.

The stated ^{218}Po activity concentration in Table 3.1 is compatible with the one of ^{222}Rn within the uncertainties, but its average value is slightly smaller. As the decays within the ^{222}Rn chain are in secular equilibrium, up to the decay of ^{210}Po, one would expect the same amount of ^{218}Po (and ^{214}BiPo) events. The phenomenon of reduced activity concentrations, relative to the one of ^{222}Rn, was already observed in LXe detectors, such as in [102–105], and can be described by the ion-drift model discussed in [106]. Therein, the authors explain that ^{222}Rn decays in LXe produce a large fraction of ^{218}Po^{+}-ions, since shell electrons of the recoiling nucleus can be stripped off. These ions are drifted towards the cathode on which they can plate-out. Thus, they are not observable anymore in the DM FV, leading to a reduced ^{218}Po activity concentration therein. This phenomenon is also called "self-cleaning" effect.

^{214}BiPo: the "self-cleaning" effect induced by ion-drift is even enhanced for ^{214}BiPo events, that are clearly accumulated at the TPC's cathode, as shown in Fig. 3.20 and Fig. 3.19. In comparison to the ^{222}Rn decay, the decay of ^{214}Pb creates an even larger fraction of positively charged ions [106]. In addition, these ^{214}Bi^{+} ions have more time to plate-out, due to their longer half-life with respect to the ^{218}Po^{+}-ions. This is the reason why a ^{214}BiPo activity concentration of only $\sim 40\,\%$ with respect to the ^{222}Rn activity concentration is measured inside the DM FV.

The ^{214}BiPo decays on the surface of the cathode suffer from light and charge loss. The light signal loss is evident from the result of the *S1-Only Analysis*, in which only two third of the initial ^{214}BiPo activity concentration is measured with respect to the ^{222}Rn activity concentration in the full FV. The absorption of the scintillation light on the metallic structure of the cathode is most likely the reason for the light loss. Besides this, also the S2 signal can be lost in charge insensitive regions as below the cathode. The S1 aft value of the ^{214}BiPo that seemingly accumulate at the top of the TPC reveals that that they are actually originating from the cathode region. These ^{214}BiPo events lose their proper S2 and another one is wrongly matched, leading to their misreconstruction at small z-values (similarly as for ^{210}Po events, detailed in section 3.3.2). In the r^2 - distribution, an increase of the ^{214}BiPo event is present at the wall of the TPC. These vast majority of these events feature the same S1/S2 ratio as ^{214}BiPo events inside the DM FV. Hence, we conclude that they do not suffer from charge loss as the events of ^{210}Po.

^{216}Po: the spacial distribution of ^{216}Po is rather inhomogeneous in both z -and r^2-direction. Fig. 3.19 shows that most of the events are present in the top-middle part and on the bottom at large radii of the TPC. The figure also depicts the approximate positions of the LXe inlet tubes from the calibration system (pink

stars). In XENON1T ^{220}Rn is used to calibrate ER interactions in the LXe. The inhomogeneous distribution of its daughter isotope ^{216}Po, located mainly close to the inlet tubes, points towards a contamination of ^{220}Rn from the calibration process. In section 3.6, we show that indeed the ^{212}BiPo event rate slightly increases after each ^{220}Rn calibration. The part of the contamination can be removed, by excluding a larger data period after each calibration run, such that constant ^{212}BiPo activity concentration is achieved through the entire science run data taking periods. However, even after the data removal the spacial distribution is unaffected. This could be explained by a constant leak from the ^{220}Rn calibration source. Such a leak was observed in the case of the ^{83m}Kr calibration source in XENON1T, presumably caused by a malfunction of the source valve, which lead to a constant trace amount of ^{83m}Kr in the data used for dark matter search [68]. Another cause could be, potentially in addition, a comparably high ^{220}Rn emanation rate from detector materials close to the observed ^{216}Po accumulation. This could also describe the enhanced event concentration at the top TPC part, opposite the calibration inlet tubes. A similar observation was made in the LUX detector, which is explained by a ^{220}Rn source in the xenon recirculation system [103].

^{212}BiPo: since the ^{212}BiPo events have more time to distribute within the xenon volume, their spacial distribution is more homogeneous than the one of ^{216}Po, which coincides with the observation made in [103]. For the selection of the ^{212}BiPo events, we applied a cut to remove ^{214}Po at lower cS1 values. As below $z = -60\,\mathrm{cm}$ the two distributions start to overlap (see Fig. 3.16a), the ^{212}BiPo z-distribution is less reliable in this region. The increase of ^{212}BiPo events at the TPC top part has the same reason as in the ^{214}BiPo case (charge loss). The increase of ^{212}BiPo events close to the TPC wall could correlate with the higher ^{216}Po activity concentration at the same location.

3.5 Light and charge yield

In this section, we discuss the light and charge yields (LY and CY) from ^{222}Rn α-decays. These signal yields are in general defined as number of photo-electrons per S1 or S2 signal, detected at a reference energy and the operational drift field. As explained in Chapter 2, the signal yields from various ER calibration sources are used to reconstruct the combined ER energy scale in XENON1T. In case of ^{222}Rn α-decays, they allow us to get insight into their energy deposition in liquid xenon. Furthermore, the signal yields can be used to control the performance of the signal corrections in XENON1T over time.

In the following study, we select ^{222}Rn events according to section 3.3.2. Since we

want to determine the LY and CY based on the corrected signal sizes (cS1 and cS2) in XENON1T, we select the events in a TPC volume without S1 saturation defined in a z-range of $-20\,\mathrm{cm} > z > -55\,\mathrm{cm}$ and a radius of $r < 42.8\,\mathrm{cm}$. As in the XENON1T analyses usually the S2 signal size is evaluated with the bottom PMT array only, we infer the CY based on $\mathrm{cS2_b}$. The average LY and CY is determined by fitting a Gaussian function to the cS1 and $\mathrm{cS2_b}$ distribution, respectively, and extracting their mean values in units of PE, that are subsequently divided by the decay energy of ^{222}Rn. The average values of both LY and CY during SR1 and SR0, are given in Table 3.3.

In general, the absolute value of the signal yields depends on various aspects: the particle type and the energy it deposits, the ionization density along its track and the applied electric field. In the following, we will use the obtained average CY and calculate the ionization yield of for ^{222}Rn α-particles to understand the underlying mechanism of their energy deposition in liquid xenon. Afterwards, we will elaborate more on the results in Table 3.3.

Ionization yield: the ionization yield is defined as fraction of measured ionization electrons per unit recoil energy ($\mathrm{e^-/keV}$) in comparison to the total amount of created electrons in the particle interaction. In the following, we want to calculate this quantity for ^{222}Rn α-particles. Therefore, we first determine the number of measured electron $\mathrm{Q(E_d)}$ from the interaction of the α-particle with the liquid xenon at the drift field $\mathrm{E_d}$ as

$$\mathrm{Q(E_d)} = \frac{\mathrm{CY}}{\mathrm{g_b}} \tag{3.5.1}$$

where $\mathrm{g_{2b}} = (11.5 \pm 0.8)\,\mathrm{PE/e^-}$ is the charge amplification factor. It is a field-independent and detector specific parameter that translate the number of created ionization electrons into the amount of photo-electrons measured in the PMTs. It is determined using mono-energetic calibration sources, as described in Chapter 2. Hence, from the mean CY values stated in Table 3.3, we obtain $\mathrm{Q(E_d = 120)} \sim 0.62\ \mathrm{e^-/keV}$ and $\mathrm{Q(E_d = 81)} \sim 0.52\ \mathrm{e^-/keV}$.

To obtain the ionization yield, $\mathrm{Q(E_d)}$ is compared to the theoretical amount of observed electrons at an infinite field, denoted as $\mathrm{Q_0}$. In the latter case, all electrons escape recombination and the number of measured electrons is the same as the number of initial electron-ion pairs created by the ionizing particle. The amount of energy to create one electron-ion is denoted as W-value and it was measured to be $\mathrm{W} = (15.6 \pm 0.3)\,\mathrm{eV}$ for ionizing particles in LXe [107]. This means that $1/\mathrm{W}$ expresses the number of electron-ion pairs created per deposited energy. At an infinite drift field the number of created electron-ion is identical to the observed number of electrons and we obtain $\mathrm{Q_0} = (64.1 \pm 1.2)\ \mathrm{e^-/keV}$. The ionization yield is defined as the ratio of $\mathrm{Q(E_d)/Q_0}$.

science run	LY [PE/keV]	CY [PE/keV]	drift field [V/cm]
SR0	9.06±0.04	7.25±0.09	120±8
SR1	9.10±0.01	6.07±0.07	81±6

Table 3.3: Light and charge yield (LY and CY) of ^{222}Rn α-decays in SR0 and SR1. The CY is based on the number of PE observed with the bottom PMT array. The drift field values are taken from [68].

It implies that at drift fields of $(120 \pm 8)\,\mathrm{V/cm}$ and $(81 \pm 6)\,\mathrm{V/cm}$ only a fraction of $\sim 0.96\,\%$ and $\sim 0.81\,\%$ of the created electrons can be actually measured from a ^{222}Rn α-particle.

The low ionization yield can be explained by the dense ionization track of α-particles. Recombination in these high charge density regions is a much faster process than the separation of electron-ion pairs caused by the external electric field. Therefore, the ionization yield has only a weak drift field dependency. The results are in good agreement with other dedicated charge yield measurements of α-particles in xenon [108]. The dedicated measurements also demonstrate that even at high drift fields of $20\,\mathrm{kV/cm}$, two orders of magnitude larger than the drift fields in XENON1T, only around $10\,\%$ of the total charge is collected.

Comparison of LY and CY: since the dense ionization track implies a high recombination probability for ionization electron, the scintillation light emission is strongly enhanced for α-particles. Similar as in the case of ionization electrons, we calculate the number of emitted scintillation photons based on the measured LY and the photon detection efficiency $g_1 = (0.144 \pm 0.007)\,\mathrm{PE}/\gamma$. We find that the number of created scintillation photons exceeds the number of ionization electrons by a factor of ~ 100 for α-particles. The similar size of LY and CY in Table 3.3 can be understood by comparing the g_1 and g_2 factor, that show that much more photo-electrons per quanta are generated in case of the amplified ionization electrons than for scintillation photons. The comparably large number of measured scintillation photons is compensated by the comparably small value of g_1, such that similar signal yields are obtained.

As already indicated, the applied electric drift field also influences the LY and CY. This can be seen from the anti-correlated change in the signal yields in Table 3.3 due to the different drift fields between SR0 and SR1. A decrease of the field strength causes a lower probability for the ionization electrons to be removed from the interaction point, leading to a decrease of the S2 signal size and hence a CY reduction. Simultaneously, the LY is enhanced.

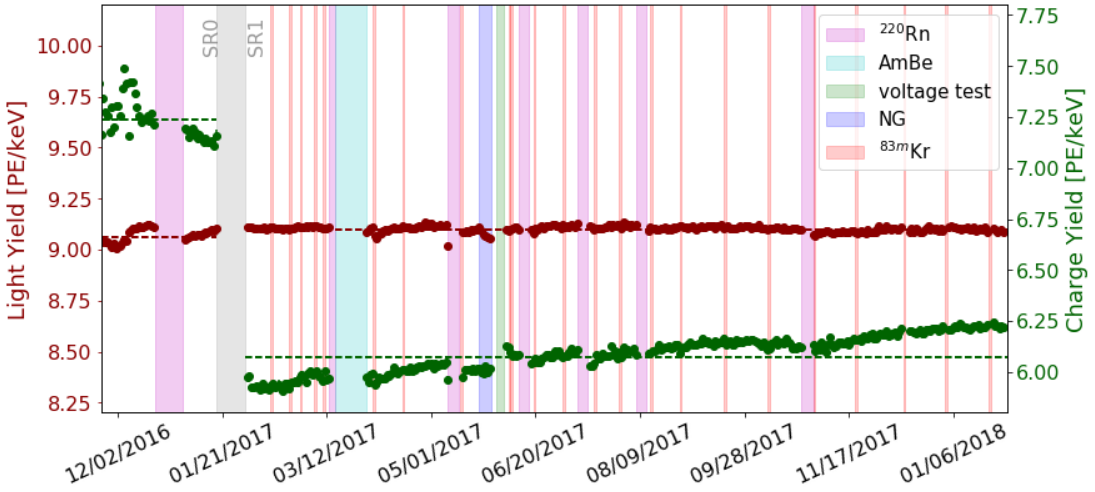

Figure 3.22: ^{222}Rn LY and CY time evolutions during SR0 and SR1. In each of them, the maximal deviation from the LY and CY mean was smaller than $1\,\%$ and $3\,\%$, respectively. The change of the LY and CY, due to the different drift fields in the science runs, is explained in the text. The shaded regions indicate calibration periods with different sources.

Furthermore, it is striking that the different drift fields between SR0 and SR1 cause the LY to change by less than $1\,\%$, whereas the CY varies by almost $20\,\%$. This difference can be understood by the large difference in created scintillation photons and ionization electrons, whereby the total amount of produced quanta is conserved at different fields. A field modification causes an anti-correlated change of the the emitted photon and electron number, by the same absolute amount. Since the number of photons exceeds the number of electrons, the relative LY change is much smaller than the relative change of the CY.

Time evolution : the time evolution of LY and CY is used to monitor the detector stability and the robustness of the signal size corrections. The CY is for example influenced by the liquid-level height in the TPC which affects the track length of the extracted ionization electrons in the gas phase. The longer this track length, the more S2 scintillation photons and consequently photo-electrons in the PMTs are generated per deposited energy and the larger is the CY. By measuring the CY, the liquid-level stability over time can be tested. Both, the LY and CY are affected by field changes as we saw in the previous section. By monitoring the signal yields, potential variations in the average drift field can be detected.

The LY and CY measurements at different energies are usually performed in dedicated calibration campaigns at time intervals of $\mathcal{O}(\text{weeks})$. However, for calibration purposes, we can benefit from the constantly present α-decays of the ^{222}Rn background that offer, due to the rather high amount of decays per day, the possibility of a *contin-*

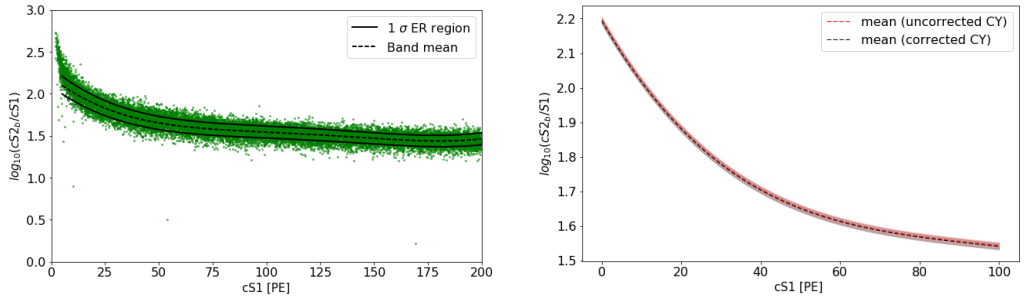

(a) *(b)*

Figure 3.23: (a) ER band from ^{220}Rn calibration data after applying the analysis selection cuts detailed in [68]. The black solid and dashed lines indicate the mean and the $\pm 1\sigma$-regions. (b) Mean of ER band with and without an additional CY correction due to its observed increase during SR1. Since the bands agree within their uncertainties no further correction was applied in the dark matter analysis.

uous LY and CY monitoring. The time evolutions of both LY and CY during SR0 and SR1 is depicted in Fig. 3.22. As explained, the change of drift field between the SR0 and SR1 results in a larger relative CY than LY change. In each science run, the LY and CY are stable with a maximum deviation from the mean of $1\,\%$ and $3\,\%$, respectively. Similar deviations from the mean value as well as the same relative CY increase during SR1 were observed with other ER calibration sources at lower energies [68]. Despite thoroughly investigation from the XENON collaboration, its cause could not be identified. Therefore, its potential impact on the dark matter analysis was determined, as explained in the following.

Impact of CY increase on analysis: in Fig. 3.23a we show the so-called discrimination space (introduced in Chapter 2). It is defined as $\log(\mathrm{cS2_b}/\mathrm{cS1})$ as function of cS1 and used to discriminate signal-like NRs from background-like ERs. For the XENON1T analyses, the ER background is calibrated in the discrimination space by means of ER data from a ^{220}Rn calibration source. In Fig. 3.23a the resulting distribution, termed ER band, is shown, whereby the selection cuts used in the dark matter analysis are applied [68]. To determine the influence of the increasing CY (which is based on the $\mathrm{cS2_b}$ size) over time, the potential variation on the shape of the ER band is investigated in the discrimination space. To characterize its shape, the ER band is sliced into cS1-intervals and the projected $\log(\mathrm{cS2_b}/\mathrm{cS1})$ distributions are fitted with a Gaussian function, similar as in [49]. The dashed and solid black line indicate a polynomial fit through the extracted $\log(\mathrm{cS2_b}/\mathrm{cS1})$ mean values and the corresponding $\pm 1\sigma$-regions.

In a second step, a time-dependent correction function of the increasing CY change is determined, that shifts the measured CY values to the average CY value in SR1. After

this time-dependent correction of the $cS2_b$ size, the shape of the ER band is evaluated. In Fig. 3.23b we compare the mean value of the ^{220}Rn ER band before and after this correction. The ER band mean values before and after the correction as agree within the uncertainty. This means that the slight increase of the CY over time has no significant impact on the ER band position in the discrimination space and hence on the discrimination power in the experiment. Therefore, it was decided in XENON collaboration that no further correction on the S2 signal size is introduced for the dark matter analysis.

3.6 Rate evolution

By monitoring the time evolution of the isotopes within the ^{222}Rn and ^{220}Rn chains, we can constrain the crucial background from ^{214}Pb and ^{212}Pb in the course of the XENON1T dark matter search data in SR0 and SR1. Furthermore, we can supervise the effect of the radon removal campaigns by xenon distillation that took place in SR0 and SR2. Parts of the presented work are published in [I].

3.6.1 Rates in SR0 and SR1

The activity concentration of the Pure α-Emitters and BiPo events is determined as explained in section 3.3.2 and 3.3.3, respectively. For the ^{222}Rn chain evolution we chose a $2\,\mathrm{day}$ binning and for the ^{220}Rn chain a binning of $45\,\mathrm{days}$ is fixed. We constrain the data selection of the homogeneously distributed ^{222}Rn and ^{218}Po to a z-range without S1 saturation of $-8\,\mathrm{cm} > z > -55\,\mathrm{cm}$. This allows us to use the standard correction of the S1 light. All other isotopes are selected in the full DM FV.

The time evolutions of the components within the ^{222}Rn and ^{220}Rn chains are depicted in Fig. 3.24 and Fig. 3.25, respectively. We determine the isotopes' average values by fitting a constant term to the stable evolutions. In Table 3.4 we state the resulting mean activity concentrations together with the red. χ^2/ndf from the respective constant fit. In the fit range, we distinguish between periods with and without radon removal. The stated activity concentrations, without radon removal, agree within the uncertainty with the values given in section 3.3.2 and section 3.3.3, respectively.

Plate-out effect: as discussed in section 3.4, the ^{218}Po and ^{214}BiPo activity concentrations are reduced with respect to the one of ^{222}Rn due their plate-out on the cathode. In the ^{220}Rn chain, the ^{216}Po and scaled ^{212}Bi activity concentrations agree within the uncertainty. In this case, the plate-out effect is assumed to be less visible due to the inhomogeneous ^{216}Po distribution.

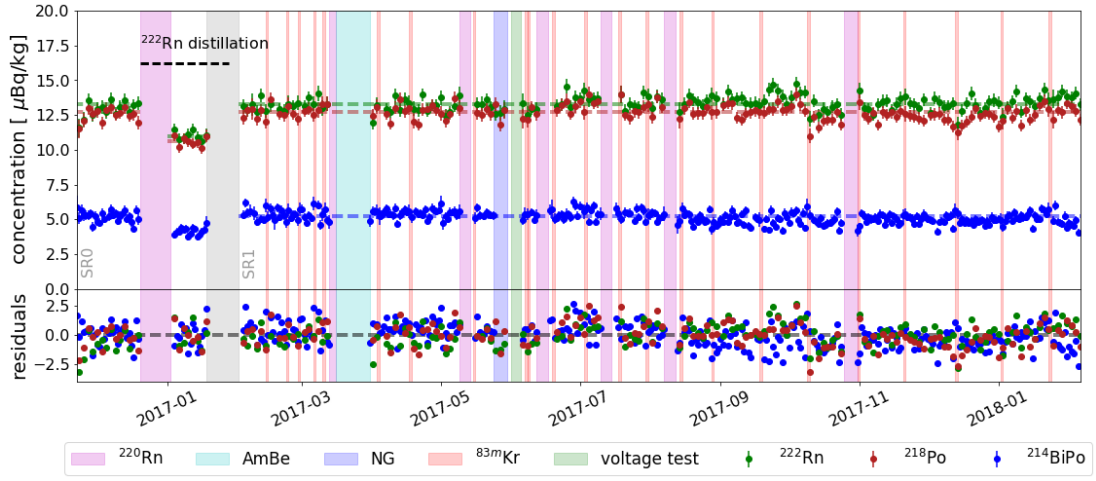

Figure 3.24: Rate evolutions of ^{222}Rn (red), ^{218}Po (green) and ^{214}BiPo (blue) during SR0 and SR1. The dashed lines indicate the average values of the individual isotopes. In SR0 the rates are reduced by $\sim 20\,\%$ due to cryogenic xenon distillation. The shaded regions indicate calibration campaigns or detector maintenance periods.

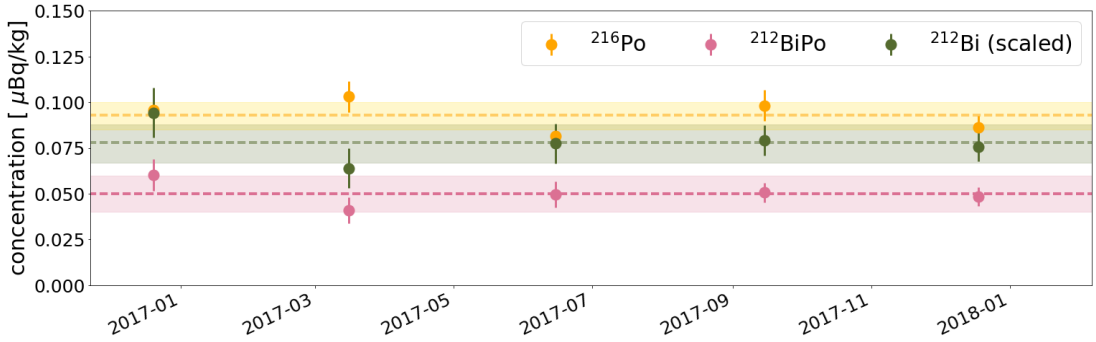

Figure 3.25: Rate evolutions of ^{216}Po (yellow), ^{212}BiPo (rose) and ^{212}Bi (green) during SR0 and SR1. The latter is calculated from the measured ^{212}BiPo activity concentration, as roughly one third of the ^{212}Bi nuclei do not decay to ^{212}Po.

isotope	nominal concentration [μBq/kg]	constant fit red. χ^2/ndf	distillation concentration [μBq/kg]	relative reduction [%]
^{222}Rn	13.3 ± 0.5	1.2	11.0 ± 0.3	17 ± 4
^{218}Po	12.7 ± 0.5	1.2	10.6 ± 0.3	17 ± 4
^{214}BiPo	5.1 ± 0.4	1.8	4.1 ± 0.3	20 ± 9
^{216}Po	0.09 ± 0.01	1.5	-	-
^{212}BiPo	0.05 ± 0.01	0.8	-	-
^{212}Bi	0.08 ± 0.01	0.8	-	-

Table 3.4: Average activity concentrations of ^{222}Rn and ^{220}Rn chain components during SR0 and SR1, in the DM FV. The second column indicates the red. χ^2/ndf of the constant fit function fitted to the evolutions. Due to xenon distillation the activity concentrations within the ^{222}Rn were reduced, as shown in the third column, by the fraction shown in the fourth column.

Radon removal: during SR0, a xenon distillation campaign was performed to remove the intrinsic radon atoms. The xenon distillation lead to an activity concentration reduction of roughly $20\,\%$ for all monitored isotopes within the ^{222}Rn chain. By lowering the ^{222}Rn activity concentration, the background arising from ^{214}Pb is reduced by the same fraction. The absolute reduction of the ^{222}Rn activity concentration is $(2.3 \pm 0.6)\,\mu\mathrm{Bq/kg}$, which will be compared to the reduction due to the radon removal in SR2 in the next section. The components of the ^{220}Rn chain should be affected in the same way as the ones of the ^{222}Rn chain, but no reduction is observed in the former case. A reason could be that the ^{220}Rn atoms first reach the liquid xenon reservoir of the TPC, before entering the xenon distillation column.

^{220}Rn contamination: in Fig. 3.26a, the number of ^{212}BiPo events is shown versus the run number. The typical run time of one data set in XENON1T is roughly $1\,\mathrm{hour}$ and the smaller time binning allows for a precise evolution monitoring. Also indicated are the ^{220}Rn calibration campaigns. It is clear that after almost each campaign, the ^{212}BiPo amount is larger than the average value. The reason is that the data after the ^{220}Rn calibration is not excluded sufficiently long from being valid for dark matter search. After this observation, the contaminated runs were excluded from analysis, leading to a data reduction of $0.5\,\%$. At the same time, the initially observed ^{212}BiPo activity concentration was reduced by $\sim 4\,\%$. All activity concentrations shown in this work are after the data removal. This result shows that even small changes of the already low ^{212}BiPo activity concentration can be identified.

Comparison to ambient radon concentration: in Fig. 3.26b the described ^{222}Rn activity concentration is shown together with the one measured in the ambient air close to gas system of XENON1T. This quantity is constantly probed with a commercial Rad7 radon monitor installed outside the detector shield. In principle, natural radon could diffuse through tiny leaks into the gas system of XENON1T and contaminate the xenon. From Fig. 3.26b we cannot identify a clear correlation among the internal ^{222}Rn evolution and the one in ambient air within the resolution of internal ^{222}Rn evolution.

In the following, we want to estimate the leak rate that can be resolved with the measurement of the internal ^{222}Rn level. For this purpose, we translate the average ^{222}Rn activity concentration of $(13.3 \pm 0.5)\,\mu\mathrm{Bq/kg}$ in SR0 and SR1, ignoring the period of radon removal, into a total number of radon decays inside the complete LXe mass of $3.2\,\mathrm{t}$ inside the detector. We obtain $\mathrm{N_{Rn}} = (13.6 \pm 0.5) \cdot 10^5$ radon decays over a period of one year. Thereby, we assumed that the radon atoms are homogeneously distributed within the entire LXe of the detector system. This assumption is reasonable, considering that the ^{222}Rn is evenly distributed within the TPC (see section 3.4) and that the circulation time of the entire amount of LXe is a few days - the same time-scale

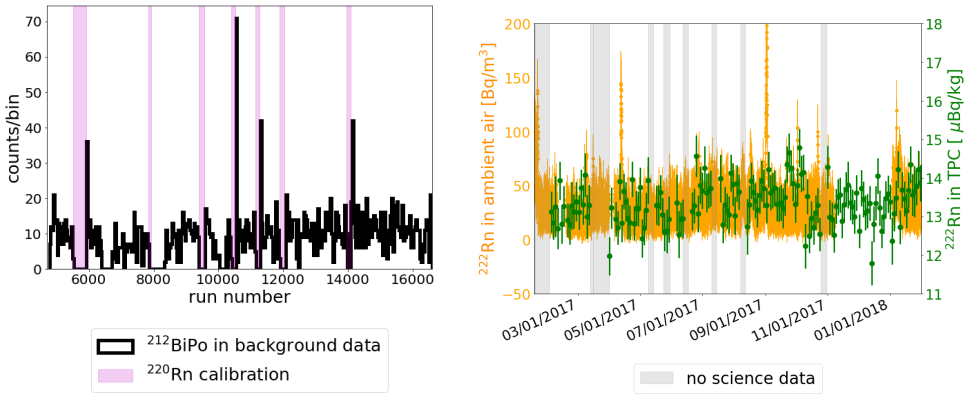

Figure 3.26: (a) ^{212}BiPo events vs. the run number, together with the ^{220}Rn calibration campaigns in SR0 and SR1. After almost each calibration a ^{212}BiPo contamination is visible in the science data. (b) Evolutions of ^{222}Rn activity concentration in the liquid xenon volume (green) and in the ambient air (orange). No correlation is observed which excludes air leaks within the resolution of the internal radon evolution.

as the ^{222}Rn half-life. The number N_{Rn} can be translated into an equivalent activity A_{Rn}, entering the system all at once

$$A_{Rn} = \frac{N_{Rn}}{\tau_{Rn}} = (2.9 \pm 0.1)\,\text{Bq} \quad . \tag{3.6.1}$$

To convert this activity into a leak volume one needs to know the radon concentration in ambient air, measured by the Rad7 monitor. For the time period of interest we estimate an average radon concentration of $C_{air} \sim 0.03\,\text{Bq/liter}$ in one liter of ambient air. This means that $R^{Rn}_{air} = (93 \pm 3)\,\text{liter/year}$ of ambient air have to enter the detector per year to explain the ^{222}Rn amount inside the detector. Leak rates smaller than the uncertainty on R^{Rn}_{air} cannot be resolved by the measurement of the internal ^{222}Rn activity concentration.

The leak rate can be also estimated based on the ^{nat}Kr concentration inside the detector which is frequently measured using rare gas mass spectroscopy (RGMS). These measurements are performed to determine the intrinsic amount of ^{85}Kr, which is another noble gas that can lead to background events inside the experiment. In contrast to background induced by ^{222}Rn, the krypton level is strongly suppressed by means of cryogenic distillation of the entire LXe. In Chapter 4, we will show the time evolution of the ^{nat}Kr concentration that indicates a slight increase during SR1. This increase could be attributed to a leak rate of $V^{Kr}_{air} < 0.9\,\text{liter/year}$ [2] [89]. This leak rate is smaller than the uncertainty on the leak rate R^{Rn}_{air}, showing that the RGMS measurements are

[2] As we will discuss in Chapter 4, the ^{nat}Kr increase could be also caused by outgassing of trapped air from the detecor materials.

much more sensitive to deduce smaller leak rates, which cannot be resolved by the measurement of the ^{222}Rn amount inside the detector.

Comparison to ^{222}Rn emanation measurements: from the emanation measurements, as introduced in section 3.2, a total ^{222}Rn activity concentration of (10.0 ± 0.7) µBq/kg is expected inside the detector [I]. In the presented data analysis, we observe a $\sim 30\,\%$ higher ^{222}Rn level of (13.3 ± 0.5) µBq/kg, in periods without radon removal. Normalized to the full liquid xenon mass of $3.2\,\mathrm{tons}$, the difference is $(10.6 \pm 2.8)\,\mathrm{mBq}$. The largest contribution to the total ^{222}Rn budget arises from the three QDrive pumps, that recirculate the xenon through the system. The emanation rate of one out of the three QDrives was not measured directly. Its value is estimated from the measured emanation rates of other QDrive pumps. The non-measured QDrive pump could emanate more than expected, causing a higher ^{222}Rn activity concentration in the experiment. Furthermore, the emanation measurements are usually performed at room temperature. In contrast, the operating QDrive pumps are at a higher thermal state, which may enhance the diffusion-driven ^{222}Rn emanation, resulting as well in a larger radon release rate. These effects could explain the discrepancy of the predicted ^{222}Rn activity concentration from the emanation measurements and the observed one in XENON1T, when the pumps are operating. In section 3.6.2, we discuss the ^{222}Rn activity concentration inside the detector after the QDrive pumps were exchanged, which offers the possibility to test these hypotheses.

3.6.2 Rates in SR2

During science run 2 (SR2), the xenon purification system was upgraded, including the subsequent removal of the three QDrive pumps and their exchange with a magnetically coupled piston pump (MagPump). The estimated radon emanation rate of the replaced QDrive pumps is in total $(11.3 \pm 0.9)\,\mathrm{mBq}$, which makes up $\sim 36\,\%$ of the entire radon budget in XENON1T during SR0 and SR1 (see Fig. 3.3). In comparison, the emanation rate of the MagPump is only $(0.29 \pm 0.09)\,\mathrm{mBq}$ [I]. Hence, we expect a ^{222}Rn reduction of after the pump exchanged of $(11.0 \pm 0.9)\,\mathrm{mBq}$, based on the results of the radon emanation measurements.
Furthermore, a second xenon distillation campaign was performed in SR2 similar to the one in SR0. The distillation and the pump exchange lead to a significant reduction of the ^{222}Rn (^{218}Po) activity concentration in the detector, as described below. Due to these upgrades, that also lead to a higher xenon recirculation speed, the detector condition are less stable in SR2. However, no correlation between the evolution of the ^{222}Rn (^{218}Po) activity concentration and the detector parameters, such as temperature or flow rate, was observed. The evolution of the ^{222}Rn activity concentration is presented in Fig. 3.27. The ^{218}Po activity concentration (not shown) is in equilibrium with the one

of its mother nuclei ^{222}Rn and hence follows the same evolution. For both isotopes, the individual activity concentration in each phase of SR2 are determined as described in the following and summarized in Table 3.5.

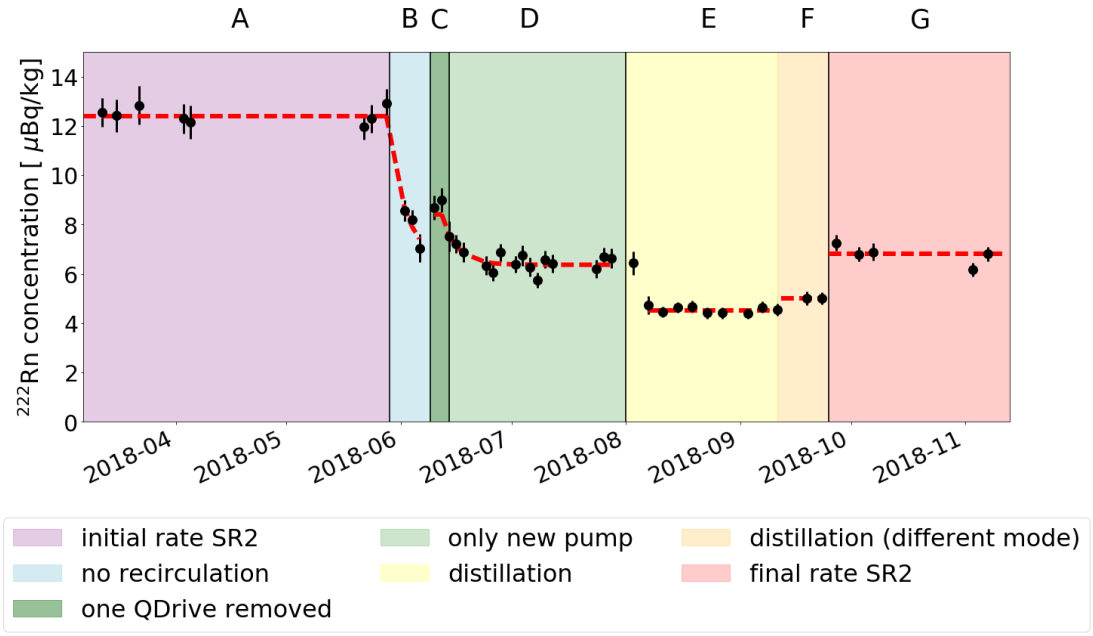

Figure 3.27: Evolution of ^{222}Rn activity concentration during science run SR2. Several operations, described in detail in the text, caused a change of the activity concentration. The letter above the figure correspond to the description of each phase in the text and the labels in Table 3.5. The red dashed lines presents the fit function to the data.

sign	description	^{222}Rn conc. [µBq/kg]	^{218}Po conc. [µBq/kg]	^{222}Rn ratio [%]	^{218}Po ratio [%]
0	rate SR0/SR1	13.3 ± 0.5	12.7 ± 0.5	107 ± 5	110 ± 6
A	initial rate SR2	12.4 ± 0.3	11.5 ± 0.4	100	100
B	no recirculation	$6.4 \pm 2.0*$	$6.1 \pm 0.7*$	52 ± 16	53 ± 6
C	one QDrive removed	8.4 ± 0.6	7.6 ± 0.6	68 ± 5	66 ± 6
D	only new pump	$6.4 \pm 0.1*$	$6.1 \pm 0.2*$	52 ± 1	53 ± 3
E	distillation	4.5 ± 0.1	4.2 ± 0.2	36 ± 1	37 ± 2
F	distillation (diff. mode)	5.0 ± 0.1	4.8 ± 0.1	40 ± 1	42 ± 2
G	final rate SR2	6.8 ± 0.3	6.7 ± 0.4	55 ± 3	58 ± 4

Table 3.5: Average ^{222}Rn and ^{218}Po activity concentrations for the different phases in science run 2 (SR2). The labels correspond to the ones used in Fig. 3.27. The values with the $*$-symbol are extracted from a fit, as explained in the text. The remaining activity concentration values are determined by averaging over the data points in the specific period. The last two columns indicate the activity concentration reduction due to the operations. Thereby, we use the activity concentrations of phase A as reference point.

A) Initial rate SR2: in this first phase of SR2, the three QDrive pumps are still operating. The average ^{222}Rn (^{218}Po) activity concentration is slightly lower than during the SR0 and SR1 period which is not fully understood. However, we are mainly interested in the relative rate reductions due to the described operations. Therefore, we will use the initial activity concentrations in this first phase of SR2 as references.

B) No recirculation: in this phase, the xenon recirculation was stopped to remove one of the three QDrive pumps from the system. Due to the recirculation stop, the radon atoms, that have emanated from the recirculation system, are not longer transported to the TPC. Consequently, their contribution to the radon level inside the TPC is decreasing as seen in Fig. 3.27. We model this decrease by the radioactive decay law and fit an exponential function plus a constant term to the ^{222}Rn and ^{218}Po evolutions. We expect for both isotopes that the decreasing rate is described by the half-life of ^{222}Rn of $T_{1/2} = 3.8\,\mathrm{days}$ (^{218}Po is in equilibrium with ^{222}Rn). The first data point in the fit is fixed to the average activity concentration value of period A. In Table 3.5 the fit result of the constant term is presented. It depends strongly on the initial parameters of the fit, due to the limited statistic, which is also reflected in the rather large uncertainty of fitted half-lives. Within their uncertainties, they are compatible with the expected half-life. In case of the ^{222}Rn evolution, we obtain a $T_{1/2} = (3.5 \pm 2.5)\,\mathrm{days}$ with a red. χ^2/ndf of 0.95. In case of the ^{218}Po evolution, a $T_{1/2} = (3.1 \pm 1.0)\,\mathrm{days}$ with a red. χ^2/ndf of 0.27 is measured.

C) One QDrive removed: before the installation of the MagPump, one of the three QDrive pumps was removed. The emanation rate of the removed QDrive pump is $(4.5 \pm 0.2)\,\mathrm{mBq}$, which translates into $(1.4 \pm 0.1)\,\mu\mathrm{Bq/kg}$ when distributed homogeneously in the $3.2\,\mathrm{tons}$ of liquid xenon. In the described data analysis a reduction of $(4.0 \pm 0.7)\,\mu\mathrm{Bq/kg}$ is observed. As explained in section 3.6.1, the discrepancy may arise from the different thermal states at which the radon emanation measurement and the presented result are performed.

D) Only new pump: from this period on, the MagPump recirculates the xenon in the system and all QDrive pumps are removed. At the beginning of this phase, there are still radon atoms present in the TPC that have emanated from the removed QDrive pumps. Similar as in period B, their decay can be modeled and the first data point in the fit is fixed to the average value in period C. We obtain a fitted ^{222}Rn half-life of $T_{1/2} = (2.8 \pm 1.0)\,\mathrm{days}$ at a red. χ^2/ndf of 0.75. In case of the ^{218}Po evolution we evaluate a $T_{1/2} = (4.9 \pm 2.7)\,\mathrm{days}$ at a red. χ^2/ndf of 1.2. Both of them agree with the expected half-life of ^{222}Rn. The average ^{222}Rn (^{218}Po) activity concentration after the pump exchange is described by the fit value of the constant term and is stated in Table 3.5.

When replacing the QDrive pumps, the ^{222}Rn rate is reduced by $(19.2 \pm 1.0)\,\mathrm{mBq}$ inside the detector, when normalizing the measured activity concentration to the total liquid xenon mass of $3.2\,\mathrm{tons}$. From the emanation measurements, we expect a ^{222}Rn total reduction of $(11.0 \pm 0.9)\,\mathrm{mBq}$. The observed difference among the two measurements is $(8.2 \pm 1.3)\,\mathrm{mBq}$. In section 3.6.1, we obtained a difference of $(10.6 \pm 2.8)\,\mathrm{mBq}$, when comparing the ^{222}Rn activity concentration during SR0 and SR1 and the expectation of the total ^{222}Rn emanation in the experiment. This difference agrees with the one measured due to the pump exchange. Thus, the hypothesis that the difference between the emanation measurement and data analysis is caused by the larger emanation rate of the QDrive pumps is further supported.

E) Distillation: similar as in the SR0, xenon distillation took place in SR2. The high removal efficiency of the distillation process is reflected in the sudden drop of the activity concentration, shown in Fig. 3.27. To minimize the fluctuations, a time binning of $4\,\mathrm{days}$, instead of $2\,\mathrm{days}$ is used from this period on. The distillation causes a ^{222}Rn reduction of $(1.9 \pm 0.1)\,\mu\mathrm{Bq/kg}$, which is compatible with the reduction in SR0 of $(2.3 \pm 0.6)\,\mu\mathrm{Bq/kg}$. In the new equilibrium state, a ^{222}Rn activity concentration of $(4.5 \pm 0.1)\,\mu\mathrm{Bq/kg}$ is measured.

F) Distillation (different modes): in this distillation phase, it was studied how different flow patterns in the detector system affect the distillation performance. As described in section 3.2, the location of ^{222}Rn sources inside the detector system can be identified by radon emanation measurements before the start of the experiment. To separate the xenon and radon atoms in the distillation process, the gas mixture is guided from different location of the detector system to the distillation column. By changing the location, from which the gas is transported to the distillation column, one can test the influence of the ^{222}Rn sources on the measured activity concentration inside the TPC. This is of particular interest, since the main detector parts from the XENON1T system will be employed in the upgrade to XENONnT. The outcome of the flow pattern test and their consequences for XENONnT are not trivial to interpret and beyond the scope of this work.

G) Final rate SR2: during the distillation, the radon atoms are separated from the xenon atoms and retained inside the distillation column, where they decay. When the distillation is stopped, the volume of the distillation column is drained into the detector system, which causes the sudden increase and presumably the slight overshoot of the ^{222}Rn activity concentration in the final phase of SR2. The average value is, as expected, in agreement with the one before the distillation period.

The obtained results support the hypothesis that the discrepancy between the predicted ^{222}Rn budget in the experiment and the measured one arises from an underestimation of the recirculation pumps' ^{222}Rn release rates. The results are also promising for the upgrade of XENON1T to XENONnT. One reason is that MagPumps will be used in the upgraded detector system. Furthermore, a dedicated large-flow xenon distillation column will be build for radon removal [76]. Since radon will be the leading background component in XENONnT, its reduction translates into nearly the same decrease of the low-energy ER background [109]. The measured ^{222}Rn activity concentration of $(4.5 \pm 0.1)\,\mu\mathrm{Bq/kg}$, after the pump exchange and during xenon distillation, is the lowest ever achieved in any xenon dark matter experiment.

3.7 Neutron background from ^{210}Po at PTFE wall of TPC

In section 3.1, we have introduced two categories of radon induced background in XENON1T. So far, we have investigated in detail the radon induced background that originates from the first category, which is defined as background distributed in the liquid xenon target. In this section, we discuss a part of the radon induced background of the second category, that originates from the PTFE surfaces of the TPC.

During the construction of the XENON1T detector, the PTFE walls of the TPC were exposed to ambient air, that contains radon. Its progenies could plate-out on the surfaces and they persist while the experiment is operational. Among them, the α-decay of ^{210}Po can trigger (α,n) reactions with the fluorine, that is present in the PTFE (C_2F_4) and features a high cross-section for these interactions [94]. The emitted neutrons can penetrate into the liquid xenon target and induce a nuclear recoil (NR), identical to a WIMP interaction. The determination of an exact ^{210}Po concentration is not trivial, due to its location on the PTFE walls that enhances the chance of light and charge loss. In the following, we estimate the upper and lower bounds on the ^{210}Po concentration which allows us to set limits on the induced neutron background. Thereby, we make the assumption that the S1 signal is not lost or reduced below $30\,000\,\mathrm{PE}$. Otherwise we cannot measure the ^{210}Po decays.

Lower constraint: we select the high-energetic α-decay in the XENON1T by requiring cS1$> 30\,000\,\mathrm{PE}$. In Fig. 3.28 we show the cS2/cS1 ratio of these events as a function of the squared TPC radius. We observe a rather constant cS2/cS1 distribution along the squared radius. The events at large radii, at the TPC wall, feature a reduced cS2/cS1 ratio. In the previous sections, we discussed several indications that these events are caused by ^{210}Po α-decays.

The reduced cS2/cS1 ratio of ^{210}Po decays is caused by the trapping of ionization elec-

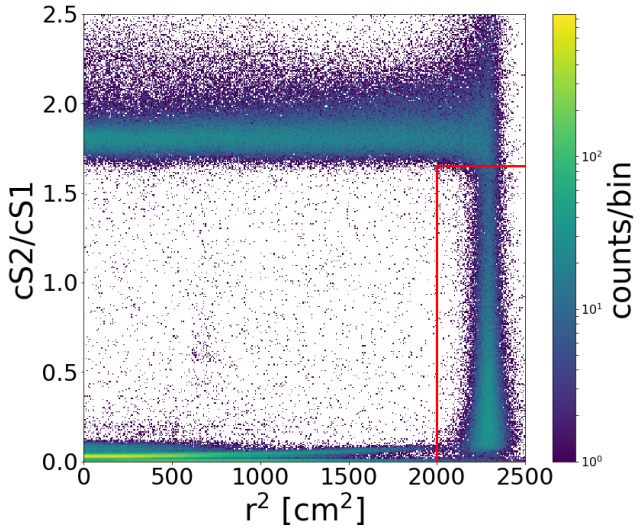

Figure 3.28: cS2/cS1 ratio vs. the radius squared for α-decays in the XENON1T. The events in the red box belong to ^{210}Po decays, that suffer from charge loss.

trons, created in the interaction of the emitted α-particle, at the PTFE walls. The position reconstruction in the (x,y) plane is dictated by the PMT hit pattern induced by the S2 signal in the top PMT array. Since the described ^{210}Po events can be reconstructed at the wall, they did not lose their S2 completely. They might be more ^{210}Po that suffer from light and charge loss but still induce neutron background. Therefore, by selecting events that have both a S1 and S2 signal we place a lower limit on the ^{210}Po amount in the TPC. In the following, we select the ^{210}Po events indicated by the red box in Fig. 3.28. By dividing the number of events by the corrected livetime, we obtain a lower bound on the ^{210}Po rate of $R_{min} \sim 19\,\mathrm{mBq}$.

Upper constraint: as in the estimation of the lower ^{210}Po constraint, we first select the high-energetic α-decay in the XENON1T by requiring cS1$> 30\,000\,$PE. We assume in the following, that all selected events originate from the α-decays within the ^{222}Rn and ^{220}Rn series and determine a total α-rate of $R_{tot} \sim 142\,\mathrm{mBq}$ inside the TPC. From this rate, we subtract the known activity concentrations of the three main contributors, namely ^{222}Rn, ^{218}Po and ^{214}Po. Based on the results in Table 3.4, we scale their activity concentrations up to the 2 t of liquid xenon inside the TPC. We obtain a ^{222}Rn, ^{218}Po and ^{218}Po activity of $R_{Rn222} \sim 27\,\mathrm{mBq}$, $R_{Po218} \sim 25\,\mathrm{mBq}$ and $R_{Po214} \sim 10\,\mathrm{mBq}$, respectively. By subtracting these contributions from R_{tot}, we obtain the maximal activity $R_{max} \sim 80\,\mathrm{mBq}$ that can be caused by the α-decay of ^{210}Po inside the XENON1T TPC.

Estimated neutron yield: the estimated ^{210}Po activity $R_{Po210} \sim (19 - 80)\,\mathrm{mBq}$ is based on the measurable ^{210}Po α-decays that enter the liquid xenon from the inner PTFE surface of the TPC and generated at least a S1 signal. We assume that an equal amount of ^{210}Po α-decays is emitted in the opposite direction, into the PTFE bulk, and triggers (α, n)-reactions. The neutron yield of (α, n)-reactions at the α-decay en-

ergy of ^{210}Po is $9.5 \cdot 10^{-6}\,\mathrm{n}/\alpha$ [94]. Thus, we translate R_{Po210} into a neutron rate of $R_{inside} \sim (6 - 24)\,\mathrm{neutrons/year}$ under the assumption that all created neutrons enter the liquid xenon reservoir.

In the described estimation, we only considered ^{210}Po decays on the inner TPC surface. However, presumably ^{210}Po decays are also present on the outer PTFE surface since the entire TPC was exposed to air during construction. These α-decays can also lead to neutron emission. We assume in the following that they cause the same neutron yield as R_{inside}. Hence, we obtain a total neutron rate of $R_{total} \sim (12 - 48)\,\mathrm{neutrons/year}$ inside XENON1T triggered by the decay of ^{210}Po. We want to remark that equal neutron rate from both PTFE sides is a simple assumption, since the inner PTFE side was surface treated with diamond tools in order to optimize the reflectivity for xenon scintillation light [51]. The treatment consists of shaving off an upper layer of the PTFE surface whereby also surface contamination could be removed. This means that the neutron contribution from the outer, untreated PTFE side of the XENON1T TPC could be higher than estimated.

This estimated neutron rate R_{total} was discussed by the XENON collaboration and an effective neutron rate was estimated (not done by the author). In this estimation, the probability of the neutrons to scatter only once in the liquid xenon is considered, as well as their the effective rate in an low energy range of $[4, 50]\,\mathrm{keV}$ used for dark matter search and inside the $1\,\mathrm{t}$ FV, that is used in the detector simulation described in [79]. Thus, a neutron rate of $\lesssim 0.2\,(\mathrm{t \cdot y})^{-1}$ from single scatter events is simulated.

We compare this result with the NR background, that was simulated in XENON1T in the same energy range and FV. It is stated in [79], that the main contributions arises from radiogenic neutrons with $(0.6 \pm 0.1)\,(\mathrm{t \cdot y})^{-1}$, generated in the detector materials. The contribution of muon-induced neutrons and neutrinos, scattering coherently off xenon nuclei, is at least one order of magnitude smaller than the rate from radiogenic neutrons. We conclude that the additional NR background from ^{210}Po surface contamination could be up to one third of the main NR in the experiment. Although this additional NR was neglected in the XENON1T analysis, the result shows that for future experiments it is an important background component. In the upgrade of XENON1T to XENONnT, a neutron veto will suppress the radiogenic neutron background by tagging events where a single scatter interaction in the TPC is coincident with a neutron detected in the neutron veto [109]. Hence, it becomes even more important to reduced the ^{210}Po contamination on the PTFE surface in XENONnT. This can be realized by a dedicated cleaning of the PTFE surfaces [II]. In addition to the cleaning, the subsequent exposure of the detector surfaces to ambient air has to be minimized to reduce the possibility of a recontamination.

3.8 Impact from radon induced background on WIMP search

The XENON1T experiment aims for detecting NRs from WIMP interactions in the liquid xenon target at a very low event rate. Despite the large discrimination power between NRs and ERs in liquid xenon, whereby only $\sim 0.3\,\%$ of the ERs are misidentified as a NR in the dark matter search region, ERs are an important background source in the rare-event search [68]. Thereby, ER background is also generated by lead decays originating from the noble gas radon that emanates into the xenon. In the previous sections, we studied in detail the decay of radon and its progenies in XENON1T. The thereby obtained activity concentrations of polonium and bismuth allow us to constrain the background arising from the intermediate decay of lead, which cannot be identified on the event-by-event basis due to its continuous energy spectrum. Most important for the background estimation are the lead decays to the ground state of bismuth in the energy region of interest for dark matter search. Therefor, the measured activity concentrations of polonium and bismuth in units of µBq/kg have to be transformed into an actual background rate at low energies.

Transformation factor: the transformation factor from an activity concentration in units of µBq/kg to the actual ^{214}Pb background rate at low energies is given by

$$\mathrm{R[mDRU]} = \mathrm{R[\mu Bq/kg]} \cdot 0.0154 \, \frac{\mathrm{mDRU}}{\mathrm{\mu Bq/kg}} \quad . \tag{3.8.1}$$

Thereby, the low energy event rate is measured in units of DRU = 1d^{-1} kg^{-1} keV^{-1} and the transformation factor is based on the simulated ^{214}Pb β-spectrum employed for the background predictions in XENON1T [79]. As described in section 3.1, the background arising from ^{212}Pb is larger by a factor of $\sim$ 3, at the same initial rate of ^{222}Rn and ^{220}Rn due to the lower end-point of the ^{212}Pb β-spectrum with respect to the one of ^{212}Pb.

^{222}Rn induced background: the upper and lower limits on the low-energy ER background from the ^{214}Pb β-decays can be determined by the ^{218}Po and ^{214}BiPo activity concentrations in the DM FV. In SR0 and SR1 we measured a ^{218}Po level of $(12.7 \pm 0.5)\,\mu\mathrm{Bq/kg}$ and a ^{214}BiPo activity concentration of $(5.1 \pm 0.2)\,\mu\mathrm{Bq/kg}$ during periods without radon removal. Hence, the ^{214}Pb background ranges between $(0.079 \pm 0.003)\,\mathrm{mDRU}$ and $(0.196 \pm 0.008)\,\mathrm{mDRU}$ in the dark matter search data of XENON1T.

^{220}Rn induced background: in this case, the upper and lower bounds are based on the measured ^{216}Po and ^{212}Bi activity concentrations of $(0.09 \pm 0.01)\,\mu\mathrm{Bq/kg}$ and $(0.08 \pm 0.01)\,\mu\mathrm{Bq/kg}$, respectively. Since these activity concentrations agree within their uncertainties, we will estimate the ^{212}Pb background with the measured ^{216}Po

level. We obtain a ^{212}Pb background rate of $(0.0042 \pm 0.0005)\,\mathrm{mDRU}$ by considering the factor of 3 as described above.

Comparison to total ER background rate: we want to put these results into perspective by comparing the measured bounds of radon induced background with the total low energy ER background rate in XENON1T. As inferred from the dark matter search results in [35], the average ER background rate is measured to be $(0.22 \pm\ 0.01)\,\mathrm{mDRU}$ in the $1.3\,\mathrm{t}$ FV and an energy range of $[1.4, 10.6]\,\mathrm{keV}$. Thus, the ^{214}Pb background contributes at a level of $\sim\ (36 - 89)\,\%$ to the total ER background in XENON1T. This is comparable with the predicted fraction of ^{222}Rn induced background of $85.4\,\%$, based on simulations of XENON1T in [79]. The prediction is based on the ^{222}Rn activity concentration of $\sim 10\,\mu\mathrm{Bq/kg}$, estimated from radon emanation measurements before the start of the experiment. In comparison to the low energy ER background rate, the ^{212}Pb background contributes with only $\sim 2\,\%$. For this reason, the source of background is neglected in the XENON1T analyses.

The ^{214}Pb background in XENON1T was also constrained by a combined fit of the low energy ER spectrum [89]. As multiple background components are present in this low energy range, the energy spectra for each of them has to be known precisely for the simultaneous fit. The determined ^{214}Pb activity concentration is $(11.1 \pm 0.2_{\mathrm{stat}} \pm 1.1_{\mathrm{sys}})\,\mathrm{Bq/kg}$, which is agreement with the obtained results of this work. In the next Chapter 4, we will relate our findings on the radon time evolution to the results obtained in [89].

The background arising from ^{222}Rn makes up the largest fraction of ER background in XENON1T. In Chapter 2, we introduced the remaining ER background sources relevant for the dark matter search results of SR0 and SR1. Besides ^{222}Rn, the other main contribution arises from low energy β-decays of ^{85}Kr. At the beginning of the SR0 data taking period, the ^{85}Kr induced background contributed at $\sim 40\,\%$ to the total ER background rate. It was significantly reduced by means of online krypton distillation campaign to level of $\sim 10\,\%$ during SR1. We will discuss the time evolution of the ER backgrounds in XENON1T in Chapter 4.

Comparison to total background rate in XENON1T: in Fig.3.29, we compare all background components in XENON1T in the dark matter reference energy region, based on the results in [35]. The different background contributions originate from ERs, neutrons, accidental coincidences (AC) and coherent neutrino scattering (CNNS), as introduced in Chapter 2.

The comparison is based on two different FV choices. The comparably small FV con-

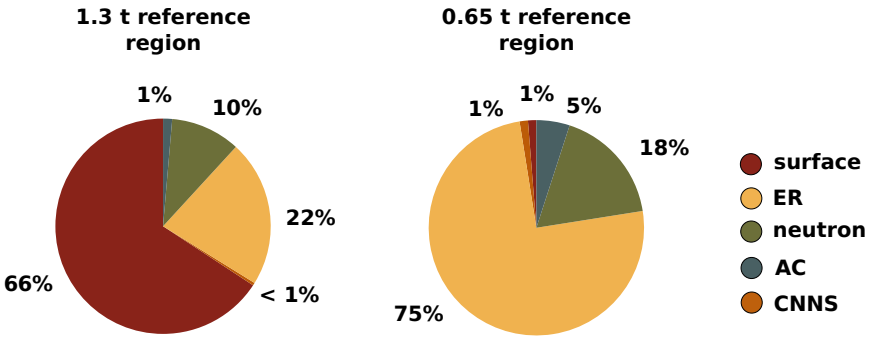

Figure 3.29: Fraction of background components in two different FVs and in the reference energy regions of WIMPs in XENON1T. The left pie chart shows the components in the DM FV that almost extends to the boundaries of the TPC. The right pie chart reflects the components when selecting an inner FV. The underlying values of each background component are taken from [35]. The components correspond to background from surface events, electronic recoils (ER), neutrons, accidental coincidences (AC) and coherent neutrino scattering (CNNS). They are introduced in Chapter 2.

taining $0.65\,\mathrm{t}$ of liquid xenon is centered in the middle of the TPC. Inside this volume, the $\sim 75\,\%$ of background arises from ERs. As discussed, the dominant ER background is induced by the homogeneously distributed ^{222}Rn decays inside the TPC.

By extending the FV to $1.3\,\mathrm{t}$, to almost the boundaries of the TPC, the ER background reduces to $\sim 22\,\%$ and background from the detector surfaces makes up the largest contribution. As explained, these background events originate from ^{222}Rn daughters that plated-out on the TPC wall, while it was exposed to ambient air during detector construction. From these observations we conclude that ^{222}Rn induces the major background in XENON1T, independent on the choice of the FV.

3.9 Summary

Great effort is invested to mitigate background in rare-event searches like XENON1T. In the experiment, external background is efficiently suppressed by different shielding methods and by profiting from the large self-shielding capacity of the target material xenon itself. Thus, intrinsic contamination gain in importance. Thereby, ^{85}Kr is reduced by around four orders of magnitude to a sub-dominant level by means of cryogenic distillation. Hence, the leading background component in XENON1T is induced from the noble gas radon. Its decay daughters can be either spread within the liquid xenon target or be accumulated on the surfaces enclosing it.

In the latter case, they have plated-out from ambient air during detector assembly and

they persist during the run time of the experiment. Thereby, the α-emitter ^{210}Po can trigger (α,n)-reactions by its decay on the PTFE walls of the TPC. In this work, we estimate the amount of emitted neutrons that can induce nuclear recoils in the liquid xenon, indistinguishable to the ones of WIMPs. The resulting background is up to one third of the main nuclear recoil background, arising from radiogenic neutrons. This result shows that great precaution has to be taken to avoid surface contamination in the next-generation experiment XENONnT, since radiogenic neutrons will be suppressed with an active neutron veto.

The main focus of this Chapter is the background induced by radon that continuously emanates from the detector materials and distributes within the whole xenon target. Thereby, the decay daughters of the ^{222}Rn and ^{220}Rn chains have the highest relevance. We identify the different isotopes within these chains by applying α-spectroscopy and delayed-coincidence methods. Using these methods, we determine their spacial distribution within the TPC. Whereas the neutral ^{222}Rn has enough time to distributed homogeneously, its progenies can accumulate at the cathode, as they can be positively charged. This "self-cleaning" effect was already observed in other TPCs and it causes a reduction of radon progenies inside the inner fiducial volume, most pronounced for ^{214}BiPo events in the present data. From the spacial distribution of the constituents within the ^{220}Rn chain, we observe that the radon sources are not distributed uniformly inside the TPCs and that the daughter isotopes spread over time within the xenon target.

Furthermore, we investigated the charge and light yield of ^{222}Rn α-decays. Due to their dense ionization track in the liquid xenon, the probability of electron recombination is increased, leading to an enhancement of scintillation photons with respect to extracted electrons by a factor ~ 100 in XENON1T. Due to the modification of the drift field in the run time of XENON1T, we were also able to study its effect on the signal yields and found consistency to measurements done in small scale TPCs. In addition, we make use of the constant ^{222}Rn amount inside the detector by employing it as continuous calibration source of the signal yields. In contrast to all other calibration sources used in the experiment, this allows for a permanent inspection of the detector stability and signal corrections.

With the described methods, we can set limits on the radon induced background and compare them to the total ER background rate. We find that the ^{220}Rn induced background is sub-dominant, whereas up to $\sim 89\,\%$ of the ER events are originating from ^{222}Rn. Hence, in inner fiducial volumes where surface background is suppressed, this source of ER background is the leading component in the dark matter search. Furthermore, the rate evolution shows a stable radon background over time, indicating that

within the sensitivity of the measurement no increase is caused by radon entering the detector through tiny leaks.

Before the start of the experiment, dedicated ^{222}Rn emanation measurements were performed to select the radio-purest construction materials. Based on these measurements, an overall ^{222}Rn budget of $10\,\mu\mathrm{Bq/kg}$ was predicted for the XENON1T detector. The ^{222}Rn activity concentration, we observe based on the described data analysis is $\sim 30\,\%$ higher than the results from radon emanation measurements. This discrepancy could be understood by an underestimation of the recirculation pumps' ^{222}Rn emanation rates. This hypothesis is supported by the presented results of the ^{222}Rn level in the detector after exchanging the pumps for a new pump of negligible radon emanation, leading to a significantly ^{222}Rn reduction in the experiment. As we show in this work, the overall ^{222}Rn level was further reduced in combination with cryogenic xenon distillation to a final activity concentration of $(4.5 \pm 0.1)\,\mu\mathrm{Bq/kg}$, which is the lowest one ever achieved in a liquid xenon dark matter experiment.

Chapter 4

Evolution of Electronic Recoil Background

XENON1T's primary analysis method to search for new particles is based on the expected energy these particles would deposit in the target material. With this method, the experiment searches for nuclear recoil (NR) interactions expected by WIMPs [35, 49]. Alternative models predict leptophilic dark matter particles to induce electronic recoils (ER) in the detector, by scattering off the atomic electrons in the xenon [110–112]. In addition, there are other postulated particles like solar axions that would create an ER in the detector. Due to its unprecedented low ER background rate, its low energy threshold and large xenon mass, XENON1T is sensitive to probe some of these models by investigating the ER energy spectrum.

In addition to the energy spectrum, the time evolution of the event rate at low energies is a powerful parameter in the search for new particles. For instance the rate of dark matter particles measured in an Earth-bound detector is expected to exhibit an annual modulation signature [32, 113]. Besides dark matter, also other particles beyond the Standard Model could induce a time varying event signature in the detector. The time evolution of the event rate does not only allow to test a signal hypothesis, but also to reject background hypotheses, since some background components exhibit a characteristic time evolution as well.

As recently reported in [89], the XENON1T Collaboration observed an excess in the ER energy spectrum at low energies over known background, most pronounced between $(2-3)\,\mathrm{keV}$. It can be attributed to different signal hypotheses but also to the β-decay of tritium, a background that has never been observed before in LXe TPCs.

Besides the thorough investigations already performed in [89], the XENON Collaboration is currently performing an additional detector stability study (DS study). Within

this study, the overall detector time stability is investigated in correlation to the time evolution of the ER rate at low energies, since potentially time varying detector parameters could have an effect on the observed excess. In the framework of the DS study, the time evolution of the ER background components is investigated to develop a time-dependent background model, as presented in this Chapter. Due to the limited statistic of the low energy rate, it is not expected that the DS study could further constrain or reject the investigated signal or background hypotheses. However, it serves as additional inspection of the reported results to improve their robustness. Additionally, the DS study forms a basis for similar studies in the successor experiment of XENON1T, XENONnT that is expected to have a higher sensitivity to investigate the origin of the observed ER excess.

Since the presented work is related to the recently published ER results, we will summarize them in section 4.1. In section 4.2, we present the results of the ongoing DS study and in 4.3, we describe the preliminary time-dependent background model.

4.1 Low energy excess in XENON1T

The XENON1T Collaboration performed a detailed search for ER signals, as described in [89]. Since a large fraction of background events in the experiment arises from ERs, the study searches for an excess above the known background level by fitting the ER spectrum at low energies with a combined background model, including the contributions of all known backgrounds in this energy range. Thereby, an excess over known background is observed, most dominant in an energy range of $(2-3)\,\mathrm{keV}$. In the following section, we want to summarize the results of the search, called from now on low energy (LE) study, and describe the investigated hypotheses that aim for an explanation of the excess events.

4.1.1 Data analysis and result

Since most of the selection cuts used in the WIMP NR search of XENON1T [35] are developed to ensure a high data quality and the selection of only valid single-scatter events, independent on the type of interaction, the LE study applies similar selection criteria as the dark matter search, which are detailed in [68]. The LE study is performed in the ER energy region of interest $\mathrm{ROI}_{\mathrm{tot}} = [1, 210]\,\mathrm{keV}$ and the same fiducial volume as in [49] is used, containing $1024\,\mathrm{kg}$ of liquid xenon (called $1\,\mathrm{t}$ FV). The contributions from surface background, accidental coincidences and neutrons are significantly mitigated in this volume and negligible for the LE study. The effective livetime of the data taking run, called science run 1 (SR1), is $226.9\,\mathrm{days}$ and the exposure is $0.65\,\mathrm{tonne}-\mathrm{years}$.

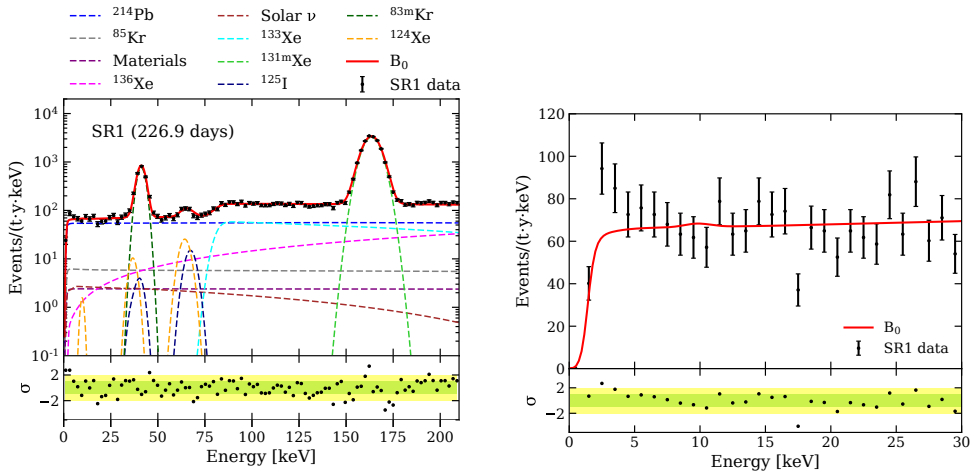

(a) *(b)*

Figure 4.1: (a) Combined fit of background components to low energy ER spectrum. The dashed lines indicate the individual background spectra used in the fit. The red solid line illustrates the combined background model B_0. (b) Same data in the low energy range, indicating an excess over the background model B_0. The light green (yellow) band in (a) and (b) indicate the 1-σ (2-σ) residuals. Figures taken from [89].

In total, 10 different background components are considered in the combined background model B_0 in the ROI_{tot}. Thereby, the continuous background spectra are either based on theoretical calculations or on GEANT4 Monte Carlo simulations. The mono-energetic peaks are described by Gaussian functions with known energies and resolutions. The background model B_0 was fitted to the SR1 data in the ROI_{tot} by maximizing the likelihood as described in [89]. The best fit of B_0 is shown in Fig. 4.1a, together with the individual background spectra. In Fig. 4.1b the background model is shown at low energies. The data displays an excess that peaks near $2-3\,\mathrm{keV}$. The excess has a significance of 3.3σ in the energy region of $1-7\,\mathrm{keV}$

In section 4.3, we will discuss in detail the background contributions from ^{214}Pb, ^{85}Kr, solar neutrinos, materials, ^{136}Xe and ^{124}Xe that are present at low energies, where the observed event excess is most pronounced. Therefore, the time-dependent background model is developed in a low energy region $ROI_{low} = [1, 12]\,\mathrm{keV}$. The remaining background components of ^{133}Xe, ^{131m}Xe and ^{125}I are created by neutron calibration in XENON1T, whereas background from ^{83m}Kr arises from a trace contamination presumably due to a momentary malfunction of the calibration source valve. Since these background components deposit energies $> 12\,\mathrm{keV}$, they are not included in the time-dependent background model.

4.1.2 Investigation of unmodeled background components

Thorough checks were performed to validate the observed excess. Thereby, several instrumental backgrounds and systematic effects were excluded. Furthermore, energy threshold effects and other mismodelings are rejected as the origin of the excess. Furthermore, the excess could have been caused by an additional, unmodeled background component, as explained below.

^{37}Ar: one potential background could arise from the decay of ^{37}Ar, yielding a $2.82\,\mathrm{keV}$ peak with a 0.9 branching ratio [114]. Two possibilities are discussed, that could explain the presence of ^{37}Ar in the detector. First, as being extracted from the atmosphere, the target material xenon contains trace amounts of ^{37}Ar. However, since ^{37}Ar has a half-life of $T_{1/2} = 35.0\,\mathrm{days}$, it decayed to a negligible level before the start of the experiment. In addition, the cryogenic ^{85}Kr online distillation lowers the ^{37}Ar concentration as well before the start of SR1, as discussed in section 4.3. For these two reasons, the presence of an initial ^{37}Ar concentration is excluded.

The second possibility is that ^{37}Ar could have been introduced into the detector by a small air leak. This hypothesis was tested by examine the $^{\mathrm{nat}}$Kr concentration in the detector, that is measured throughout SR1 as explained in section 4.3. The potential amount of air can be inferred by this $^{\mathrm{nat}}$Kr concentration and be used to constrain the corresponding ^{37}Ar concentration. The thereby estimated upper limit on ^{37}Ar is at least one order of magnitude larger than the hypothetical ^{37}Ar event rate causing the excess. With this method, ^{37}Ar from a constant air leak could be excluded as an explanation of the observed excess. Tritium was discussed as further unmodeled background contribution that might account for the excess, as explained in the next section. In contrast to ^{37}Ar, the tritium hypothesis could not bet rejected.

Tritium: tritium is a β-emitter with a half-life of $T_{1/2} = 12.3\,\mathrm{years}$ and a Q-value of $18.6\,\mathrm{keV}$ [115]. Two possibilities are considered, that might have introduced tritium into the detector. One of them is the cosmic activation of xenon during its storage above-ground [116]. The other possibility is that abundant tritiated water (HTO) and hydrogen (HT) might be stored inside the detector materials and subsequently emanate during detector operation. The tritium amount can be constrained by considering it as potential signal above the background model B_0. The thereby fitted tritium events correspond to a ^{3}H/Xe concentration of $(6.2 \pm 2.0) \cdot 10^{-25}\,\mathrm{mol/mol}$ at a significance of $3.2\,\sigma$. A possible tritium contribution from cosmogenic activation was estimated and is considered to be negligible. To test the second hypothesis of emanating HTO and HT, the fitted ^{3}H/Xe concentration is transformed into a combined (H_2O + H_2) concentration. An independent constraint on the H_2O concentration can

be placed by the measured light yields in the detector, as scintillation photons can be absorbed by H_2O. The obtained H_2O concentration appears too small to account for the excess. However, HT cannot be sufficiently quantified with a direct measurement at the moment. Furthermore, the estimation of the tritium concentration is affected by several uncertainties that cannot be tested as the relevant information is not available. Therefore, the results of the analysis are reported based on B_0 and by including an unconstrained additional background component from tritium.

4.1.3 Investigation of signal models

There are various yet unobserved processes that could describe the excess. Within the LE study, three signal models are investigated, as described below. Thereby, the individual signal model is fit together with the combined background model B_0 to the low energy spectrum. Moreover, as an additional background component from tritium could be present, the signal model is also fit together with B_0 and an unconstrained tritium component (B_0 + ^{3}H).

Solar axions

The axion is a hypothetical Nambu-Goldstone boson predicted by Peccei and Quinn as a solution of the strong CP problem in quantum chromodynamics (QCD) [22, 117]. Furthermore, QCD axions are also an interesting candidate for dark matter with very light masses, well below the keV scale [118–120]. While QCD axions at these low energies cannot be observed in XENON1T, axions produced in the Sun with higher energies are expected to create ERs in the keV range, above the energy threshold of the experiment [121–123]. The measurement of solar axions would be a proof for Physics beyond the Standard Model, but would not probe the existence for dark matter axions. Three production mechanism of axions in the Sun are considered. The first one are ABC reactions: **A**tomic axio-recombination and atomic axio-deexcitation, axio-**B**remsstrahlung and **C**ompton scattering [124]. The axion flux from ABC reactions is proportional to the axion-electron coupling g_{ea}. The second production mechanism under consideration arises from a mono-energetic nuclear transition of ^{57}Fe in the Sun and the generated axion flux is proportional to the effective axion-nucleon coupling g_{an}^{eff} [122]. Lastly, the Primakoff conversion of photons to axions was examined, whereby the resulting axion flux is proportional to the axion-photon coupling $g_{a\gamma}$ [125]. The three fluxes could be measured via the axioelectric-effect in XENON1T. This process is the analogue of the photoelectric process with the absorption of an axion instead of a photon. Thereby, the cross-section of the axio-electric effect scales with g_{ea} [126]. Combining the described production and detection mechanism of solar axion, the analysis attempts to constrain the coupling parameters $|g_{ea}|$, $|g_{ea}g_{an}^{eff}|$ and $|g_{ea}g_{a\gamma}|$, that could be all present at the same time. The axion mass depends on the axion coupling to matter under a specific model,

whereby the DFSZ [127] and the KSVZ model [128] are discussed. In case of a signal observation, the three parameters can be constrained and the axion mass can be inferred.

Results: the solar axion signal model constrains the three described coupling parameters simultaneously. Under this signal model, B_0 is rejected at $3.4\,\sigma$. To account for the axion couplings to electrons, photons and nucleons, a three-dimensional confidence volume ($90\,\%$C.L.) is constructed in the space of g_{ea} vs. $g_{ea}g_{an}^{eff}$ vs. $g_{ea}g_{a\gamma}$. The surface of this volume is inscribed in a cuboid defined by $g_{ea} < 3.8 \cdot 10^{-12}$, $g_{ea}g_{a\gamma} < 7.7 \cdot 10^{-22}\,\mathrm{GeV}^{-1}$ and $g_{ea}g_{an}^{eff} < 4.8 \cdot 10^{-18}$. This volume suggests either a non-zero Primakoff component or a non-zero ABC component due to the observed excess. However, these results are in strong tension with stellar cooling constraints in most of the couplings' parameter space [129–133]. If the tritium hypothesis is included into the background model, the solar axion signal is still preferred but at a lowered significance of $2.0\,\sigma$.

Neutrino magnetic moment

The observation of neutrino oscillation implies that at least two neutrino mass values are non-zero, which requires an extension of the Standard Model that considers neutrinos to be massless. In the extended Standard Model, the neutrinos acquire also electromagnetic properties such as a neutrino magnetic moment of $\mu_\nu \sim 10^{-20} \cdot \mu_B$, where μ_B is the Bohr magneton [134–136]. Larger values of μ_ν would imply beyond Standard Model physics and could determine whether neutrinos are Dirac or Majorana particles. The most stringent direct constraint on the neutrino magnetic moment arises from Borexino at $\mu_\nu < 2.8 \cdot 10^{-11} \cdot \mu_B$ [137]. From the cooling of globular clusters and white dwarfs, an indirect constraint of $\mu_\nu \sim 10^{-12} \cdot \mu_B$ is obtained [138, 139]. The cross-section at low energies for neutrino scattering on electrons and neutrons depends on the size of the neutrino magnetic moment, whereby only ERs are studied. An enhancement of the neutrino magnetic moment would result in an enlarged cross-section, causing an increase of the neutrino scattering rate at low energies on top of the Standard Model neutrino elastic scattering events.

Results: the background model B_0 is rejected at $3.2\,\sigma$ in case of the neutrino magnetic moment signal model. In Fig. 4.2a the low energy spectrum is shown with the best-fits of B_0 and B_0 with the signal model in addition. A $90\,\%$ confidence interval for the neutrino magnetic moment is obtained at $\mu_\nu \in (1.4, 2.9) \cdot 10^{-11} \cdot \mu_B$. In Fig. 4.2b this confidence interval is shown together with the results of other experiments. The current best-limit on μ_ν is measured by Borexino [137]. The result is also in agreement with another XENON1T analysis based on the charge signal only at low energies (S2-only). As in the solar axion case, the result is in tension with stellar constraints from

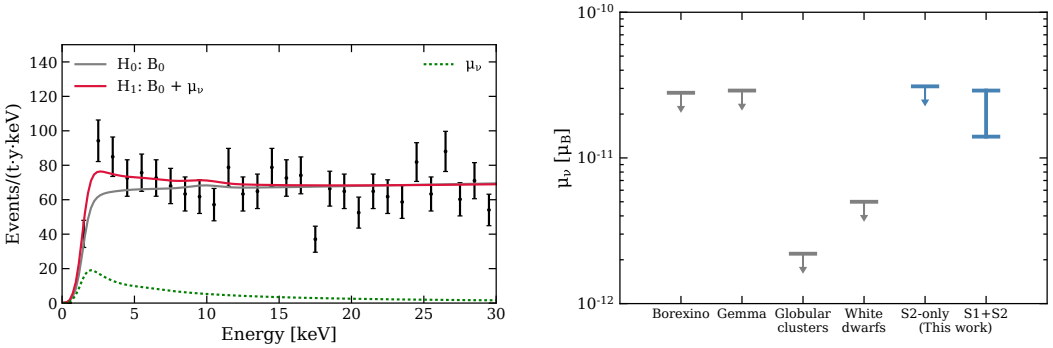

(a) *(b)*

Figure 4.2: (a) Best fit of neutrino magnetic moment model to low energy spectrum. The null hypothesis (gray solid line) is the background model B_0 and the alternative hypothesis is B_0 plus the μ_ν signal (red solid line). Contributions from the μ_ν signal is illustrated by a dashed line. (b) Determined constraints ($90\,\%$ C.L.) on the neutrino magnetic moment in comparison to results from Borexino [137] and Gemma [141], along with astrophysical limits from the cooling of white dwarfs [140] and globular clusters [139]. The constraint from XENON1T using ionization signal only (S2- only) is also shown. Arrows denote allowed regions. Figures taken from [89].

globular clusters [139] and white dwarfs [140], when interpreted as enhanced μ_ν. In case tritium is included into the background model, the significance of the neutrino magnetic moment signal is reduced to $0.9\,\sigma$

Bosonic dark matter

Axion-like particles (ALPs) are pseudoscalars as QCD axions and postulated by many extensions of the Standard Model. They do not necessarily solve the strong CP problem, but they are a well motivated cold dark matter candidate [142]. As the QCD axions, they could be absorbed by the axioelectric effect in XENON1T. For non-relativistic ALPs in the galaxy, assuming that they constitute the whole dark matter halo density, the expected signal is a monoenergetic peak at the axion mass.

Results: to search for peak-like excesses in the bosonic dark matter search, it was iterated over fixed masses in the ROI. No global significance over $3.0\,\sigma$ was found under the background model B_0. Hence, only upper limits on the pseudoscalar and vector bosonic dark matter couplings can be set as a function of the particle mass. These limits are the most stringent ones in the considered mass range for direct detection experiments.

4.1.4 Additional checks

SR2 data: several additional checks on the presented results were performed. In one of them, the additional data from science run 2 (SR2), a data taking period subsequent to SR1 is investigated. During SR2, the purification system was upgraded which lead to a higher purification speed. The upgrade also included the exchange of the QDrive recirculation pumps, the main ^{222}Rn sources in the detector system, with a new pump of negligible ^{222}Rn emanation rate, as discussed on Chapter 3. The ^{222}Rn induced background was further reduced by online xenon distillation. Thus, an additional data set of $24.4\,\mathrm{days}$ with an improved xenon purity and a $\sim 20\,\%$ lower ER background rate had a sufficient data quality to be investigated. Due to the higher xenon purity, the rate of non-noble contaminants like tritium are expected to be reduced in SR2, while the signal event rate is unaffected. However, due to the low statistics of SR2, the obtained results are largely inconclusive. The tritium signal hypothesis was tested and a slightly reduced significance of $2.0\,\sigma$ is obtained. The fitted tritium rate is consistent with the one obtained in SR1. Furthermore the results obtained for the neutrino magnetic moment and solar axion hypothesis agree within SR1 and SR2.

First time dependence check: furthermore, a first time-dependency test of the low energy rate was performed. The time evolution of the event rate could disclose a time-dependent signature that matches either the signal or the background hypotheses. Therefore, the low energy rate in the energy region of $1-7\,\mathrm{keV}$ was fitted with several models:

^{37}Ar and ^{3}H: the time evolution of the ^{37}Ar and ^{3}H decays is described by an exponential decrease. To test the background hypthoses of the two isotopes, the rate was fitted with a constant background rate B_0 plus an exponentially decreasing function. Thereby, the half-life of the exponential decrease was fixed to the ones of ^{37}Ar and tritium, respectively.

Solar axions and neutrino magnetic moment: the number density of the solar signals is proportional to $1/r^2$, whereby r is the distance between the Earth and the Sun. Since the Earth is moving on an elliptical orbit around the Sun, the distance to the Sun is largest at the Aphelion (in July) and smallest at the Perihelion (in January). Hence, the rate of the solar signals has a seasonal dependency, whereby the largest rate is expected in January and the lowest rate in July. The peak-to-peak amplitude of this modulation is expected to be $\sim 7\,\%$. To test the solar axions and the neutrino magnetic moment signal hypotheses a constant term plus a the described subtle peak-to-peak modulation is fitted.

Bosonic dark matter: the Earth's motion in the galactic rest frame is a superposition of the Earth's rotation around the Sun and the Sun's rotation around the galactic

center through the dark matter halo. In June, when the Earth's velocity is in the same direction as the Sun's orbital velocity, the observed dark matter velocity achieves the maximum. On the contrary, the dark matter velocity is minimal in December. In case of WIMP dark matter, the detected event rate depends on the observed dark matter velocity, for which reason the WIMP rate exhibits an annual modulation signature throughout the year [32,113]. In contrast, the event rate of bosonic dark matter is independent from the observed velocity [143]. In addition, the kinetic energy of the bosonic dark matter particle is negligible with respect to its rest mass. This causes a monoenergetic peak in the energy spectrum at the rest mass of the particle, which is independent from the particle's velocity. Hence, a seasonal shift of the particles' energies above or below the fixed energy threshold of the detector can also not lead to variation of the event rate. For these reasons, no time dependence of the bosonic dark matter rate is expected.

Besides the described models, the event rate is also fitted with a constant term only. However, due to the limited statistic, the rate evolution is statistically consistent with all the described fit models and non of the hypothesis can be excluded at the moment.

We want to bring out that the described LE study did not account for potential instabilities of the ER rate over time. In the next section, we will describe the status of a preliminary study currently performed by the XENON Collaboration that aims at an inspection of the detector's overall the time-stability to further scrutinize the results of the LE study.

4.2 Detector stability study in XENON1T

First validations on the overall detector stability were already performed for the main dark matter results of XENON1T [68]. Nevertheless, so far no systematic study was carried out to investigate a potential correlation between the low energy ER rate and other detector parameters over time. For this reason, the XENON Collaboration currently performs a detector stability study (DS study) at the time of writing. Due to the limited statistic of the presented data, it is not expected that the described background or signal models can be further constrained by their time evolution (see section 4.1). However, the DS study aims at adding more confidence in the presented LE results and the observed excess. In this section, we will summarize the preliminary results of the DS study.

The DS study is carried out on the same SR1 data set as used for the LE study. Thereby, the same selection cuts and FV is used. Since the observed excess is most prominent between $2 - 3\,\mathrm{keV}$, the DS study is based on the low energy region rather than the

complete $\mathrm{ROI_{tot}} = [1, 210]\,\mathrm{keV}$. Therefore, the low energy rate over time is calculated in the $\mathrm{ROI_{low}} = [1, 12]\,\mathrm{keV}$. The DS study investigated several detector parameters that could affect the low energy rate, as described below:

Signal yields: the light (charge) yield is defined as number of detected photo-electrons contributing to the S1 (S2) signal per deposited energy of a mono-energetic calibration source. These signal yields from various calibration sources are used to reconstruct the combined ER energy scale in the experiment, as described in Chapter 2. Hence, a change in the signal yields over time could have an effect on the event rate selected in a certain energy range. The time evolution of the signal yields was monitored throughout SR1. The values are stable within a maximum deviation from the mean of $1\,\%$ and $3\,\%$, respectively. In Chapter 3 we showed that these variations do not impact the shape of the ER calibration data in the S1-S2 discrimination space. Hence, no impact from the signal yields is expected on the ER rate.

Thermodynamical parameters: the slow control system of XENON1T monitors parameters that define the detector condition, such as the temperature and the pressure inside the cryostat. Since these parameters could affect e.g. the size of the light and charge signals, their stability has to be investigated. It was found that, during the SR1, the detector was operated under stable thermodynamic conditions [68]. In further ongoing studies, the potential correlations between detector parameters and the low energy rate is tested. In these preliminary tests, no significant correlation could be identified.

Selection cuts: a further important input to the DS study is the stability of the applied selection cuts over time. Several calibration campaigns were performed during the XENON1T data taking period. Thereby, the ^{220}Rn calibration is most relevant for the DS study, as the generated low energy events are ER interactions. The ^{220}Rn calibration was performed six times during the $\sim$ one year SR1 data taking period in similar intervals. The acceptance for each selection cut is usually defined on the full ^{220}Rn calibration data of SR1. For the DS study, the acceptance is calculated for each calibration campaign to validate the cut selection stability. For some selection cuts a slight time dependency was found, that has to be further investigated [64].

Another important parameter to the DS study is the time evolution of the ER background, as described in the next section.

4.3 Background model

Potential variations of the ER background rate over time could also have an impact on the observed low energy ER rate. Within the context of the DS study, we want to investigate if the background components at low energies, in the $\mathrm{ROI_{low}} = [1, 12]\,\mathrm{keV}$ where the observed excess is present, exhibit a time-dependency. In this energy region, the background model $\mathrm{B_0}$ of the LE study includes the following components: ^{214}Pb, ^{85}Kr, solar neutrinos, materials, ^{136}Xe and ^{124}Xe. The rate and time dependencies of the former two, ^{214}Pb and ^{85}Kr are constrained by data analysis and regular rare gas mass spectrometer (RGMS) measurements, respectively. The rate and time dependencies of the remaining background components are based on simulations.

The absolute background rates per component in the time-dependent background model are based on energy spectra from the XENON1T background simulations in [79]. These spectra are slightly different than the spectra used in the LE study. However, we assume that the differences in the inferred absolute background rates based on the different spectra is small. More importantly, we expect that the relative rate changes in the time-evolution of the background components are not affected in our preliminary study.

In Table 4.1, we summarize the modeled background components and their respective average low energy rate given in units of (kg·day·keV)$^{-1}$, also defined as DRU, that we derive in the following. At the end of this section, we show the preliminary time evolution for each background component.

background component	rate [(kg·day·keV)$^{-1}$]	fraction [%]
^{214}Pb	$(1.7 \pm 0.2) \cdot 10^{-4}$	79.8
^{85}Kr	$(2.4 \pm 0.6) \cdot 10^{-5}$	11.3
solar neutrinos	$(8.9 \pm 0.2) \cdot 10^{-6}$	4.2
materials	$(7.3 \pm 0.7) \cdot 10^{-6}$	3.4
^{136}Xe	$(2.3 \pm 0.3) \cdot 10^{-6}$	1.0
^{124}Xe	$(6.2 \pm 0.1) \cdot 10^{-7}$	0.3
total	$\mathbf{(2.13 \pm 0.21) \cdot 10^{-4}}$	**100**

Table 4.1: Average event rate per background component and their sum during SR1. Thereby, the $\mathrm{ROI_{low}} = [1, 12]\,\mathrm{keV}$ and the $1\,\mathrm{t}$ FV is used. In the last column, we state the individual fraction per background component in comparison to the total average background rate.

4.3.1 Background components

^{214}Pb: this isotope is created within the decay chain of the noble gas ^{222}Rn, that continuously emanates from the inner detector parts. The emanated radon atoms

spread within the xenon target and the resulting background events cannot be minimized by fiducialization. The β-decay of ^{214}Pb to the ground state of ^{214}Bi induces background events at low energies. From a fit of the low ER energy spectrum in the LE study, a total ^{214}Pb activity concentration of $(11.1 \pm 0.2_{\text{stat}} \pm 1.1_{\text{sys}})\,\mu\text{Bq/kg}$ is evaluated in SR1, whereby the $10\,\%$ systematic uncertainty mainly arises from the assumed uncertainty on the branching ratio of the ^{214}Pb decay to the ground state [144]. We transform the evaluated ^{214}Pb activity concentration into a low energy rate, whereby $1.54 \cdot 10^{-4}\,\text{DRU}$ correspond to $10\,\mu\text{Bq/kg}$ [79]. Thereby, we quadratically add the statistical and systematic uncertainty of the fitted ^{214}Pb activity concentration and obtain a low energy rate of $R_{214\text{Pb}} = (1.7 \pm 0.2) \cdot 10^{-4}\,\text{DRU}$. The time evolution of the ^{214}Pb activity concentration throughout SR1 is obtained from the ^{222}Rn evolution that we fit with a constant term, as discussed in detail in Chapter 3. The goodness of fit is at $\chi^2/\text{ndf} = 1.1$. We describe the time evolution of ^{214}Pb with a constant fixed at $R_{214\text{Pb}}$ and neglect the fit uncertainty of $0.3\,\%$ in the aforementioned total combined uncertainty.

^{85}Kr: the β-emitter has an endpoint energy of $687\,\text{keV}$ and can lead to background events in the low energy range. The man-made noble gas is produced in uranium and plutonium fission and released into the atmosphere. Since xenon is extracted from air, trace amounts of krypton are distributed within the target material. Due to the small ^{85}Kr abundance of $^{85}\text{Kr}/^{\text{nat}}\text{Kr} = 2 \cdot 10^{-11}$ [84], one typically measures the concentration of $^{\text{nat}}$Kr in xenon samples to determine the amount of ^{85}Kr, using the $^{85}\text{Kr}/^{\text{nat}}\text{Kr}$ ratio. Before and during the dark matter runs of XENON1T, xenon samples were extracted from the LXe reservoir of the detector. These measurements are performed with a rare gas mass spectrometer (RGMS) [145]. In Fig. 4.3 we show the time evolution of the $^{\text{nat}}\text{Kr/Xe}$ concentration in XENON1T. Thereby, the indicated uncertainty arises from the measurement procedure and statistics of ion counting in the employed mass spectrometer [146].

The initial $^{\text{nat}}\text{Kr/Xe}$ concentration of purchased xenon would induce an unacceptable large background rate in the experiment. Therefore, the initially high concentration of $\sim 1000\,\text{ppt}$ after filling the detector with xenon was lowered by four order of magnitude by means of cryogenic online distillation [85]. Due to the lower evaporation pressure, krypton naturally accumulates in the gaseous xenon phase of the detector. From there, a continuous gas flow of krypton enriched xenon is fed into the distillation column and cleaned before being flushed back into the detector. We refer to [76] for more details on the employed distillation column and the distillation campaign in XENON1T.

In the following, we want to outline the fit model, that was developed within

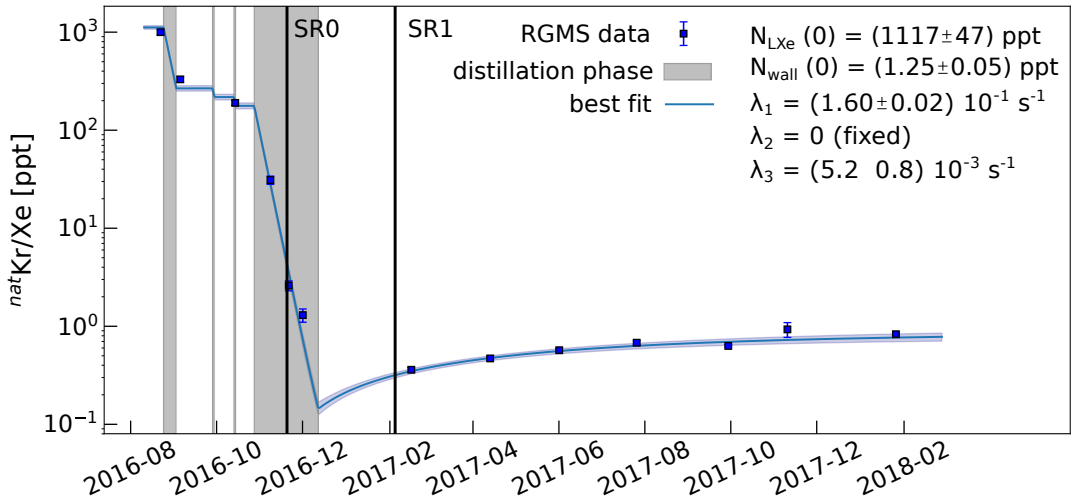

Figure 4.3: Rare gas mass spectrometer (RGMS) measurements over time to constrain the ^{nat}Kr/Xe concentration in XENON1T. Before the start of the experiment, the krypton concentration was lowered by cryogenic distillation. The krypton concentration increase is assumed to be caused by material outgassing. The blue line indicates a fit of the measurements, detailed in the text. Figure courtesy of Stefan Bruenner.

the XENON Collaboration [147], to describe the time evolution of ^{nat}Kr/Xe and hence ^{85}Kr. In the fit model we assume that the krypton atoms are mixed homogeneously within the liquid and gaseous xenon phase, respectively. Krypton which enters the gas phase is assumed to be extracted and removed by the distillation column with 100 % efficiency. Besides the efficient reduction of the ^{nat}Kr/Xe concentration, there is also a slight increase of the concentration once the distillation is stopped. During the TPC construction, small traces of ambient air, containing krypton, could have diffused inside the PTFE wall of the TPC. In the fit model, we assume that the increase of krypton in the liquid xenon is solely caused by material outgassing and not by an air leak. Under the described assumptions, the krypton concentration $N(t)_{LXe}$ in the LXe can be described as

$$\frac{dN(t)_{LXe}}{dt} = -\lambda_1 \cdot N(t)_{LXe} - \lambda_2 \cdot N(t)_{LXe} + \lambda_3 \cdot N(t)_{wall} \tag{4.3.1}$$

where λ_1 accounts for the krypton removal from the distillation column. The parameters λ_2 and λ_3 describe the krypton absorption of the PTFE wall enclosing the LXe reservoir and the krypton outgassing from the wall, respectively. The krypton concentration inside the wall $N(t)_{wall}$ is given as

$$\frac{dN(t)_{wall}}{dt} = +\lambda_2 \cdot N(t)_{LXe} - \lambda_3 \cdot N(t)_{wall} \quad . \tag{4.3.2}$$

The solution of the coupled differential equations 4.3.1 and 4.3.2 defines the fit

function. By fitting it to the RGMS data, it turned out that the krypton absorption parameter λ_2 can be neglected in the model, which can be explained in the following way. Before the distillation, the comparable high krypton concentration inside the LXe reservoir was balanced with the concentration inside the wall. The distillation causes a lower krypton concentration inside the LXe than inside the wall. Consequently, the probability of a krypton atom to be released from the wall is higher than being absorbed. In the following, we set $\lambda_2 = 0$. Fig. 4.3 shows the fit function and the obtained fit results. The goodness of fit is at a $\chi^2/\text{ndf} = 5.8$, which is similar to the one considering λ_2. A more complex model, developed in [76], yields a similar χ^2/ndf. It takes into account e.g. the GXe and LXe flows in the system as well as the mitigation from krypton atoms into the xenon gas phase. The uncertainty of the here presented fit is estimated by determining the maximal variation of the fit function within the uncertainty ranges of the fit results. The fit uncertainty is indicated as gray shaded area in Fig. 4.3. To calculate the average $^{\text{nat}}$Kr/Xe concentration in SR1, we also have to account for the systematic uncertainty induced from the calibration process of the RGMS which causes an $16.5\,\%$ uncertainty on the $^{\text{nat}}$Kr/Xe concentration [146]. By quadratically adding the fit uncertainty and the systematic uncertainty, we obtain an average $^{\text{nat}}$Kr/Xe concentration in SR1 of $(0.61 \pm 0.11)\,\text{ppt}$.

The fitted $^{\text{nat}}$Kr/Xe time evolution is transformed into a low energy rate, whereby $0.2\,\text{ppt}$ correspond to $7.7 \cdot 10^{-6}\,\text{DRU}$ [79]. The uncertainty of the β-spectrum's shape causes a $20\,\%$ uncertainty on the low energy rate. We include it into the overall uncertainty and obtain an average low energy rate of $R_{^{85}\text{Kr}} = (2.4 \pm 0.6) \cdot 10^{-5}\,\text{DRU}$ induced by ^{85}Kr.

Solar neutrinos: solar neutrinos can scatter elastically off the xenon electrons which induces an irreducible ER background. The expected average low energy rate is $R_{\text{neutrino}} = (8.9 \pm 0.2) \cdot 10^{-6}\,\text{DRU}$ [79]. The eccentricity of the Earth's orbit induces a modulation of the detected solar neutrino rate proportional in amplitude to the solid angle subtended by the Earth with respect to the Sun (similar as for the solar signal models of the LE study, see section 4.1). The effect appears as a $\sim 7\,\%$ peak-to-peak seasonal amplitude modulation, with a maximum at the Perihelion [148]. We model the neutrino rate with a cosine function of this amplitude.

Materials: the background events are generated by γ-rays originating from radioactive decays inside the detector material. They can penetrate into the xenon target volume and lead to Compton-scatter electrons at low energies. The background is significantly reduced due to the strict FV selection. The low energy rate from materials is constrained by radioassay measurements [74] and predicted by simulations to be $R_{\text{materials}} = (7.3 \pm 0.7) \cdot 10^{-6}$ DRU [79]. Thereby, the highest con-

tribution arises from the stainless steel of the cryostat with $61\,\%$, mainly from its ^{60}Co contamination. Of all external γ-sources, ^{60}Co is the only isotope that might decay fast enough ($T_{1/2} = 5.27\,\text{years}$) to induce a measurable change in the event rate over the $\sim$ one year exposure of SR1. Within this period, the ^{60}Co amount is reduced by $\sim 12\,\%$. If we assume that $61\,\%$ of the material induced background is generated by ^{60}Co, we expect a maximal rate reduction of $(0.53 \pm 0.05) \cdot 10^{-6}$ DRU, which is smaller than the uncertainty of the total material induced background. Therefore, we model the material background as a flat component fixed at $R_{\text{materials}}$.

^{136}Xe: natural xenon contains the two-neutrino double β-emitter ^{136}Xe at a natural abundance of $8.9\,\%$ in natural xenon. Its rate within the $1\,\text{t}$ FV is predicted by simulations to be $R_{136\text{Xe}} = (2.3 \pm 0.3) \cdot 10^{-6}\,\text{DRU}$ within the $[1, 12]\,\text{keV}$ energy range [79]. Due to its long half-life of $T_{1/2} = 2.17 \cdot 10^{21}\,\text{years}$ [149], we consider ^{136}Xe as a constant contribution.

^{124}Xe: the first observation of the two-neutrino double electron capture 2νECEC of ^{124}Xe was recently reported in [88] based on mainly the same data set as used in this study. With an half-life of $T_{1/2} = 1.8 \pm 0.5 \cdot 10^{22}\,\text{years}$, the longest ever measured directly, this background is considered to be constant. The dominant branching ratio is the capture of two K-shell electrons, whereas also other electron captures are possible with decreasing probability. After the capture of the two atomic electrons, the filling of the vacancies results in a measurable cascade of Auger electrons and X-rays. The two L-shell electron capture induces a peak at $9.8\,\text{keV}$, which is in our energy region of interest of $[1, 12]\,\text{keV}$. In the spectral fit performed in [89], only 2.56 ± 0.55 events are fitted for the described L-shell capture within the SR1 run time. This corresponds to $R_{124\text{Xe}} = (6.2 \pm 0.1) \cdot 10^{-7}\,\text{DRU}$.

4.3.2 Discussion

Summing up the described background event rates, we obtain a total average background rate of $R_{\text{sum}} = (2.13 \pm 0.21) \cdot 10^{-4}\,\text{DRU}$ during SR1. Thereby, ^{214}Pb and ^{85}Kr contribute the most, with $79.8\,\%$ and $11.3\,\%$, respectively, as shown in Table 4.1. In Fig. 4.4 we show the time evolution for each background component. Except of the ^{85}Kr and the solar neutrino component, all backgrounds are considered to be stable over time. The mean value of R_{sum} is shown in Fig. 4.4 as green dashed line, whereby we neglect the uncertainty band for visual purpose.

The ^{85}Kr concentration exhibits a concentration increase of $\sim 40\,\%$ during SR1, which is the largest relative change of all background components. This increase corresponds to $\Delta R_{85\text{Kr}} = (1.8 \pm 0.9) \cdot 10^{-5}\,\text{DRU}$. Since $\Delta R_{85\text{Kr}}$ is comparable to the uncertainty of the

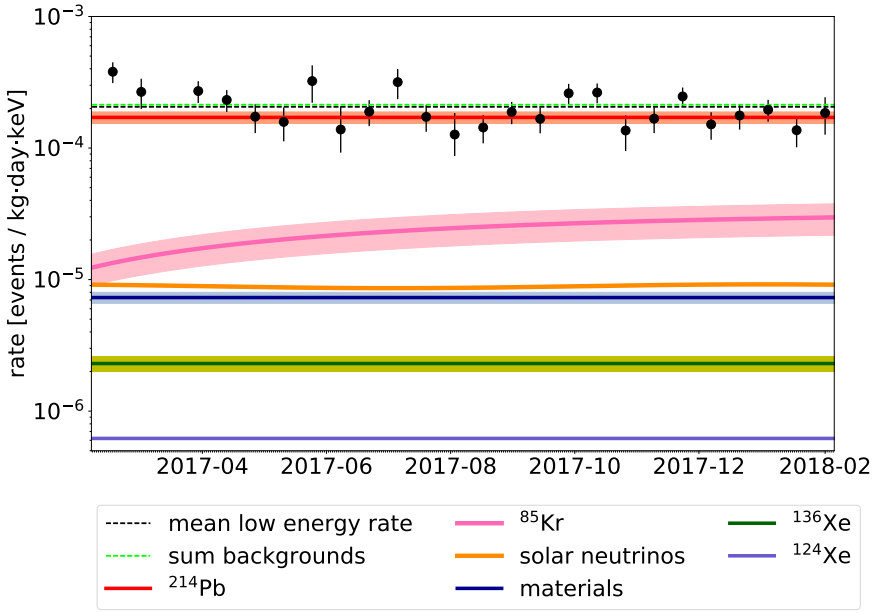

Figure 4.4: Time evolution of the ER background of components during SR1 (solid lines). Thereby, the $\mathrm{ROI}_{\mathrm{low}} = [1, 12]\,\mathrm{keV}$ and the $1\,\mathrm{t}$ FV is used. Besides the ^{85}Kr and the solar neutrino components, all backgrounds are considered to be stable over time. The green dashed line indicates the sum of all background rates. The black dashed line is the fitted mean value of the low energy rate (black data points) in the same energy range and FV. Uncertainty bands of the summed background rate and the low energy rate are omitted for visual purpose.

summed background rate $\mathrm{R}_{\mathrm{sum}}$, the increase of the ^{85}Kr concentration is presumably not resolvable in the overall low energy rate. The same is true for the subtle rate modulation of the solar neutrinos. Therefore, it can be assumed that the total background rate is constant over time.

Furthermore, we show the preliminary low energy rate in Fig. 4.4 (black data points). Its fitted mean value and statistical uncertainty is $\mathrm{R}_{\mathrm{lowE}} = (2.06 \pm 0.05) \cdot 10^{-4}\,\mathrm{DRU}$ in an energy interval of $[1, 12]\,\mathrm{keV}$ and a 14 days binning [150]. The mean value is indicated as black dashed line in Fig. 4.4, whereby we neglect the uncertainty band. The low energy rate is compatible with the summed background rate $\mathrm{R}_{\mathrm{sum}}$ within the uncertainty ranges, whereby the here presented total background rate is slightly higher than the low energy rate. Due to the observed low energy excess, the background rate is expected to be smaller than the observed event rate. There are several reasons that cause this discrepancy. For one, the background rates used in this preliminary work are based on energy spectra developed in detector simulations before the start of XENON1T that are slightly different than the improved spectra used in the LE study [144]. This causes the total background in the LE study to be slightly lower than the presented one. Furthermore, the here presented low energy rate is not corrected for efficiency losses arsing from the data selection cuts. Additionally, it is also not cor-

rected for a potential time dependence of the applied data selection. The influence of these two effects is expected to be small but requires further studies, that are ongoing at the time of writing. After these corrections, the event rate is slightly higher than the shown one.

A time-dependent correlation of the low energy rate to the summed background rate could disclose whether the observed excess is caused indeed by a signal or by an unmodeled background. In a first correlation study performed in the LE study, the rate evolution does not show a clear preference for one hypothesis. The main reason are the large uncertainties of the event rate due to the limited statistics and the short exposure time, as discussed in section 4.1. Therefore, it is thought that the event's rate time evolution cannot further constrain one hypothesis.

However, so far, there was no dedicated study performed in XENON1T on the robustness of the low energy rate over time. The presented background model shows that the overall background rate in the detector is constant over time and that it neither has the signature of the signal nor background hypothesis. Once the low energy rate is corrected for potential instabilities of the cut selection efficiencies, it will be correlated to the time-dependent background model. Thus, the stability study could confirm that no systematic effect or an unmodeled background evolution is affecting the low energy results.

Chapter 5

The HeXe System

The HeidelbergXenon (HeXe) detector was built for R&D studies to improve the performance of current experiments employing xenon as target material. The set-up contains a small-scale liquid xenon (LXe) TPC, which has been developed during this work and which was used for the purity measurements described in Chapter 6 [II].

The sub-systems of the HeXe detector are shown in Fig. 5.1, and they will be explained in the following. In section 5.1, we start with the description of the HeXe TPC. Its support structure is explained section 5.2. Subsequently, the gas system is presented, which is employed for xenon purification and calibration. Safety precautions and a slow control system were elaborated to reduce the risk of xenon loss or the damage to the system itself. They are explained in section 5.4. The data acquisition system (DAQ) and the data processor are outlined in section 5.5.

5.1 Time Projection Chamber

In Fig. 5.2 shows a lateral cut and a top view of the HeXe Time-Projection-Chamber (TPC). The TPC consists of a cylindrical Polytetrafluorethylen (PTFE) structure that incorporates electrodes for the generation of electric fields. Various sensors are integrated in the structure to measure e.g. the thermodynamic properties of the xenon. For signal detection, two photomultiplier tubes (PMTs) are employed. They detect the light signals created by particle interactions inside the so-called active volume of the TPC which is filled with the xenon target. The general working principle of a TPC is described in Chapter 2 and in the following, the individual components of the HeXe TPC are explained in detail.

5.1.1 PTFE structure

PTFE is often used in the construction of TPCs, since it offers several advantages. One of them is the material's high electric strength of $\sim 20\,\mathrm{kV/mm}$ [151], which makes

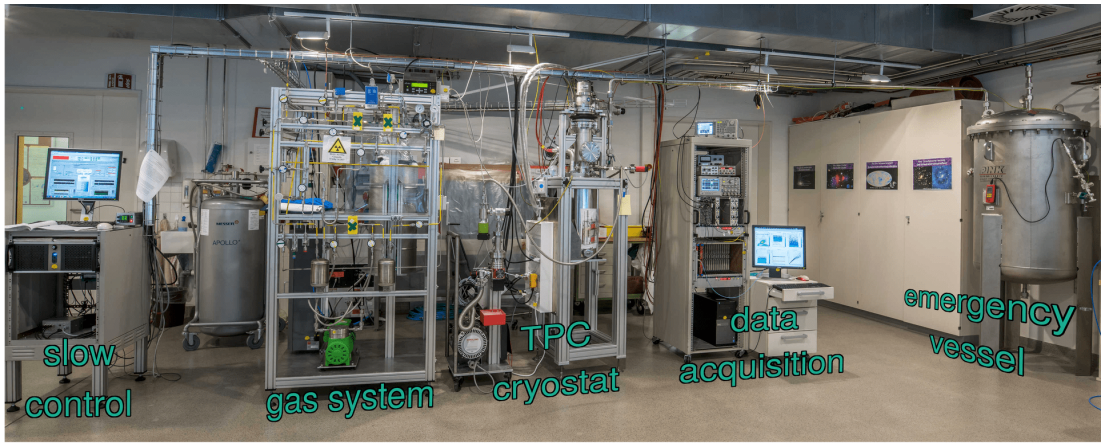

Figure 5.1: Picture of the entire HeXe detector system. The Time-Projection-Chamber (TPC) is contained in a cryostat, which is in turn connected to the gas system and the emergency vessel. Various sensors of the detector are read out by the slow control system. Data recording is performed with the data acquisition system. Detector system is explained in detail in this Chapter.

it well suitable as insulator that withstands the high voltage (HV) applied inside the TPC. Furthermore, the PTFE's dielectric constant of 2.1 is similar to the one of LXe at 1.9, which reduces discontinuities in the equipotential lines of the electric field [151]. Moreover, PTFE has high reflectivity for the VUV scintillation light created by particle interactions inside the LXe. Therefore, the inner surfaces of the active volume are made of PTFE.

The PTFE is also used as filling material in the HeXe TPC to reduce the total amount of employed xenon, since the cryostat was reused from previous measurements without a TPC, as detailed in [93, 152]. Hence, the outer diameter of PTFE structure is $19.8\,\mathrm{cm}$ and it was chosen such that the distance from the TPC to the inner walls of the cryostat is $2\,\mathrm{mm}$. The total height of the structure is $16\,\mathrm{cm}$. To further reduce the amount of xenon, dead volumes inside the PTFE structure are minimized in the design or filled with PTFE spacers. All PTFE parts were cleaned in an ultrasonic bath before the TPC assembly. The PTFE dimensions in this work are stated at room temperature as PTFE shrinks by $\sim 1.5\,\%$ at LXe temperature [153].

The largest part of the PTFE structure is formed by three stackable main PTFE structure rings. A fourth, thinner PTFE ring is used as spacer between the anode and gate electode. The central opening of the middle main ring contains four stackable PTFE rings with an outer diameter of $10\,\mathrm{cm}$. They are used to support the stainless steel (SS) field shaping rings, and they surround a PTFE cylinder with an inner diameter of $5.6\,\mathrm{cm}$ and a height of $5\,\mathrm{cm}$. This cylinder encloses the active volume and it can be exchanged. Copies of it are used as samples to test different PTFE surface cleaning techniques in

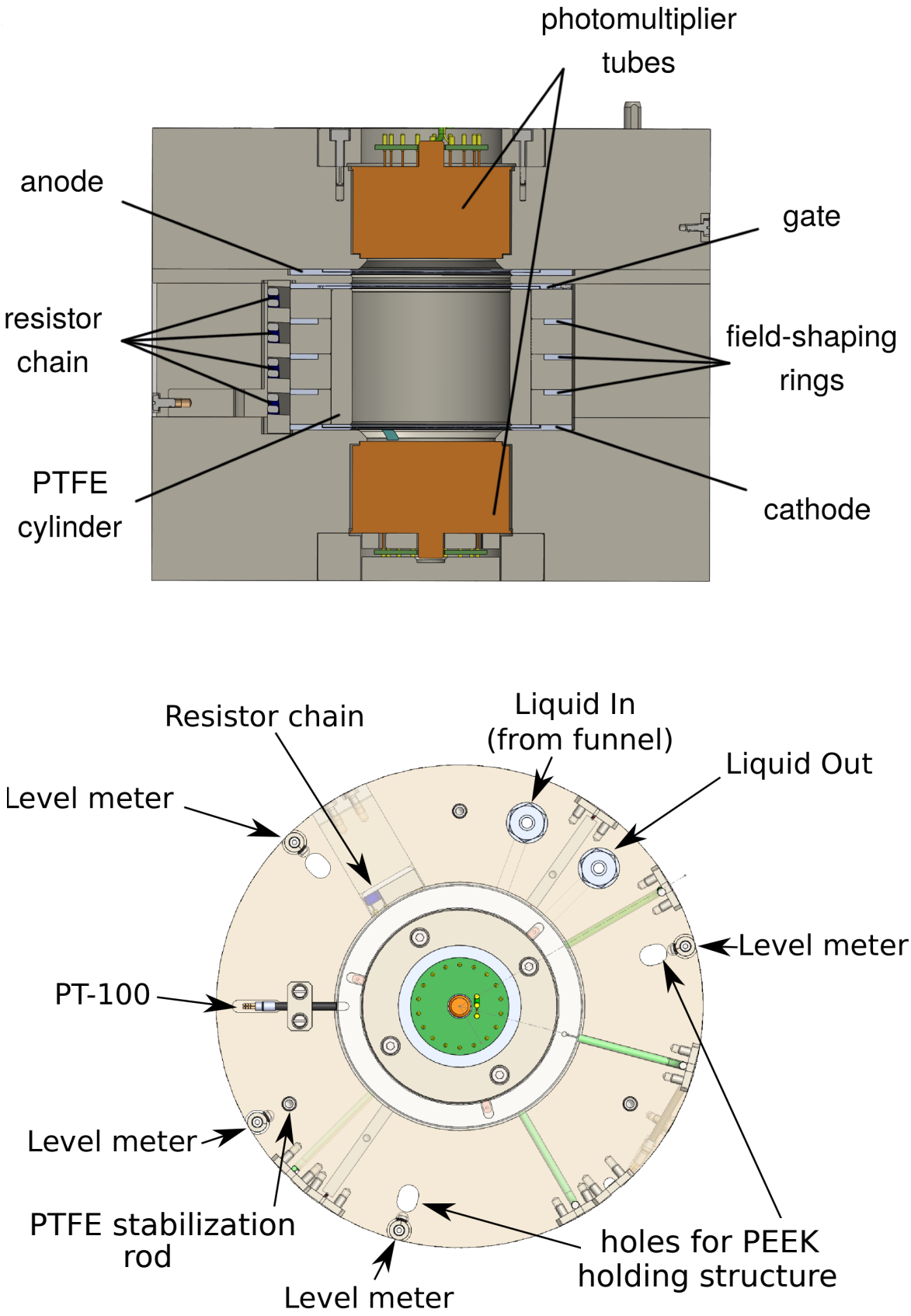

Figure 5.2: Lateral cut and top view on TPC. The individual items, indicated by arrows are explained in detail in the text.

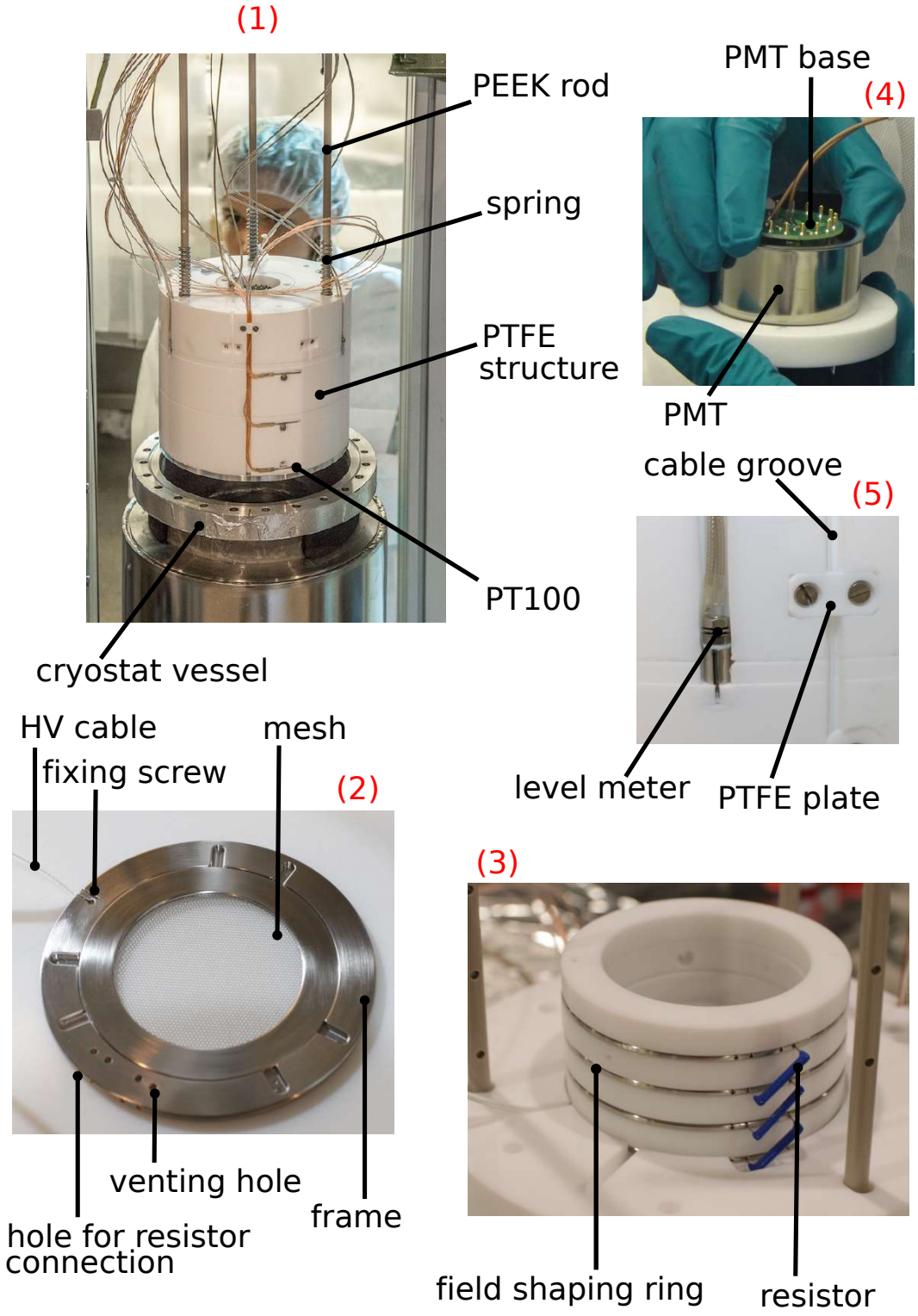

Figure 5.3: Pictures of the TPC and its components. (1) The TPC fixed in its holding structure. (2) Electrode mesh and its frame. (3) PMT and its base. (4) Side view of the TPC showing a short LM and a cable groove. (5) Field cage with resistor chain to connect the field shaping rings with the cathode and gate.

the purity measurements of this work. The frequent exchange of the sample cylinder is one reason why the TPC was designed to be easily disassembled and re-mounted again. The top and bottom main structure ring embodies a PMT each, that faces the active volume.

The HV and sensor cables are led upwards along the outer surface of the PTFE structure inside grooves. In some cases, the cables are fixed by small PTFE plates that are screwed inside the PTFE. All drilled holes are vented to avoid residual gases from being trapped. The PTFE structure rings are aligned with three PTFE stabilization rods, placed in vertical holes through the entire structure at an angular distance of $120°$. The TPC is placed in a holding structure, consisting of three PEEK rods that are inserted through the PTFE structure as well. The PEEK rods are screwed to an aluminum plate at the bottom of the TPC. A picture of the TPC and the holding rods is shown in Fig. 5.3 (1). At the top part, the PEEK rods are sticking out of the PTFE structure, each surrounded by a SS spring. This spring is used to press the entire PTFE structure on the bottom plate to compensate the buoyancy forces of the LXe. During operation, the holding structure is attached to the croystat vessel at the top and the TPC is freely suspended inside the cryostat. The holding structure is adjustable in height which allows for TPC leveling in three dimensions.

5.1.2 Electric field

A particle interaction inside the active volume creates ionization electrons. A drift field guides the electrons upwards to the liquid-gas interface. At this interface, the electrons are extracted from the LXe into the GXe and amplified by an extraction field. The electric fields in the TPC are generated by three hexagonal pitched electrodes. In standard configuration, the bottom mesh electrode is set to negative potential (cathode), the central mesh electrode (gate) is at ground potential, and the top mesh electrode is at a positive potential (anode). The drift field is defined by the cathode and gate over a distance of $5\,\mathrm{cm}$. The extraction field is applied between gate and the anode over a distance of $5\,\mathrm{mm}$. The meshes are custom-made by the company Great Lakes Engineering and etched out of a SS sheet. The mesh and its frame are shown in Fig. 5.3 (2). Each mesh has a thickness of $100\,\mathrm{m}$ and a pitch of $1\,\mathrm{mm}$ (minimum hexagonal cell diameter). A mesh is placed inside a $2\,\mathrm{mm}$ thick, circular SS frame and fixed by SS ring, that is pressed on the frame by the enclosing PTFE blocks. Flexible, single-wire and PTFE insulated HV cables are attached to the frame. The cable's end is crimped, sticked into the frame and fixed by a small screw. The frame is polished to remove sharp edges that could cause electrical discharges once the field is applied. The three electrode frames are rotated horizontally by $45°$ relative to one another. Like this the field homogeneity and the distance between the HV cables is increased.

A field cage, shown in Fig. 5.3 (3), is employed to enhance the homogeneity of the drift field. It consists of three SS field shaping rings (FSR), enclosing the active volume equidistantly. The gate electrode, FSRs and the cathode electrode are connected in series with in total four $1\,\mathrm{G}\Omega$ resistors that have a tolerance of $1\,\%$ each. Both sides of each resistor features a thin wire, which is sticked into one of the designated spring-loaded pins inserted in an electrode's frame or a FSR, respectively. When applying a voltage to the cathode and gate electrodes, the resistor chain generates a gradual drop of the electrical potential over the entire depth of the active volume.

The HV is applied to the electrodes by two ISEG modules that provide a maximal voltage of $5\,\mathrm{kV}$. The electrical stability of all components, required for the field generation was tested thoroughly, such as the HeXe TPC can be operated at a stable electric field. The tests were either performed separately for the individual components and after connecting them to one another.

In order to optimize the homogeneity of the electrical field in the design process of the TPC, a detector simulation was developed. It is based on the commercial finite element software COMSOL Multiphysics [154]. Different geometries of the relevant electrical components were simulated, such as the number of field shaping rings and the electrode mesh geometry. Moreover, the type of the HV connection to the individual electrodes was varied and the geometry of the electrodes' frames. The meshes were designed to ensure both a homogeneous field and a high optical transparency. The latter is $\sim 80\,\%$ for each mesh. After the optimizations, the hardware parameters were fixed to the described geometry.

In addition, different voltage configurations can be simulated. Thus, the degree of field inhomogeneity can be studied at different field settings. Drift field inhomogeneities are created by field leakage from the fields between cathode and the bottom PMT, the field in the extraction gap and the field between the anode and the top PMT. The inhomogeneities can be significantly decreased in the data analysis by excluding regions close to the gate and cathode mesh. Thus, the drift field applied for the purity measurements is $(394 \pm 5)\,\mathrm{V/cm}$ and the degree of field inhomogeneity is at the percent level. The extraction field is set at $\sim 10\,\mathrm{V/cm}$.

5.1.3 Photomultiplier tubes

The active volume of the TPC is monitored from top and bottom by a Hamamatsu 2-inch PMT (R6041 − 406). The PMTs' windows, made from synthetic silica glass, are located at a distance of $4\,\mathrm{mm}$ to the TPC's anode and cathode mesh, respectively. The

PMTs were selected for their high quantum efficiency (QE) at $\sim 39\,\%$ at the xenon scintillation wavelength of $175\,\mathrm{nm}$ [57]. They are designed to operate stably in GXe and LXe at cryogenic temperatures. During the measurements in this work, the bottom PMT was operated at $-950\,\mathrm{V}$ and the top PMT at the reduced voltage of $-900\,\mathrm{V}$ to minimize saturation effects caused by the rather large S2 signals. A custom-made voltage divider circuit (base) is attached to each PMT, featuring a total resistance of $2.5\,\mathrm{M}\Omega$ each. A picture of the PMT and its base is shown in Fig. 5.3 (4). The PMT signals are read via flexible $50\,\Omega$ RG196 coax cables with a PTFE jacket. A Kapton single-wire UHV cable (Accuglass 26 AWG, TYP$28-30$) is connected to the base to bias the PMT with HV provided by a ISEG module. Contact between helium gas, typically used in the laboratory for e.g. leak checks, and the PMTs was avoided, since this could lead to an increase of the PMTs' afterpulse rate.
Two optical fibres are inserted into the TPC's PTFE structure for *in-situ* PMT calibration measurements. The fibres point on the outer surface of the inner PTFE cylinder, that defines the active volume, at roughly its medium height. Like this, the light pulses from a LED illuminates both PMTs equally with photons. The LED has a peak wavelength of $350\,\mathrm{nm}$ and is mounted on a trigger board, that its connected to the optical fibres' feedthroughs at the cryostat flange. The PMT calibration is performed before and after each measurement to check the stability of the PMT gain. The gain is the amplification factor of one photoelectron, released from the PMT's bialkali photocathode by the photoelectric effect, to a measurable electric current. The average gain during the measurements was $\sim 10^6$. More information on the PMT calibration performed in the HeXe set-up can be found in [155].

5.1.4 Level meters

A precise measurement of the LXe level is performed by four custom-made concentric capacitor level meters (LMs). They consist of a SS cylinder with an inner diameter of $4\,\mathrm{mm}$ and a wall thickness of $1\,\mathrm{mm}$. A SS rod with a diameter of $2\,\mathrm{mm}$ is centered in the cylinder by PTFE plates on top and bottom of the LM. When the LXe streams inside the sensor, its height is determined by the relative capacitance increase of the LMs based on the different dielectric constants of GXe and LXe. To avoid capillary action, a $1\,\mathrm{mm}$ thick slit is milled inside the cylinders surface, from top to bottom. Two Universal Transducer Interface (UTI) sensor chips from Smartec Company are used as measurement device for the LMs [156]. The company provides an evaluation board which has several different measurement modes for capacitances. Each UTI and its evaluation board is place in a metal shielding box. A RG178 coaxial cable is connected to both the outer cylinder of the LM and the inner rod. The outer cylinder is set on ground potential and the inner rods is biased with a negative voltage.

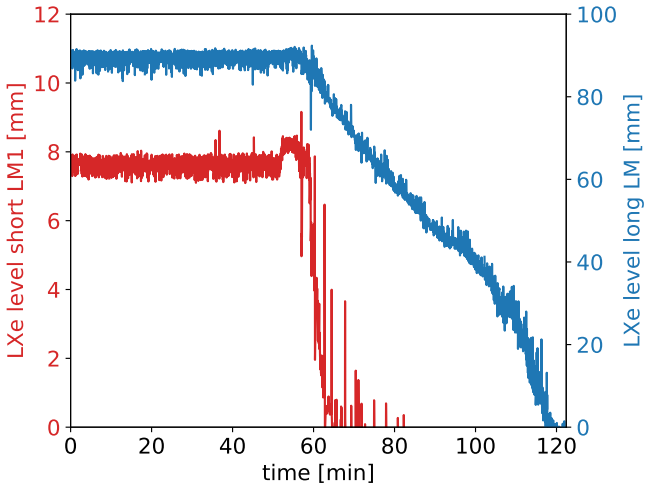

Figure 5.4: Time evolution of LXe level monitored by a short LM (red) and the long LM (blue). At a time of $\sim 60\,\mathrm{min}$ the measurement is stopped and the LXe is recuperated, causing the level to decrease in both sensors.

LMs of three different lengths are employed in the TPC. One of them has a length of $10\,\mathrm{cm}$. It is placed with a distance of $2\,\mathrm{cm}$ from the TPC's bottom inside a notch, milled vertically in the PTFE structure. Thus, this long LM covers almost the entire height of the TPC and is used to monitor the liquid level during the xenon filling and recovery. In addition, there are three shorter LMs. Two of them have a lengths of $1\,\mathrm{cm}$ each and the third one has a length of $3\,\mathrm{cm}$. They are also placed in notches inside the PTFE outer surface and cover the range between the gate and anode's height, as shown in Fig. 5.3 (5). They are used to measure the liquid level between these two electrodes and to adjust the required level height for an efficient electron extraction. They are installed with an angular distance of $120°$ along the TPC's circumference which allows for a level measurement in three dimensions. The short LM with a length of $3\,\mathrm{cm}$ is additionally used to monitor the level up to the top PMT, which is required if the TPC is operated in LXe single-phase.

In Fig. 5.4 the time evolution of the LXe level is shown at the end of a measurement and when the xenon is recuperated. Thereby, the red curve indicates the level in one of the short LMs of $1\,\mathrm{cm}$ length. In blue, the level evolution monitored by the long LM is presented. The LMs were calibrated by measuring the readout of the LMs once they are empty and once they are completely filled with LXe. By assuming a linare performance, the corresponding height in units of mm can be calculated based on the LMs dimensions.
The LXe level is stable up to a time of $\sim 60\,\mathrm{min}$, when the xenon recirculation is stopped and the recuperation starts. The short LM is emptied after a few minutes since it is located at the height of the liquid-gas interface and it covers a smaller range than the long LM. At $\sim 100\,\mathrm{min}$ the active volume, featuring the largest xenon volume in the TPC, is emptied. Afterwards, the draining speed in the long LM increases since a comparably small amount of LXe per TPC height has to be recuperated.

5.1.5 Temperature sensors

In total four sensors are used to monitor the temperature of the TPC. One of them is installed on top of the PTFE structure to measure the temperature in the gas phase. The remaining three are located at different heights of the TPC. They are fixed equidistantly inside notches of the PTFE structure's outer surface with screws and small PTFE plates. The sensors are PT100 resistance thermometers connected to either two or four-wire copper cables with a PTFE insulation. The cabels are led upwards in channels, milled into the PTFE structure. Besides measuring the temperature, they are also used to monitor the level height of the LXe when the cryostat ist filled. The PT100 sensors were calibrated by inserting them in an mixture of liquid nitrogen and ethanol at different, known temperatures.

5.2 Support structure

The TPC and the LXe are hosted in a SS cryostat during the measurement. The cryostat's 200CF flange is mounted on a cuboid structure made from aluminum profiles. A cold head and three flanges are welded on top of this main flange. A cold head is required for the xenon liquefaction. The flanges are necessary to establish the xenon recirculation stream, to mount various cable feedthroughs and to install several safty arrangements. In the following, we will explain in more detail their individual functionalities.

5.2.1 Cryostat and glove bag

A SS support ring is clipped to the bottom side of the cryostat main flange, providing a fixation of the PEEK rods of the TPC's holding structure, as shown in Fig. 5.5 (1). Like this, the TPC can be freely suspended from the main flange. The cryostat vessel is placed on a platform, that can be lifted by a hoist to close the cryostat, as shown in Fig. 5.5 (2). The inner height and diameter of the cryostat vessel is $54\,\mathrm{cm}$ and $20\,\mathrm{cm}$, respectively. Both the cryostat vessel and its flange are double-walled and evacuated for insulation, which is necessary to maintain the cryogenic temperature of LXe during operation. To reduce the heat intake, the inner cryostat is wrapped into a multi-layer insulation foil on the vacuum facing side. The insulation vaccum is monitored by a vacuum sensor and pumped continuously during operation with a turbomolecular pump and a rouhing pump connected in series. The croystat vessel is equipped with a heating plate at the bottom. By using the additional heating power, the xenon evaporation can be enhanced which allows for a faster xenon recuperation. An oil-free turbomolecular pump is connected directly to one of the cryostat's flanges to increase the pumping efficiency when the cryostat is evacuated.

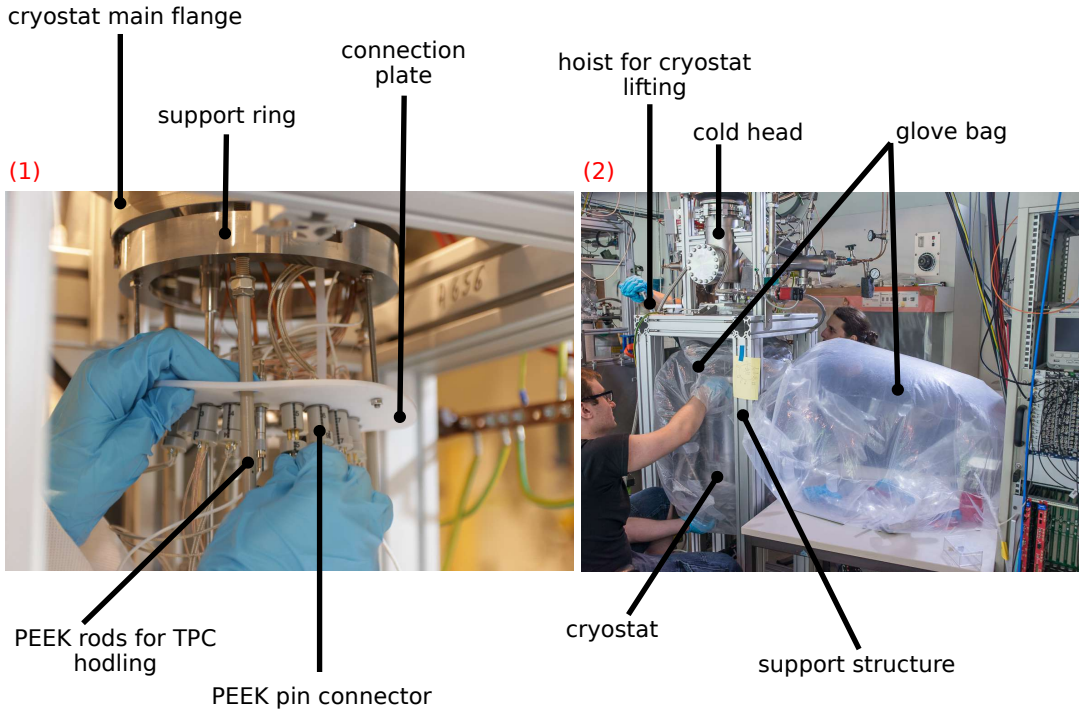

Figure 5.5: Parts of the TPC's support structure. (1) Support ring and connection plate. (2) Glove bag and aluminum stucture to support the cryostat and the cold head.

In addition to the PEEK rods, three thinner metal rods are screwed inside the support ring. They are used to hold a connection plate. This plate is made of PTFE and it is equipped with several plug-and-socket connectors. HV and signal cables are plugged into both side of the connection plate, as shown in Fig. 5.5 (1). On its top, the cables are guided to their specific feedthroughs. On the bottom side, the cables are lead to the respective TPC items. Due to this intermediate step, the cables of the TPC components do not have to be connected directly to the feedthroughs. This facilitates the assembly and dismounting of the TPC. The pin connectors for the LM and temperature sensor cables were custom-made from PEEK. To ensure their correct orientation, both parts of the PEEK connector have a laser engraved mark.

A glove bag is connected to cryostat's main flange, enclosing the entire cryostat vessel, depicted in Fig. 5.5 (2). When the croystat vessel is lowered to access the TPC, the glove bag is flushed with N_2 at a sligh overpressure. Hence, a contact of the TPC and ambient air, which contains oxygen or water vapor, is avoided. These gases affect the signal yields measured by the TPC, whereby the charge yield is the parameters of interest in the purity measurements. After dismounting the TPC from the cryostat flange, it can be placed on a small table next to the support structure, while keeping it inside the glove bag. This facilitates the modifications of the TPC, which are required

cable feedthrough	connected TPC item	quantity
32-Pin Connector	Level Meter, Pt100	1
SHV-10	HV grid	3
SHV	HV PMT	2
BNC	PMT signal	2
FC/PC	optical fibre	2

Table 5.1: Various feedthrougths to guide the cables from the TPC components to the DAQ system and the voltage supply.

for the measurements.

5.2.2 Cryogenics and xenon flow

A cooling system is installed on top of the cryostat flange to liquefy xenon gas. A Leybold COOLPAK $6000-1$ helium-driven pulse tube refrigerator (PTR) provides a constant cooling power of $200\,\mathrm{W}$ for xenon liquefaction. This cold head is in thermal contact with a copper block which acts as a cold finger. Four PT100 sensors are installed inside the copper block to monitor its temperature. Three heating cartridges are placed between the copper block and the cold head. They can provide a maximum heating power of $300\,\mathrm{W}$ and are controlled by a proportional integral-derivative (PID) controller. The heating cartridges are used to partly compensate the cold headâ€™s cooling power. Thus, the copper block's temperature is continuously kept at a temperature of $\mathrm{T_{LXe}} = -107.5°\mathrm{C}$ for xenon liquefaction. The GXe is carried from the gas system inside the cryostat and to the copper block where it gets liquefied and drops into a funnel, feeding the LXe through a vacuum insulated pipe into the cryostat.

Inside the croystat, the xenon drops fall into a second funnel, which is connected to the TPC. Thus, the purified LXe is lead into the TPC's active volume, at an inlet below the cathode mesh. The LXe is extracted from an outlet below the bottom PMT inside a tube, evaporates and is looped back to the gas system. In a second gas outlet, the xenon can be extracted from the gas phase inside the cryostat. However, in standard operation this port was not used. The combination of absolute xenon mass filled into the system, the gas recirculation speed and the temperature setting of the cold head has to be correctly adjusted to establish the thermal stability of the system.

5.2.3 Cable feedthroughs

The signal and HV cables are guided out of the cryostat by means of specific cable feedthrough connectors, that are listed in Table 5.1. In case of the electrode's HV supply, a custom-made CF40 flange was designed, equipped with three SHV-10 connectors. They feature additional PTFE insulation layers which are inserted inside the

SHV-10 connectors to increase their electrical breakdown voltage. By the usage of BNC feedthroughts for the PMT signal read-out, noise could be significantly reduced.

5.3 Gas system

The gas system (GS) is made of SS 1/4 inch tubes and it is connected to the cryostat via a go-and-return line. A sketch of the GS is shown in Fig. 5.6. It contains the xenon storage bottle that can hold up to $10\,\mathrm{kg}$ of xenon, whereby a total mass of $\sim 2.3\,\mathrm{kg}$ was employed. A S-type load cell is used to measure the bottle's weight. The first step for filling xenon inside the cryostat is to expand the warm and high-pressure gas from the storage bottle into the high pressure line of the GS, marked in green in Fig. 5.6. By means of a pressure reducer, the gas pressure is lowered from $50\,\mathrm{bar}$ to $2\,\mathrm{bar}$ when filling it into the low pressure line of the GS and expanding it into the cryostat. The gas gets liquefied at the cold finger and filled up to the required level. After filling, the storage bottle is always cooled down by immersing it into LN_2. This allows for a fast xenon recovery via cryo-pumping in case of emergency. The same method is used to recuperate the xenon after operation.

During operation, a double diaphragm pump (KNF N 143.12) recirculates the xenon through the GS and the TPC at a flow of $2.75\,\mathrm{SLPM}$, which is monitored by a mass flow meter. The gas stream during recirculation is indicated in red in Fig. 5.6. A buffer volume is installed before and after the recirculation pump to dampen flow variations. The mass flow is adjusted by a manual valve that is installed in the bypass-line of the recirculation pump. The gas continuously passes a rare-gas purifier (getter, SAES PF3−C3−R−2) that consists of a highly chemically-active zirconium-alloy which is operated at $400°\mathrm{C}$. It removes oxide, carbide and nitride impurities by forming irreducible chemical bonds with the getter material (zirconium). These impurities are constantly outgassing and desorbing into the xenon from all detector components, leading to a reduction of the signal sizes.

The GS has several ports to the atmosphere which can be used to install e.g. calibration sources or draw gas samples. For the measurements in this work, a ^{83m}Kr calibration source is employed which is permanently installed in the GS. The ^{83m}Kr emanates from a ^{83}Rb source loaded in zeolite beads [157]. The beads are stored in a tube that features a particle filter on each side. The xenon stream can be guided through the tube to transport the ^{83m}Kr atoms inside the TPC. In the decay of ^{83m}Kr, conversion electrons at $32.1\,\mathrm{keV}$ and $9.1\,\mathrm{keV}$ are emitted coincidently, which allows for their clear event selection.

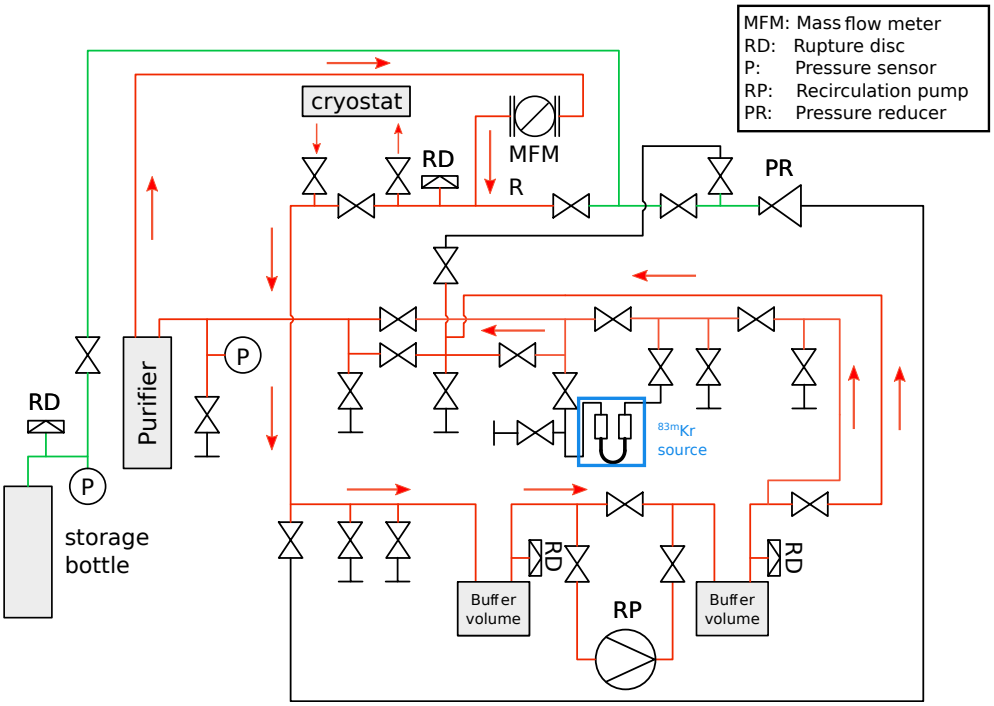

Figure 5.6: Gas system of the HeXe set-up. The green line indicates the high pressure side into which the xenon is expanded before being filled. The red line presents the low pressure side, which is used to recirculate the GXe. The arrows indicate the xenon flow direction during operation. The ^{83m}Kr calibration source is shown in blue.

5.4 Safety precautions and slow control system

The entire system is designed such as it meets certain safty requirements to avoid the loss of xenon and the damage to the set-up in case of any failure. Therefore, some hardware and software precautions are applied.

In case of a sudden pressure rise inside the croystat, various safety precautions are successively activated. The cryostat is connected via a SS one inch tube that features an in-line rupture disk to a large emergency vessel with a volume of 480 l. In case the rupture disk bursts, the entire xenon content of the system can be safely stored in this evacuated container. As further safeguard, an overflow valve is connected to the cryostat that only opens if the adjusted pressure limit is reached and closes again if some xenon gas is released and the pressure decreases again. Its opening pressure is fixed slightly above the one of the in-line rupture disk. Thus, not all the GXe is lost at once and the reaction time is increased. At an slightly higher pressure setting, a further rupture disk is installed that opens directly to the atmosphere, in case the described safety measures do not work.

In case of power failure, the xenon cooling and the continuous pumping of the cryo-

stat's insulation vacua stop. Therefore, a shutter valve is installed at the pump that prevents the ambient air from streaming into the insulation volume which would cause a sudden temperature and pressure increase of the xenon inside the cryostat. With existing insulation vacua, the xenon can be stored $\mathcal{O}(\text{hours})$ inside the cryostat, even without cooling.

The GS is equipped with several rupture disks as well, that open towards the air-side. One of them is installed at the outlet of the xenon storage bottle with a minimal burst pressure of $80\,\text{barg}$. Three rupture disks are mounted in the GS's low pressure side as shown in Fig. 5.6. The burst pressure of all rupture disks in the system are still below the rated maximal pressure of each sub-component, which was tested in dedicated pressure tests.

In addition to the hardware safeguards, a slow control (SC) system monitors various critical detector parameters. One part of the SC system is based on a program developed in LabVIEW that reads outs and displays the following parameters on a display:

- pressure inside the cryostat and the gas system
- cryostat insulation vaccum
- temperature measured by Pt100 at the TPC and the copper block
- level meter capacities
- mass flow in gas system
- weight of storage bottle

The read out values are saved in a PostgreSQL database that is frequently backed-up [158]. Warning and alarm ranges can be defined for each parameter. In case the specific parameter exceeds or falls below the threshold value, notification e-mails and SMS messages are sent to the HeXe operators. An MPIK internal infrastructure based on Nagios monitors if the database and the SC computer are running and sends alarm messages in case they are not responding [159].

The other part of the SC system is based on a Python program to control the HV modules supplying the PMTs and TPC electrodes. The HV values of each component is read-out and stored in the same database as mentioned above. The HV settings of the electrical components can be changed automatically by a previously defined ramp schedule. In case of a sudden HV outage of one of the PMTs or HV electrodes, a notification is sent and the program can be used to reramp the affected component automatically.

5.5 Data flow

5.5.1 Data acquisition system

The data acquisition system (DAQ) is used to digitize the PMT signals. The signals are first fed into a custom-made voltage amplifier module. One output is connected to a digitizer and the other one via a fan-out module to a discriminator per PMT channel. If the signal in both PMT channels pass coincidently a certain threshold, a NIM signal triggers the digitizer and the PMT waveform per channels is recorded. For the measurements in this work a V1724 digitizer is used from CAEN. At a sampling rate of $100\,\mathrm{MHz}$ and a bandwidth of $40\,\mathrm{MHz}$ up to 8 channels can be recorded simultaneously. Custom-made software is used to control the DAQ and to store the recorded waveforms on disk.

5.5.2 Data processing

The data processor is based on the same software as described in [152]. The waveform samples of each PMT channel are extracted from the acquired data and baseline corrected by subtracting the baseline, which is estimated from the average of the first 25 samples. The baseline corrected waveforms are then added up to the summed waveform. In Fig. 5.7 the summed waveform of a $^{83\mathrm{m}}$Kr decay inside the HeXe TPC is shown.

A peak finding algorithm is applied to the waveforms. In the first step, a base threshold is calculated and the ranges of samples, in which the voltage rises below this base threshold and exceeds it again, are defined as excursion intervals. Signals above the base threshold are not considered in the algorithm. The voltage range between the base threshold and the minimal voltage in an excusion intervall is divided into several equidistantly voltage steps. The peak finding algorithm iterates over these voltage steps and calculates the number of threshold excusions per peak candidate. A peak candidate is accepted if it passes more than $25\,\%$ of the voltage steps.

In a next step, several peak parameters are calculated. The peak's area is determined by integrating over the peak interval and it is converted into units of photoelectrons (PE) by taking the PMT gains into account. In the data analysis a PMT coincidence level is applied, which defines that the contribution from a single PMT signal to the summed signal must be at least $0.33\,\mathrm{PE}$. Furthermore, area quantiles are calculated. They are defined as the upper integration limit, starting from the beginning of the peak's interval to reach a certain fraction of the peak's total area. The 80p peak width is defined as the time interval between the 0.9 and 0.1 area quantiles and the peak's rise time is calculated by the time interval of the 0.5 and 0.1 area quantile. If the peak's rise time

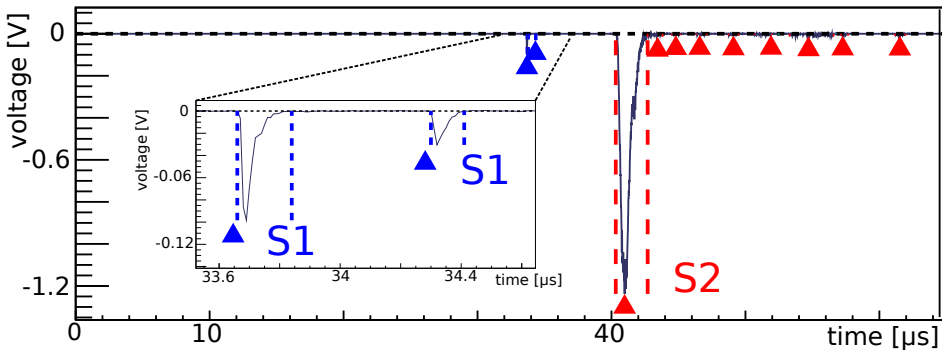

Figure 5.7: Summed waveform of a ^{83m}Kr decay inside the active volume, recorded by both PMTs. Whereas the S1 signals can be separated, the corresponding broader S2 signals cannot be resolved in this example waveform. The small S2s after the main S2 signal presumably arise from single electrons.

is $< 200\,\mathrm{ns}$ it is classified as an S1 and in case of a rise time of $< 500\,\mathrm{ns}$ it is defined as an S2. The DAQ system and the data processor are in detail explained in [155].

Fig. 5.7 illustrates the two S1 signals from the energy depositions of $32.1\,\mathrm{keV}$ and $9.1\,\mathrm{keV}$ created by the ^{83m}Kr decay. Whereas the S1 signals are separable, the corresponding S2 signals are merged, due to their broad width. The S2 signals subsequent to the main S2 signal are presumably generated by single-electron charge signals. They are originating from photoionization of impurities in the LXe and of the metal components inside the TPC [67].

Chapter 6

Xenon Purity Measurements

An essential background contribution in experiments searching for rare-events can be caused by surface contamination. The contamination can originate from ambient radon, because its daughter isotopes can plate-out on the detector surfaces and still be present during the run-time of the experiment. Typically, the largest surface area in a TPC which is exposed to the detection medium is made from PTFE. Therefore, it is most relevant to remove the the radon-daughters from this material. It was shown that chemical treatments on the PTFE surfaces can remove the described contamination at a large part. Testing if the employed chemicals affect the xenon purity and the detector performance motivates the xenon purity measurements described in this work. For this purpose, we used the HeXe set-up, discussed in the previous Chapter 5. Studies on radon removal from PTFE surfaces and the main results of the presented work are published in [II].

In section 6.1, we describe the motivation for the measurements in more detail. Subsequently, in section 6.2, we discuss the general concept of the purity measurements and how the xenon purity is determined. In section 6.3, we describe the purity measurements and in section 6.4 we explain the evaluation of the acquired data. Afterwards, in section 6.5, we interpret the results of the purity measurements and close in section 6.6 with a summary.

6.1 Motivation

In Chapter 3 we introduced and studied the background arising from the disintegration of radon progeny in XENON1T. We divided the background into two categories, depending on the location of the decays within the detector and mainly discussed the radon induced background which spreads within the xenon target. The work in this Chapter is motivated by the second category of radon induced background that originates from the detector surfaces.

Surface background from radon: the noble gas radon essentially emanates from all materials and distributes within the ambient air. Thus, detector surfaces that are exposed to air can get contaminated by radon daughters that plate-out on the surface. Thereby, most important in terms of background are the radon daughters featuring a long half-life and their corresponding decay products because they are still present after detector assembly, and they persist during the entire run-time of the experiment. The most relevant background contribution arises from the decay of the long-lived ^{210}Pb ($T_{1/2} = 22.3\,\mathrm{years}$) in the ^{222}Rn series and its progenies.

Surface background is an essential source of background in XENON1T. On one hand, β-and γ-radiation limits the radial extension of the analysis volume and hence the sensitivity of the experiment in the dark matter search [62]. On the other hand, the ^{222}Rn progeny ^{210}Po can induce (α,n)-reactions on the inner PTFE surface of the TPC. This is especially important, since neutrons have the same event signature as a WIMP signal. However, background from radon daughters plated-out on detector surfaces is not only an important source of background in XENON1T, but in general in many other rare-event searches (e.g. [36,160–162]). To meet the low level background requirements of these experiments, it is important to avoid and reduce the surface contamination from plated-out radon progeny. Another source of surface contamination, which is not the focus in this work, can arise from environmental dust that can also deposit on detector surfaces and emanate radon [163, 164].

Surface background on PTFE surfaces: in this work, we focus on the removal of radon progenies that have plated-out on *PTFE* (Polytetrafluorethylen) surfaces. In liquid xenon detectors, PTFE is mainly used due to its high reflectivity for the VUV scintillation light created by particle interactions inside the xenon target volume [95,165–167] but also other experiments searching for rare-events employ this material close or directly in contact to the detection target [168,169]. PTFE tends to carry a negative charge due to the triboelectric effect [170–172]. On the contrary, radon daughters have a high probability to be positively charged, because some shell electrons may be stripped off from the recoiling atom in the decay processes [106]. Therefore, their plate-out probability onto PTFE surfaces can be orders of magnitude larger than the plate-out rate onto other materials [173].

To achieve the highest cleanliness standards in an experiment, dedicated surface treatments have to be applied to all PTFE components in contact with the detection target, before the detector is assembled. In [II] different cleaning procedures are tested for their ability to remove radon daughters from PTFE surfaces. One of the investigated surface treatments is based on a $32\,\%$ nitric acid (HNO_3) solution, a chemical that is often employed in the cleaning of PTFE components [168]. It leaches the radon daugh-

ters from the PTFE, in contrast to e.g. cleaning procedure applied to metallic surfaces which take off the surface on the micrometer-scale and thus remove the contamination. Depending on the duration of the $32\,\%$ HNO_3 surface treatment, reduction factors > 20 could be achieved for radon daughters removal from the PTFE surface.

In order to apply a cleaning treatment on the inner PTFE surfaces of a TPC, it has to be verified that potential chemical residues do not have a negative impact on the detector performance. Testing this is particularly important, since the main part of the TPC's inner wall is made from PTFE, directly in contact with the adjacent LXe target volume. Examining this potential effect is the goal of the purity measurements described in the following sections. Thereby, we employed the HeXe set-up and tested a surface cleaning recipe based on $32\,\%$ HNO_3. For a detail description of the set-up we refer to Chapter 5.

6.2 Xenon purity

The ability to measure the number of scintillation photons and ionization electrons, created in a particle interaction in LXe, at a minimal loss of quanta, is an essential requirement in detecting particles at low energies in a TPC. Their amount can be reduced by impurities that constantly outgas from the detector material into the xenon. We refer to Chapter 2 and Chapter 5 for a detailed description of the dual-phase TPC detection principle.

Contamination of xenon by impurities: one of the most serious impurity for the xenon scintillation light is water vapor, as its absorption spectrum overlaps largely with the xenon scintillation spectrum [174]. In case of ionization electrons, electro-negative impurities can permanently attach the drifting electrons and thereby reduce their total amount. In [69] the attachment cross-section as a function of applied electric drift field is measured for SF_6, N_2O and O_2. Among these contaminants, O_2 is thought to be the most relevant impurity causing charge loss in LXe detectors as it is present in ambient air. Hence, small traces of O_2 could get absorbed by the the detector's materials during its construction and diffuse into the xenon during the detector operation. Additionally, small air leaks could be present during the run-time of the experiment. To minimize the loss of quanta, the highest possible chemical purity of the xenon target has to be achieved and maintained during the experiment.

Xenon purification: previous detectors such as ZEPLIN-III achieved a sufficiently high xenon purity by employing clean construction techniques with low-outgassing materials [175]. Since the outgassing rate is larger in current and future large-scale LXe detectors, the impurities in the xenon are actively removed. For this purpose, the

xenon is continuously recirculated through a gas purifier during the run time of the experiment. Zirconium is a commonly used getter material in LXe experiments and it is also employed in the gas purifier of the HeXe set-up [51,95]. This material chemically binds basically any non-noble gas species, such as H_2O, O_2, CO, CO_2, N_2, H_2 and CH_4 to its surface [176, 177]. The getter material is heated up to several hundred degrees Celsius, which causes the impurities bonded to the surface to diffuse into the bulk of the material. Thus, the surface is available for additional gettering.

Quantifying the xenon purity: the xenon purity can be quantified by measuring the light and charge yield of particle interactions in the detection medium. Thereby, a water contamination of $\sim 100\,\mathrm{ppb}$ results in a light absorption length of $\mathcal{O}(1\,\mathrm{m})$ [56]. Typically, much smaller water contamination are achieved in LXe detectors, resulting in larger absorption lengths. More realistic is a O_2 equivalent impurity concentration of $\sim 1\,\mathrm{ppb}$, resulting in an attenuation length of $\mathcal{O}(1\,\mathrm{m})$ for ionization electrons [56], which is comparable to the drift lengths in current LXe TPCs. Hence, light absorption by impurities is commonly considered of secondary importance in comparison to the charge reduction due to electron attachment. Therefore, most research on the xenon purity is based on potential charge loss [178–181]. This is one reason, why we quantify the xenon purity with the charge yield in this work. In addition, the HeXe TPC has no liquid level control and the level is adjusted manually, which causes slight variations among different measurements. These variations complicate a light yield study, since the liquid level height also affects the measured light yield, as described below.

In the following, we will explain how the xenon purity is measured based on the charge signal in a TPC. A mono-energetic calibration source is employed to produce energy depositions in the entire LXe volume, as illustrated in Fig. 6.1 by yellow stars. The generated electrons are drifted along the depth of the TPC. In our study, the depth is measured in units of the electron drift time t. This is the time difference between the S1 and S2 signals, which is maximal at the bottom of the TPC. During their drift, the electrons can be trapped by electro-negative impurities diluted in the xenon. The remaining electrons are extracted at the liquid-gas interface of the TPC into the gas gap region and are amplified, causing S2 scintillation light signal. The size of the S2 signal is proportional to the amount of extracted electrons. To quantify the xenon purity, the S2 signal size is measured as a function of electron drift time t, shown in the right panel in Fig. 6.1. If the level of the xenon purity is low, electrons from deeper TPC depth are more prone to being trapped than electrons created at shallow depths. In this case, the measured S2 size decreases towards larger drift times (green line). If the purity level is high, the charge loss is reduced and more electrons generated at large drift times reach the liquid-gas interface and contribute to the S2 signal (blue line). The amount

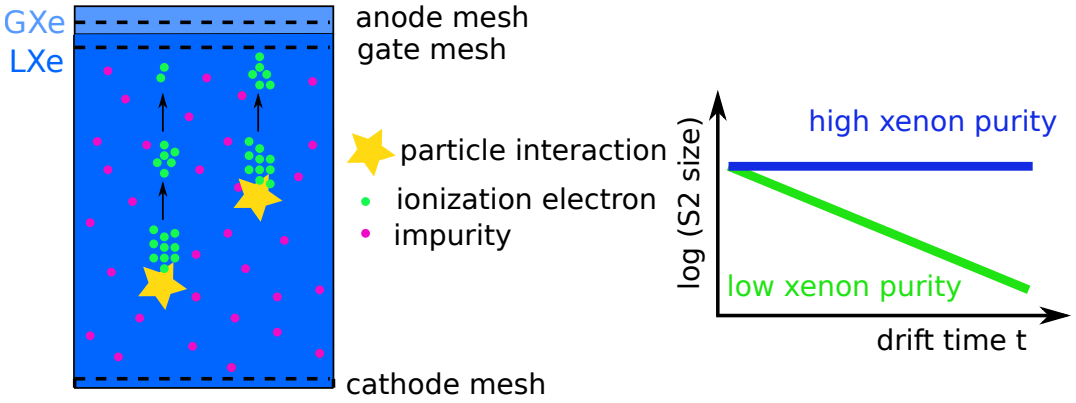

Figure 6.1: Left panel: TPC lateral cut. Particle interactions (yellow stars) in the LXe produce ionization electrons (green dots) that are drifted upwards to the liquid-gas interface by an electric field between the gate and cathode meshes. The electrons are extracted from the LXe by a strong electric field between the gate and the anode meshes and produce the S2 scintillation light signal. During their drift through the LXe volume, the ionization electrons can get attached by electro-negative impurities (pink dots) diluted in the xenon. Particle interactions at large depths are more prone to the described charge loss. Right panel: Parameter space of interest in purity measurements that shows the logarithm of the measured S2 signal size as function of electron drift time t (depth) in the TPC. Depending on the xenon purity, more electrons created at large drift times can be extracted.

of ionization electrons per drift time is defined as

$$N_e(t) = N_e(0) \cdot e^{-t/\tau} \tag{6.2.1}$$

whereby $N_e(0)$ is the initial amount of ionization electrons created by a mono-energetic energy deposition and τ is the decay constant, termed electron lifetime. The S2 signal size distribution as function of drift time is called electron lifetime band in the following. It is fitted with the function of Eq. 6.2.1 to extract the electron lifetime, which quantifies the xenon purity level. The higher the value of τ , the higher is the xenon purity.

The electron lifetime τ can be translated into an impurity concentration with following relation [56]:

$$\tau = \frac{1}{N_S \cdot k_S} \tag{6.2.2}$$

where N_S is the impurity concentration of an impurity S measured in mol(S)/liter(Xe). The parameter k_S describes the impurity and field dependent electron attachment rate in units of liter(Xe)/mol(S)/s. In Fig. 6.2 the electron attachment rate is shown for different impurities as a function of the applied drift field. The red dashed line indicates the drift field $E_{purity} = (394 \pm 5)\,V/cm$ during the purity measurements. Since the exact composition of impurities in a LXe experiment is usually unknown, one typically

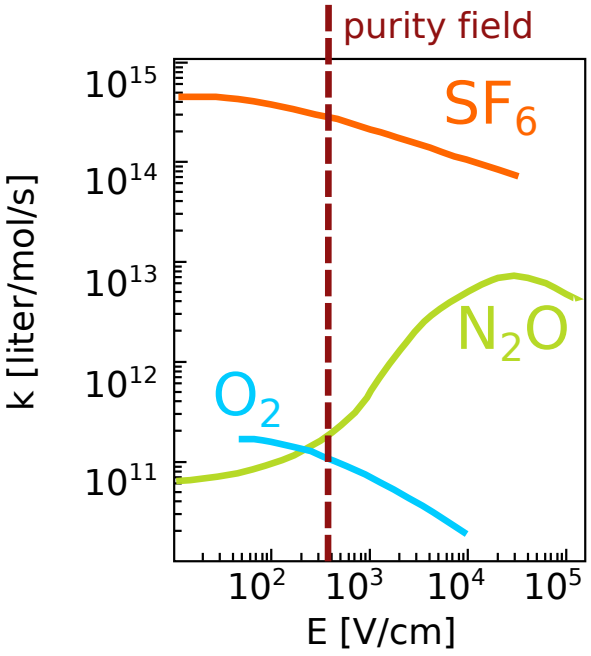

Figure 6.2: Electron attachment rate k of SF_6, N_2O and O_2 as function of applied drift field in LXe. The red dashed line indicates the drift field applied throughout the purity measurements. The impurity amount in the xenon is expressed in an O_2 equivalent concentration, as this impurity is most relevant for LXe TPC among the shown impurities, as detailed in the text. Figure adapted from [69]. Due to its comparably high cross-section for electron attachment, SF_6 is often used as insulation gas [182] and it is typically not present in LXe detectors.

expresses the measured electron lifetime in an O_2 equivalent concentration in units of ppb as

$$N_{O_2}(\text{ppb}) = \frac{V_{\text{Mol(Xe)}}}{\tau(\mu s) \cdot k_{O_2}} \tag{6.2.3}$$

where $V_{\text{Mol(Xe)}}$ is the molar volume of LXe with $V_{\text{Mol(Xe)}} = 0.046\,\text{liter/mol}$. The O_2 electron attachment rate at E_{purity} is $k_{O_2} = 1.08 \cdot 10^5\,\text{liter/mol/}\mu\text{s}$. Hence, we obtain a transformation factor of

$$N_{O_2}(\text{ppb}) = \frac{426(\text{ppb}/\mu s)}{\tau(\mu s)} \quad . \tag{6.2.4}$$

The transformation of the measured electron lifetime into an O_2 equivalent concentration allows for a field-independent comparison of the xenon purity among different LXe TPCs.

Concept of purity measurements: in our study, we want to test if the $32\,\%$ HNO_3 surface treatment degrades the xenon purity under application-oriented conditions. Therefore, we apply it to the PTFE surface of the HeXe TPC's active volume that is directly exposed to the LXe. Thus, potential outgassing of the cleaning agent into the cold medium can be examined. The active volume is confined by an exchangeable PTFE cylinder. In each purity measurement, the surface treatment is applied to a new duplicate of this sample cylinder, which is then inserted into the TPC (see Chapter 5 for a detailed description of the TPC and the set-tp). During a purity measurement, the xenon is continuously purified by a gas purifier and the electron lifetime parameter is determined over the run time of a measurement. We compare the electron lifetime

evolution of PTFE samples treated with a basic soap cleaning and the ones treated additionally with $32\,\%$ HNO_3, as the surface treatment could slow down the xenon purification process or even reduce the maximal achievable level of xenon purity. Additionally, we stop the xenon purification after several measurement days to monitor the resulting degradation of the xenon purity.

6.3 Sample preparation and measurements

date	sample item	surface treatment
Jun 17 - Jul 8, 2019	T1	ELMA CLEAN 65 + $32\,\%$ HNO_3
Jul 8 - Jul 29, 2019	B1	ELMA CLEAN 65
Sep 23 - Oct 14, 2019	B2	ELMA CLEAN 65
Oct 21 - Nov 11, 2019	B3	ELMA CLEAN 65
Nov 11 - Dec 2, 2019	T2	ELMA CLEAN 65 + $32\,\%$ HNO_3
Dec 2 - Dec 23, 2019	T3	ELMA CLEAN 65 + $32\,\%$ HNO_3

Table 6.1: List of purity measurements ordered by date. A blank sample (indicated with "B") is cleaned with the neutral soap ELMA CLEAN 65 and a test sample (indicated with "T") is treated with ELMA CLEAN 65 and $32\,\%$ HNO_3.

Sample preparation: the confining surface of the HeXe TPC's active volume consists of a PTFE cylinder with a height and diameter of $\sim 5\,\mathrm{cm}$. The cylinder can be exchanged and copies of it serve as samples in the different purity measurements. After the fabrication process, the PTFE cylinders are contaminated with residuals of water and oil. Since these contaminants caused an unacceptable low xenon purity in first measurements, all cylinders undergo a basic cleaning step with the neutral detergent ELMA CLEAN 65 [183]. In our study, we compare the time evolution of the electron lifetime of these so-called blank samples with the one of test samples. Thereby, a test sample is cleaned with ELMA CLEAN 65 and subsequently with $32\,\%$ HNO_3 in addition. In Table 6.1 we list the samples according to the date of measurement, whereby the item "B" indicates blank samples, and "T" test samples. In the following, we describe the sample preparation in more detail:

- blank/test sample: $15\,\mathrm{min}$ in ultrasonic bath filled with deionized-water (DI-water) and $3\,\%$ of ELMA CLEAN 65 at $40°\mathrm{C}$
- blank/test sample: rinsing with fresh DI-water three times for $3\,\mathrm{min}$ each
- test sample: submerge sample for $2\,\mathrm{hours}$ in $32\,\%$ HNO_3 (same duration as applied in [II])
- test sample: rinsing with fresh DI-water three times for $3\,\mathrm{min}$ each

After the cleaning procedure, the blank/test sample is dried with N_2 to clear away liquid residues. To remove moisture from the bulk of the sample, it is additionally dried. For this purpose, it is placed in a gas tight stainless steel vessel which is flushed for $\sim 3\,\mathrm{days}$ with a N_2 flow of $200\,\mathrm{SCCM}$ at an absolute pressure of $50\,\mathrm{mbara}$. After this drying step, the sample is always kept under a N_2 atmosphere to avoid a contamination from gaseous impurities present in ambient air.

Measurement cycle: in total we measured three blank and three test samples, whereby a complete measurement cycle per sample takes three weeks and the corresponding run period of data taking $\sim 16\,\mathrm{days}$. The measurement cycle includes several steps per sample and it is performed according to a strict time schedule, described below. In Fig. 6.3 we show the duration of the described steps per measurement. No correlation between the results of the purity measurements and the slight deviations in the described steps has been observed.

Sample insertion in TPC: the insertion of either a blank or test sample requires to partly disassemble the HeXe TPC. Therefore, the TPC has to be dismounted from the system and be placed on a working table. To avoid a contamination from ambient air, the TPC is always kept under a N_2 atmosphere during this operation. This is realized by using a glove bag made from a plastic foil which is fixed to the system and constantly flushed with N_2 at a slight over pressure. After having inserted the new cylinder inside the TPC, it is mounted back and the cryostat vessel is closed. During this procedure the TPC and the sample is exposed to N_2 for $\sim 7\,\mathrm{hours}$ on average.

Cryostat evacuation: the cryostat is evacuated by pumping it for $20\,\mathrm{hours}$ to a final pressure at $\mathcal{O}(10^{-4}\mathrm{mbar})$. The subsequent steps in the measurement cycle are always performed after the same time interval with respect to the pumping start time.

Pre-cooling: GXe is filled inside the gas system and the cryostat at $2\,\mathrm{bara}$. This gas is pre-cooled for $19\,\mathrm{hours}$ by setting the cold head's temperature to $-107.5\,°\mathrm{C}$. This is done to enhance the liquefaction speed of the additional GXe, that is filled after the pre-cooling. During the pre-cooling, the xenon is looped through the gas purifier to remove outgassing impurities from the gas and the set-up.

Liquid xenon filling and run start: in this step, the gas recirculation is stopped and additional GXe is filled into the cryostat and liquefied [1]. The filling is monitored by the level meter sensors and stopped when the correct liquid level for dual-phase operation is reached. The start of the measurement run and data taking is

[1] Even though gaseous xenon is filled in the cryostat, we call this step "liquid filling", due to the fast liquefaction of the gas at the cryostat's cold head.

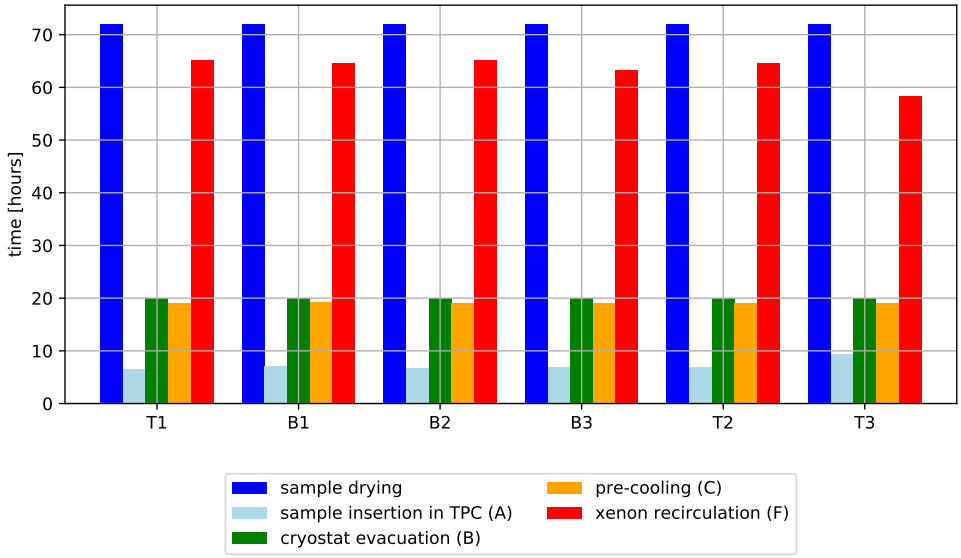

Figure 6.3: Duration of single steps in a measurement cycle per investigated sample, whereby the item "B" indicates blank samples (cleaned with the detergent ELMA CLEAN 65), and "T" test samples (cleaned with detergent and subsequently with 32 % HNO_3). The single steps follow a strict time schedule to establish consistent conditions throughout the measurements. As it exceeds the duration of the other steps by far, we do not show the xenon purification step D of the procedure, for visual purpose. The largest deviation of this step arises from the intentional reduction of the xenon purification time during the measurement campaign, as detailed in the text. The duration per step, among different measurements is comparable and we do not observe a correlation of the slight variations and the results of the purity measurements.

defined at the moment of starting the GXe recirculation through the gas purifiers.

Purification stop: the gas purifier is bypassed and the GXe is recirculated through the system without being purified, which causes a decrease of the electron lifetime. In case of the T1 and B1 measurements the xenon purification was stopped after 15 days. Since the electron lifetime plateaus already before 14 days, the xenon purification time was shortened by one day after the T1 and B1 measurements, to increase the data taking period during of the electron lifetime decrease. Hence, the the remaining measurements of B2, B3, T2 and T3 have a reduced xenon purification time of 14 days. This step (D) is not shown in Fig. 6.3 for visual purpose. The largest time deviation for this step arises from the described purification time reduction.

Run stop and xenon recirculation: the run is terminated after $\sim$ 16 days. The gas recirculation is stopped and the xenon is recuperated into the storage bottle. An amount of 1 bara GXe is left in the system and recirculated for 3 days to enhance the warming-up speed of the TPC. When the sample cylinder is exchanged for

the next measurement cycle, the TPC has to be at room temperature to avoid gaseous contaminants from being frozen inside its PTFE structure.

Detector stability during measurements: in Fig. 6.4 we present the most relevant detector parameters during the run period of each purity measurement. Thereby, the pressure in the cryostat and the temperature of the LXe are stable within $3\,\%$ throughout each measurement. The largest flow variation is $5\,\%$ in the measurement of sample B3. Between the measurements, the largest relative deviations are $(8.7 \pm 0.3)\,\%$, $(1.8 \pm 0.1)\,\%$ and $(9 \pm 6)\,\%$ for the average values of the cryostat pressure, the LXe temperature and the xenon flow rate, respectively.

The variations of the detector parameters between different purity measurements depend on the initial conditions of a measurement and the dynamics of the complex thermodynamical system during the run period. One aspect is the total LXe mass employed during a purity measurement, that varies between $\sim 2.2\,\mathrm{kg}$ and $\sim 2.6\,\mathrm{kg}$ during the measurement campaign. The distance of the suspended TPC from the bottom of the cryostat changes slightly between the different measurements, since the TPC has to be dismounted for each sample exchange. This distance determines the size of the volume below the TPC that is filled with LXe, whereby a $1\,\mathrm{mm}$ larger distance corresponds to $\sim 100\,\mathrm{g}$ more LXe. The total LXe mass inside the HeXe system influences the e.g. pressure in the cryostat, which consequently also slightly changes among the measurements.

A further aspect is the xenon recirculation flow during the run period. As shown in Fig.6.4 it is set at an almost identical flow rate at the start of a run and then it slightly evolves over time. No flow controller was installed in the system, that would keep the flow rate at a constant level. These devices bear the risk to close in case of failure, which could lead to an increase of pressure in the system and its damage. For this reason, a flow meter is installed that measures the flow rate. The initial flow rate is adjusted manually at a valve in the gas system, as explained in Chapter 5, at the start of a run. Since the recirculation flow rate impacts the thermodynamical stability of the system, we did not readjust it during a measurement in case of a stable flow. In the B3 measurement the flow increase could have lead to an unstable system and was readjusted. The increase of the flow fluctuations after $\sim 14\,\mathrm{days}$ can be explained by the reduced resistance of the system when the gas purifier is bypassed and the xenon purification is stopped.

No correlation between the detector parameters and the results of the purity measurements is observed, as detailed in section 6.5.2. The large complexity of the system does not allow for a more accurate alignment of the detector parameters throughout

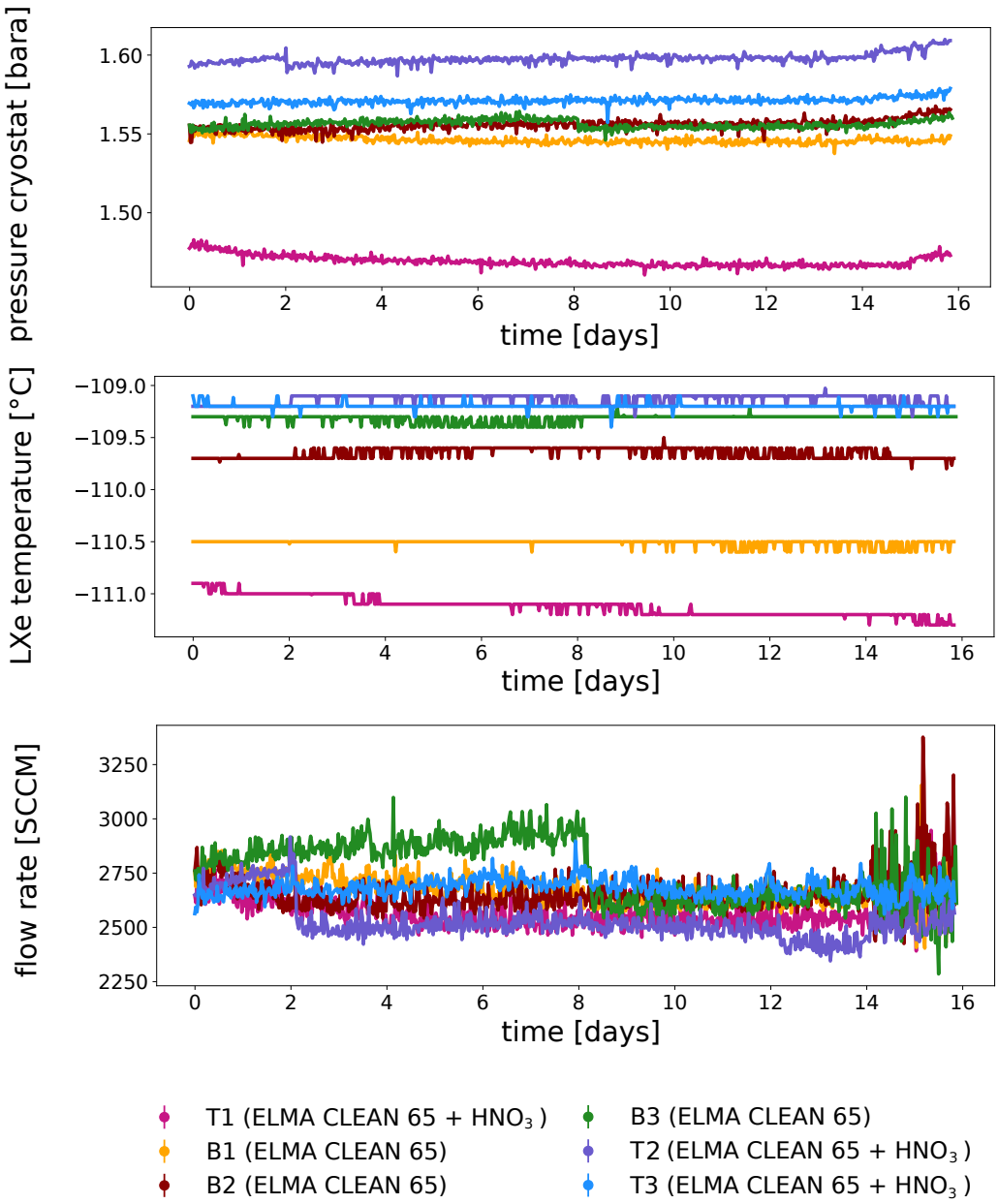

Figure 6.4: Time evolution of the cryostat pressure, LXe temperature and flow rate per measurement. The largest variation within the evolution of one parameter ($5\,\%$) arises in the flow rate of the B3 measurement. Since the flow might have led to an unstable system, it was readjusted after $\sim 8\,\mathrm{days}$. All measurements show an increase of the flow fluctuations in the last few days of a measurement that can be explained by the reduced resistance of the system when the gas purifier is bypassed and the xenon purification is stopped. No correlation between the detector parameters and the results of the purity measurements is observed, as detailed in section 6.5.2.

the measurements in the current set-up. However, most important for the purity measurements is a stable detector system, which could be achieved in all measurements.

6.4 Electron lifetime evolution

In the following, we will focus on the determination of the electron lifetime evolution. In a first step, we apply several data selection cuts as described in section 6.4.1. In a second step, the electron lifetime is calculated, as described in section 6.4.2.

6.4.1 Data selection

The electron lifetime is measured by employing a ^{83m}Kr calibration source at an initial rate of $\sim 100\,\mathrm{Hz}$ inside the liquid xenon target [184]. The mother nuclei of ^{83m}Kr, ^{83}Rb is absorbed in zeolite beads which are contained in a source box installed in the gas system of the HeXe set-up. ^{83}Rb decays with a half-life of $86.2\,\mathrm{days}$ via pure electron capture to any of the numerous excited states of Kr. Independent on the initial excited state of Kr, the nucleus rapidly de-excites to the isomeric state of ^{83m}Kr at $41.5\,\mathrm{keV}$ above the ground state. This state has a half-life of $1.83\,\mathrm{hours}$. The Kr atoms emanate from the beads and are transported inside the TPC by flushing GXe through the source box. Since krypton is a noble gas as xenon, Kr distributes uniformly within the active volume of the TPC. As shown in Fig.6.5, ^{83m}Kr disintegrates in two steps to the ground state, whereby mainly internal conversion electrons are emitted. Due to the short half-life of $154\,\mathrm{ns}$ of the first excited state, the two energy depositions at $32.1\,\mathrm{keV}$ and $9.4\,\mathrm{keV}$ appear coincidently within the same recorded event window. This signature allows for a basically background-free ^{83m}Kr identification in the data analysis.
In the following, we will introduce a S1 light collection efficiency (LCE) correction and the data selection cuts that are applied to identify ^{83m}Kr events and to subsequently calculate the electron lifetime. Thereby, acceptance losses are secondary, because or main requirement is to select a ^{83m}Kr sample with a negligible amount of background events and with sufficient statistics.

Basic Cuts: on the right panel in Fig.6.5, a sketch of a typical ^{83m}Kr event waveform is illustrated. In our ^{83m}Kr selection, we require that at least two S1 signals must be present in the waveform. Thereby, the largest S1, denoted as S1[0] has to occur before the second largest S1, termed S1[1], based on the time ordering of the $32.1\,\mathrm{keV}$ and $9.4\,\mathrm{keV}$ transition lines. The maximal tolerated time difference between these two S1 signals is $300\,\mathrm{ns}$, which includes the main fraction of ^{83m}Kr decays. The width of an S1 signal is at $\mathcal{O}(\mathrm{ns})$ due to the rapid decay of the LXe eximers generating the S1 signal [2] (see section 2.2). In contrast, the width of a

[2] The pulse shape of S1 scintillation light was measured in the HeXe set-up for different calibration sources, as detail in [155]

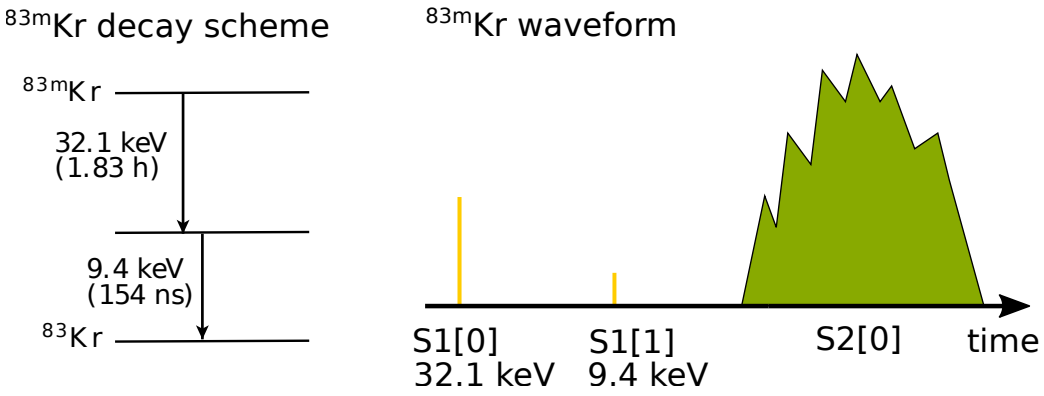

Figure 6.5: Left panel: simplified decay scheme of ^{83m}Kr, which is used as calibration source in the HeXe TPC to measure the electron lifetime parameter. ^{83m}Kr decays via a coincident $32.1\,\mathrm{keV}$ and $9.4\,\mathrm{keV}$ transition. Most of the times, these energy depositions are recorded within the same event window of the HeXe DAQ and the data analysis uses the coincident signature for the selection of ^{83m}Kr events. Right panel: sketch of typical ^{83m}Kr waveform in one event window. Whereas the two S1 signals can be separated in most cases by the data processor, a large part of the corresponding S2 signals is merged due to their comparable large width.

S2 signal is rather broad at $\mathcal{O}(\mu\mathrm{s})$. S2s consist of several single electron signals generated close together. Several parameters influence the S2 width, such as the electron diffusion on the LXe and the mean free path for electrons to produce photons in xenon gas gap of the TPC. Since the S2 width is large in comparison to the time scale of the two ^{83m}Kr transitions, the two S2 signals are typically merged to the largest S2 in the waveform, denoted as S2[0]. Therefore, we require at least one S2 signal within the waveform. Furthermore, we demand that the S1[1] occurs before the S2[0]. All involved signals must be recorded by both PMTs to reduce background events. To minimize potential effects from field leakage on the signal sizes, we will determine the electron lifetime in a subregion of the in total $5\,\mathrm{cm}$ electron drift length. In our data analysis, we will use the electron drift time as measure of the TPC depth, whereby small drift times correspond to the top part of the TPC. We calculate the electron lifetime inside an interval of $[5, 28]\mu\mathrm{s}$, which corresponds to the drift length subregion of $\sim [0.8, 4.7]\,\mathrm{cm}$.

S1 LCE Correction: Fig. 6.6a shows the uncorrected S1[0] signal size as function of electron drift time. The signal size exhibits an increase towards the bottom part of the TPC (larger electron drift times) due to the higher LCE in this region, which can be explained as follows: most of the created scintillation light is reflected at the liquid-gas interface and the photons have to undergo more reflections at the PTFE walls, the further away they are created from the bottom PMT. In this process, signal loss can occur because of the limited reflectivity for xenon scintillation light on PTFE and the light attenuation due to impurities diluted in the

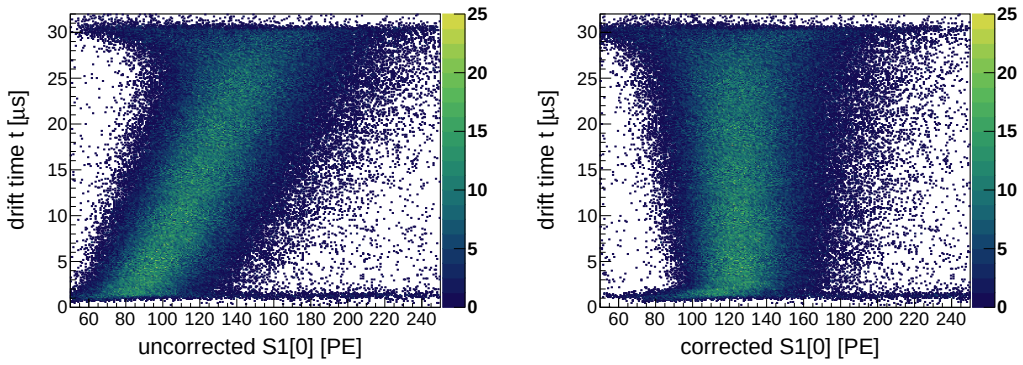

Figure 6.6: (a) Uncorrected light signal S1[0] of the $32.1\,\mathrm{keV}$ energy deposition in the $^{83\mathrm{m}}$Kr decay as function of TPC depth, measured in units of electron drift time t. Thereby, the orientation of the drift time axis is reversed to the orientation of the TPC, meaning that the top TPC part corresponds to small drift times and vice versa. The light collection efficiency and hence the S1[0] size is largest at the bottom of the TPC, as detailed in the text. (b) Corrected S1[0] as function of drift time, after applying the *S1 LCE Correction*.

xenon. Close to the bottom PMT, the light path is shortest and hence the LCE highest. After applying the *Basic Cuts*, we correct the light signal size for this depth dependency. We divide the histogram into $300\,\mathrm{bins}$ along the drift time axis and determine the mean value per histogram bin. The S1 signal size of each event in each bin is shifted by a correction value. Thereby, the correction value is defined as the difference between the mean value in each bin and the reference mean value at the medium drift time. The corrected S1[0] signal size is shown in 6.6b as a function of drift time. Within the drift time range of $[5, 28]\,\mu\mathrm{s}$, the resolution of the projected S1[0] peak changes from $17\,\%$ to $15\,\%$ by applying the *S1 LCE Correction*. The same correction was performed for the second largest S1 signal S1[1], whereby the resolution improved from $23\,\%$ to $20\,\%$. The LCE is marginally affected by the height of the liquid level inside the TPC. The higher the liquid level, the longer is the average path length of the scintillation light, before being detected and the lower is the measured S1 signal size. Since the level changes slightly among different measurements, the *S1 LCE Correction* is determined for each run.

S1 AFT Cut: the S1 area-fraction-top parameter (aft) describes the fraction of light observed by the top PMT in comparison to the total light detected. Hence, it is a measure for the particle interaction depths inside the TPC, whereby large S1 aft values correspond to the top TPC part. The S1 aft is expected to correlate with the drift time, a shown in Fig. 6.7a. To remove spurious events that do not fulfill the correlation, we apply a drift time dependent S1[0] aft cut. Therefore, we

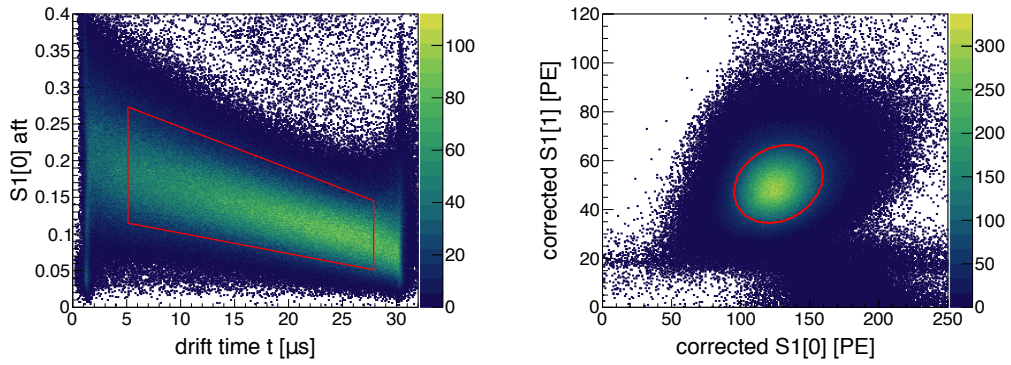

(a) *(b)*

Figure 6.7: (a) Fraction of the S1[0] signal observed by the TPC's top PMT vs. drift time. The further the S1 scintillation light is created from the top PMT, the lower is the measured S1 signal size. The events in the red box are selected by the *S1 AFT Cut*. (b). Distribution of corrected S1[0] and S1[1] signals. The events inside the red ellipse are selected by the *Elliptical S1 Cut*, as they feature the correct ratio of the $32.1\,\mathrm{keV}$ and $9.4\,\mathrm{keV}$ emission of the $^{83\mathrm{m}}$Kr decay.

divide the histogram in Fig. 6.7a into $300\,\mathrm{bins}$ drift time bins. Subsequently, the $5\,\%$ and $95\,\%$ quantile of the S1[0] aft distribution per bin is determined. Linear fits through these upper and lower quantile bounds are performed, respectively. Events beyond the fit functions are rejected in the following.

Elliptical S1 Cut: Fig. 6.7b shows the distribution of the corrected largest and second largest S1 signals in a waveform. Events with a S1[0] $\sim 125\,\mathrm{PE}$ and S1[1] $\sim 50\,\mathrm{PE}$ belong to the $32.1\,\mathrm{keV}$ and $9.4\,\mathrm{keV}$ emission of the $^{83\mathrm{m}}$Kr decay, respectively. The events with the correct S1 size ratio are identified by fitting an elliptical function to the 2D histogram and select events within the $95\,\%$ contour of the ellipse.

We would expect a S1 signal size ratio of $9.4\,\mathrm{keV}/32.1\,\mathrm{keV} \sim 0.3$ from a linear energy dependence. However, we observe a ratio of $\sim 50\,\mathrm{PE}/125\,\mathrm{PE} \sim 0.4$ meaning that more S1[1] scintillation light is created than expected. This can be explained by a dependence of the S1[1] amplitude on the intervening time delay between the two energy emissions, explained in [185]. The authors describe that the $32.1\,\mathrm{keV}$ emission could leave behind a cloud of electron-ion pairs that do not recombine. The ions (electrons) created in the $9.4\,\mathrm{keV}$ emission could recombine with the remaining electrons (ions) of the $32.1\,\mathrm{keV}$, which leads an enhancement of the scintillation photons contributing to the S1[1] signal size.

If the light signals of the $^{83\mathrm{m}}$Kr decay occur close in time, such as the data processor cannot separate them, they are merged as S1[0], which corresponds to the combined energy deposition of $41.5\,\mathrm{keV}$. These merged S1 signals are shown in

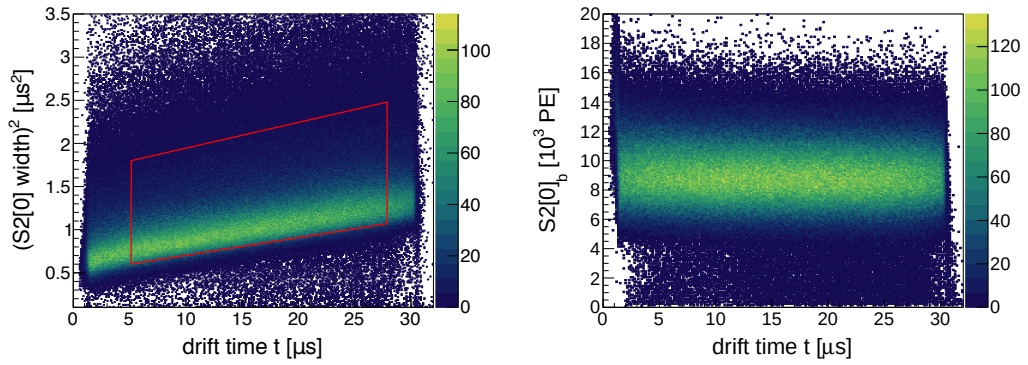

(a) *(b)*

Figure 6.8: (a) The square of the S2[0] width depends linearly on the drift time, as detailed in the text. Events outside the red box are not selected by the *S2 Width Cut*. (b). Electron lifetime band defined as S2 signal size as function of electron drift time, after applying the *Basic Cuts*, the *S1 LCE Correction*, the *S1 AFT Cut*, the *Elliptical S1 Cut* and the *S2 Width Cut*. Events below the band at $S2[0]_b \lesssim 5 \cdot 10^3\,\mathrm{PE}$ bias the electron lifetime determination and are removed as described in the text.

Fig. 6.7b at rather low S1[1] values and at $S1[0] \sim 175\,\mathrm{PE}$. In these cases, the second largest S1 originates from an additional falsely light signal in the waveform.

S2 Width Cut: since the S2-forming electron cloud is affected by longitudinal diffusion (parallel to the electric field) during its drift, the width of the S2 signal depends on the drift time, as shown in Fig. 6.8a. We can use this dependence to reject events with an unusual correlation between these two parameters.

Due to Brownian motion, an initially pointlike source broadens to a normal distribution with standard deviation σ during its drift through the LXe. Thereby, σ depends on the drift time t of the electron cloud, its drift velocity v and the diffusion constant D. Furthermore, one has to account for the width of single electrons σ_0, due to the scintillation of the extracted electron in the gas gap. Hence, we can write for the S2 width [186]

$$\sigma = \sqrt{\frac{2 \cdot D}{v^2} \cdot t + \sigma_0^2} \quad . \tag{6.4.1}$$

In the HeXe TPC, we do not measure the S2 width by the standard deviation σ, but by the interquantile range $\Delta t_{50\%}$ of the S2 signal, whereby $\Delta t_{50\%} \propto \sigma$. The range $\Delta t_{50\%}$ is the time between the moments when 25 % and 75 % of the charge signal has arrived. We square Eq. 6.4.1 and obtain

$$\Delta t_{50\%}^2 \propto c \cdot t + \sigma_0^2 \,, \tag{6.4.2}$$

where the constant c includes the drift velocity v and diffusion constant D. Since we always applied the same drift field, c is identical among the purity measurements.

Eq. 6.4.2 describes a linear relation of the squared S2 width and the drift time t, that we will use in our next selection cut. In Fig. 6.8a the squared width of S2[0] is shown as a function of the drift time. Similar as in the previous cuts, we determine the $5\,\%$ and $95\,\%$ quantiles of the squared S2 width as a function of the drift time and reject events beyond the red contour.

After applying the *S1 LCE Correction* and the described cuts, we show the electron lifetime band in Fig. 6.8b, which we defined as size of the largest S2 signal as a function of drift time. Thereby, we use S2[0]_b, which is the S2 signal size observed with the bottom PMT, due to a reduced S2 saturation and a more spatially homogeneous LCE. For the electron lifetime calculation we need to determine the mean value of the electron lifetime band as a function of drift time. However, due to the population of events leaking towards smaller S2[0]_b values, the electron lifetime fit is significantly biased towards smaller electron lifetime values. In the following, we will define the *S2 Shape Cut* to remove these spurious events.

S2 Shape Cut: we define a characteristic to describe the shape of a S2 signal as

$$\text{S2 shape} = \Delta t_{100\%}/\text{S2 height} \tag{6.4.3}$$

where the full width of a S2 peak $\Delta t_{100\%}$ is divided by its total height. In Fig. 6.9a we show the S2[0] shape parameter as a function of the S2[0]_b area. Besides the main population at $\text{S2[0]}_\text{b} \sim 9 \cdot 10^3$ PE at rather large S2 shape values, we observe an event population leaking towards smaller S2[0]_b values that feature a smaller S2 shape parameter. These low-S2 events have an untypical small S2 total height in comparison to the full width of the S2 peak and they bias the electron lifetime fit. The main fraction presumably arises from events close to the TPC wall, as we will see in the description of the *S2 AFT Cut*. The S2 shape depends on the S2[0]_b area and consequently also on the drift time, as illustrated in Fig. 6.9b. Hence, we define the *S2 Shape Cut* in this parameter space and reject events beyond the $5\,\%$ and $95\,\%$ quantiles along the drift time, as indicated by the red box in Fig. 6.9b. With this cut, we can remove the events below the electron lifetime band in Fig.6.8b.

A further class of spurious events affects the electron lifetime determination. These events are presumably caused by a small geometrical structure within the extraction region of the TPC, as we will explain in the following. Eventually, we will remove these events by a further selection cut, the *S2 AFT Cut*.

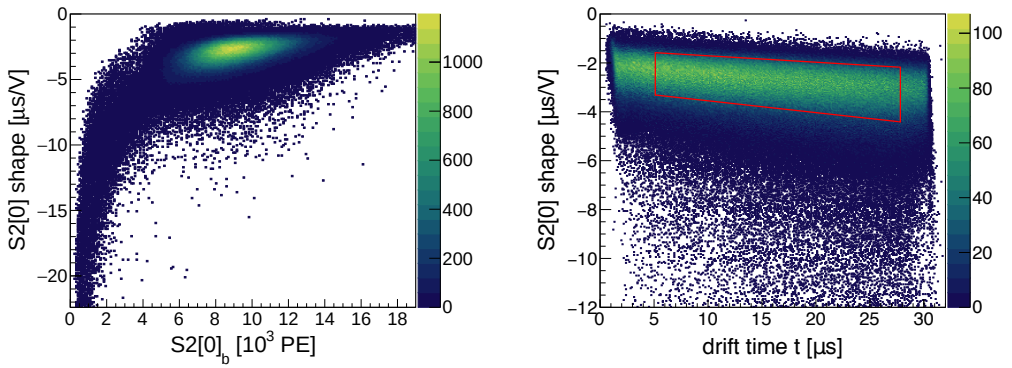

(a) *(b)*

Figure 6.9: (a) The S2 shape is defined as ratio of full S2 width divided by the total S2 height, whereby the signal height is measured as negative voltage. Events with a rather small S2 height feature also an untypical small S2 size and correspond to the leakage below the electron lifetime band in Fig. 6.8b (b). S2 shape as function of drift time. Events inside the red contours are selected by the *S2 Shape Cut*.

Within a TPC, the electrons generated by energy depositions in the xenon are extracted from the LXe into the gas phase and cause S2 scintillation light. As in the case of the S1 scintillation light, we introduce an area fraction top parameter for the S2 scintillation light. It describes the fraction of S2 light observed by the top PMT in comparison to the total light observed by both PMTs. Since the electrons are extracted in a horizontal plane, the S2 aft parameter is typically centered around a mean value. However, in the HeXe TPC we observe an unexpectedly broad S2 aft distribution, as shown in Fig. 6.10a. Thereby, the red histogram presents the distribution before having applied the *S2 Shape Cut* and the black histogram after this cut, which we want to compare further below.

Shadow effect: first, we have a closer look at the electron extraction region in the HeXe TPC, shown in Fig. 6.10b, that should give insight on the origin of the broad S2 aft distribution. The ionization electrons, illustrated in green, are extracted from the LXe into the GXe by the electric field generated between the gate and anode. The amplified electrons cause S2 scintillation light, indicated as yellow stars. Right above the anode, a PTFE edge is not flush-mounted with the PTFE wall. The S2 scintillation light can be reflected by this protruding PTFE surface towards the bottom of the TPC which increases the detected light signal in the bottom PMT. Thus, we assume that the S2 aft parameter is reduced for events close to the TPC wall and below the PTFE edge. Contrawise, we presume that S2 scintillation light created in the center of the liquid-gas interface is less affected by this shadowing effect and features a higher S2 aft. Under this assumption, we assign the peak at an S2 aft of ~ 0.69 in Fig. 6.10a to

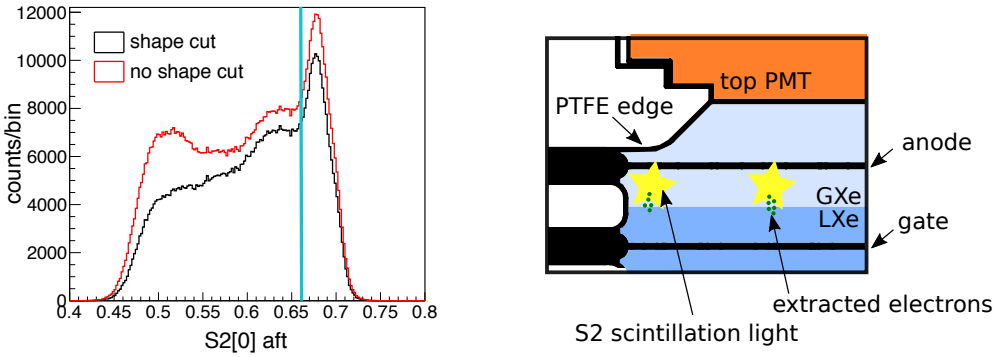

(a) *(b)*

Figure 6.10: (a) S2 area fraction top distribution with an unexpected broad tailing towards small values, supposedly caused by a shadowing effect. The black histogram shows the distribution after the *S2 Shape Cut*, that removes a large fraction of events at low S2 aft values. (b) Electron extraction region in the HeXe TPC. Due to the PTFE edge, the created S2 scintillation light is can be reflected towards the bottom PMT, probably causing the broad S2 aft distribution in (a).

events in the center of the TPC. We refer the broad tailing towards smaller S2 aft values to events closer to the TPC wall. The assumption that a geometrical effect is causing the broad S2 aft distribution is supported by an optical simulation of the HeXe TPC. In this simulation, photon emission was simulated in a horizontal plane at the height of the liquid-gas interface. Thereby, the radial dependency of the fraction of light observed by the top PMT could be reproduced [187].

S2 AFT Cut: since we only want to select events free from the described shadowing effect, we apply a cut on the S2 aft parameter. Therefore, we select events that have a high S2 aft value, above the threshold indicated as blue line in Fig. 6.10a. The threshold is set at the $80\,\%$ percentile of the S2 aft distribution.

Furthermore, we compare the two histograms in Fig. 6.10a. A large fraction of events at a S2 aft of ~ 0.5 are removed by applying the *S2 Shape Cut*. We remember that the removed events feature an unusual small S2 area and an untypical small S2 height in comparison to the total S2 width. This untypical shape could be understood as follows: since a large fraction of events with an untypical shape is presumably created close to the TPC wall, the created S2 scintillation light might be reflected by the PTFE edge and traverses the LXe volume before being detected by the bottom PMT. Thereby, a fraction of the scintillation photons are absorbed by trace impurities in the LXe, which reduces the measured size of the S2 area. Whereas the width of S2 signal is determined by the drift of the electron cloud and therefore unaffected by the described effect, we assume that the height of the S2 signal is reduced due to the lowered S2 area.

In Fig. 6.10a we observe that the main part of events rejected by the *S2 Shape Cut* is also

removed by the *S2 AFT Cut*. Due to this redundancy and the larger rejection power of the *S2 AFT Cut* in comparison to the *S2 Shape Cut*, we will not use the latter for the determination of the electron lifetime evolution. By comparing the electron lifetime evolution without applying the *S2 Shape Cut* with the evolution considering this cut, we show in the next section that the difference is indeed small. However, to account for the small fraction of spurious events that might be additionally removed by the *S2 Shape Cut*, we include the slight difference of electron lifetime evolution into in the uncertainty.

6.4.2 Electron lifetime evolutions

In this section, we describe the fitting procedure to determine the electron lifetime evolution for each of the six purity measurements. First, we apply the *Basic Cuts*, the *S1 LCE Correction*, the *S1 AFT Cut*, the *Elliptical S1 Cut*, the *S2 Width Cut* and the *S2 AFT Cut*, that are introduced in section 6.4. The *S2 Shape Cut* will be used in the calculation of the electron lifetime uncertainty.

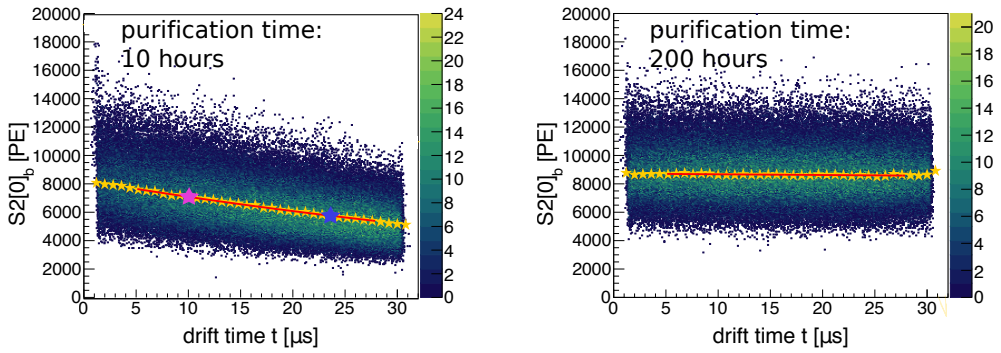

(a) *(b)*

Figure 6.11: Electron lifetime band measured after a xenon purification time of (a) 10 hours and (b) 200 hours. Due to the continuous impurity removal, more electrons from larger drift times contribute to the S2 signal over time. The yellow stars indicate the S2[0]$_b$ mean per drift time slice, that are fit by an exponential function shown as red line. The pink and purple star indicate the drift time slices of the S2[0]$_b$ distributions presented in Fig. 6.12.

Electron lifetime band at different purification times: in Fig. 6.11a and Fig. 6.11b we show the resulting distribution of the S2[0]$_b$ area as function of drift time, which we termed electron lifetime band. It is presented at two different points of xenon purification time. Thereby, Fig. 6.11a illustrates the electron lifetime band after a xenon purification time of 10 hours. Due to electron attachment from impurities, ionization electrons from larger drift times have a higher probability of being trapped than electrons created at shallow depths. This results in the decrease of the S2 size towards

larger drift lengths. While purifying the xenon and removing the electro-negative impurities, more electrons from deeper TPC depths reach the liquid-gas interface and contribute to the S2 signal. This is shown in Fig. 6.11b that depicts the electron lifetime band after $200\,\text{hours}$ of xenon purification. At an infinite xenon purity, basically all generated electrons from a particle interaction would be extracted and contribute to the S2 signal. In this case, the S2 signal size is constant over the drift time. During the xenon purification time, the electron lifetime band is approaching this constant S2 signal size distribution.

Electron lifetime fit: as described in section 6.2, the drift time dependence of the electron lifetime band can be modeled by an exponential decay function, whereby its decay constant is called electron lifetime (see Eq. 6.2.1). The higher the xenon purity, the larger is the value of the electron lifetime. In the following, we use Fig. 6.11a to explain the fitting procedure of the electron lifetime band. First, the histogram is sliced into 40 drift time bins with a bin width of $\Delta t = 0.8\,\mu s$ and the $S2[0]_b$ distribution per Δt interval is determined. We show two of these $S2[0]_b$ distributions as example in Fig. 6.12. They correspond to a drift time interval of $[9.6, 10.4]\,\mu s$ and $[24.0, 24.8]\,\mu s$, respectively, as indicated by a pink and purple star in Fig. 6.11a. To fit the electron lifetime band, the mean value of each of the $S2[0]_b$ distributions has to be determined. Therefore, we test three different fit models.

Gaussian fit: the individual $S2[0]_b$ distributions can be modeled by a Gaussian fit function. The fit is illustrated in green for the two drift time slices in Fig. 6.12 and the fitted mean value μ_G is marked as dashed green line. In most cases, the Gaussian function yields good fit results, especially at high electron lifetime values when the $S2[0]_b$ distributions are most symmetric.

Crystal Ball fit: at lower electron lifetime values, the $S2[0]_b$ distribution feature a slight tailing, that can be modeled by a Crystal Ball function. This function can be used to fit a Gaussian distribution with some tailing that is described by a power law function [188]. The Crystal Ball function is defined as

$$f(S2;\alpha,n,\mu,\sigma) = N \cdot \begin{cases} \exp(-\frac{(S2-\mu)^2}{2\cdot\sigma}) & \text{for } \frac{S2-\mu}{\sigma} > -\alpha \\ A \cdot (B - \frac{S2-\mu}{\sigma})^{-n} & \text{for } \frac{S2-\mu}{\sigma} \leq -\alpha \end{cases} \tag{6.4.4}$$

with

$$A = \left(\frac{n}{|\alpha|}\right)^n \cdot \exp\left(-\frac{|\alpha|^2}{2}\right) \quad \text{and} \quad B = \frac{n}{|\alpha|} \cdot -|\alpha|.$$

Thereby, μ describes the mean and σ the standard variation of the Gaussian part of the function. The parameter N is a normalization factor, α determines the transition point between the part modeled with the Gaussian function and the power

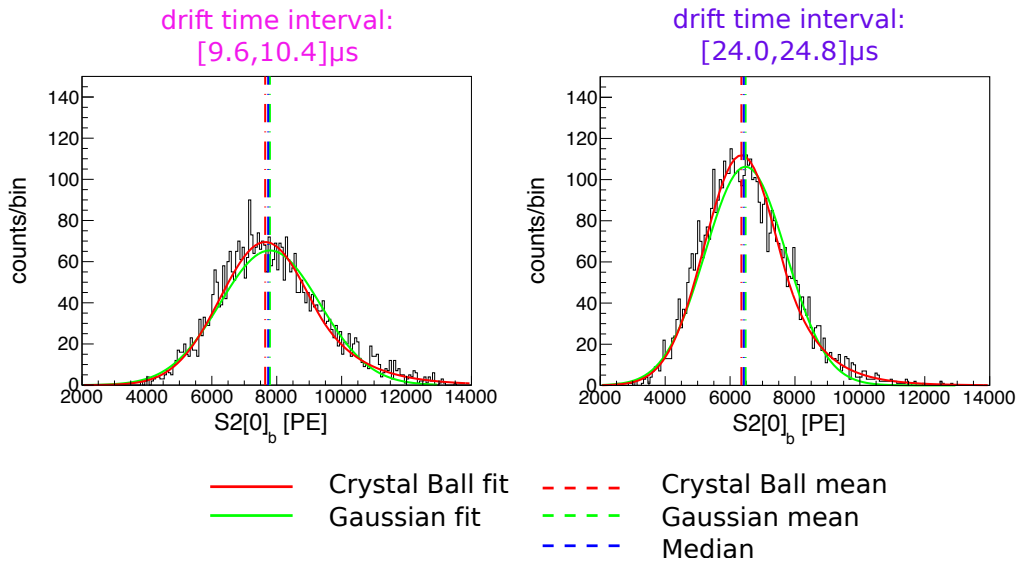

Figure 6.12: $S2[0]_b$ distributions of drift time slices as indicated in Fig. 6.11a by a pink and purple star. The mean distributions of the distribution is determined by three different method, presented as dashed lines.

law of order n. The Crystal Ball fit is indicated as red line in Fig. 6.12 and the position of the calculated mean μ_C as dashed red line.

Median: furthermore, we determine the mean value by calculating the median of the $S2[0]_b$ histogram. The median is the $S2[0]_b$ value, at which the integral of the distribution is equally separated. The median M is shown as blue dashed line in Fig. 6.12.

As depicted in Fig. 6.12, the fitted mean values μ_G and μ_C, as well as the median M are almost identical, independent on the drift time interval. We will use the Crystal Ball function for the evaluation of the electron lifetime to account for the small deviations of the $S2[0]_b$ distribution from a Gaussian function. The corresponding μ_C positions per drift time slice are marked as yellow stars in Fig. 6.11a and Fig. 6.11b. The fitted μ_G and M values are used for the estimation of the electron lifetime uncertainty, as described below.

Electron lifetime evolutions: the μ_C as function of drift time interval are fit with an exponential function, introduced in Eq. 6.2.1, and the electron lifetime value is extracted. The evolution of the electron lifetime is determined by dividing the run time into 6 hours-bins and repeat the described fitting procedure per bin. This is done for each of the six purity measurements. The resulting electron lifetime evolution are shown in Fig. 6.13 and we make the following observations:

- during the period of xenon purification, the electron lifetime is increasing until it reaches a plateau value. It is thought that in this plateau region the outgassing

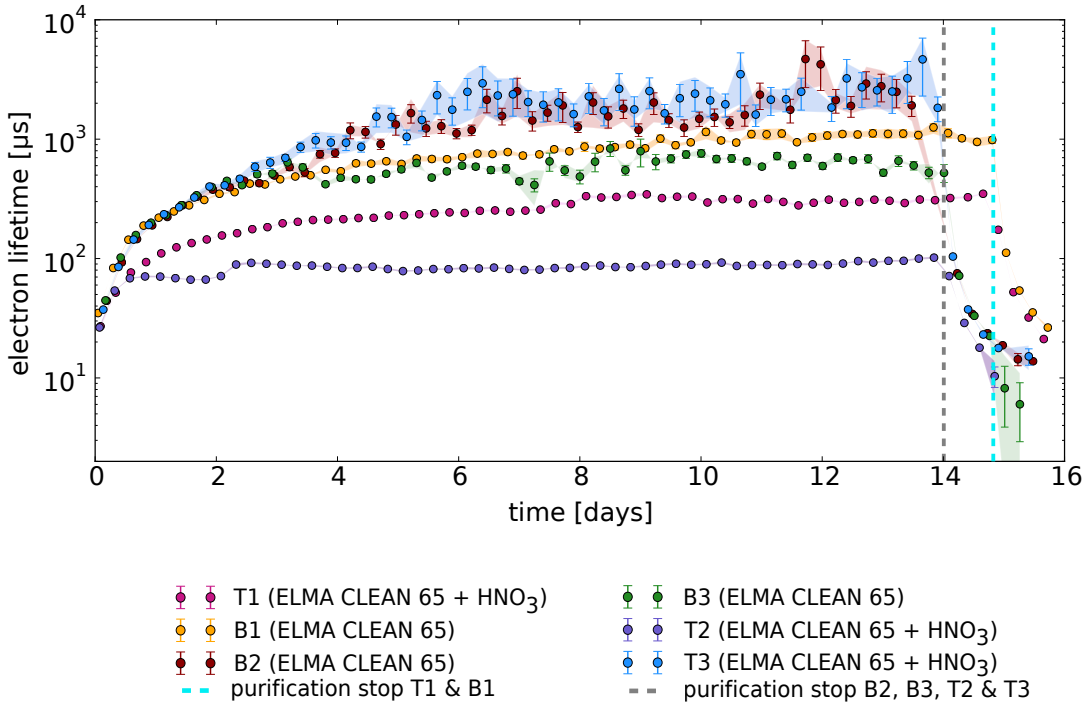

Figure 6.13: Electron lifetime evolutions of purity measurements. The error bars indicate the uncertainty from the electron lifetime fit, whereas the shaded area corresponds to the uncertainty based on the average relative deviation between different analysis methods. The electron lifetime is increasing due to the continuous xenon purification until it reaches a plateau region. It is assumed that in the plateau region, the impurity removal rate and the impurity outgassing rate are equivalent. The dashed lines present the xenon purification stop which causes the decrease of the electron lifetime.

rate of the HeXe system (including the PTFE surface treatment) is equivalent to the xenon purification rate. This observation will be used to determine the outgassing rate of the system in section 6.5.

- the measurement of sample B2 and T3 show an almost identical electron lifetime evolution that plateaus at a comparable electron lifetime value. In contrast, the remaining measurements of the samples T1, B1, B3 and T2 feature different evolutions and lower electron lifetime plateaus, which is presumably caused by systematic effects of the HeXe system. Therefore, we will discuss the B2 and T3 separately from the remaining measurements, in section 6.5.1 and 6.5.2, respectively.

- after some period, the xenon purification is stopped, indicated by dashed vertical lines in Fig. 6.13. As soon as the xenon is not purified anymore, the overall purity decreases resulting in an electron lifetime decrease. In case of sample T1 and B1, the xenon purification was stopped after 15 days. In the subsequent measurements, this period was shortened to 14 days, to increase the data taking time

of the electron lifetime decrease. In section 6.5.3, we discuss the period without xenon purification in more detail.

- the electron lifetime at the start of a measurement is slightly larger than the final electron lifetime without xenon purification. This could be explained by the pre-cleaning steps applied to the system, before each data taking run. The pumping and xenon purification during the pre-cooling, described in section 6.3, removes already outgassing impurities which impacts the initial purity level of the system, that is the same among the measurements.

- the error bars in Fig. 6.13 show the uncertainty of the electron lifetime based on the exponential fit of the electron lifetime band. With increasing xenon purity, the electron lifetime band approaches a constant distribution over the full depth of the TPC. If the constant distribution is reached within the sensitivity of the set-up, the electron lifetime parameter diverges to infinity. Therefore, the error bars and fluctuations become larger with increasing electron lifetime values, which also indicates that the sensitivity of the set-up is reached.

In addition to the the uncertainty of the electron lifetime based on the exponential fit, we include two more uncertainties due to different applied analysis methods, as described in the following, indicated by shaded area in Fig. 6.13.

Uncertainty from analysis methods: the first uncertainty is based on the different fit methods of the $S2[0]_b$ distribution per drift time slice, shown in Fig. 6.12. As discussed, the exponential fit is performed through the mean values μ_C of the $S2[0]_b$ distribution per drift time slice. Thereby, μ_C is determined by a Crystal Ball fit. We call the electron lifetime value obtained by this method τ_C. In addition, we introduced a Gaussian fit to obtain the mean value μ_G and the calculation of the median M. The electron lifetime value based on μ_G and M are denoted as τ_G and τ_M, respectively. For the estimation of the electron lifetime uncertainty based on the fit method we determine the relative deviations

$$d_{CG} = \frac{(\tau_G - \tau_C)}{\tau_C} \quad \text{and} \quad d_{CM} = \frac{(\tau_M - \tau_C)}{\tau_C} \quad . \tag{6.4.5}$$

The second uncertainty arises from the *S2 Shape Cut*, introduced in section 6.4.1. It is applied to remove events that have an untypical S2 shape. Since the main part of these events is also removed by the *S2 AFT Cut*, we did not include the *S2 Shape Cut* in the electron lifetime calculation. Fig. 6.14 shows for the T3 sample in green the electron lifetime $\tau_{ShapeCut}$ including the *S2 Shape Cut* and in red the electron lifetime $\tau_{NoShapeCut}$ excluding the *S2 Shape Cut*. Both evolution agree within their uncertainty of the fit. We include the small difference between the two cut selections in the overall electron

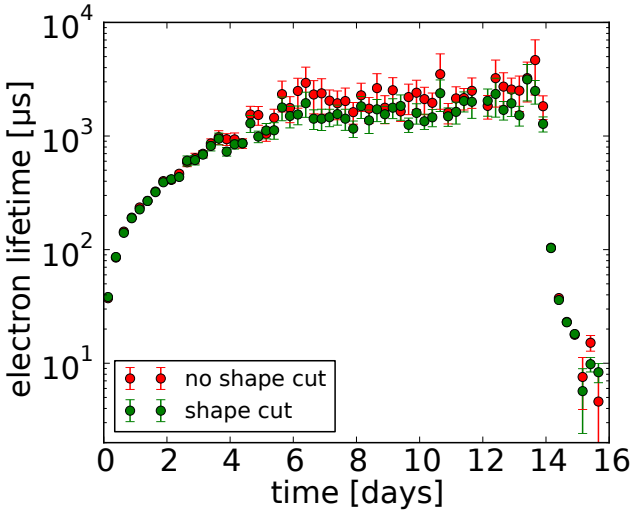

Figure 6.14: Electron lifetime evolution of T3. In red, no *S2 Shape Cut* is included, in green this cut is applied. The two evolutions agree within their uncertainties. We include the slight deviation into the overall uncertainty of the electron lifetime, as described in the text.

lifetime uncertainty. Therefore, we calculate the relative deviation

$$d_{\text{ShapeCut}} = \frac{(\tau_{\text{ShapeCut}} - \tau_{\text{NoShapeCut}})}{\tau_{\text{NoShapeCut}}} \quad . \tag{6.4.6}$$

For the uncertainty estimation due to the different analysis methods, we calculate the combined relative deviation as

$$\overline{d} = \frac{(|d_{CG}| + |d_{CM}| + |d_{\text{ShapeCut}}|)}{3} \quad , \tag{6.4.7}$$

which is multiplied with the respective electron lifetime value τ_C. The uncertainty from the analysis method is illustrated as shaded area in Fig. 6.13 and has a similar value as the uncertainty from the electron lifetime fit. Except of the B2 and T3 measurement, the electron lifetime evolution do not agree within the described uncertainties, supposedly due to a systematic effect of the system which will be further discussed in section 6.5.2.

6.5 Interpretation of results

Two measurements, the one of sample B2 and T3, show a comparable electron lifetime evolution that plateaus at $\sim$ 1700 µs, as presented in Fig. 6.13. We will discuss these two measurements in section 6.5.1. In contrast to the remaining measurement, it is thought that the B2 and T3 measurements are not affected by the mentioned systematic effects of the HeXe set-up. The remaining measurements reach lower electron lifetime plateaus that are inconsistent among each other. These measurements are described separately in section 6.5.2. In the next section 6.5.3, we discuss the electron lifetime decrease in more detail.

6.5.1 B2 and T3 measurement

In this section, we want to discuss the comparable measurements of the blank sample B2 and test sample T3. The measurements exhibit rather large electron lifetime uncertainties and fluctuations in the electron lifetime plateau region. We consider this is an indication that the sensitivity of the system is reached. For this reason, we want to quantify a maximal measurable electron lifetime of the system based on the B2 and T3 measurements. This is then translated into a minimal measurable impurity concentration and a minimal measurable outgassing rate, the base outgassing rate, of the system, as described below. At the end of this section, we interpret the obtained results.

Maximal lifetime in HeXe system: in section 6.4.2, we introduced the combined relative deviation $\overline{d}$ to describe the uncertainty of different analysis methods used in the electron lifetime calculation. We use $\overline{d}$ to define a maximal electron lifetime τ_{max} that is measurable in the HeXe TPC. In Fig. 6.15a and Fig. 6.15b, $\overline{d}$ is shown as a function of the electron lifetime for the measurement B2 and T3, respectively. We fit the distribution with a linear function shown in red. We specify τ_{max} at when the uncertainty of different analysis methods starts being larger than $\overline{d} = 15\,\%$, indicated by an orange line. Thus, we obtain a $\tau_{B2} \sim 1300\,\mu s$ and $\tau_{T3} \sim 1000\,\mu s$ for the B2 and T3 measurement, respectively. We conservatively define the maximal measurable electron lifetime of the HeXe set-up at $\tau_{max} = 1000\,\mu s$. As described in section 6.2, the measured electron lifetime values depend on the drift field applied across the sensitive volume of the HeXe TPC. This can be explained by the drift field dependent attachment rate of ionization electrons to electro-negative impurities. Hence, $\tau_{max} = 1000\,\mu s$ corresponds to the maximal measurable electron lifetime at the given drift field during the purity measurements of $E_{purity} = (394 \pm 5)\,V/cm$.

Minimal impurity concentration in HeXe system: as described in section 6.2, the measured electron lifetime corresponds to an impurity concentration in the xenon volume (see Eq. 6.2.4). Thereby, the impurity concentration is typically expressed in an O_2 equivalent concentration and we transform τ_{max} into a minimal measurable impurity concentration of $N_{min} = 0.43\,ppb\,O_2$ equivalent. Note that, in contrast to the measured electron lifetime, the corresponding impurity concentration is drift field independent. Since the electron lifetime and the impurity concentration are anti-correlated, electron lifetime values smaller than τ_{max} correspond to impurity concentrations larger than the impurity concentration N_{min}.

The electron lifetime evolutions of all samples plateau after several days of xenon purification, as shown in Fig.6.13. We consider this as indication that the xenon purification rate and impurity outgassing rate of the system are equivalent. This allows us to

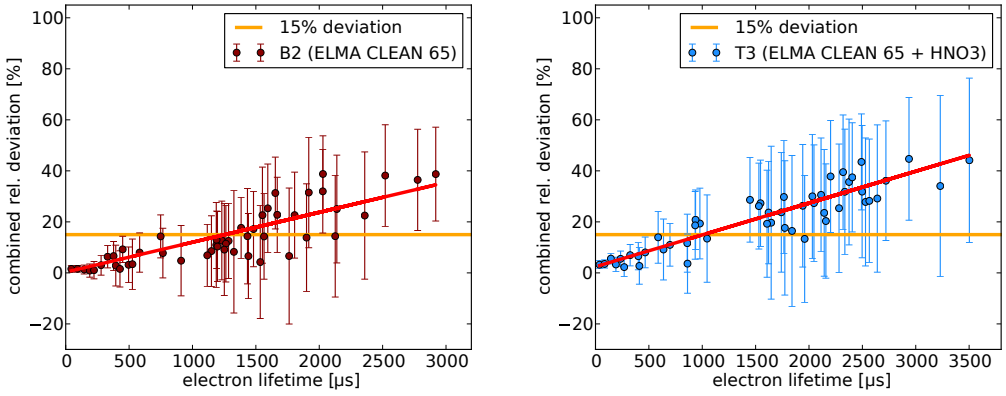

(a) *(b)*

Figure 6.15: Combined relative deviation $\overline{d}$ as function of electron lifetime for (a) the B2 and (b) the T3 measurement. The red line presents a linear fit to the data. The orange line indicates $\overline{d} = 15\,\%$, at which we define the maximal measurable electron lifetime value of the HeXe system.

transform the measured impurity concentration into an outgassing rate of the system, including the PTFE surface treatment, and obtain a more general description of the results. In the following, we generally describe the transformation of a measured impurity concentration into an outgassing rate. We apply this transformation then on the results of the B2 and T3 measurement, whereby we conservatively assume that already at the maximal measurable electron lifetime $\tau_{max} = 1000\,\mu s$ the xenon purification and the impurity outgassing are equivalent. We consider the resulting outgassing rate as base outgassing rate of the system, as we cannot resolve small outgassing rates. In the next section 6.5.2, we determine the outgassing rates of the remaining measurements.

Outgassing rate: in the calculation of the outgassing rate, we assume that the outgassing impurities are homogeneously distributed within the xenon of the system and that all impurities are removed when streaming through the gas purifier. This means that the xenon recirculation flow of the system is identical the xenon purification flow $\overline{F}$, measured in units of standard liter per minute (SLPM). For the following discussion, we transform $\overline{F}$ into a molar rate F_M as

$$F_M = \overline{F} \cdot \frac{\rho_{GXe}}{M_{Xe}} \tag{6.5.1}$$

with the GXe density of $\rho_{GXe} = 5.894\,g/liter$ at standard conditions and the molar mass $M_{Xe} = 131.29\,g/mol$ [189]. At an O_2 equivalent impurity concentration N_{O_2} measured in units of (mol O_2)/(mol Xe) and the molar xenon purification rate F_M measured in

units of (mol Xe)/time, we can calculate the impurities removal rate I as

$$I = F_M \cdot N_{O_2} \quad . \tag{6.5.2}$$

In the electron lifetime plateau region, the amount of impurities removed by the gas purifier and the amount of outgassing impurities is assumed to be equivalent. Hence, the outgassing R is

$$R = I = F_M \cdot N_{O_2} \quad . \tag{6.5.3}$$

The outgassing rate R describes the molar amount of O_2 that is outgassing from the system per time.

Base outgassing rate of HeXe system: based on the discussion of the B2 and T3 measurement, we calculate the outgassing rate for these measurements. We transform the minimal measurable impurity concentration N_{min} in the HeXe system into an O_2 equivalent outgassing rate. For this purpose, we average the measured xenon purification rate F of the B2 and T3 measurement, that agree within their uncertainties. Thus, at an average purification flow of $2.66\,\mathrm{SLPM}$, we translate $N_{min} = 0.43\,\mathrm{ppb}$ into an O_2 equivalent outgassing rate $R_{base} = 5 \cdot 10^{-11}$ (mol O_2)/min.

In our discussion, we assumed that at the maximal measurable electron lifetime τ_{max}, the sensitivity limit of the HeXe set-up is reached. Hence, τ_{max} corresponds to a lower limit. Since higher electron lifetimes are not accurately measurable, the corresponding impurity concentration N_{min} is only an upper limit and the true impurity concentration in the system might be lower. Consequently, the true base outgassing rate of the HeXe system might be smaller than R_{base}. However, we consider R_{base} as base outgassing rate of the entire system in the following.

Comparison of B2 and T3 measurement: the blank sample B2 was surface treated with ELMA CLEAN 65 and the test sample T3 was treated additionally with $32\,\%$ nitric acid (HNO_3). During the measurement of the blank sample, the xenon purity is only affected by the base outgassing of the entire system. In case of the test sample's measurement, the xenon purity might additionally be affected by the impurity release of the $32\,\%$ HNO_3 surface treatment. Since the blank and test sample's measurement achieve the maximal measurable electron lifetime τ_{max} of the HeXe TPC within the same xenon purification time, we conclude that no additional impurity release above the base outgassing rate $R_{base} = 5 \cdot 10^{-11}$ (mol O_2)/min of the system is observed from the $32\,\%$ HNO_3 surface treatment. This means that, within the sensitivity of the HeXe system, the xenon purity is not degraded by a $32\,\%$ HNO_3 surface treatment on PTFE. This result will be further discussed in section 6.5.4.

sample	$\tau_{plateau}$ [µs]	impurity conc. N_{O_2} [ppb]	outgassing rate R $[10^{-11}$ (mol O_2)/min]	xenon flow $\overline{F}$ [SLPM]
T1	300	1.42	16	2.56 ± 0.06
B1	1000	0.43	5	2.68 ± 0.07
B2	1000	0.43	5	2.64 ± 0.06
B3	640	0.67	8	2.77 ± 0.14
T2	90	4.73	54	2.53 ± 0.10
T3	1000	0.43	5	2.68 ± 0.04

Table 6.2: Maximal measured electron lifetime $\tau_{plateau}$ per purity measurement and corresponding impurity concentrations N_{O_2} and outgassing rates R. We also show the average flow rates $\overline{F}$ per measurement that are required to determine the outgassing rates.

6.5.2 Remaining measurements

The electron lifetime evolutions of the T1, B1, B3 and T3 measurement exhibit large variations and the maximal electron lifetimes are not consistent among the measurements, as shown in Fig. 6.13. These measurements are the subject of this section.

To compare the measurements, we determine the maximal electron lifetime value per measurement by fitting its plateau region with a constant function. The maximal achieved electron lifetime values are listed in Table 6.2 of all purity measurements, whereby the values of B2 and T3 are calculated as explained in section 6.5.1.

As in the case of the B2 and T3 measurement, we furthermore translate the maximal electron lifetimes into the corresponding O_2 equivalent impurity concentrations and outgassing rates. The results are also shown in Table 6.2 together with the average flow rates per measurement which are required for the calculation of the outgassing rates. Since the average purification flows agree within their uncertainties, the variations of the maximal electron lifetime values among the measurements translate into a similar variation of the outgassing rates.

The maximal measurable electron lifetime τ_{max} of the HeXe system is also reached in the measurement of sample B1. However, as the purification time is longer than in the measurements of sample B2 and T3 to reach this value, we did not include the B1 measurement in the discussion of section 6.5.1. The largest outgassing rate is measured for the sample T2, which is a factor of ~ 10 larger than the base outgassing rate of the system.

The inconsistency of the measurements lacks a definite explanation. In the following, we want to summarize some hypotheses that might explain the variations among the measurements. Whereas some of them can be investigated, others require further dedicated measurements to be tested. In addition, we describe some modifications of

the HeXe set-up that might improve future studies.

Measurement sequence: one potential explanation could be that the outgassing of a test sample contaminates the detector material. These impurities could still be present in the subsequent measurement and impact the xenon purity. However, we did not observe such an effect. This becomes most evident in the measurement of sample T2 and T3, that were performed one after another. Both samples were treated with the detergent ELMA CLEAN 65 and HNO_3. Whereas sample T2 shows the lowest purity level among all measurements, the maximal measured electron lifetime of sample T3 reaches the sensitivity limit of the TPC. Additionally, the contrary maximal lifetime values indicate that the efficiency of the gas purifiers to remove impurities is not reduced during the measurement campaign. Such inefficiencies can occur, if the cartridge of the gas purifier becomes saturated over time [176].

Detector parameters: the thermodynamical parameters of the measurement could affect the measured outgassing rate of the system. In Fig. 6.16 we show the outgassing rates of the individual samples as a function of (a) the average purification flow, (b) the average LXe temperature, (c) the average pressure in the cryostat and (d) the total LXe mass used in the measurement. For example, a higher temperature of the xenon could lead to a larger impurity outgassing rate of the system, due to an enhanced diffusion. The total LXe mass used to fill the detector varies slightly among the measurements, as it is determined by the height at which the TPC is suspended from the cryostat flange, adjusted manually in each measurement. The larger the distance of the TPC to the cryostat's bottom, the more xenon is employed. A change the LXe mass might affect the xenon flow dynamics and the mixing of the impurities within the LXe. This could also affect the measured outgassing rate. However, as shown in Fig. 6.16, no correlation between the detector parameters and the outgassing rate is observed.

Air leak: a further hypothesis is that temporally changing air leaks could be an explanation for the variation of the measured maximal electron lifetimes. The sample insertion requires the opening of the cryostat vessel. If the cryostat vessel is not tightened sufficiently after the insertion operation, small air leaks could be present, varying in size among different measurements. Dedicated leak rate measurements before each run could not be performed, since they are based on the usage of helium gas. Any contact of helium and the PMTs of the TPC has to be avoided, because it can diffuse inside the PMTs and cause an increase of their after-pulse rate [190].

However, the helium leak rate of the cryostat vessel under vacuum was mea-

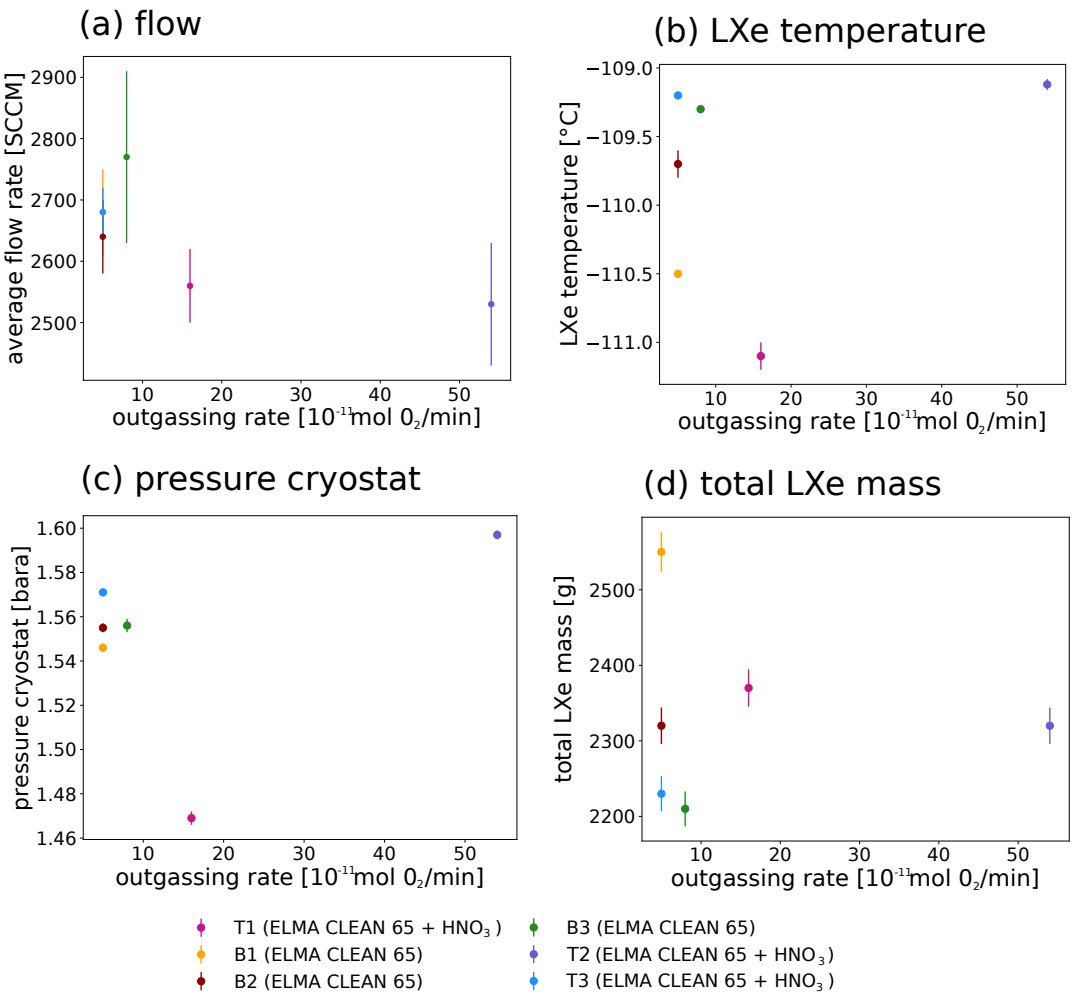

Figure 6.16: Correlation between the calculated outgassing rates per measurement and the (a) xenon flow rate, (b) LXe temperature, (c) pressure in the cryostat and (d) total LXe mass. No clear correlation is identified, as detailed in the text.

sured without TPC at $R^{HE}_{CRY} < 2 \cdot 10^{-9}\,\mathrm{mbar \cdot liter/sec}$. For the following discussion, we translate R^{HE}_{CRY} into an air equivalent leak rate as $R^{AIR}_{CRY} < R^{HE}_{CRY} \cdot 0.347 < 8 \cdot 10^{-10}\,\mathrm{mbar \cdot liter/sec}$ [191]. Next, we translate the measured outgassing rates of the purity measurements into air equivalent leak rates and compare the results with R^{AIR}_{CRY}. Thereby, we make the assumption that indeed all impurities of the O_2 equivalent outgassing rate are O_2 molecules, that leaked inside the croystat from the atmosphere. The measured outgassing rate R is translated into a leak rate as

$$R_{leak} = R \cdot V_{mol} \cdot 1/f_{O_2} \quad , \tag{6.5.4}$$

whereby $V_{mol} = 22.4\,\mathrm{liter/mol}$ is the molar volume of xenon and $f_{mol} = 0.2095$ is the fraction of oxygen in ambient air [192]. The measured outgassing rates R vary between $5 \cdot 10^{-11}$ (mol O_2)/min and $54 \cdot 10^{-11}$ (mol O_2)/min. Consequently, the corresponding leak rates R_{leak} are in a range of $9 \cdot 10^{-8}\,\mathrm{mbar \cdot liter/sec}$ to $1 \cdot 10^{-6}\,\mathrm{mbar \cdot liter/sec}$, which is at least two orders of magnitude larger than R^{AIR}_{CRY}. Hence, under the assumption that R^{AIR}_{CRY} did not change during the measurement campaign, it is thought that the impurity concentration of the purity measurements cannot be caused by an air leak.

Before the start of a purity measurement, the cryostat is always pumped for the same duration and then filled with xenon. In future measurements, the presence of a leak could be tested by measuring the pressure increase after the pumping with a vacuum sensor. With this method, the helium usage of a dedicated leak check is avoided.

Contamination during sample exchange: to access the TPC and exchange the sample cylinder, the cryostat has to be opend and the TPC has to be dismounted from its holding structure and placed on a working table. The entire operation is performed under N_2 atmosphere by means of a glove bag that is connected to the croystat and permanently flushed with N_2 at a slight overpressure.

A possible cause for the inconsistent measurements might be temporary air leaks in the glove bag during the opening operation. This might have caused small amounts of air to stream inside the glove bag. The main part of the TPC is made from a PTFE filling structure. As PTFE is a porous material, the potential air inside the glove bag could have diffused inside the bulk of the PTFE structure and slowly be released again during the measurement. The amount of air contamination per measurement is hard to control, since the diffusion rate into the glove bag is not known. Furthermore, the exact composition of contaminants contained in ambient air might change during the different opening operations.

As described in the next section 6.5.4, it is thought that the employed PTFE contributes to the overall outgassing rate of the system. Hence, its reduction might lead to an improvement of the base outgassing rate and its sensitivity to measure the impact of a surface treatment on the xenon purity. A reduction of the PTFE amount might also mitigate the impact of the described contamination effect on the stability of the purity measurements.

In addition, the potential contamination could be suppressed by improving the tightness of the glove bag. As a consequence, it is planned to permanently install a glove box purged with N_2 for future studies. It will be made from plexiglass structure, which is more robust against damage than the currently employed glove bag made from a plastic foil, that is prone to rip after several operations. Furthermore, the contact surface between the glove box and the cryostat's holding structure will be tightly sealed. In addition, the glove box could be also equipped with sensors to measure the stability of the N_2 atmosphere among different opening operations, such as the humidity and temperature.

Inefficient purification: to exchange the sample cylinder in the HeXe TPC, the upper PTFE structure rings of the TPC has to be removed. After the sample insertion, it is mounted back and the entire PTFE structure of the TPC is pressed together by means of stainless steel springs. It is thought that the PTFE rings could be pressed too tightly onto each other, such as the gas phase inside the TPC could be partly or completely sealed from the gas volume outside the PTFE structure. In this case, the GXe and the containg impurities cannot diffuse out of the active volume and be purified. The described mechanism could vary among different measurements, since the top PTFE rings have to be temporally removed for each sample exchange. Hence, the leakage of impurities from the gas into the liquid could limit the measured electron lifetime of the system.

This effect might be enhanced by two more aspects. One of them is the potential accumulation of impurities in the gas phase, due to their higher vapour pressure with respect to xenon. It was e.g. shown in [193] that, if only the LXe phase is purified in a TPC, the electron lifetime decreases with respect to the purification of both LXe and GXe simultaneously. The second aspect is a potential insufficient purification of the LXe reservoir inside the active volume. The inlet of the purified and liquefied xenon is below the cathode. To return the xenon to the gas purification system it is extracted below the bottom PMT. This flow pattern might not be ideal to exchange the entire liquid xenon target, which could also affect the xenon purification.

A planned HeXe TPC upgrade includes a modification of the flow pattern to enhance the xenon mixing in the active volume. A potential realization could be to position the xenon inlet and outlet at a larger distance across the active volume. Furthermore, it is planned to modify the top TPC part, such as the gas phase is permanently connected to the gas volume outside the PTFE structure. Thus, the purification of the GXe might be increased.

The last two hypotheses, describing a potential contamination during sample exchange and a potential inefficient purification require further investigations to be tested. It is thought that both options or a combination of them could explain the inconsistent electron lifetime evolutions.

6.5.3 Decrease of electron lifetime

Besides the increase of the electron lifetime, due to the xenon purification, we also monitor the electron lifetime decrease after the gas purifier is bypassed and the xenon is recirculated through the system without being purified. In Fig. 6.17, we show an enlarged view of the electron lifetime decrease for each purity measurement. During the measurement campaign, the time of the xenon purification was reduced by one day. For a better comparison among the measurements, we align the data points to a common purification stop time.

The electron lifetime decreases rather fast in comparison to its increase time at the start of a purity measurement. Whereas it takes $\mathcal{O}(\text{days})$ until the maximal xenon purity per measurement is reached, the xenon contamination by impurities is at $\mathcal{O}(\text{hours})$ in each measurement. Thereby, the electron lifetime per run degrades to a similar value in a comparable time, independent of the maximal electron lifetime value τ_{max} in the plateau region. This points to a rather strong and continuous outgassing rate of the system that leads to a quick xenon contamination as soon as the purification is stopped. We do not observe a clear correlation between the electron lifetime in the plateau region and the rate at which the electron lifetime decreases. Even though the T3 and B2 measurements show a compatible electron lifetime at the moment of purification stop, the electron lifetime of the latter decreases faster. Furthermore, we do not observe a clear correlation between the electron lifetime in the plateau region and at the end of the measurement. For example, sample B2 reaches τ_{max} but its final electron lifetime value is below the one of sample B1, that reached a significantly lower plateau value. Similarly, the B3 and T2 measurement end at a similar level, even though the B3 measurements showed a higher maximal lifetime value. Due to the described systematic effects of the set-up, we do not expect a clearly measurable dependence between the plateau region of the electron lifetime and its decrease rate or final value.

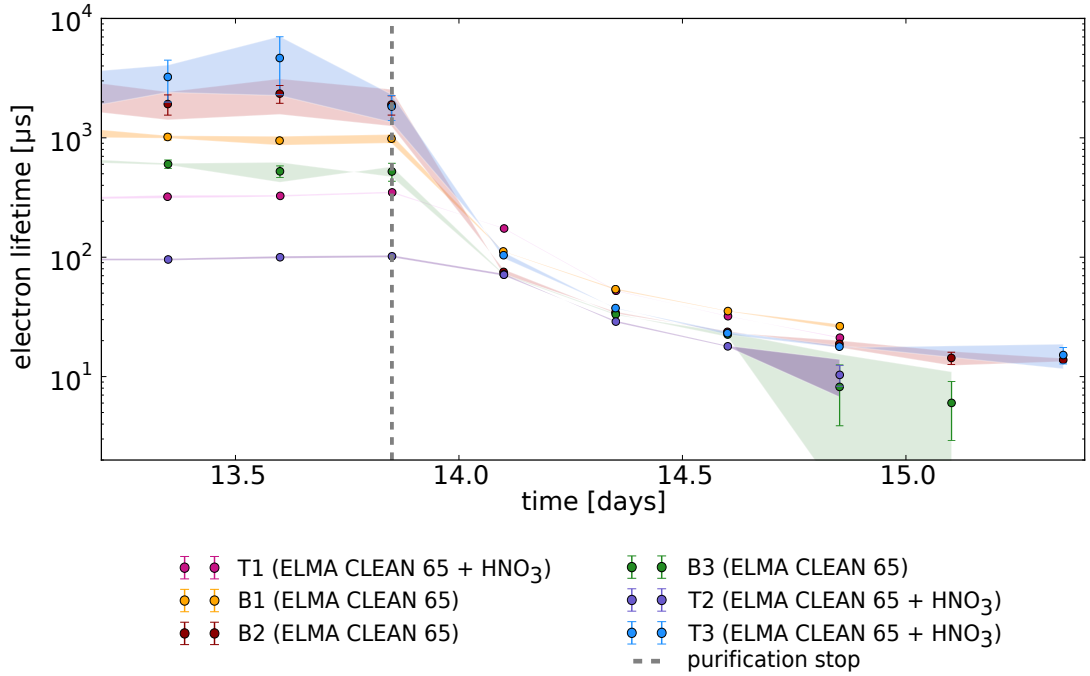

Figure 6.17: Enlarged view on the electron lifetime decrease after the xenon purification is stopped. The data points are aligned to time when the gas purifier is bypassed.

6.5.4 Discussion

Comparison between HeXe and DARWIN outgassing rates: for the further discussion, we want to estimate the total outgassing rate of a large-scale LXe TPC, such as the future project DARWIN [166]. In total, the experiment will use $50\,\mathrm{t}$ of xenon and employ a TPC with $2.6\,\mathrm{m}$ diameter and $2.6\,\mathrm{m}$ height. The DARWIN project aims at an electron lifetime of $2000\,\mu\mathrm{s}$ at a drift field of $500\,\mathrm{V/cm}$ [166]. The xenon purification flow is expected to be $\sim 1000\,\mathrm{SLPM}$ [194]. Hence, we estimate a total outgassing rate R_D of the DARWIN detector at $\mathcal{O}(10^{-8})$ (mol O_2)/min.

As expected, the total outgassing rate R_D of this large-scale detector is several orders of magnitude larger than the outgassing rate $R_{base} = 5 \cdot 10^{-11}$ (mol O_2)/min of the HeXe detector. However, a more direct comparison of the outgassing rates between both detectors is not trivial since this requires an exact knowledge on the outgassing sources.

In the following, we make the simple assumption that the entire outgassing originates from the PTFE of the HeXe and DARWIN TPCs with a mass of $6\,\mathrm{kg}$ and $300\,\mathrm{kg}$ [194], respectively. Since PTFE is a rather porous material and permeable for gases, it might absorb gaseous impurities while being exposed to air. Despite the careful cleaning of the PTFE structure before the operation starts, small impurity amounts might still out-

gass during the run-time of the experiments. When normalizing R_D and R_{base} to the total employed PTFE volumes, we obtain an outgassing rate of $\mathcal{O}(10^{-14}\,(\text{mol O}_2)/(\text{min}\cdot\text{cm}^3))$ for both the DARWIN and the HeXe detector. The total PTFE surface is presumably also an important parameter for the outgassing rate. However, the transfer from the surface to volume ratio to the impact on the outgassing rates is not trivial. When normalizing the outgassing rates R_D and R_{base} to the total PTFE surfaces, we obtain a similar outgassing rate of $\mathcal{O}(10^{-14}\,(\text{mol O}_2)/(\text{min}\cdot\text{cm}^2))$ for both detectors as well. Thereby, we use the entire PTFE surface of the HeXe TPC of $4100\,\text{cm}^2$. For the surface estimation of the the DARWIN TPC we assume an open cylinder with the described dimensions. Since the DARWIN TPC is more complex than this simple assumption, its true PTFE surface is likely larger and hence the outgassing rate normalized to the surface smaller than the estimated one. Under the simple assumption that the outgassing solely arises from the employed PTFE, the normalized results show that the base PTFE outgassing per volume (surface) is similar in both detectors. Thereby, the HeXe base outgassing rate was measured to be identical to the one after applying the PTFE surface treatment to the sample cylinder. However, from this result we cannot conclude that the surface treatment would leave the outgassing rate in the DARWIN detector unaffected, as described in the following.

In our discussion, we normalized the HeXe outgassing rate to the total amount of employed PTFE. However, the surface cleaning treatment is only applied to the sample cylinder that confines the active volume of the TPC. Its volume (surface) is a factor of $\sim$ 39 ($\sim$ 19) smaller than the total volume (surface) of the TPC's PTFE structure. Hence, an increase of the outgassing rate from a surface treatment on the comparably small PTFE sample cylinder might not be measurable with respect to the outgassing of the remaining PTFE structure. Reducing the volume (surface) ratio of the PTFE structure to the sample cylinder could lower the total outgassing rate of the system. This could increase the general sensitivity of the set-up to measure small potential changes in the outgassing rate due to a surface treatment. At the same time, this could allow for a normalization of the measured outgassing rate to the volume (surface) of the sample cylinder alone, which might be more accurate as only this component is treated with a surface cleaning. This could then also enable a more precise projection of the HeXe results on large-scale detectors.

Our result shows that the $32\,\%$ HNO_3 surface treatment is not degrading the xenon purity in the HeXe set-up at a measurable level. Even though we cannot make a precise prediction of the resulting outgassing in large-scale TPCs, such as the DARWIN detector, the result is already a first promising indication that the xenon purity is not affected by the surface treatment, that can be further tested in set-ups of higher sensitivities, as described below.

We want to stress that the discussion above has to be considered with caution, as the simple assumption that PTFE is the only outgassing source in the system might not hold. Therefore, it is not a priori clear if the outgassing rates can be normalized to the PTFE volume (surface). Within the HeXe system, further outgassing could originate from other components or dead volumes in which small amounts of gas could be trapped and slowly diffuse into the xenon during the operation. Even though the large effort to minimize outgassing sources in the HeXe set-up, we cannot exclude further contributions to the overall outgassing rate.

Increasing the sensitivity of the set-up: in section 6.5.1 we determined the maximal measurable electron lifetime τ_{max} in the HeXe set-up from which we eventually inferred the base outgassing rate R_{base} of the system. As described, this outgassing rate corresponds to an upper limit and the true outgassing rate of the system might be lower. In the following, we want to discuss how the sensitivity of the HeXe TPC could be enhanced to increase its capability in measuring lower outgassing rates.

At the same employed xenon purification flow, a smaller outgassing rate directly translates into a lower impurity concentration inside the xenon (see Eq. 6.5.3). Since the measured impurity concentration is inverse to the measured electron lifetime, the capacity to measure larger electron lifetime values has to be increased in the TPC to be able to measure lower purity concentrations (see Eq. 6.2.2). The electron lifetime describes the charge reduction in a TPC as function of the electron drift time. By increasing this drift time, the sensitivity to measure larger electron lifetime values is enhanced. This can be achieved in two ways. First, the drift field and thus the drift velocity can be reduced, causing the ionization electrons requiring more time to reach the liquid-gas interface. A drift-field reduction also causes a higher electron attachment rate to O_2 (see Fig. 6.2). Under the assumption that the electro-negative impurities inside the xenon constitute of O_2, the higher attachment rate allows measuring smaller impurity concentrations. The second option to increase the electron drift time is to elongate the TPC's active volume [181]. This second option is preferred, since the reduction of the drift field might lead to field inhomogeneities in a TPC. The second method is foreseen in an upgrade of the HeXe TPC to increase its sensitivity.

The comparable measurements of sample B2 and sample T3 show that the xenon purity is not degraded to an unacceptable low level by the $32\,\%$ HNO_3 surface treatment which suggests that the cleaning method could be a favorable option in future detectors. Based on this result, futher measurements at higher senistivities can confirm that it can also be used in large-scale detectors

6.6 Summary

A fundamental requirement to detect rare events at extremely low energies in current and future LXe TPCs is the quality to measure the signal size of a particle interactions at minimal losses. Spurious amounts of electro-negative impurities are continuously outgassing from the detector materials into the xenon reservoir. They can cause a reduction of ionization electrons that form the S2 scintillation signal in the TPC. This would lead to e.g. a worse signal-background discrimination, an unwanted high energy threshold and larger signal corrections.

In our work, we tested if a $32\,\%$ HNO_3 treatment on the PTFE surfaces of the TPC's active volume releases additional trace amounts of impurities into the xenon. This might result in an unacceptable degradation of the xenon purity and a negative effect on the detector performance. Testing a cleaning treatment based on $32\,\%$ HNO_3 is motivated by its large efficiency to remove radon progenies from PTFE surfaces. The mitigation of the long-lived radon daughters is important to meet the low background requirements in rare event searches.

We applied either a basic surface cleaning with a detergent (blank sample) or the same treatment and $32\,\%$ HNO_3 in addition to a PTFE sample cylinder (test sample). Per measurement, we inserted either a blank or test cylinder into the HeXe TPC. As it constitutes the surrounding walls of the TPC's active volume, it is directly immersed into the liquid xenon. This novel technique allows us to directly test potential outgassing of the surface treatment into the cold medium. During a purity measurement, the xenon is purified and we monitor the resulting increase of the xenon purity over time. We then compare these evolutions among test and blank samples.

Four out of six purity measurements exhibit inconsistent evolutions at a low level of xenon purity. The origin of this inconsistency is not entirely understood and we discuss in detail several potential causes. Some of these hypotheses can be excluded, whereas others require more investigations.

In the remaining two measurements, we tested a blank and a test sample. The two measurements show a comparable xenon purity evolution, which allows us to draw several conclusions. The xenon purity is not affected by an additional $32\,\%$ HNO_3 surface treatment within the HeXe set-up. This means that no additional impurity release into the liquid xenon is measurable above the base impurity outgassing rate $R_{base} = 5 \cdot 10^{-11}$ (mol O_2)/min of the entire system. Potential outgassing enhancements from a surface treatment smaller than this base outgassing rate cannot be resolved in the system and we discussed several methods to increase the sensitivity. We

conclude that, since the measured xenon purity is identical for the base and the test sample in our set-up, that a $32\,\%$ HNO_3 surface treatment has the potential to be applied in large-scale detectors. Additional studies at higher sensitivities are necessary for a further inspection. Our results mark the first step towards this direction.

Summary and Outlook

This thesis was carried out in the framework of the dark matter search experiment XENON1T. Being the largest and most sensitive liquid xenon (LXe) detector to date, the XENON1T experiment sets the most stringent limits on the spin-independent WIMP-nucleon cross-sections for WIMP masses $> 6\,\mathrm{GeV/c^2}$. Currently, XENON1T is being upgraded to the next-generation detector XENONnT to probe cross-sections more than an order of magnitude below the current best limits. In the following, we summarize the main results of this thesis and provide an outlook on the related XENONnT upgrades.

Background suppression is of utmost importance for the success of low energy rare-event search experiments. In XENON1T, the noble gas ^{222}Rn induces the dominant source of background. In the first part of this thesis, we studied the radon induced background which is present inside the whole LXe target, generating electronic recoil (ER) interactions. Although ERs can be efficiently discriminated from nuclear recoils (NRs), statistical leakage of the ER population can still produce events indistinguishable from WIMPs. In central volumes of the Time-Projection-Chamber (TPC), where surface background is suppressed, ERs constitute the largest background contribution in the experiment. Our study allows us to constrain the most dominant ER background component arising from the β-decays of the ^{222}Rn progeny ^{214}Pb. Furthermore, we monitored the evolution of the ^{222}Rn activity concentration throughout the entire $2\,\mathrm{years}$ of detector operation and showed thereby that the induced ER background is stable over time in the dark matter search data. In addition, we measured the significant reduction of the ^{222}Rn level caused by two improvements to the experiment: first, the main ^{222}Rn sources in the detector, the recirculation pumps, were exchanged by a magnetically coupled piston pump that features a negligible ^{222}Rn release rate. This measurement also supports the hypothesis that the prediction of the ^{222}Rn level in the experiment, by means of dedicated ^{222}Rn emanation measurements, underestimated the contribution from the recirculation pumps leading to a $\sim 30\,\%$ higher ^{222}Rn activity concentration in the experiment. Second, an online radon removal system based on cryogenic distillation was employed in the experiment. The combination of the two improvements lead to a final ^{222}Rn activity concentration of $(4.5 \pm 0.1)\,\mu\mathrm{Bq/kg}$. The result

presents the lowest ^{222}Rn level ever achieved in a LXe dark matter experiment, which is also very promising for the XENONnT experiment. The upgraded detector will employ magnetically coupled piston pumps as well as a dedicated large-flow distillation column to further suppress radon induced background, aiming at a ^{222}Rn activity concentration of $1\,\mu\mathrm{Bq/kg}$.

Besides ER background, there are new particles beyond the Standard Model that are expected to create ERs as an event signature in the LXe. The XENON Collaboration recently reported an observed ER event excess over known ER background in the energy spectrum at low energies. Detailed checks of the result were performed and the excess could be attributed to different signal hypotheses but also to the β-decay of tritium, a background that has never been observed before in LXe TPCs. To add even more confidence in the results, the XENON Collaboration is currently carrying out an additional study to exclude potential effects from slightly changing detector and analysis parameters over time. In this context, we developed a preliminary time-dependent ER background model, including our findings on the aforementioned ^{222}Rn evolution in the experiment. First results indicate that the overall ER background rate in the experiment is, as expected, stable over time. This result further provides proof of the correctness and robustness of the interpretation of the observed excess. Future studies in XENONnT, with more data, could benefit from the improved background understanding. With an increased target mass by a factor of ~ 3 and a reduced ER background by a factor of ~ 6, XENONnT is able to study the excess in more detail and potentially rule out some hypotheses already after a few months of data.

We furthermore investigated a second class of ^{222}Rn induced background in XENON1T. It arises from the plate-out of long-lived ^{222}Rn daughters on the inner PTFE walls of the TPC's active volume during detector construction. This surface contamination constitute the largest background component at outer TPC volumes, consequently limiting the size of the LXe fiducial volume and the sensitivity of the dark matter search. Thereby, the decay of plated-out ^{210}Po can trigger (α,n)-reactions, leading to neutron background which has an identical NR event signature as WIMP interactions. In our work, we estimated an upper limit on the resulting NR background, which is only three times smaller than the main NR background in XENON1T, arising from radiogenic neutrons. We expect that the NR background caused by surface contamination becomes even more relevant in XENONnT, as the upgraded detector includes an active neutron veto that efficiently suppresses radiogenic neutrons. Additionally, the result shows that removing surface contamination from plated-out radon daughters before the start of the experiment is essential to meet the low background requirements of next-generations experiments. This can be achieved by dedicated surface cleaning methods. If these methods are suitable to be applied in a LXe TPC requires dedicated

tests, since residual trace amounts of the cleaning chemicals might affect the xenon purity and the TPC performance. This question motivates the second part of this work.

The second part of this thesis is devoted to xenon purity studies performed with the small-scale LXe TPC of the Heidelberg Xenon (HeXe) system. The TPC and large parts of the detector system were designed and built during this work. It was shown that the detector can be safely and stably operated over weeks, a prerequisite for the long-term xenon purity measurements. In our studies, we tested a PTFE surface cleaning based on $32\,\%$ HNO_3 as it shows a large removal factor for plated-out radon daughters. To reflect realistic conditions, we applied the surface treatment directly on the PTFE surface of the HeXe TPC's active volume, which is exposed to the cold LXe medium during the measurements. This novel technique allowed us to test if the PTFE cleaning method induces trace amounts of electro-negative impurities in the xenon. This would lead to a reduction of the charge signal in the TPC, causing e.g. a worse signal-background discrimination and an unwanted high energy threshold in the experiment. In our study, we were able to show for the first time that, within the set-up's sensitivity, a $32\,\%$ HNO_3 surface treatment does not affect the xenon purity. This shows that the chemical PTFE treatment is a promising surface cleaning candidate in LXe TPCs and further studies with higher sensitivities are necessary to confirm that it can be applied in large-scale detectors.

The commissioning phase of the XENONnT detector is still ongoing and proceeding fast. At the time of writing, final checks are being performed on the already filled TPC and the detector is almost ready for the exciting search for dark matter, with first results expected in 2021.

Bibliography

[1] K. Garrett and G. Duda. Dark matter: A Primer. *Adv. Astron.,2011:968283*, 2011.

[2] J. Einasto. Dark Matter. *Braz. J. Phys., 43:369−374*, 2013.

[3] M. Schumann. Direct Detection of WIMP dark matter: Concepts and Status. *J. Phys. G46 no.10, 103003*, 2019.

[4] T. Marrodán Undagoitia and L. Rauch. Dark matter direct−detection experiments. *J. Phys. G43 no.1, 013001*, 2016.

[5] F. Zwicky. Die Rotverschiebung von extragalaktischen Nebeln. *Helv. Phys. Acta 6, 110−127*, 1933.

[6] V. C. Rubin et al. Extended rotation curves of high−luminosity spiral galaxies. *Astrophys. J 225 L107*, 1978.

[7] M. Milgrom. A modification of the Newtonian dynamics as a possible alternative to the hidden mass hypothesis. *Astrophys. J. 270 365−370*, 1983.

[8] J. E. Felten. Milgroms revision of Newtons laws − dynamical and cosmological consequences. *Astrophysical Journal 286 3−6*, 1984.

[9] M. Bartelmann and P. Schneider. Weak gravitational lensing. *Phys. Rept. 340 291*, 2001.

[10] L. Van Waerbeke et al. Dealing with systematics in cosmic shear studies: New results from the VIRMOS-Descart survey. *Astron. Astrophys. 429 75*, 2005.

[11] T. Treu. Strong Lensing by Galaxies. *Ann. Rev. Astron. Astrophys. 48 87*, 2010.

[12] D. Clowe et al. A direct empirical proof the existence of dark matter. *Astrophys. J., 648:L109−L113*, 2006.

[13] W. A. Dawson et al. Discovery of a Dissociative Galaxy Cluster Merger with Large Physical Separation. *Astrophys. J. 747 L42*, 2012.

[14] C. L. Bennett et al. 4-Year COBE DMR Cosmic Microwave Background Observations: Maps and Basic Results. *Astrophys.J.464:L1−L4*, 1996.

[15] W. A. Dawson et al. Nine-Year Wilkinson Microwave Anisotropy Probe (WMAP) Observations: Cosmological Parameter Results. *Astrophys. J. Suppl. 208 19*, 2013.

[16] Planck Collaboration. Planck 2018 results. VI. Cosmological parameters. *arXiv:1807.06209*, 2018.

[17] V. Springel et al. The large−scale structure of the Universe. *Nature 440, pp. 1137−1144*, 2006.

[18] 2dFGRS Collaboration. The 2dF Galaxy Redshift Survey: Final data release. *arXiv:astro−ph/0306581*, 2003.

[19] S. D. White et al. Clustering in a Neutrino Dominated Universe. *Astrophys. J. 274 L1*, 1983.

[20] S. Tremaine and J. E. Gunn. Dynamical role of light neutral leptons in cosmology. *Phys. Rev. Lett. 42 407*, 1979.

[21] K. N. Abazajian et al. Light Sterile Neutrinos: A White Paper. *arXiv:1204.5379*, 2012.

[22] R. D. Peccei and H. R. Quinn. CP conservation in the presence of pseudoparticles. *Phys. Rev. Lett. 38, 1440*, 1977.

[23] H. Baer et al. Dark matter production in the early Universe: beyond the thermal WIMP paradigm. *Phys. Rept. 555 1*, 2015.

[24] A. B. Lahanas. LSP as a Candidate for Dark Matter. *Lect. NotesPhys.720:35−68*, 2007.

[25] D. Hooper and S.Profumo. Dark Matter and Collider Phenomenology of Universal Extra Dimensions. *Phys.Rept.453:29−115*, 2007.

[26] L. Roszkowski. Particle dark matter − A theorists perspective. *Pramana 62 389*, 2004.

[27] ATLAS Collaboration. The ATLAS experiment at the CERN Large Hadron Collider. *JINST 3 S08003*, 2008.

[28] CMS Collaboration. The CMS experiment at the CERN LHC. *JINST3 S08004*, 2008.

[29] F. Kahlhoefer. Review of LHC Dark Matter Searches. *International Journal of Modern Physics A 32.13*, 2017.

[30] J. Conrad. Indirect Detection of WIMP Dark Matter: a compact review. In Interplay between Particle and Astroparticle physics. *arXiv:1411.1925*, 2014.

[31] J. D. Lewin and P. F. Smith. Review of mathematics, numerical factors, and corrections for dark matter experiments based on elastic nuclear recoil. *Astropart. Phys., vol. 6*, 1996.

[32] K. Freese et al. Annual modulation of dark matter: A review. *arXiv:2003.04545*, 2013.

[33] D. N. Spergel. The Motion of the Earth and the Detection of WIMPs. *Phys. Rev. D37 1353*, 1988.

[34] L. E. Strigari. Neutrino Coherent Scattering Rates at Direct Dark Matter Detectors. *New J.Phys.11:105011*, 2009.

[35] E. Aprile et al. (XENON Collaboration). Dark Matter Search Results from a One Tonne x Year Exposure of XENON1T. *Phys. Rev. Lett. 121, 111302*, 2018.

[36] D. Akerib et al. (LUX Collaboration). Results from a Search for Dark Matter in the Complete LUX Exposure. *Phys. Rev. Lett. 118, 021303*, 2017.

[37] X. Cui et al. (PandaX-II Collaboration). Dark Matter Results from 54 Ton Day Exposure of PandaX II Experiment. *Phys. Rev. Lett. 119, 181302*, 2017.

[38] L. E. Strigari. Improved EDELWEISS−III sensitivity for low-mass WIMPs using a profile likelihood approach. *Eur. Phys. J. C 76 548*, 2016.

[39] R. Agnese et al. (SuperCDMS Collaboration). First Dark Matter Constraints from a SuperCDMS Single-Charge Sensitive Detector. *Phys. Rev. Lett. 121, 051301*, 2016.

[40] A.H. Abdelhameed et al. (CRESST-III). First results from the CRESST−III low−mass dark matter program. *Phys. Rev. D 100, 102002*, 2019.

[41] P. Agnes et al. (DarkSide-50 Collaboration). Low-Mass Dark Matter Search with the DarkSide-50 Experiment. *Phys. Rev. Lett. 121 081307*, 2018.

[42] E.Aprile et al. (XENON Collaboration). Light Dark Matter Search with Ionization Signals in XENON1T. *Phys. Rev. Lett. 123, 251801*, 2019.

[43] C. Kouvaris and J. Pradler. Probing Sub-Gev Dark Matter with Conventional Detectors. *Phys. Rev. Lett. 118, 031803*, 2017.

[44] M. Ibe et al. Migdal effect in dark matter direct detection experiments. *JHEP 03,194*, 2018.

[45] E. Aprile et al. (XENON Collaboration). Search for Light Dark Matter Interactions Enhanced by the Migdal effect or Bremsstrahlung in XENON1T. *Phys. Rev. Lett. 123, 241803*, 2019.

[46] Z. Z. Liu et al. (CDEX-1B Collaboration). Constraints on Spin−Independent Nucleus Scattering with sub-Gev Weakly Interacting Massive Particle Dark Matter from the CDEX−1B Experiment at the China Jin-Ping Laboratory. *Phys. Rev. Lett. 123, 161301*, 2019.

[47] E.Aprile et al. (XENON Collaboration). Design and Performance of the XENON10 Dark Matter Experiment. *Phys. Rev. Lett. 100, 021303*, 2008.

[48] E.Aprile et al. (XENON Collaboration). The XENON100 Dark Matter Experiment. *Astropart. Phys. 35, 573−590*, 2012.

[49] E. Aprile et al. (XENON Collaboration). First Dark Matter Search Results from the XENON1T Experiment. *Phys. Rev. Lett. 119, 181301*, 2017.

[50] J. Xu et al. Electron extraction efficiency study for dual−phase xenon dark matter experiments. *Phys. Rev. D 99, 103024*, 2019.

[51] E. Aprile et al. (XENON Collaboration). The XENON1T Dark Matter Experiment. *Eur.Phys.J. C77*, 2017.

[52] Internal XENON document/conversation.

[53] E.Aprile et al. Simultaneous Measurement of Ionization and Scintillation from Nuclear Recoils in Liquid Xenon as Target for a Dark Matter Experiment. *Phys. Rev. Lett. 97, 081302*, 2006.

[54] V. Chepel and H. Araujo. Liquid noble gas detectors for low energy particle physics. *JINST 8, R04001*, 2013.

[55] E. Aprile et al. Noble gas detectors. *Weinheim: WILEY VCH Verlag GmbH Co. KGaA*, 2006.

[56] E. Aprile and T. Doke. Liquid xenon detectors for particle physics and astrophysics. *Rev. Mod. Phys. 82, 2053*, 2010.

[57] F. Keiko et al. High−accuracy measurement of the emission spectrum of liquid xenon in the vacuum ultraviolet region. *Nucl. Instrum. Meth. A795 293.*, 2015.

[58] J. Mock et al. Modeling pulse characteristics in xenon with NEST. *Journal of Instrumentation 9 T04002−T04002*, 2014.

[59] P. Kryczynski (WARP Collaboration). Pulse Shape Discrimination in liquid argon and its implications for Dark Matter searches using depleted argon. *Acta Phys.Polon.B 43 1509−1520*, 2012.

[60] C. Dahl. The physics of background discrimination in liquid xenon, and first results from XENON10 in the hunt for WIMP dark matter. *Ph.D. thesis, Princeton University*, 2009.

[61] J. Lindhard et al. Integral Equations governing radiation effects. *Mat. Fys. Medd. Dan. Vid. Selsk 33, 1*, 1963.

[62] E. Aprile et al. (XENON Collaboration). XENON1T Dark Matter Data Analysis: Signal and Background Models, and Statistical Inference. *Phys. Rev. D 99, 112009*, 2019.

[63] A. Lansiart et al. Development research on a highly luminous condensed xenon scintillator. *Nuclear Instruments and Methods, 135(1):47 − 52*, 1976.

[64] M. A. Vargas Jara. Data Analysis in the XENON1T Dark Matter Experiment. *Ph.D. thesis, University Muenster*, 2019.

[65] L. Baudis et al. Performance of the Hamamatsu R11410 Photomultiplier Tube in cryogenic Xenon Environments. *JINST 8 P04026*, 2013.

[66] C. H. Faham et al. Measurements of Wavelength−Dependent Double Photoelectron Emission from Single Photons in VUV−Sensitive Photomultiplier Tubes. *Journal of Instrumentation 10 P09010 P09010*, 2015.

[67] E Aprile et al. (XENON Collaboration). Observation and applications of single−electron charge signals in the XENON100 experiment. *J. Phys. G: Nucl. Part. Phys. 41 035201*, 2014.

[68] E. Aprile et al. (XENON Collaboration). XENON1T Dark Matter Data Analysis: Signal Reconstruction, Calibration and Event Selection. *Phys. Rev. D 100, 052014*, 2019.

[69] G. Bakale et al. Effect of an Electric Field on Electron Attachment to SF_6, N_20, and O_2 in Liquid Argon and Xenon. *Phys. Chem., 80 (23)*, 1976.

[70] T. Doke et al. Absolute Scintillation Yields in Liquid Argon and Xenon for Various Particles. *Japanese Journal of Applied Physics 41*, 2002.

[71] S. Agostinelli et al. (GEANT4 Collaboration). GEANT4: A Simulation toolkit. *Nucl. Instrum. Meth. A506, 250*, 2003.

[72] M. Yamashita et al. Scintillation response of liquid Xe surrounded by PTFE reflector for gamma rays. *Nucl. Instr. Meth. A 535, 692*, 2004.

[73] E. Aprile et al. (XENON Collaboration). Lowering the radioactivity of the photomultiplier tubes for the XENON1T dark matter experiment. *Eur. Phys. J. C75:546*, 2015.

[74] E. Aprile et al. (XENON Collaboration). Material radioassay and selection for the XENON1T dark matter experiment. *Eur. Phys. J. C77: 890*, 2017.

[75] E. Aprile et al. (XENON Collaboration). Conceptual Design and Simulation of a Water Cherenkov Muon Veto for the XENON1T Experiment. *arXiv: 1406.2374*, 2014.

[76] M. Murra. Intrinsic background reduction by cryogenic distillation for the XENON1T dark matter experiment. *Ph.D. thesis, University Muenster*, 2019.

[77] J. Aalbers and C. Tunnell. The Pax Data Processor v6.4.2. Zenodo. *https ://zenodo.org/record/546239.WZWq1CdLfb0*, 2017.

[78] E. Aprile et al. (XENON Collaboration). The XENON1T Data Acquisition System. *JINST 14 no.07, P07016*, 2019.

[79] E. Aprile et al. (XENON Collaboration). Physics reach of the XENON1T dark matter experiment. *arxiv: 1512.07501*, 2015.

[80] G. Heusser et al. Low-level germanium gamma-ray spectroscopy at the μBq/kg level and future developments towards higher sensitivity. *Povinec, P.P. and Sanchez-Cabeza, J.A. (eds.): Radionuclides in the Environment 495*, 2006.

[81] L.Baudis et al. Gator: a low-background counting facility at the Gran Sasso Underground Laboratory. *JINST 6 P08010*, 2011.

[82] G. Heusser et al. GIOVE: a new detector setup for high sensitivity germanium spectroscopy at shallow depth. *JINST 6 P08010*, 2015.

[83] S. A. Bruenner et al. Radon depletion in xenon boil−off gas. *Eur. Phys. J., C77(3):143*, 2017.

[84] X. Du et al. An atom trap system for practical ^{81}Kr dating. *Rev.Sci.Instr. 75 3224−3232*, 2004.

[85] E.Aprile et al. (XENON Collaboration). Removing krypton from xenon by cryogenic distillation to the ppq level. *Eur. Phys. J. C 77, 275*, 2017.

[86] E.Aprile et al. (XENON Collaboration). First results on the scalar WIMP−pion coupling, using the XENON1T experiment. *Phys. Rev. Lett. 122, 071301*, 2019.

[87] E.Aprile et al. (XENON Collaboration). Constraining the Spin−Dependent WIMP−Nucleon Cross Sections with XENON1T. *Phys. Rev. Lett. 122, 141301*, 2019.

[88] E.Aprile et al. (XENON Collaboration). First observation of two-neutrino double electron capture in ^{124}Xe with XENON1T. *Nature 568, p.532−535*, 2019.

[89] E. Aprile et al. (XENON Collaboration). Excess electronic recoil events in XENON1T. *Phys. Rev. D 102, 072004*, 2020.

[90] J. Aalbers. Dark matter search with XENON1T. *Ph.D. thesis, University Amsterdam*, 2018.

[91] K. Mora. Statistical Modelling and Inference for XENON1T. *Ph.D. thesis, University Stockholm*, 2019.

[92] Laboratoire National Henri Becquerel "Recommended Data of Radionuclides". *http://www.lnhb.fr/nuclear-data/nuclear-data-table*, 2020.

[93] S. A. Bruenner. Mitigation of ^{222}Rn induced background in the XENON1T dark matter experiment. *Ph.D. thesis, University of Heidelberg*, 2017.

[94] G.N. Vlaskin et al. Neutron yield of the reaction (α, n) on thick targets comprised of light elements. *At. Energy 117 5, 357-365*, 2015.

[95] B.J. Mount et al. (LZ Collaboration). LUX−ZEPLIN (LZ) technical design report. *arXiv:1703.09144*, 2017.

[96] XMASS Collaboration. Radon removal from gaseous xenon with activated charcoal. *NIMA A 661 50 57*, 2012.

[97] S. A. Bruenner. Study of radon adsorption on activated carbon for a purification system in XENON1T. *Master thesis, University of Graz*, 2013.

[98] E. Aprile et al. (XENON Collaboration). Online ^{222}Rn removal by cryogenic distillation in the XENON100 experiment. *Eur.Phys.J. C77*, 2017.

[99] P.A. Breur. Backgrounds in XENON1T. *Ph. D. thesis, University of Amsterdam*, 2019.

[100] M. Weber. Gentle Neutron Signals and Noble Background in the XENON100 Dark Matter Search Experiment. *Ph.D. thesis, University of Heidelberg*, 2013.

[101] G. Plante. The XENON100 dark matter experiment: Design, construction, calibration and 2010 search results with improved measurement of the scintillation response of liquid xenon to low-energy nuclear recoil. *Ph.D. thesis, Columbia University*, 2012.

[102] E. Aprile et al. (XENON Collaboration). Intrinsic backgrounds from Rn and Kr in the XENON100 experiment. *Eur. Phys. J. C78: 132*, 2018.

[103] A. Bradley et al. (LUX Collaboration). Radon-related backgrounds in the LUX dark matter search. *Phys. Procedia 61 658−665*, 2015.

[104] S. Li et al. (PandaX Collaboration). Krypton and radon background in the PandaX−I dark matter experiment. *JINST 12 T02002*, 2017.

[105] J.B. Albert et al. (EXO-200 collaboration). Investigation of radioactivity-induced backgrounds in EXO−200. *Phys. Rev. C 92 015503*, 2015.

[106] EXO-200 Collaboration. Measurements of the ion fraction and mobility of alpha and beta decay products in liquid xenon using EXO−200. *Phys. Rev. C 92, 045504*, 2015.

[107] T. Takahashi et al. Average energy expended per ion pair in liquid xenon. *Phys. Rev. A12, 1771*, 1975.

[108] E. Aprile et al. Ionization of liquid xenon by ^{214}Am and ^{210}Po alpha particles. *Nucl.Instrum.Meth.A 307 119−125*, 1991.

[109] E. Aprile et al. (XENON Collaboration). Projected WIMP sensitivity of the XENONnT dark matter experiment. *arXiv:2007.08796v1*, 2020.

[110] R. Essig et al. Direct detection of Sub−Gev dark matter. *Phys. Rev. D85 076007*, 2012.

[111] R. Essig et al. New constraints and prospects for sub−Gev dark matter scattering off electrons in xenon. *Phys. Rev. D 96, 043017*, 2017.

[112] J. Kopp et al. DAMA/LIBRA and leptonically interacting dark matter. *Phys.Rev.D80:083502*, 2009.

[113] K. Freese et al. Signal modulation in cold dark matter detection. *Phys. Rev., vol. D37*, 1988.

[114] V. Barsanov et al. Artificial neutrino source based on the ^{37}Ar isotope. *Phys. Atom. Nucl. 70, 300*, 2007.

[115] L. L. Lucas and M. P. Unterweger. Comprehensive review and critical evaluation of the half−life of tritium. *Journal of research of the National Institute of Standards and Technology 105, 541*, 2000.

[116] C. Zhang et al. Cosmogenic activation of materials used in rare event search experiments. *Astroparticle Physics 84, 62*, 2016.

[117] S. Weinberg. A new light boson? *Phys. Rev. Lett. 40, 223*, 1978.

[118] J. Preskill et al. Cosmology of the invisible axion. *Physics Letters B 120, 127*, 1983.

[119] M. Dine and W. Fischler. The not−so−harmless axion. *Phys. Lett. B 120, 137*, 1983.

[120] G. G. Raffelt. Astrophysical axion bound. *Springer Berlin Heidelberg*, 2007.

[121] J. Redondo. Solar axion flux from the axion−electron coupling. *Journal of Cosmology and Astroparticle Physics 2013, 008*, 2013.

[122] S. Moriyama. Proposal to search for a monochromatic component of solar axions using ^{57}Fe. *Phys. Rev. Lett. 75, 3222*, 1995.

[123] K. van Bibber et al. Design for a practical laboratory detector for solar axions. *Phys. Rev. D 39, 2089*, 1989.

[124] S. Dimopoulos et al. Axiorecombination: A new mechanism for stellar axion production. *Phys. Lett. B 179, 223*, 1986.

[125] H. Primakoff. Photo−production of neutral mesons in nuclear electric fields and the mean life of the neutral meson. *Phys. Rev. 81, 899*, 1951.

[126] S. Dimopoulos et al. Atomic enhancement in the detection of axions. *Mod. Phys. Lett. A 1, 491*, 1986.

[127] M. Dine et al. A simple solution to the strong CP problem with a harmless axion. *Physics LettersB 104, 199*, 1986.

[128] J. E. Kim. Weak-interaction singlet and strong CP invariance. *Phys. Rev. Lett. 43, 103*, 1979.

[129] M. M. Bertolami et al. Revisiting the axion bounds from the galactic white dwarf luminosity function. *Journal of Cosmology and Astroparticle Physics 2014, 069*, 2014.

[130] A.Ayala et al. Revisiting the bound on axion−photon coupling from globular clusters. *Phys. Rev. Lett. 113, 191302*, 2014.

[131] N. Viaux et al. Neutrino and axion bounds from the globular cluster M5 (NGC 5904). *Phys. Rev. Lett. 111, 231301*, 2013.

[132] M. Giannotti et al. Stellar recipes for axion hunters. *Journal of Cosmology and Astroparticle Physics 2017, 010010*, 2017.

[133] L. Di Luzio et al. The landscape of QCD axion models. *arXiv:2003.01100*, 2020.

[134] J. E. Kim. Neutrino magnetic moment. *Phys. Rev. D 14, 3000*, 1976.

[135] K. Fujikawa and R. E. Shrock. Magnetic moment of a massive neutrino and neutrino−spin rotation. *Phys. Rev. Lett. 45, 963*, 1980.

[136] N. F. Bell et al. Model independent bounds on magnetic moments of majorana neutrinos. *Phys.Lett. B642 377−383*, 2006.

[137] M. Agostini et al. (Borexino collaboration). Limiting neutrino magnetic moments with Borexino Phase−II solar neutrino data. *Phys. Rev. D 96, 091103*, 2017.

[138] S.A.Daz et al. Constraint on the magnetic dipole moment of neutrinos by the tip−RGB luminosity in Omega-Centauri. *Astroparticle Physics, 10.1016/j.astropartphys.2015.03.006*, 2015.

[139] S.A.Daz et al. Constraint on the axion−electron coupling constant and the neutrino magnetic dipole moment by using the tip−RGB luminosity of fifty globular clusters. *arXiv:1910.10568*, 2019.

[140] A. Corsico et al. Constraining the neutrino magnetic dipole moment from white dwarf pulsations. *Journal of Cosmology and Astroparticle Physics 2014, 054*, 2014.

[141] A. G. Beda et al. Gemma experiment: The results of neutrino magnetic moment search. *Physics of Particles and Nuclei Letters 10, 139143*, 2013.

[142] P. Arias et al. WISPy cold dark matter. *Journal of Cosmology and Astroparticle Physics 2012, 013*, 2012.

[143] J. Ye. Searches for WIMPs and axions with the XENON1T experiment. *Ph.D. thesis, University of California*, 2020.

[144] S. J. Haselschwardt et al. Improved calculations of beta decay backgrounds to new physics in liquid xenon detectors. *arXiv:2007.13686v2*, 2020.

[145] S. Lindemann. Intrinsic ^{85}Kr and ^{222}Rn backgrounds in the XENON dark matter search. *Ph.D. thesis, University of Heidelberg*, 2013.

[146] Internal conversation with H. Simgen.

[147] Internal conversation with S. Bruenner.

[148] The Borexino Collaboration. Comprehensive measurement of pp−chain solar neutrinos. *Nature volume 562, pages505−510*, 2018.

[149] EXO-200 Collaboration. Improved measurement of the $2\nu\beta\beta$ half-life of ^{136}Xe with the EXO−200 detector. *Phys. Rev. C89 015502*, 2014.

[150] Internal conversation with L. Althueser.

[151] CRC handbook of Chemistry and Physics. *87th, CRC Press, Boca Raton, FL*, 2006.

[152] D. Cichon. Identifying ^{222}Rn decay chain events in liquid xenon detectors. *Master thesis, University of Heidelberg*, 2015.

[153] Richard K. Kirby. Thermal expansion of polytetrafluoroethylene (Teflon). *https://nvlpubs.nist.gov/nistpubs/jres/057/jresv57n2p91A1b.pdf*, 1956.

[154] Introduction to comsol multiphysics. *https://cdn. comsol.com/documentation/5.2 1.*

[155] D. Cichon. Liquid xenon detector physics with xenon1t and hexe − electric noise stability, background discrimination studies and measurements of the scintillation pulse shape. *Ph.D. thesis, University of Heidelberg*, 2020.

[156] Smartec Company. *http://www.smartec-sensors.com/en/products/uti-interface-en.html*.

[157] A. Manalaysay et al. Spatially uniform calibration of a liquid xenon detector at low energies using ^{83m}Kr. *Rev. Sci. Instrum. 81:073303*, 2010.

[158] PostgreSQL Global Development Group. *https://www.postgresql.org/*.

[159] Nagios Enterprises. *https://www.nagios.org*.

[160] SuperCDMS Collaboration. Projected sensitivity of the SuperCDMS SNOLAB experiment. *Phys. Rev. D 95, 082002*, 2017.

[161] J. Amsbaugh et al. An array of low-background ^{3}He proportional counters for the Sudbury Neutrino Observatory. *Nucl. Inst. Meth. A 579, 1054−1080*, 2007.

[162] M. Leung. Surface contamination from radon progeny. *AIP Conf. Proc. 785, 184−190*, 2005.

[163] E. H. Miller et al. Constraining radon backgrounds in LZ. *arXiv:1708.08533v1*, 2017.

[164] D. Akerib et al. (LZ Collaboration). The LUX−ZEPLIN (LZ) radioactivity and cleanliness control programs. *arXiv:2006.02506*, 2020.

[165] L. Zhao et al. (PandaX Collaboration). PandaX: A deep underground dark matter search experiment in China using liquid xenon. *Mod. Phys. Lett. A33*, 2018.

[166] DARWIN Collaboration. DARWIN: towards the ultimate dark matter detector. *JCAP 1611 no.11, 017*, 2016.

[167] nEXO Collaboration. nEXO pre−conceptual design report. *arXiv:1805.11142*, 2018.

[168] C. Alduino et al. (CUORE Collaboration). CUORE−0 detector: design, construction and operation. *JINST 11 P07009*, 2016.

[169] GERDA Collaboration. The GERDA experiment for the search of $0\nu\beta\beta$ decay in ^{76}Ge. *Eur. Phys. J. C 73 2330*, 2013.

[170] H. Zou et al. Quantifying the triboelectric series. *Nat. Commun. 10, 1427*, 2019.

[171] J. Henniker. Triboelectricity in polymers. *Nature 196, 474*, 1962.

[172] C. Liu and A. J. Bard. Electrostatic electrochemistry at insulators. *Nat. Mater. 7, 505*, 2008.

[173] E.S. Morrison et al. Radon daughter plate−out onto teflon. *arXiv: 1708.08534v1*, 2017.

[174] K. Ozone. Liquid xenon scintillation detector for the new μ search experiment. *Phd. Thesis, University of Tokyo*, 2005.

[175] P. Majewski et al. (ZEPLIN-III). Performance data from the ZEPLIN−III second science run. *arXiv:1112.0080*, 2011.

[176] A. Dobi et al. Study of a zirconium getter for purification of xenon gas. *arXiv:1002.279*, 2010.

[177] N.Stojilovic et al. Surface chemistry of zirconium. *Progress in Surface Science. 78: 101-184*, 2005.

[178] E. Aprile et al. Measurements of the lifetime of conduction electrons in liquid xenon. *Nucl. Instrum. and Meth. A 300, 343−350*, 1991.

[179] M.Ichige et al. Measurement of attenuation length of drifting electrons in liquid xenon. *Nucl. Instrum. and Meth. A 333, 355−363*, 1993.

[180] A.Ferella et al. Purity measurements in liquid xenon. electron lifetime dependence on circulation time and rate. *www.lngs.infn.it/images/REIS/AnnualReport/PREPRINT/preprint97.pdf*, 2006.

[181] University of Zuerich. Xenoscope set-up. *https://www.physik.uzh.ch/en/groups/baudis/Research/Xenoscope.html*, 2020.

[182] S. Xiao et al. A review on sf_6 substitute gases and research status of cf_3i gases. *Energy Reports Volume 4*, 2018.

[183] Elma Ultrasonic. *https://www.elma-ultrasonic.com*.

[184] A. Manalaysay et al. Spatially uniform calibration of a liquid xenon detector at low energies using ^{83m}Kr. *Rev.Sci.Instrum.81:073303*, 2010.

[185] L. Baudis et al. Response of liquid xenon to compton electrons down to 1.5 keV. *Phys.Rev.D87:115015*, 2013.

[186] P. Sorensen. Anisotropic diusion of electrons in liquid xenon with application to improving the sensitivity of direct dark matter searches. *Nucl. Instr. Meth. A 635 41-43*, 2011.

[187] Internal conversation with D. Cichon and F. Joerg.

[188] T. Skwarnicki. Study of the radiative cascade transitions between the upislon−prime and upsilon resoncances. *Ph.D. thesis, Cracow Institute of Nuclear Physics, DESY*, 1986.

[189] Liquid xenon general properties. *https://userswww.pd.infn.it/ conti/LXe.html*.

[190] Hamamatsu Photonics. Handbook photomultiplier tubes basics and applications. *https://www.hamamatsu.com*, 2020.

[191] Leak detection technology. *http://www.leakdetection-technology.com/science/the-flow-of-gases-in-leaks.html*.

[192] P. Theodorsson. Background Components of low−level beta and gamma detectors. *Low-level measurements of radioactivity in the environment*, 1993.

[193] Z. Greene. The XENON1T spin-independent WIMP dark matter search results and a model to characterize the reduction of electronegative impurities in its 3.2 tonne liquid xenon detector. *Ph.D. thesis, Columbia University*, 2018.

[194] F. Agostini et al. (Darwin Collaboration). Sensitivity of the DARWIN observatory to the neutrinoless double beta decay of ^{136}Xe. *Eur. Phys. J. C 80, 808*, 2020.

List of Tables

List of Figures